

Applications of microRaman spectroscopy to the study of petrological, mineralogical and natural structural materials

by

Matthew J. Bloomfield
MSc (Leics) BSc (Anglia)

A thesis submitted for the degree of
Doctor of Philosophy
at the University of Leicester



Department of Geology
University of Leicester

September 2002

UMI Number: U164124

All rights reserved

INFORMATION TO ALL USERS

The quality of this reproduction is dependent upon the quality of the copy submitted.

In the unlikely event that the author did not send a complete manuscript and there are missing pages, these will be noted. Also, if material had to be removed, a note will indicate the deletion.



UMI U164124

Published by ProQuest LLC 2013. Copyright in the Dissertation held by the Author.
Microform Edition © ProQuest LLC.

All rights reserved. This work is protected against
unauthorized copying under Title 17, United States Code.



ProQuest LLC
789 East Eisenhower Parkway
P.O. Box 1346
Ann Arbor, MI 48106-1346

Applications of microRaman spectroscopy to the study of petrological, mineralogical and natural structural materials

MicroRaman spectroscopy represents a powerful tool for the study of crystal structure and identification of materials. Despite being widely used in other areas of scientific research it has yet to become a routine analytical technique within the Earth Sciences.

Case studies are used to describe the application of this technique. Using the different approaches available, a variety of materials of a mineralogical and petrographic nature are used to assess the usefulness and applicability of the technique.

Following a brief review of the fundamental theory of Raman scattering, a description of the analytical instrument is given and the format of the thesis explained. An existing database of mineral spectra is assessed, comprehensively edited and suggestions made for improvements. Mineral identification is implemented on several samples to emphasize advantages over other techniques. Investigations of changes in crystal structure are performed on biotite radiohaloes, zircons and quartz on the basis of spectra acquired. Dimension stone and brick provide examples of the suitability of microRaman spectroscopy to analysing the processes and transformations of natural materials, for industrial benefit. The potential to enhance the technique became evident and a gemstone macrochamber and 'well-plate' – type sample holder constructed to realise this. Circularly polarised light was investigated for collecting orientation-independent spectra.

The ability to collect structural information over a micrometer scale in the form of maps and images makes the technique attractive to mineralogists. Lack of sample preparation, disparity of sample type and sensitivity are all advantages over XRD, a favoured technique in the investigations considered.

MicroRaman spectroscopic study of minerals has been found to have few limitations. Notably, these are largely unpredictable fluorescence and potential for ambiguity of results. The technique has great prospects in the Earth Sciences and will become a routine analytical method.

Acknowledgements

I am grateful to EPSERC (award ref: 9800394X) for funding this research project and to the foresight of Prof David Pitt for recognising the need to get a mineralogist on board! The project was set up jointly with Mr. Kip Jeffrey and I thank them both for giving me the opportunity to get involved in this exciting and fascinating branch of science.

A number of people that have enabled me to complete this project and I am indebted to them. Acknowledgements are made to members of the Spectroscopy Products Division at Reinshaw plc, past and present. Dr. Annette Zimmerman for providing training all those years ago; Dr. Ian Hayward for helpful discussions, guiding me through some of the physics and for support. Thanks also to Dr. Ken Williams, Tim Smith, Dr. Laura Pickard and a host of others for encouragement and support.

I wish to thank the technical staff at the University of Leicester for their assistance in what was a fairly light burden, compared to many research projects. I owe a great deal to my contemporaries, Drs. Craig Buchan, Pat Thompson and Craig Storey. I hope you know how important you were (if you lot can do it, so can I!).

Samples for aspects of this study were gratefully received (eventually!) from Dr. Gavin Foster and Prof Randy Parrish and also from the Buildings Research Establishment. As well as providing minerals for this study, Dr. Jamie Nelson is thanked for offering fascinating scientific diversions, inspiration, friendship and for truly unbelievable stories. I hope we can continue to work together.

To my family and friends; thank you for your patience and support.

Lastly, and by no means least, I would like to thank Liz, whose unerring belief saw me through to the end. You were always there for me, even when you were going through unimaginable hardships (although there were many times when I would have gladly swapped you for the hours of drill, trench-digging and freezing rivers). I'll always look up to you.

Abstract	i
Acknowledgements	ii
Contents	iii
List of Figures	ix
List of Tables	xiii
Chapter 1 – Introduction	1
1 – Background	2
1.1 - Introduction	2
1.2 - Comparison between microRaman spectroscopy and analytical techniques used in the Earth Sciences	3
1.3 – Summary of Raman spectroscopy in the Earth sciences	5
Fluid inclusion analysis	6
Gemmology	6
Geological processes	7
Object d’Art and historical pieces	7
Palaeontology	8
1.4 - Related literature	8
2 – Basic theory	10
2.1 - Introduction	10
2.2 - Fundamental theory	11
Quantum theory	11
Classical theory	12
Internal motions of crystals	15
2.3 - The Raman spectrum	19
Line broadening and Intensity	22
Resolution and Signal to noise	24
2.4 - Fluorescence	25
2.5 - Polarisation studies	28
3 – Instrumentation and operation	29
3.1 - Introduction	29
3.2 - Spectral acquisition mode	29
CCD detector	37
Spectral analysis experimental set-up	38
Mapping experiments	39
3.3 - Imaging Mode	41
Image analysis experimental set-up	42
Flat-fielding	43
3.4 - Confocal arrangement	43
3.5 - Sampling	44
3.6 - Calibration	46
3.7 - Optimisation	47
3.8 - Data manipulation	47
Baseline correction	47

Smoothing	48
Curve-fitting	48
3.9 - Limitations and drawbacks of the technique and instrument	49
3.10 - Other manufacturers	51
4 – Aims of the project and outline	53
4.1 – Introduction	53
4.2 – Possible areas of exploration	53
Mineral identification	54
Crystal structure	55
Mapping	55
Imaging	55
4.3 – Format of the project	56
Chapter 2 – Fingerprint applications	57
5- Inorganic database development	58
5.1 – Introduction	58
5.2 – The Renishaw Raman Database of Minerals and Inorganic Materials	58
5.3 – Database development	60
5.4 – New additions	62
5.5 – Conclusion	64
6 - Suspected coesite inclusion	66
6.1 – Introduction	66
6.2 - Sample description	66
6.3 – Coesite	68
Chemistry and structure of coesite	68
Occurrence	68
Petrographic significance	69
Transformation of coesite to quartz	70
Textures	71
Identifying coesite based on textural evidence	73
6.4 - Vibrational spectroscopy of coesite	73
6.5 - Analysis and Results	74
EMPA	75
SEM	75
MicroRaman spectroscopy	76
6.5 Silica glasses (vitreous silica)	81
Introduction	81
The structure of vitreous silica	82
The spectrum of vitreous silica and band assignments	83
High frequency region	84
Mid frequency region	85
Low frequency region	85
6.6 - Discussion	86
Geological significance	88

6.7 - Conclusion	90
6.8 – Further work	91
TEM	91
SNOM, AFM, STM	92
NMR	92
IR spectroscopy	92
ESI (Electron Spectroscopy Imaging)	93
Chapter 3 – Crystal structure investigations	94
7 – Inclusion haloes in biotite	95
7.1 - Introduction	95
Inclusion haloes	95
Biotite chemistry and structure	95
Raman and vibrational spectroscopy of layer silicates	97
7.2 – Sample	99
7.3 – Experimental	100
7.4 - Results	103
MicroRaman spectroscopy	103
EMPA	112
7.5 - Discussion	113
Contemporaneous studies – Nasdala <i>et al</i>	116
7.5. – Conclusion	117
8 – Investigation of Cubic Zirconia	119
8.1 – Introduction	119
8.2 - Crystal structure of cubic zirconia	120
8.3 - Samples	121
8.4 - Review of colour theory	121
8.5 - Analysis	126
XRF	127
Raman spectroscopy	127
8.6 - Results	127
XRF and spectroscopy	127
Raman spectroscopy	128
8.7 – Discussion	133
Low wavenumber region	134
Mid wavenumber region	135
High wavenumber region	139
Comparison of the spectra	140
Raman spectra and colour centres	141
8.8 – Conclusion	142
8.9 – Further work	143
9 - Applications of Raman spectroscopy to geochronological zircon	146
9.1 Introduction	146

9.2 Geochronology/Isotopic dating	146
9.3 Pb loss in zircon	147
9.4 Mass Spectrometry techniques	148
Grain selection for MS	149
9.5 Metamictisation	150
Annealing	154
9.6 Raman spectroscopy of zircon	155
Samples	160
9.7 Global Raman imaging	160
Introduction	160
Samples	161
Experimental	161
Results and Discussion	161
9.8 Depth profiling	163
Introduction	163
Samples	164
Experimental	164
Results and Discussion	165
9.9 Line focus mapping of zircon grains	171
Introduction	171
Line focus mapping	172
Samples	173
Experimental	173
Results and Discussion	174
9.10 Analysis of laser ablation ejecta	177
Introduction	177
Samples	178
Experimental	178
Results and Discussion	179
9.11 Conclusions	181
Chapter 4 – Processes and transformations affecting natural materials	183
10 - Investigation of strained silica	184
10.1 – Introduction	184
The ASR reaction	184
Reactive silica	185
Samples	185
10.2 – Stress measurement using Raman spectroscopy	186
10.3 – Vibrational spectroscopy of quartz	187
10.4 – Experimental procedure	189
10.5 – Results	191
10.6 – Discussion	193
10.7 – Conclusion	195
10.8 – Further work	196

11 - Investigation of stained dimension stone	197
11.1 - Introduction	197
Review of discolouration mechanisms	197
11.2 - Samples	199
11.2 - Experimental procedures	200
XRD analysis	201
SEM analysis	201
Raman microprobe analysis	202
Mineral separation	202
11.3 Results	202
Filter paper and residue analysis	206
11.4 - Discussion	208
11.5 - Conclusion	212
11.6 - Further work	213
12 - Investigation of fired clay bodies	214
12.1 – Introduction	214
Previous work	214
12.2 – Sample material	215
Preparation of briquettes	215
Firing conditions	216
Petrography	216
500 °C	216
1000 °C	217
2.3 – Analysis and Results	219
X-ray diffraction	219
MicroRaman spectroscopy	220
2.4 – Discussion	223
2.5 – High temperature Raman analysis	228
2.6 – Conclusion	229
2.7 – Further studies	230
13 - Investigation of limestone organic content	232
13.1 – Introduction	232
13.2 – Samples	233
Petrography	233
13.3 – Experimental procedure	235
13.4 – Results	238
13.5 – Discussion	235
13.6 – Conclusion	244
13.7 – Further work	245
Chapter 5 – Technique development	248
14 – Gem analysis macrochamber	249
14.1 – introduction	249
14.2 – Macrochamber design and use	249

14.3 - Conclusion	252
14.4 – Further work	253
15 - Investigation of circularly polarised light	254
15.1 – Introduction	254
15.2 – Polarisation of Raman bands	255
15.3 – Circularly polarised light	256
15.4 – Samples	261
15.5 – Results	261
15.6 – Discussion	263
15.7 – Conclusion	266
15.8 – Further work	267
16 - Automated mineral discrimination	269
16.1 - Introduction	269
16.2 - Decay schemes	269
16.3 - Physical properties	270
16.4 - Raman spectroscopy	270
Sample holder	271
Analytical procedure	273
16.5 - Software/Graphical User Interface	273
Acquisition	273
Auto options	273
Select discrimination method	274
Precision	275
Displaying results	275
16.6 - Conclusion	278
Chapter 6 – Conclusions and suggestions for further work	279
17 – Conclusions and further work	280
17.1 - Introduction	280
17.2 - Chapters 2, 3 4 and 5	280
17.3 – Summary of conclusions	284
14.4 – General conclusions	286
17.5 – Further work	288
Appendix	291
References	317

List of Figures

	page
Fig. 2.1. Energy level diagram	12
Fig. 2.2. Changes in the polarisability ellipsoid of CO ₂ during vibrations	14
Fig. 2.3. A Raman spectrum from a linarite crystal.	20
Fig. 2.4. Definition of FWHM (full width at half maximum).	21
Fig. 2.5. Comparison of Lorentzian, Gaussian and mixed Lorentzian and Gaussian distributions.	23
Fig. 2.6. Effect of using alternative excitation wavelength.	25
Fig. 3.1. Schematic diagram and photo image of Renishaw RM2000 Raman microscope	30
Fig. 3.2. Removal of the PLRF.	32
Fig. 3.3. An example of the computer monitor image recorded by the microscope camera.	32
Fig. 3.4. Position of the switching mechanism below trinocular head.	33
Fig. 3.5. Motorised kinematically mounted filters on rotary mount.	34
Fig. 3.6. Location of the mechanical slit within the instrument.	35
Fig. 3.7. Software-controlled double-sided grating.	36
Fig. 3.8. Kinematic lenses: the lens-before-the-slit, pre-grating lens, pre-camera lens.	36
Fig. 3.9. Experiment parameters set-up 'window'.	38
Fig. 3.10. Screen-grab of the results of Raman area mapping of an etched Si chip.	41
Fig. 3.11. Example of Raman global imaging results.	42
Fig. 3.12. Loading a slide on the mapping stage beneath the objective.	45
Fig. 3.13. Manual multi point baseline correction.	48
Fig. 3.14. Multiple curves fitted to complex Raman band system.	49
Fig. 5.1. Example of library searching.	60
Fig. 5.2. 'Hit' text available for search matches.	61
Fig. 5.3. Representation of one-mode behaviour in solid solution Raman spectra.	63
Fig. 5.4. Representation of two-mode behaviour in solid solution Raman spectra.	63
Fig. 6.1. Approximate stability field of coesite.	67
Fig. 6.2. CalTech coesite Raman spectrum.	70
Fig. 6.3. PPL image of suspected coesite inclusion in omphacite.	74
Fig. 6.4. Fore-scatter SEM image of suspected coesite inclusion.	75
Fig. 6.5. Suspected coesite inclusion surrounded by α -quartz.	77
Fig. 6.6. Representative Raman spectrum from suspected coesite inclusion.	78
Fig. 6.7. Reference Raman spectra of omphacite and mounting medium.	79
Fig. 6.8. Raman spectrum showing characteristic Raman band of α -quartz.	80
Fig. 6.9. Map showing area under 670 cm ⁻¹ band	80
Fig. 6.10. Map showing area under 464 cm ⁻¹ band.	80
Fig. 6.11. Polarised Raman spectra of vitreous silica.	81
Fig. 6.12. Simplified diagram showing difference between long- and short-range order.	83
Fig. 7.1. Plan view of phyllosilicate structure.	96
Fig. 7.2. y-axis view of biotite structure.	97
Fig. 7.3. Image of typical biotite grain from Bodmin Granite.	100
Fig. 7.4. Raman spectrum of monazite microinclusion. Inset: white light image of inclusion and halo.	104

Fig. 7.5 Raman spectrum of analysed apatite inclusion. Inset: white light image of inclusion.	104
Fig. 7.6. Biotite Raman spectrum from sample and that from a reference biotite.	105
Fig. 7.7. Raman spectrum of normal biotite and the dark halo regions.	105
Fig. 7.8. Raman spectrum of the OH stretching region of normal biotite grain (confocal mode).	106
Fig. 7.9. Raman spectrum of the OH-stretching region of the dark halo region (confocal mode).	107
Fig. 7.10. Example area map showing prismatic inclusion, halo and unaltered biotite.	108
Fig. 7.11. Reflected light image of an inclusion and halo region analysed.	108
Fig. 7.12. Line map from inclusion to unaltered region of biotite.	109
Fig. 7.13. Line map showing portion of OH-stretching region.	109
Fig. 7.14. CPL image of a prismatic apatite inclusion with halo in biotite.	110
Fig. 7.15. Line map from apatite inclusion through halo to unaltered biotite.	110
Fig. 7.16. Line map from inclusion to unaltered biotite using 785 nm excitation.	111
Fig. 7.17. Raman spectra from the near-IR line map, glass and mounting medium.	111
Fig. 7.18. EMPA results from biotite and halo (perpendicular to cleavage).	113
Fig. 7.19. EMPA results from biotite and halo (parallel to cleavage).	113
Fig. 8.1. Cubic zirconia crystals.	122
Fig. 8.2. Divalent cation impurity in monovalent ion lattice	123
Fig. 8.3. Monovalent cation impurity in divalent ion lattice	123
Fig. 8.4. Raman spectra of sample cubic zirconia.	131/132
Fig. 8.5. Complex band systems for the low, middle (F_{2g}) and upper regions of the Raman spectra.	132
Fig. 8.6. Position of the F_{2g} band for the samples highlighted.	137
Fig. 8.7. Relationship between F_{2g} band and dopant by XRF and light spectroscopy.	137
Fig. 8.8. Relationship between F_{2g} band and Y, Cr and Nd dopants determined by XRF and spectroscopy.	138
Fig. 8.9. The 952 cm^{-1} band of sample cubic zirconia.	139
Fig. 8.10. The high wavenumber 'doublet' feature of sample cubic zirconia.	140
Fig. 9.1. Zircon Raman spectrum.	156
Fig. 9.2. PPL white light image and Raman image (1003 cm^{-1}) of zircon grain.	162
Fig. 9.3. Detail of Raman spectra from regions of grain shown in Figure 9.2.	163
Fig. 9.4. Depth profile of Si.	166
Fig. 9.5. Intensity profile of Si depth map.	166
Fig. 9.6. Screen capture showing results of Si intensity profile with depth.	167
Fig. 9.7. Depth mapping experiment through zircon.	168
Fig. 9.8. Raman spectrum of immersion oil and expanded portion to show mid-wavenumber range.	168
Fig. 9.9. Zircon sample spectrum and reference zircon spectrum.	169
Fig. 9.10. $\nu_3(\text{SiO}_4)$ band through zircon core.	170
Fig. 9.11. FWHM and position of zircon $\nu_3(\text{SiO}_4)$ band with depth.	170
Fig. 9.12. Line focus mapping of large area with four different species.	173
Fig. 9.13. White light image and FWHM map from Raman experiment using line focus attachment.	174
Fig. 9.14. Intensity map of the zircon ν_3 band for the first LFM experiment.	175
Fig. 9.15. White light image and FWHM map from second Raman experiment using line focus attachment.	175
Fig. 9.16. Indication of the importance of truly flat zircon surface.	176
Fig. 9.17. Image of crystalline zircon with four ablation pits.	178
Fig. 9.18. Variation in FWHM for $\nu_3(\text{SiO}_4)$ in ablated zircon.	179

Fig. 9.19. Mapped area of ablated zircon and map of the FWHM of $\nu_3(\text{SiO}_4)$	179
Fig. 9.20. Comparison of Raman spectra from regions within ablated sample.	180
Fig. 10.1. Unpolarised and polarised Raman spectra of stressed CVD diamond	186
Fig. 10.2. α -quartz Raman spectrum.	189
Fig. 10.3. Quartz grain showing undulose extinction.	190
Fig. 10.4. Individual curves fitted to the complex band shapes of the A_1 modes at $\sim 207 \text{ cm}^{-1}$ and $\sim 464 \text{ cm}^{-1}$.	191
Fig. 10.5. Frequency positions of pressure and temperature dependent quartz Raman bands.	192
Fig. 10.6. Selected region of the quartz Raman line map experiment highlighting the change in intensity of the 207 cm^{-1} band.	193
Fig. 11.1. Photographs of sample BRE02.	200
Fig. 11.2. Overlaid XRD spectra of the upper and lower surfaces of sample BRE 02.	203
Fig. 11.3. Raman analysis of spot adjacent to pyrite grain.	204
Fig. 11.4. Raman analysis of spot adjacent to pyrite grain.	204
Fig. 11.5. Raman spectrum of stained area.	205
Fig. 11.6. Red brown crystal retained in filter paper.	206
Fig. 11.7. Comparison of the Raman spectra of filter paper and red crystal trapped in the filter.	207
Fig. 11.8. Image of particle aggregate found in filter paper.	208
Fig. 11.9. Raman spectrum of aggregate shown in Figure 11.8.	208
Fig. 11.10. Raman spectrum of melanterite, an Fe sulphate crystal.	211
Fig. 12.1. White light image from section through middle of sample fired to 500°C .	217
Fig. 12.2. White light image from section through outer edge of sample fired to 500°C .	217
Fig. 12.3. PPL image from 1050°C sample showing pore space layer.	218
Fig. 12.4. PPL image from 1050°C sample showing acicular crystal.	218
Fig. 12.5. Hematite reference spectrum and hematite from sample 5M.	221
Fig. 12.6. Goethite reference spectrum and goethite from sample 5M.	222
Fig. 12.7. Reference anatase spectrum.	222
Fig. 12.8. α -quartz Raman spectrum from needle in sample 5M and reference sample	223
Fig. 12.9. Reference ilmenite spectrum.	225
Fig. 12.10. Reference mullite spectrum.	226
Fig. 13.1. Low magnification PPL images of bioclastic limestone.	234
Fig. 13.2. White light images (PPL) of bituminous matter in limestones.	234
Fig. 13.3. Raman spectrum of amorphous, bituminous matter.	236
Fig. 13.4. Curve fitting of five first order carbon Raman bands.	236
Fig. 13.5. Filter spectrum of G band.	236
Fig. 13.6. Curvefit of G band and a defect band.	236
Fig. 13.7. Defocused spots with green and red excitation.	237
Fig. 13.8. Raman image of pyrite in quartz to highlight spatial resolution.	238
Fig. 13.9. Imaging of bituminous matter in limestones.	239
Fig. 13.10. Imaging of bituminous matter in limestones.	240
Fig. 13.11. Raman image from uncorrected data and two images from flat-field corrected data	241
Fig. 13.12. Filter spectrum of G band and approximate position of filter bandpass.	242
Fig. 13.13. Grating spectrum of calcite from limestone used and the position of the filter.	242
Fig. 13.14. Raman imaging of calcite grains with organic matter.	243
Fig. 13.15. Possible response of chemically zoned crystal to Raman imaging.	246

Fig. 14.1. Hardware configuration of RA 100 equipped with fibre probe head and camera.	250
Fig. 14.2. Gem analysis macrochamber.	252
Fig. 15.1. Effect of adding a quarter wave plate at 45° to the linear polarisation direction.	257
Fig. 15.2. Procedure to test circularity of polarised light using quarter wave plate.	258
Fig. 15.3. Effect of adding a quarter wave plate to red and green linearly polarised excitation.	258
Fig. 15.4. Ellipses fitted approximately to the vectors from Figure 15.2.	259
Fig. 15.5. Tourmaline Raman spectra using linear and circular polarised light.	260
Fig. 15.6. Orientations of the nepheline crystal used for experiments.	265
Fig. 16.1. Technical drawing of the design submitted for the manufacture of a prototype sample holder.	272
Fig. 16.2. Photograph of the prototype aluminium sample holder.	272
Fig. 16.3. Impression of the graphical user interface for mineral discrimination.	276
Fig. 16.4. Raman spectrum recorded for zircon.	277
Fig. 16.5. Raman spectrum recorded for rutile.	277

List of Tables	page
Table 1.1. Summary of common analytical techniques in mineralogy.	4
Table 2.1. Character table for molecules of C_{4v} symmetry.	17
Table 2.2. The most common excitation wavelengths used in Raman spectroscopy.	26
Table 8.1. Cubic zirconia samples.	126
Table 8.2. XRF analysis of CZ crystals.	128
Table 8.3. Positions of bands by curve fitting.	129
Table 8.4. Irreducible representations for cubic zirconia	130
Table 8.5. Atomic masses and ionic radii of the REE ³⁺ suspected to be dopants in sample CZs.	133
Table 8.6. Summary of spectral comparisons for related samples.	141
Table 9.1. Positions of the most intense Raman vibrational modes of zircon and their assignments.	156
Table 9.2. Classification of the degree of metamictisation.	157
Table 10.1. Summary of the vibrational modes of α -quartz.	188
Table 10.2. Pressure dependence of quartz Raman bands.	191
Table 11.1. Raman band positions of calcite, dolomite and siderite.	203
Table 11.2. Positions of some Raman bands in some sulphates and apatite	210
Table 12.1. Results of XRD analyses	219
Table 13.1. Properties of the 20x and 50x objectives for imaging experiments.	235
Table 15.1. Sample minerals selected and their system.	262
Table 15.2. Summary of circularly polarised light experiments.	263
Table 16.1. Summary of minerals frequently used for isotopic dating.	270
Table 16.2. Common methods of separating minerals on the basis of physical properties.	271

Chapter 1 – Introduction

This chapter comprises sections 1, 2, 3 and 4 of the current work. It aims to introduce the research project undertaken and place Raman spectroscopy in the context of analytical techniques in the Earth sciences.

A brief review of the theory of Raman spectroscopy is provided and a description of the microRaman instrumentation used throughout this work.

Finally, the outline and aims of the project are discussed with an explanation of the format used and the subject areas undertaken.

1- Project background

This opening section is intended to introduce the research study and place microRaman spectroscopy in the context of analytical methods used in the Earth sciences.

1.1 - Introduction

The premise of this project had inauspicious beginnings. The obituary of Prof. Ansell Dunham detailed his extensive knowledge of, amongst many things, clay minerals. Dr. David Pitt, then the M.D. of the Spectroscopy Products Division of Renishaw, plc (based in Wotton-under-Edge, Gloucestershire) had recognised the need for expanding his Division's knowledge and experience of mineralogical materials in the burgeoning market of analysis by Raman spectroscopy. Contact with Mr. C.A. Jeffrey at the University of Leicester resulted in the instigation of a Ph.D. research project to investigate the *application of Raman spectroscopy to a range of mineralogical materials and mineral based processes*. Post-war technological advances have led this technique to an almost exponential rise in applications. It is successfully employed in all areas of manufacturing and scientific research and development. In the Earth sciences its use has been less dramatic; traditional X-ray techniques have remained central despite the method offering a new perspective.

It serves here to mention that the technique of microRaman spectroscopy uses laser energy to provide a sensitive probe of a material's structure. Qualitative information on the presence of molecular functional groups can be easily and rapidly obtained in a non-destructive manner. The technique provides no chemical information except that indicated by matching reference spectra of known materials.

Following a general introduction to the instrumentation and theory underlying the Raman phenomenon, sections 2 and 3 respectively, a detailed account of the project aims is given in section 4.

1.2 - Comparison between microRaman spectroscopy and analytical techniques used in the Earth Sciences

The analytical tools available to those studying minerals are many and varied both in their complexity and *scale* of analysis. The type of information required largely dictates the instrument used. A geologist or mineralogist may, for example, only require a simple loupe to identify the constituent mineral species of a rock, but a mass spectrometer to quantify the Pb isotope ratio in a zircon grain. Whilst generalisations in a field as broad as mineralogy are impossible, it can be stated that the interests of the mineralogist and petrologist often lie in the micro-scale. That is to say, features that exist on a scale measured in micrometers and, with advances in instrumentation, nanometers. A mineralogist may then use the EMPA or XRF for quantitative chemical analysis and XRD to provide crystal structural information. There are of course a multitude of other analytical techniques, however, few could be considered routine. Of these, Raman spectroscopy is a relatively new addition to the array of methods on offer, even though the technique was described in 1930. Named after the Indian scientist C.V. Raman, it is, as the name suggests, a technique involving the study of energy (light) and has much in common with the more familiar technique of infrared (IR) spectroscopy. Table 1.1 compares the more commonly available techniques in mineralogy for comparison with Raman spectroscopy.

From Table 1.1 it can be seen that when combined with a microscope, Raman spectroscopy offers the user a means of investigating his mineralogical samples that could not be achieved by any other single method. Samples may be presented as thin sections that can also be used in the SEM, for example; as powders that can then be analysed by XRD; as a hand specimen; or even as pellets used in the XRF instrument, all without the need for further preparation. Structural information derived from Raman spectra can be likened to that from XRD but with the advantage that spatial relationship is preserved. Chemical information can often be derived by interrogation of the data and by reference to known samples and, whilst not comparable to the quantitative X-ray techniques, can often be used to comment upon light elements. And since the spectra are a function of functional groups in the sample, the chemical information from Raman spectra can be more useful than that from other methods. The ability to perform 'mapping experiments' allows discussion of the spatial distribution of components and cannot be achieved

Technique	Information	Sample prep.	Destructive?	Other remarks
SEM	Textural (quantitative/qualitative chemical if EDX/WDX fitted)	Sample size limited by chamber (max. few cm's). Generally must be coated (C or Au/Pt). (polished) thin sections possible.	No. Can be re- analysed in SEM. Coating non- removable.	<ul style="list-style-type: none"> • High requirement for consumable liquid N. • Can be combined with Raman • Instrumentation cost very high
Powder XRD	Structural. Mineral identification	Very finely comminuted by crushing, milling and grinding.	Yes, although powder may be re-analysed	<ul style="list-style-type: none"> • Poor sensitivity
Single crystal XRD	Crystallographic structure	Very minute crystals required	No, although may induce colour change	<ul style="list-style-type: none"> • Interpretation of information quite specialised
XRF	Quantitative chemical	Crushing, milling and grinding. Powder pressed into pellet or melted in flux to form fused bead	Yes, although pellets and beads may be re- analysed.	<ul style="list-style-type: none"> • Sample prep. highly time-consuming. • Instrumentation costs relatively high • Data can be ambiguous • Analysis automated
EMPA	Quantitative chemical	C-coated uncovered polished thin sections	No	<ul style="list-style-type: none"> • High requirement for consumable liquid N. • Poor detection limits for some elements • <i>In situ</i> 'point' technique preserves textural relationships • C-coating may be polished off
ICP-MS/AES	Quantitative chemical	Extensive. Bulk samples of finely comminuted rock or separated mineral species must be dissolved in acid	Yes. Sample in solution is vapourised.	<ul style="list-style-type: none"> • High requirement for consumables. • Instrumentation costs high • Sample prep. can be very time-consuming and potentially hazardous
CL	Qualitative chemical	Polished sections	No	
Raman	Crystallographic structure (single points, 2D maps, depth profiles), chemistry may be inferred, mineral identification	Negligible. Thin sections, bulk samples, liquids, gases. Powders can be intractable.	No, unless thermally sensitive (any damage is highly localised)	<ul style="list-style-type: none"> • Very rapid analysis • Can also perform PL • Consumables negligible (lasers have lifetimes of many thousands of hours) • Relatively inexpensive • Easy to use • Fluorescence can be problematic

Table 1.1. Summary of common analytical techniques in mineralogy.

by other methods. The ability to store mineral spectra and create searchable databases can be compared only with XRD, however, Raman spectra are easier to interpret than diffraction patterns and are more revealing. The instrumentation is relatively cheap, requires no consumables and is easy to use.

Exploiting the Raman scattering phenomenon has enabled studies as diverse as *in vivo* medical examinations to the study of cosmic dust particles. Consequently, the number of published texts relating to Raman spectroscopy is equally large. However, the current range of applications in mineralogy is restricted.

1.3 – Summary of Raman spectroscopy in the Earth sciences

Probably the most voluminous area of published Raman studies in the Earth Sciences belongs to the identification of minerals. The growth in the use of Raman scattering in this respect is attributed to the unequivocal and unambiguous assignment of a mineral to its Raman spectrum; every substance can be considered to have its own characteristic Raman spectrum, essentially based on the response of the structure to a laser beam. Proprietary Raman databases exist alongside those held in the public domain that allow an unknown crystal's spectrum to be compared against reference spectra and the identity determined. The general form of the relevant literature is to relate the structure and crystal symmetry to the spectra by use of Factor Group Analysis (FGA), and the application of selection rules. Examples of these include: Bühn *et al* (1999), Porto *et al* (1967), McKeown *et al* (1999), Forbes *et al* (1988), Frost *et al* (1997), Mernagh *et al* (1993) and Wopenka *et al* (1999). These works provide excellent reference sources since an increasingly broad database of the positions and behaviour of different functional groups in mineral crystal systems can be built up. In particular are studies by Mernagh (1991) and Frost (1996) that provide invaluable spectral data on the feldspars and kaolinite polymorphs, respectively. Raman spectroscopy is an extremely useful tool for this purpose. Other mineral polymorph determination studies can be found in Rodgers (1992) and Ervin (1952). There are, however, some minerals that, for various reasons, are intractable to analysis by Raman spectroscopy. Theoretical considerations dictate that minerals with strongly ionic structures, i.e. metals, will not produce Raman spectra. Galena, with the highly ionic zinc blende structure, is an example. Fluorescence is the single greatest impediment to Raman analysis. The

mechanisms, and methods to circumvent the problem, are explained further in Section 2 (Basic Theory of Raman Scattering).

A growing number of minerals can be considered to be very well understood in terms of their Raman spectra in relation to their structure. Among these are the relatively simple molecules diamond, quartz, zircon and the carbonates. However the long-established use of IR spectroscopy in organic chemistry means that the state of knowledge in this field is far more advanced. Indeed, explanations of the theory of the phenomenon are invariably based on organic compounds. The monograph of Farmer (Ed. 1974) entitled 'The Infrared Spectra of Minerals' covers all aspects of the vibrational study of minerals. As will be highlighted later, many of the considerations of the IR analysis of minerals apply to Raman spectroscopy.

Roberts & Beattie (**In:** Potts, Bowles, Reed and Cave, 1995) provide a clear and concise contemporary précis of the use of microRaman spectroscopy in the Earth sciences. Some of the more widely addressed areas are mentioned here.

Fluid inclusion analysis

The analysis of fluid inclusions represents an important area in the analysis of some minerals, particularly ore suites, which can lead to detailed information concerning the paragenesis. This information can be used for modelling and to improve the understanding of the formation of economically important deposits. Temperature and pressure conditions and some aspects of composition, for example, salinity, can all be determined using the traditional methods. Recently, Raman spectroscopy has been combined with the more traditional microthermometric approach to enhance these studies. A powerful analytical tool, microthermometric data can be ambiguous since it does not permit the unambiguous identification of the components. The use of microRaman spectroscopy achieves this.

Gemmology

Raman spectroscopy is playing an increasingly important role in gemmology. However, the relatively high cost of the instrumentation still largely precludes it from all but the large gem-testing laboratories; significantly less complex instruments can achieve the identification of gemstones. Raman spectroscopy offers advantages in that considerably more information can be

determined and without the potential to induce colour modification that X-ray methods have been associated with. In an attempt to remain ahead of gem treaters and synthesisers, Raman spectroscopy is seen as an effective tool. In a recent study (for example, Collins *et al*, 2000) it was shown that natural colourless type IIa diamonds could be distinguished from colourless diamonds that had been heat-treated at high pressure to remove their natural brown colour. It can be expected that this technique will play an increasingly important role in the field of coloured gemstones.

Geological processes

Applications of the technique to geological processes include Myneni *et al* (1998), Rodgers *et al* (1989), Liu *et al* (1990) and Cesare *et al* (1999). The latter used Raman spectra to distinguish between four different types of graphite to indicate grades of metamorphism and the extent of disequilibrium during anatexis. Liu *et al* (1990) were able to define a P-T curve for the entrapment of garnet in diamond in an attempt to define the conditions of formation of eclogite-paragenesis diamonds. Raman spectroscopy in these studies allows very precise analysis of modifications in the behaviour of specific functional groups in molecules to model geological conditions. Vibrational spectroscopy appears to be the only technique that permits this. Of the spectroscopic techniques, Raman spectroscopy appears to have many advantages over IR spectroscopy in the analysis of minerals. Although complementary to IR spectra, Raman bands are sharper and due to theoretical considerations, Raman spectra are more populated with features than IR spectra. In addition, Raman spectroscopy is a true microtechnique, allowing more specific analyses to be performed.

Object d'Art and historical pieces

One area in which the Raman spectroscopic analysis of minerals is rising is in the analysis of inorganic pigments used in manuscripts, paintings, frescos and ceramics. Such analysis aids conservators and restorers and may become important in the authentication of artwork. Clark (2001) cites the major advantages of microRaman spectroscopy in this area as the ability to perform *in situ*, non-destructive analyses that are highly reproducible. The technique is established as a highly sensitive method of determining the nature of individual pigment particles without interference from binding agents or other pigment particles. Examples of the minerals forming early artists' palettes are pyrolusite (black), azurite (blue), goethite (brown/orange),

malachite (green), realgar (red), anatase (white) and orpiment (yellow). All are easily determined using the technique and distinguishable between similar colours and hues based on their Raman spectra. An increasing body of literature is building as more curators recognise the potential, especially when combined with Laser-Induced Breakdown Spectroscopy (LIBS) (see Clark, 2001 for numerous references) of microRaman spectroscopy and the instrumentation becomes more widely accessible.

Other museum and archaeological objects, too, are benefiting from the recent ascent of the technique. Mineral particles detected in the markings of maps (Brown, *unpublished*, In: Clark, 2001) and ancient skeletal remains (Edwards *et al* 2001) are examples of where the method has contributed to our understanding of the objects that, perhaps, could not have been learned otherwise.

Palaeontology

Perhaps one area of the Earth sciences where the technique has yet to make a significant impact is in the analysis of fossils and remains preserved in rock. Analysis by Raman microprobe may be able to contribute to preservation, particularly where organic matter has been preserved.

Often, these samples are very delicate, limiting the applicable techniques. In contrast, microRaman spectroscopy is non-contact and nominally non-destructive.

In a recent study, Schopf *et al* (2002) used the method to help demonstrate that organic matter in rocks over three billion years old represented the poorly preserved remnants of microbial life.

1.4 - Related literature

Roberts *et al* (1995) are just one of the many that state that it was the advent of continuous wave, CW, lasers in the 1960's that sparked the rapid increase in Raman spectroscopy and saw the technique begin to increase in mineralogical analytical work. However, it is still a relatively new tool to the Earth Sciences. Indeed, as recently as 1973 Wilkinson (In: Anderson, 1973) acknowledged the work done on minerals and encouraged its development. In the field of mineralogy the literature falls into several general areas. Raman spectroscopy is often included in texts covering absorption spectroscopy, particularly alongside Infrared, IR. Mottana *et al* (1990),

McMillan *et al* (1988), Roberts *et al* (1995), Griffith (1974, 1975) and Ahrens (1995) all describe the phenomenon with respect to crystals, generally using molecular systems familiar to the mineralogist. Several of these accounts provide summaries of work up to that point relating to the various mineral structure groups. McMillan *et al* (1988), particularly, but also Griffith (1987), summarise the extent of crystal structure knowledge gained from Raman spectroscopy on these groups. Texts more specific to Raman spectroscopy in the Earth Sciences include McMillan (1989), Griffith (1975) and White (1975). Indeed, the work published by Griffith (1975) remains a *vade mecum* for the mineralogist using Raman spectroscopy by providing peak positions for a very large number of minerals. Similarly, Wilkinson (**In:** Anderson, 1973) provides a useful guide to the analysis of crystals. Although largely based on the theoretical prediction of Raman peaks on pure synthesised crystals it contains several naturally-occurring species as examples.

Far more generalised texts concerning microRaman spectroscopy, covering the optical theory of Raman spectrometers and related spectroscopic techniques, e.g. Fourier-Transform (F-T) spectroscopy (both FT-IR and FT-Raman), CARS and Surface Enhanced Raman Scattering (SERS), can be found in Gardiner *et al* (1989) and Rosasco (1982). These rather specialised forms of the phenomenon will not be considered further in any detail in this study .

An excellent general text accurately entitled the ‘Fundamentals of Molecular Spectroscopy’ (Banwell and McCash, 1994) guides the reader of modest solid state physics background through the principles of electromagnetic radiation and the related spectroscopic methods. In-depth treatments of Raman phenomenon theory can be found in Long (1977) and Colthup *et al* (1964). The latter describes itself as presenting theory on an elementary level but is still largely beyond the reach of the novice spectroscopist. A discussion of crystal symmetry and point groups, subjects familiar to the mineralogist, is given and leads to a treatment of more esoteric topics such as selection rules and FGA. Long (1977) provides a summaritive account of the theory of Raman scattering. The text takes a very mathematical approach but all aspects of the phenomenon are covered in detail. A very readable text covering theoretical considerations as well as instrumentation and applications is given by McCreery (2000).

2 – Basic Theory of Raman Scattering

In order to understand the potential mineralogical applications of Raman spectroscopy, a brief review of the underlying theory is presented. The aim is to provide a brief, simplified outline of the principles that will aid the understanding of subsequent chapters and subsections. The reader is directed to the references cited in section 1 for a more complete discussion.

2.1 - Introduction

Raman spectroscopy is one of a group of techniques that can collectively be described as molecular spectroscopic techniques. Fundamentally, each is concerned with the interaction of some region of the electromagnetic spectrum with matter on a molecular level. The precise nature of the interaction differs with each of these regions.

As with infrared region interactions, Raman spectroscopy is concerned with molecular vibrations. The basic tenet is that a beam of electromagnetic radiation, a source of energy that interacts with a molecule, for example, will have its energy reduced as it elevates that molecule to a new energy level. A molecule in space may possess rotational, vibrational or electronic energy and may exist in a variety of levels, the transitions between which require a finite quantity of energy. A plot of the frequency range of incident energy against absorbance will exhibit a peak corresponding precisely to the frequency of this quantity of energy. If we consider an incident monochromatic beam of radiation in the visible region of the spectrum interacting with a sample, components of the light may be transmitted, absorbed and re-emitted or ‘elastically’ scattered with unchanged energy. This latter component may account for around 0.001% (Roberts *et al*, 1995) of the incident energy. Of this small fraction, a further, minor component, of the order 0.001% (McMillan *et al*, 1988), is scattered with a *change* in energy. It has been ‘inelastically’ scattered. This discrete energy difference occurs both above and below that of the incident energy. C.V. Raman predicted the occurrence of this inelastically scattered light caused by molecular vibrations; “the periodic displacements of atoms from equilibrium positions” (Banwell and McCash, 1994).

2.2 - Fundamental theory

Both quantum mechanics and a classical mechanical approach are routinely invoked to explain the phenomenon. Again, the reader is referred to the texts listed in section 1 for a more complete discussion.

Quantum theory

The incident radiation can be considered to be a stream of photons with a distinct value of energy, $E = h\nu$ (where h is Planck's constant and ν is the frequency). The interactions with molecules may be 'elastic' and the photon is scattered with unchanged energy. 'Inelastic' collisions arise when energy is exchanged between molecule and photon; the molecule either gains or loses energy, ΔE , corresponding to the transition to a new rotational or vibrational energy level in accordance with quantal laws (Banwell *et al*, op. cit.). The scattered photon consequently has energy $\Delta E = \pm h\nu$ and frequency $\nu = \pm \Delta E/h$. Photons colliding with molecules have been likened to ball bearings striking a drum. The interactions may be perfectly elastic; the ball bearing is bounced from the drum with identical energy. Inelastic interactions may see the ball bearing lose energy equal to that needed to set the drum oscillating ($\Delta E = -h\nu$) or it may strike in phase with an oscillating drum and be bounced with greater energy ($\Delta E = +h\nu$). These inelastic interactions are collectively called Raman scattering. Photons with less energy after interaction are termed the Stokes scattered photons and those with greater energy are the Anti-Stokes photons. Elastic scattering is termed Rayleigh scattering.

Energy level diagrams are used to represent vibrational level transitions of the system as energy is either absorbed or emitted. Rayleigh transitions arise from transitions that start and finish at the same energy level; the ground state, $\nu = 0$, where ν is the vibrational quantum number. The molecule is excited to a 'virtual' energy level by interaction with a photon of energy E_0 from which it decays with the creation and release of a photon, E_0 . Stokes Raman scattering arises when the molecule is elevated to some virtual energy level from which it decays either to some permitted energy level, i.e. $\nu = 1$. Anti-Stokes Raman scattering is statistically (from the Maxwell-Boltzmann distribution equation) far less likely to occur at room temperature conditions. It requires the molecule to be in an elevated vibrational state from which it is excited

to the virtual energy level, subsequently decaying with the release of a photon with greater energy than E_0 . The different transitions discussed are depicted in an energy level diagram in Figure 2.1. Routinely, only Stokes Raman scattering is recorded because the anti-Stokes signal is such a weak component.

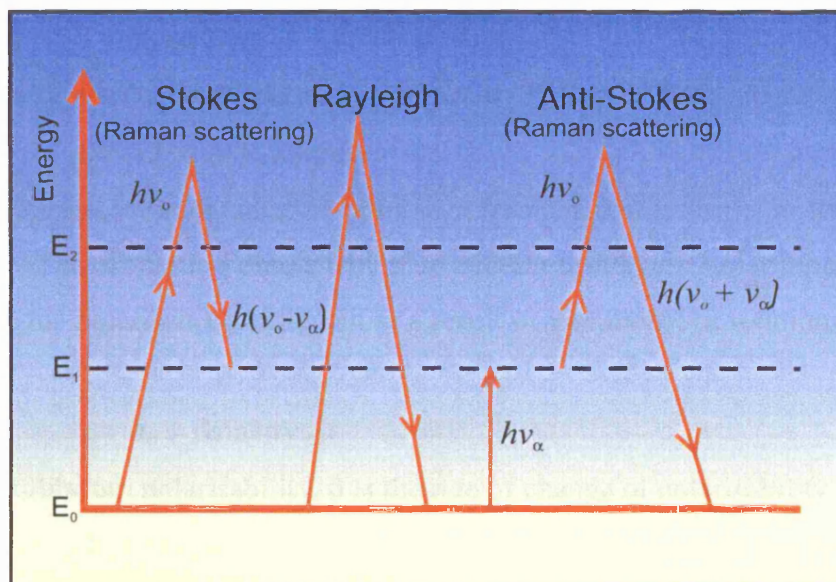


Fig. 2.1. Energy level diagram. After Mottana and Burrigato (1990)

Classical theory

The Raman effect can also be viewed by considering the scattering molecule as a collection of atoms undergoing simple harmonic vibrations. This model takes no account of the quantisation of energy. Whilst said not to be wholly adequate in describing the phenomenon the mechanical model does permit a better understanding of the molecular dipole and molecular polarisability (Banwell and McCash, *op. cit.*). It is this concept that forms the basis of all forms of molecular spectroscopy. The different techniques arise as a result of the different possibilities of interaction of the incident radiation's electric or magnetic field with the dipole. More specifically, there must be some electric or magnetic change in the dipole. Small positive and negative charges on atoms in molecules result in an induced dipole moment as positively charged nuclei are attracted to the negative pole of the incident electric field and electrons to the positive pole. The magnitude of the induced dipole moment depends upon the size of the electric field and also the ease by which the molecule can be deformed, the polarisability, α .

$$\mu = \alpha E$$

where μ is the induced dipole. Since the electrons forming a molecular bond are more easily deformed in the direction of the electric field than perpendicular to it, it follows that the polarisability is anisotropic. A polarisability ellipsoid can be drawn for any molecule, the lengths of the axes of which are inversely proportional to the square root of polarisability along that axis. The electric field experienced by a molecule irradiated by energy of frequency, ν , varies as:

$$E = E_0 \sin 2\pi\nu t$$

where t = time. And the induced dipole undergoes an oscillation of frequency ν :

$$\mu = \alpha E = \alpha E_0 \sin 2\pi\nu t$$

Thus, the oscillating dipole emits radiation of its own frequency; the elastic, or Rayleigh scattered radiation. The oscillating dipole will have another oscillation superimposed upon it if a periodic change in the polarisability ellipsoid as a result of vibrational or rotational deformation or motion occurs:

$$\alpha = \alpha_0 + \beta \sin 2\pi\nu_{\text{vib}} t$$

where α_0 is the equilibrium polarisability, β is the rate of change of polarisability with vibration and ν_{vib} is the vibration that changes the polarisability. The above equation can be expressed in terms of μ and expanded using the trigonometric relationship:

$$\mu = \alpha_0 E_0 \sin 2\pi\nu t + \frac{1}{2} \beta E_0 \{ \cos 2\pi(\nu - \nu_{\text{vib}}) t - \cos 2\pi(\nu + \nu_{\text{vib}}) t \}$$

The equation thus has terms that account for the occurrence of Rayleigh scattering as well as Stokes and Anti-Stokes Raman scattering. Importantly, it also predicts that for interactions that do not lead to an alteration, either in the magnitude or direction, in the polarisability, i.e. $\beta = 0$ the oscillating dipole only emits radiation of the frequency of the incident energy. Thus Raman activity is in contrast to infrared activity where a change in the electric dipole moment is required. For simple molecules and for those possessing little symmetry it is relatively simple to assess whether the various vibrations will be Raman active. Banwell and McCash (1994) state that for these molecules, for example H_2O , one can generally assume that all the vibrational modes are Raman active. More complex molecules and those with high degrees of symmetry require more detailed consideration of the effect of vibrations on the polarisability in order to predict Raman activity of the fundamental modes of vibration as well as of overtones and combination modes.

The symbol ν (not to be confused with frequency whose symbol is traditionally also ν) is used with a subscript, e.g. ν_1 to denote the fundamental vibrational mode frequencies. By convention the subscripts are numbered in order of decreasing symmetry of the vibration and within that in order of decreasing frequency. Figure 2.2 shows the fundamental vibrations of CO_2 and the polarisability ellipsoids for each vibration. Equilibrium positions are shown as the central molecule in each case. As a general rule symmetric vibrations produce more intense Raman lines whilst non-symmetric vibrations are weak or may even be unobservable. Bending motions are also typically weak.

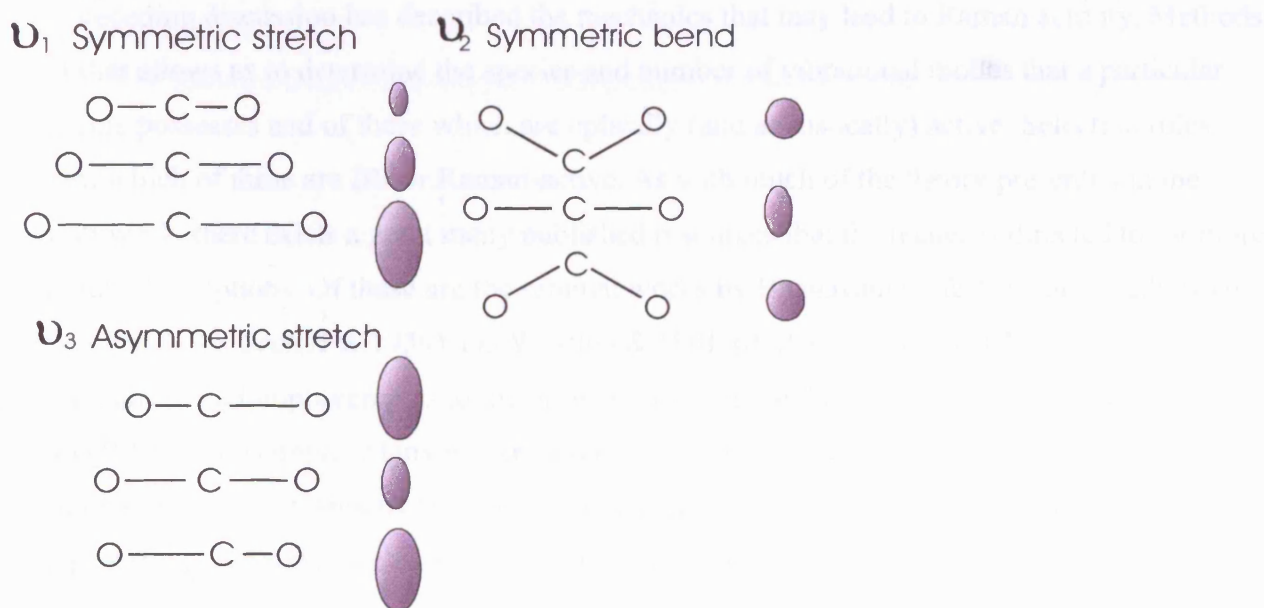


Fig. 2.2. Changes in the polarisability ellipsoid of CO_2 during vibrations. Redrawn from Banwell & McCash (1994).

For CO_2 only ν_1 is Raman active. Clearly, the molecule and therefore the polarisability ellipsoid, changes in size and shape during the symmetric stretch (also commonly called the ‘breathing mode’). The fundamental vibrations ν_2 and ν_3 are Raman inactive. If the extension or compression of the bond (or angle) is measured it can be seen that for small displacements there is no effective change in the polarisability and so the vibration is Raman inactive.

It follows from the discussion of polarisability that the more covalent in character a molecular bond is the stronger its Raman activity is likely to be. Bonds more ionic in character possess a much smaller net dipole and thus have no Raman activity. A great many factors contribute to the

specific frequency at which a vibration occurs. These include the masses of the atoms and any charge on them, the local symmetry of the molecule and the nature of the bonding. If we consider a simple diatomic molecule as point masses attached by a spring that obeys Hooke's Law it is obvious that heavier atoms will oscillate at a lower frequency than lighter atoms and that stronger bonds lead to higher frequencies (Whiffen, 1972). Indeed, this concept has been extrapolated further and details of the Raman spectrum used to provide information about the bond lengths, molecular shapes and electronic structure of molecules.

Internal motions of crystals

The preceding discussion has described the mechanics that may lead to Raman activity. Methods exist that allows us to determine the species and number of vibrational modes that a particular molecule possesses and of these which are optically (and acoustically) active. Selection rules govern which of these are IR- or Raman-active. As with much of the theory presented in the current work, there exists a great many published resources that the reader is directed to for more elaborate descriptions. Of these are the seminal works by Bhagavantam & Venkatarayudu (*Proc. Indian Acad. Sci. Sect. A* **9**, 1939) and Winston & Halford (*J. Chem. Phys.* **17**, 1949).

Modifications and improvements to the original methods can be found in Rosseau, Bauman and Porto (1981), for example. Many worked examples of the application exist. For example, the work of White and De Angelis (1967) and more recently those of Graves, Johnston and Campaniello (1988) on spinels serve as useful examples.

Factor Group Analysis, FGA, is such a method that can enable us to predict the number of Raman and IR modes for a molecule. It cannot, however, predict the frequency at which they will occur or their relative strength. As an example, coesite has 33 predicted Raman-active modes (Liu *et al*, 1997) but fewer than half of these have been observed. One explanation for this is that some bands may be too weak to detect with current technology. Simply, FGA considers symmetry aspects of the molecule and the effect on the symmetry by performing certain operations. Correlation with published tables allows one to determine which vibrations are Raman- or IR-active. A simple derivation and discussion of the procedure follows:

The atomic positions of molecule of n atoms in space can be described by reference to three

mutually perpendicular axes, i.e. the Cartesian coordinates x , y and z , giving $3n$ coordinates. Each coordinate can be defined independently so the molecule possesses $3n$ degrees of freedom (Banwell & McCash, 1994). If the molecule translates (a symmetry operation that transforms the molecule to an equivalent, identical position) about a reference, e.g. its centre of gravity, three of the coordinates are used to describe the reference, leaving $3n-3$ degrees of freedom. A further three are required to describe rotations, leaving $3n-6$ degrees of vibrational freedom. This simple rule allows us to begin to calculate the number of vibrations possessed by a crystal.

For crystals, n can be very large, so it is logical to consider only the unit cell in discussion of the vibrational behaviour. The vibrations of a single unit cell define those of the whole crystal (Farmer & Lazarev **In**: Farmer, 1974). The unit cell can be identified by the point group, a more convenient method of describing the set of symmetry operations that the space group conforms to. The atoms are related by the symmetry elements and operations – rotations, reflections, inversions and improper rotations. Screw and glide operations contribute to the point group but they are not considered further since they are translations of the entire unit cell. The resulting unit cell group is also called the factor group. They are isomorphous with one of the 32 crystallographic point groups familiar to the mineralogist and can be assigned on the basis of the external form of a crystal. The 32 point groups, through various rules, exceptions and permutations, lead to 230 unit cell groups. Point groups and factor groups thus provide a summary the symmetry of molecule. The notation used by crystallographers and mineralogists is the Hermann-Mauguin system whilst spectroscopists favour the Schoenflies notation. For example, using the Schoenflies notation, C_{2v} describes all the symmetry properties of the water molecule (the identity operation, E , the C_2 rotation axis and the σ_v' and σ_v'' reflections) that are described by the $Pmm2$ space group.

Each factor group has a character table. These have been published in many sources. Character tables provide a summary of the effect the symmetry operations have on different properties of the molecule (e.g. the polarisability along a particular axis). An example of a character table is presented in Table 2.1. A +1 or –1 in the table signifies that property being unchanged or changed, respectively, for that operation. The row headings of the character table are called the

irreducible representations and are symmetry operations. They have the symbols A , B , E and T . A and B operations are one-dimensional symmetry species' that have different effects on the principal rotation axis. They may have numerical subscripts (a 1 or 2, typically) to distinguish between species that would have the same label.

C_{4v}	E	$2C_4$	C_2	$2\sigma_v$	$2\sigma_d$	
A_1	+1	+1	+1	+1	+1	z, x^2+y^2, z^2
A_2	+1	+1	+1	-1	-1	R_z
B_1	+1	-1	+1	+1	-1	x^2-y^2
B_2	+1	-1	+1	-1	+1	xy
E	+2	0	-2	0	0	$(x,y), (xz,yz), (R_x,R_y)$

Table 2.1. Character table for molecules of C_{4v} symmetry.

Additionally, they may have the subscripts g or u , from the German *gerade* (meaning even) and *ungerade* (meaning uneven). These are assigned depending upon how the species' effect the inversion, i , symmetry operation. The A_1 representation defines the totally symmetric effect (A_{1g} if the molecule possess a center of symmetry and A_{1u} if it does not). The prime superscripts, ' , or " , (or more, in highly symmetric molecules) are used to describe the behaviour under the different mirror symmetry operations. E is used to describe the effect of a degenerate pair; it comprises two separate operations that have identical symmetry properties and therefore identical energies. E is a two-dimensional symmetry species. T signifies a three-dimensional symmetry species and describes how a triply degenerate item behaves. Three operations have identical symmetry and thus three bands with identical energy (and therefore wavenumber shift) will appear in the spectrum. This species only occurs in highly symmetric molecules, for example, silicon, germanium and diamond which all have cubic symmetry. This explains why the example in Table 2.1 has no T modes; it does not possess the high degrees of symmetry. The last column in the character table lists the vectors, rotational vectors or tensors (using the conventional Cartesian co-ordinates x , y and z , where z is ascribed to the principal symmetry operation rotation axis) that are affected by the irreducible representations. From this it is simple to determine which of the symmetry species give rise to Raman active modes since the polarisability ellipsoid is a second order, or tensor, property (IR active modes depend on the change in the dipole moment, a first order, or vector, property. The last column may contain first

order terms, second order terms or both or neither, i.e. the symmetry species may be Raman and/or IR active or vibrationally inactive. Thus IR and Raman vibrational spectroscopic methods are complementary. In the example in Table 2.1, the A_1 and E species are both Raman and IR-active, B_1 and B_2 are Raman active only and A_2 , a rotation, is IR-active only).

The application of character tables to predict the nature of vibrations of molecules is relatively straightforward (for simple molecules, at least). The correlation method of Fately *et al* (1971) for determining crystal lattice vibrations is particularly rapid. Several worked examples are provided. The technique merely requires the knowledge of the crystal structure, which for a known mineral can be obtained from the literature or from tables of X-ray structure determinations. It may also be possible to determine the structure from euhedral crystals. From the crystal structure the Bravais unit cell is determined. For each equivalent atom the site symmetry is found from the table given in Fately *et al* (1971). Each site group for the unit cell is then correlated to the factor group of the whole crystal to give a sum of the irreducible representations.

A reducible representation can be determined by considering the number of bonds that are unchanged by the symmetry operations. From the character table for a molecule of this symmetry it is possible to see which of the irreducible representations it is 'reduced' to. For larger character tables a simple projection formula exists to determine which lines of the table contribute to the representation. Reference to the character table tells us what form the vibration takes, e.g. symmetric or asymmetric stretching. It is important to note that any given set of symmetry related bonds have one totally symmetric vibration.

The frequency positions at which vibrations appear depend upon the bond force constants, k , the atomic masses and the molecular geometry (Farmer, 1974). Vibrational spectra have been used to establish the values of interatomic force fields, which are directly related to the properties of chemical bonds, such as the bond disassociation energy and bond length. General relationships have been determined for both covalent and ionic bonds such that observed changes in band frequency correlate to known changes in certain properties of the molecules. Knowledge of force

constants can be used to predict the frequencies of vibrations predicted to occur, for example, from FGA.

2.3 - The Raman spectrum

The Raman spectrum has axes of arbitrary intensity units against Raman shift, expressed most commonly, in wavenumbers, cm^{-1} . An example of a Raman spectrum is displayed in figure 2.3. The wavenumber unit occurs in most forms of spectroscopy and is simply the reciprocal of the value of the wavelength. It is the number of waves in one centimetre, instead of the length in centimetres of one wave. The incident energy is ascribed the value of zero and the Raman peaks are said to have frequencies 'shifted' from this. It allows a more convenient unit than the unwieldy absolute wavenumber. The Raman shifted frequencies thus have values that are simply the difference between the absolute wavenumber of the peak frequency and that of the incident laser energy. For example, 514 nm green excitation, may be expressed as:

$$1/514 \times 10^{-9} \text{ m} = 19,455.25 \text{ Absolute wavenumbers, Abs. cm}^{-1}.$$

A Stokes-Raman band at a position of 1006 cm^{-1} shift from the 514 nm excitation can be expressed as:

$$\begin{aligned} 19,455.25 - 1006 &= 18,449.25 \text{ Abs. cm}^{-1} \\ &= 1/18,449.25 \text{ cm} \\ &= 0.0000542 \text{ cm} \\ &= 542 \text{ nm} \end{aligned}$$

Correspondingly, an anti-Stokes band at -1006 cm^{-1} has a wavelength of 488 nm.

Since it is the energy of the vibration that is represented as a band in the spectrum, the excitation wavelength is irrelevant; a quartz spectrum recorded with 488 nm excitation will have the same bands, shifted the same amount, as a quartz spectrum recorded using 633 nm excitation. That is not to say the *selection* of the excitation wavelength is irrelevant. In fact, it is often quite the opposite.

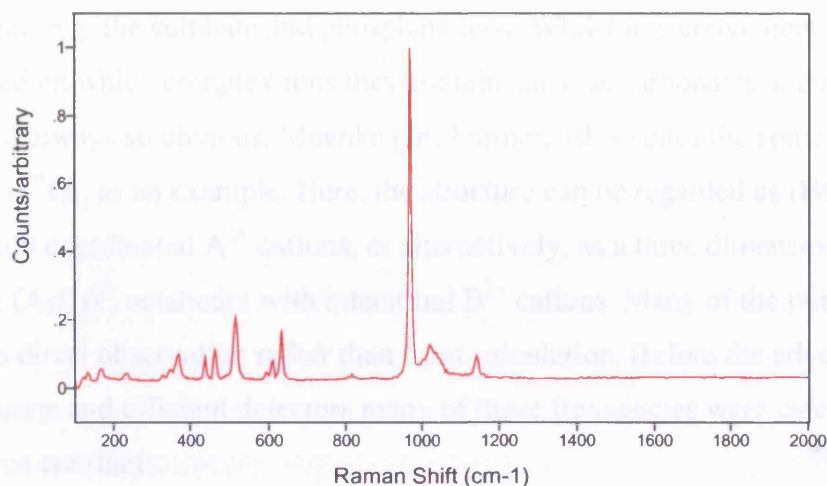


Fig. 2.3. A Raman spectrum from a linarite crystal. Note the sharp bands.

The spectrum itself is thus a record of the frequency distribution of the Raman scattered photons. The routine analysis of minerals and inorganic molecules is usually concerned with Raman shifts of between 0 cm^{-1} and 2000 cm^{-1} . This frequency range is often split into internal and external vibration regions. Internal vibrations relate to the types of motion represented in figure 2.2. These, typically, are the stretching and bending motions although other translations are possible, for example wagging and rocking. They involve changes in the bond lengths and bond angles. An example of internal vibrations is provided by thortveitite, $\text{Sc}_2\text{Si}_2\text{O}_7$. The silicate anion, Si_2O_7 , can be considered as two SiO_3 molecules connected by a bridging O atom. The local symmetry of the SiO_3 groups (which in a crystal may be less than that of an isolated SiO_3 molecule) will determine which of the vibrations (e.g. stretching and bending) are optically active. The vibrations will combine and then be added to the motions of the bridging O (Lazarev **In**: Farmer, 1974), whose own vibrations will depend upon its local symmetry. External vibrations, also called lattice modes, refer to the rotational and translatory motions of molecules relative to each other and occur at low wavenumbers. In the thortveitite example, the external modes comprise the rotations and translations of the Si_2O_7 anion with translations of the Sc^+ ions (Lazarev **In**: Farmer, 1974). The region of the Raman spectrum below about 500 cm^{-1} is often referred to as the ‘lattice region’. The frequency at which the lattice region passes into the ‘internal’ region depends on the sample.

Many textbooks of molecular spectroscopy contain tables of the Raman peaks of organic and inorganic molecules and functional groups that can be directly extrapolated to those in common mineral crystals e.g. the sulphate and phosphate ions. Whilst it is convenient to subdivide minerals based on which complex ions they contain, such as carbonates and sulphates, the division is not always so obvious. Moenke (In: Farmer, 1974) cites the spinels, of general formula $A_2^{3+}B^{2+}O_4$, as an example. Here, the structure can be regarded as $(BO_4)^{6-}$ anions bound by octahedrally coordinated A^{3+} cations, or alternatively, as a three dimensional network of edge-sharing $(A_2O_4)^{2-}$ octahedra with interstitial B^{2+} cations. Many of the published tabulated data are from direct observation rather than from calculation. Before the advent of high-powered continuous lasers and efficient detectors many of these frequencies were calculated based on FGA and force constants.

As a consequence of the inherently sharp peaks in a Raman spectrum and the sensitivity of the technique to composition and structure we might consider every substance to have a characteristic Raman spectrum. The position, width (usually expressed as the full width at half maximum, FWHM), shape and intensity of bands are all important features recorded in the Raman spectra of a sample. The FWHM is defined in Figure 2.4. The means of calculating the FWHM of a band is covered in section 3.8.

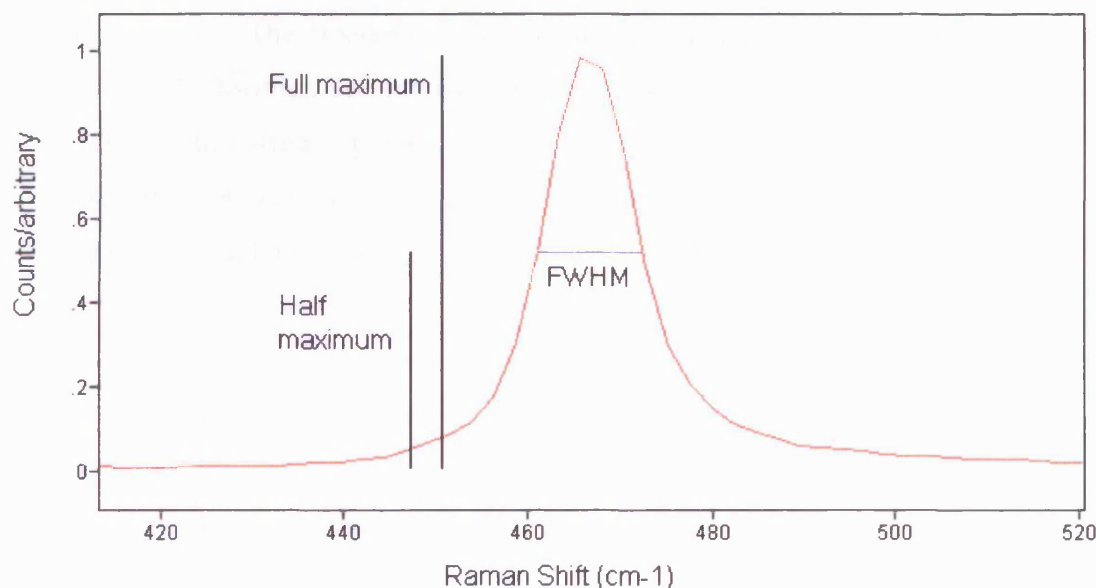


Fig. 2.4. The FWHM is defined as the width of a band, in cm^{-1} , at half the maximum intensity of that band.

Line broadening and Intensity

Vibrational transitions have a natural half width, i.e. the FWHM, which cannot be reduced by the spectrometer. Peaks are not infinitely sharp, however, since the energy levels involved are not precisely defined. Although spectrometer design varies in some respects between manufacturers each incorporates an entrance slit. Increasing the slit width allows greater throughput of light (i.e. signal) but at the expense of increased stray light (i.e. background) and also peak broadening. The latter is the consequence of a broader range of frequencies being allowed to fall on the detector. A typical slit width for a dispersive Raman instrument might be between 10 micrometers and 50 micrometers.

Line broadening also occurs independently of the slit. Some of the main factors relevant to this study are:

- Loss of crystallinity and ordering - the Raman bands of a mineral will increase as the bond angles and bond lengths within the structure change. The most extreme forms, i.e. glasses may have very broad bands compared to their crystalline parents.
- Deviations from stoichiometry. White (**In:** Farmer, 1974) cites studies on LiNbO_3 and LiTaO_3 where deviations of a few mol % from ideal compositions led to more than doubling of band widths. The broadening phenomenon remains poorly studied but was ascribed to translational disorder. The intensity was observed to decrease as the widths increased (Scott and Burns **In:** Farmer, op. cit.).
- Crystallite size. Very finely comminuted particles e.g. clay particles, may produce Raman bands with broader bands than larger, single crystals of the same species.

Additional, weak physical factors can affect the Raman spectrum. Although more applicable to liquids and gases and of minor relevance to this study, these are collision broadening, Doppler broadening and the Heisenberg Uncertainty Principle. Increase in temperature of the sample can also cause line broadening and is perhaps, the most significant in the Raman analysis of minerals. To this end, caution must be taken that the excitation does not lead to excessive local heating.

The intensity of spectral peaks depends upon three factors. Firstly, the transition probability relates to the likelihood of a system changing state. Detailed quantum mechanics calculations and considering the selection rules are possible but only very rarely carried out. It is possible, however, to predict the intensity of spectral peaks. Secondly, population density. Simple statistical rules are used to describe the population: the number of atoms or other components present in a particular state. If there are two energy levels from which particles may be excited to a third the most intense spectral line will originate from the most populated state. Thirdly, the concentration of a particular component in a sample obviously relates to the intensity of the band.

Raman scattering, as well as other absorption and dispersion methods, produces bands that are Lorentzian in shape under ideal circumstances (Denney, 1982). However, instrument processes impose a Gaussian function. Consequently, the resultant peaks are a mixture of these. Computer software is used to iteratively apply a mixed-function to solve the peak and supply values for the peak center, FWHM, peak height above background and peak area. Figure 2.5 illustrates the differences between Lorentzian, Gaussian and mixed Lorentzian and Gaussian distribution curves fitted to a Raman band.

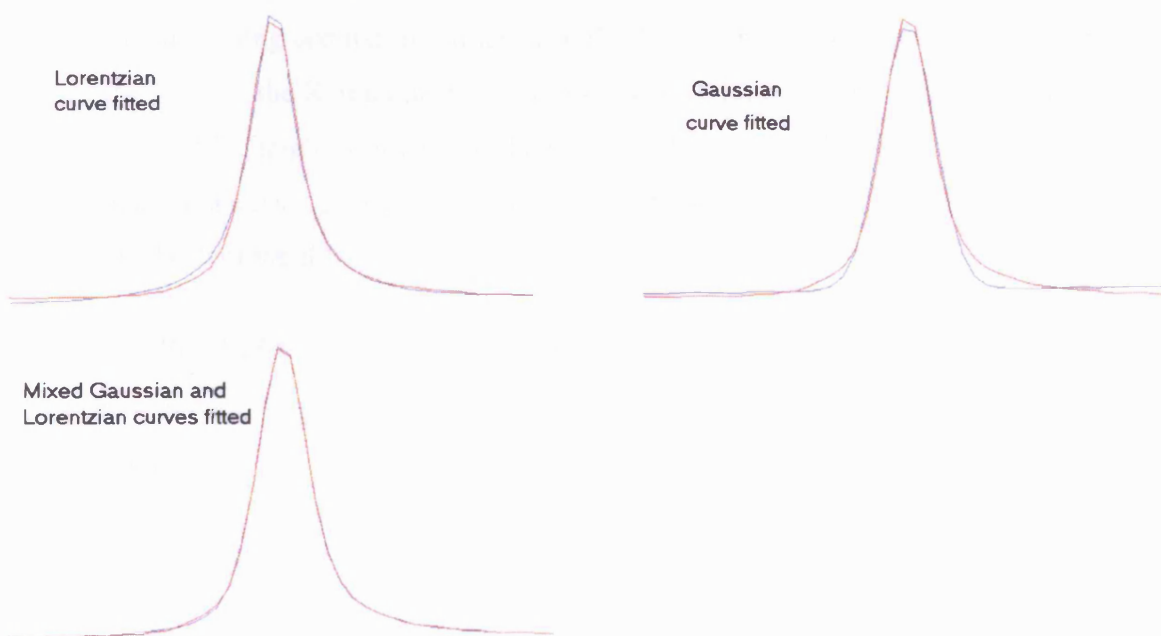


Fig. 2.5. Comparison of Lorentzian, Gaussian and mixed Lorentzian and Gaussian distributions. Red line is the raw data, blue is the fitted distribution curve. Note the difference in the width of the tails between Lorentzian and Gaussian curves. The mixed curve represents an excellent fit to the data.

Resolution and Signal to noise ratio

A high spectral resolution is usually a key requirement of a research Raman instrument. The ability to distinguish between two very closely spaced peaks with certainty is largely a function of the spectrometer. The distinction of a peak into two components may have vital bearing on the interpretation of a sample. For example, the first order triply degenerate single phonon mode of diamond splits upon the application of a uniaxial stress field into two peaks. The response is linear and so the stress field may be calculated on the degree of splitting. Instrument manufacturers are fond of quoting a low value and it is often a test of an instrument's performance. There appears to be no single test of resolution that manufacturers and those that use Raman spectroscopy agree on. Commonly, tetrachloromethane is used because isotopic differences between the Cl atoms create three very closely spaced peaks in the Raman spectrum. Occasionally, the FWHM of the very sharp Ne emission bands are used to define the resolution of the spectrometer.

Random noise caused by spurious electrical signals can be introduced from the source and the detector. Modern CCD cameras are thermoelectrically cooled to virtually eliminate dark current. Experimentally, long acquisition times or multiple spectra are co-added by software to reduce noise effects since the Raman peaks are non-random features. Ideally, the ratio of the maximum peak height to the height of the noise fluctuations should be at least 3 or 4 to 1 for reliable peak determination. Raman spectra of excellent signal to noise ratio might have values two orders of magnitude better than this.

2.4 - Fluorescence

Other than the inherent weakness of the effect, the principle problem associated with analysis by Raman spectroscopy is fluorescence. Occasionally, an intense climbing signal completely swamps the Raman peaks. Visible wavelength excitation of dark or strongly coloured samples, can be problematic with excessive fluorescence. Many minerals rich in iron also fluoresce very strongly. Fluorescence arises from the coincidence of the excitation energy with an electronic transition of the sample. Logically, the most effective way of avoiding the problem is to select an alternative excitation wavelength. An example of selecting alternative excitation is demonstrated

in Figure 2.6 in the analysis of a rough emerald crystal.

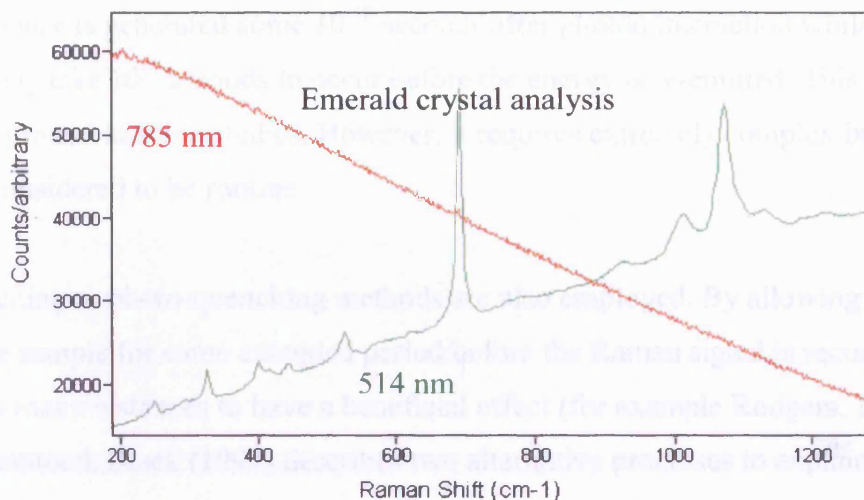


Fig. 2.6. Effect of using alternative excitation wavelength.

Clearly, despite the modest fluorescence signal, the choice of visible excitation at 514 nm in the analysis of this sample yields far greater information than the near-IR excitation (785 nm). With the latter, the strongest band in the emerald spectrum is barely resolved above the fluorescence. The laser wavelengths that are more commonly encountered and that can be readily supplied are listed in Table 2.2. It should be borne in mind that since the efficiency of the Raman scattering is far greater towards the 'blue' end of the spectrum, i.e. visible to UV wavelengths, the potential for fluorescence is greater. At the 'red' end, the fluorescence is less likely but the Raman scattering efficiency is less. In many cases, a compromise between strong Raman signal and acceptable fluorescence is sought.

Tunable lasers are also available for specific applications. However, it is uncommon for Raman instruments to be supplied with more than two lasers, indeed the majority probably are only equipped with one. Additionally, there are other practical and experimental problems associated with some analysis by UV or near-IR lasers.

Other practical solutions to the fluorescence problem exist. The effect is often much weaker in the anti-Stokes region of the Raman spectrum of a sample, although the peak intensities are very

greatly reduced. Time-gated detectors can also be used to reduce the effect of fluorescence. The Raman response is generated some 10^{-12} seconds after photon interaction whilst the fluorescent transition may take 10^{-8} seconds to occur before the energy is re-emitted. This time difference has been exploited in some studies. However, it requires extremely complex instrumentation and cannot be considered to be routine.

Photo-bleaching or photo-quenching methods are also employed. By allowing the laser to irradiate the sample for some extended period before the Raman signal is recorded has been observed in many instances to have a beneficial effect (for example Rodgers, 1993). Although poorly understood, Black (1997) describes two alternative processes to explain photo-quenching: the driving off of fluorescent materials or localized recrystallisation and subsequent elimination of crystal defects.

Wavelength (λ)/ nm	Region of the spectrum/colour	Laser type
244	UV	Frequency doubled Ar ⁺ gas (488 nm line)
257	UV	Frequency doubled Ar ⁺ gas (514 nm line)
325	UV	HeCd mixed gas
442	UV-deep visible	HeCd mixed gas
457	Visible/blue	Ar ⁺ gas
488	Visible/blue-green	Ar ⁺ gas
514	Visible/green	Ar ⁺ gas
532	Visible/green	Frequency doubled NdYAG (1064 nm) or solid state
633	Visible/red	HeNe mixed gas
785	Near-IR/red	Diode
830	Near-IR	Diode

Table 2.2. The most common excitation wavelengths used in Raman spectroscopy. Many more are available and tunable lasers can provide any wavelength.

Photo-bleaching should be used with caution. The very high power densities of some lasers can cause local damage of a sample or the conversion of one compound into another. At the very least, sample heating may have the effect of broadening the peaks. In reality the low power lasers routinely used very rarely damage mineral samples. Typically, the power at the sample may only approach 5 mW over a 'spot' of 1 to 2 micrometer diameter. Fourier-Transform Raman and Infrared spectroscopic methods have the advantage that fluorescence is not encountered. Also, they have no requirement for external calibration sources and the low laser powers used do not lead to thermal decomposition of the sample (McMillan *et al* 1988).

Theoretically, it should also be possible to record a spectrum from a known highly fluorescent (at the same excitation) species and subtract this from the Raman plus fluorescence signal from the sample of interest. To the author's knowledge, this is not a common method.

2.5 - Polarisation studies

The positions and relative intensities of bands in a Raman spectrum may be all that is required of the analysis of a material but much use can be made of the depolarisation ratios for the elucidation of molecular structure. There have been many polarisation studies of minerals, for example, those with the rutile-type structure (e.g. Farmer, 1974). Lasers are sources of plane polarised light and have an electric vector and a magnetic vector, oriented mutually perpendicular to one another and the direction of propagation. If the ratio of the height of a band recorded with a polarising sheet parallel to the polarisation direction of the laser to that with the sheet perpendicular to the laser polarisation tends towards zero, then that band is said to be polarised. Depolarised bands have ratios of around 0.75. Generally, totally symmetric modes are polarised and non-symmetric modes are depolarised.

The Renishaw RM instruments can be used to measure depolarisation ratios. A polarising sheet within the instrument is rotated into the beam path, immediately before the entrance to the spectrometer. The perpendicular component of the Raman scattering is measured by inserting a $\lambda/2$ accessory before the polariser to rotate the scattered signal by 90° .

McMillan & Hoffmeister (**In:** Hawthorne, 1988) note that accurate single crystal polarisation

studies require that the crystal be properly oriented. Failure to do so results in incorrect mode symmetries. Small errors in crystal orientation can lead to leakage of strong modes of one symmetry that may then appear weakly in the spectrum of another orientation. Polished entrance/exit faces of crystal are required and cracks and inclusions must be avoided to reduce excess parasite scattering of the laser beam. Importantly, McMillan & Hoffmeister point out that the polarizing effects of the gratings must be taken into account.

3 – Instrumentation and operation

This section aims to introduce the reader to the Raman microprobe used, in various configurations, throughout this work. Explanation of the layout of components as well as an understanding of the sampling considerations and some of the post-processing issues are provided so that the uses and limitations of the technique are placed in context.

3.1 – Introduction

Raman spectroscopic instruments referred to in the literature are variously termed Raman Microprobe (RMP), MicroRaman and Raman Microscopes. The terms are, however, synonymous. The instruments used throughout this project are the Renishaw RM 1000 and 2000 models of research grade instruments. A reproduction of a photograph of the RM instrument appears in Figure 3.1. Both models consist of a spectrometer (mechanical slit, dispersion grating and detector) coupled to a Leica DM/LM microscope with trinocular heads and video camera to view the sample. Both instruments perform the basic function of Raman spectral analysis and as such share many of the basic components. It will be explained that component specifications are dependent largely on the laser used (excitation source). Excitation wavelength was sample-dependent and was either by the 514 nm or 633 nm lines of air-cooled Ar ion or HeNe gas lasers, respectively, or 785 nm solid state source. The Renishaw proprietary software, WiRE[®], is used to control the instrument. The Galactic Industries GRAMS/32[®] software package is used for much of the data handling and manipulation. The IR Search software package is used for database searching.

The layout of the RM instrument is best described by following the beam path. An excellent description of the design of modern Raman spectrometers is given by Baldwin *et al* (2001).

3.2 - Spectral acquisition mode

With reference to Figure 3.1 the beam path traced in spectral mode utilises the components coloured blue. The polarised laser beam enters the main body at the lower rear right corner. Two adjustable angled mirrors are used to direct the beam. A set of neutral density (ND) filters, software-controlled on newer instruments, allow the incident energy to be supplied at 100%, 50%, 25%, 10% or 1% of the laser's output intensity. The collimated beam is directed by means of a fixed mirror into the beam expander, where fitted, which is a device that consists of a pair of objective lenses that are used to control the degree of focus of the beam

i.e. the spot size and also improves the beam profile. The second lens is motor-linked and driven by the software. This allows the accurate setting of the beam expander position such that the laser is mutually in focus on the sample with the view down the microscope. For instruments equipped with lasers with many emission lines, for example the Ar ion ‘gas’ laser, the next component in the path is the plasma line rejection filter. This filter has a very narrow bandpass and is specific to the excitation wavelength. Figure 3.2 indicates the removal of this component. Although the original intensity may be reduced by around 50% through this filter it ensures that only the wavelength of interest is supplied.

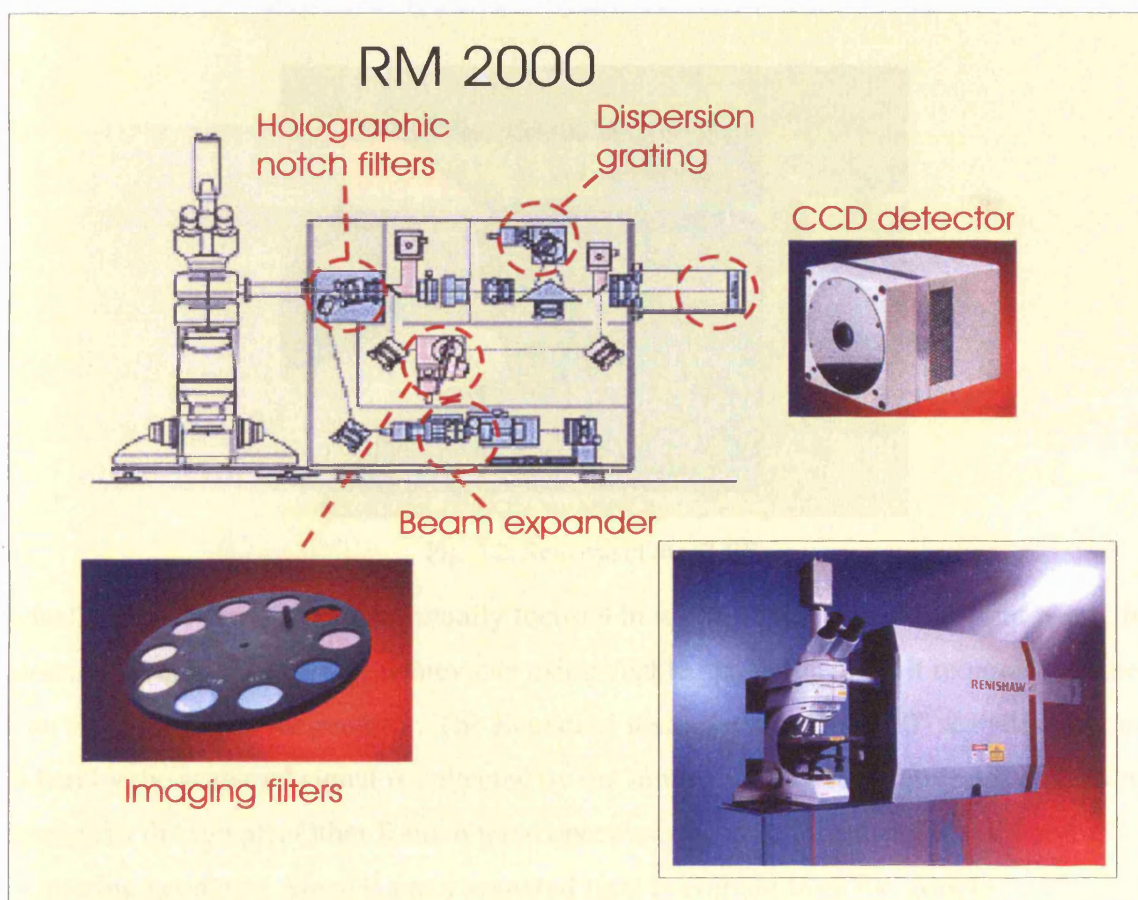


Fig. 3.1. Schematic diagram and photo image of Renishaw RM2000 Raman microscope with inserted images of some of the optical components.

The beam-steering mirror in the lower left corner deflects the beam upwards and onto another reflecting component. It is possible to produce a very narrow line on the sample rather than a spot by the insertion of a hemispherical lens at this stage in the Renishaw instrument. Fixing holes provide easy mounting of the ‘line focus attachment’. In either case, the beam is reflected into the microscope and down through the ocular column and whichever objective is selected from the nosepiece. Typically, a 50x objective with an NA of 0.75 (defined as the sine of the collection angle of the objective lens multiplied by the RI of the medium. NA can be simply thought of as the ‘light collecting ability’ of the objective; generally speaking for

dry objectives, values closer to 1 are most effective) produces a spot with a diameter around one micrometer is used for spectral analysis. It is important that the 6 mm back aperture of the objective is filled to create a diffraction-limited laser spot on the sample. The beam expander is adjusted to achieve this. Failure to ensure efficient filling would result in poor excitation of the sample and a weak Raman response. The sample can be viewed conventionally through the microscope eyepieces or via the computer monitor. An example of a sample viewed through the camera attached to the trinocular head can be seen in Figure 3.3.

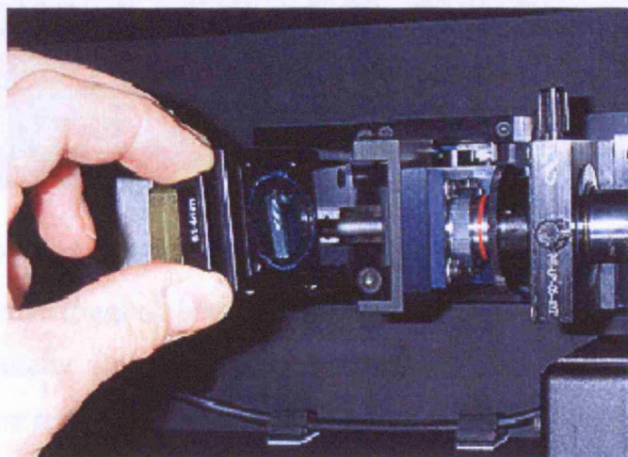


Fig. 3.2. Removal of the PLRF.

Ideally, the system would be mutually focused in white light and with the laser beam. In practice, this is usually only achievable using visible excitation since it requires that the spot can be observed on the monitor. The Renishaw instrument utilises 180° scattering geometry, whereby the scattered signal is collected by the same objective that delivers the incident energy to the sample. Other Raman microspectroscopic instruments utilise 90° or 135° scattering geometry. Since Raman scattered light is emitted from the sample in all directions (e.g. Whiffen, D.H. 1966) the collection geometry is usually influenced by design considerations. Many studies of oriented crystals have made use of 90° scattering geometry.

Incident and scattered light passes between instrument and microscope by means of a 45° beam-splitter mirror that is rotated into the light path by means of a switching system located just below the nosepiece of the Leica DM/LM microscope. Figure 3.4 indicates the position of the switching mechanism.

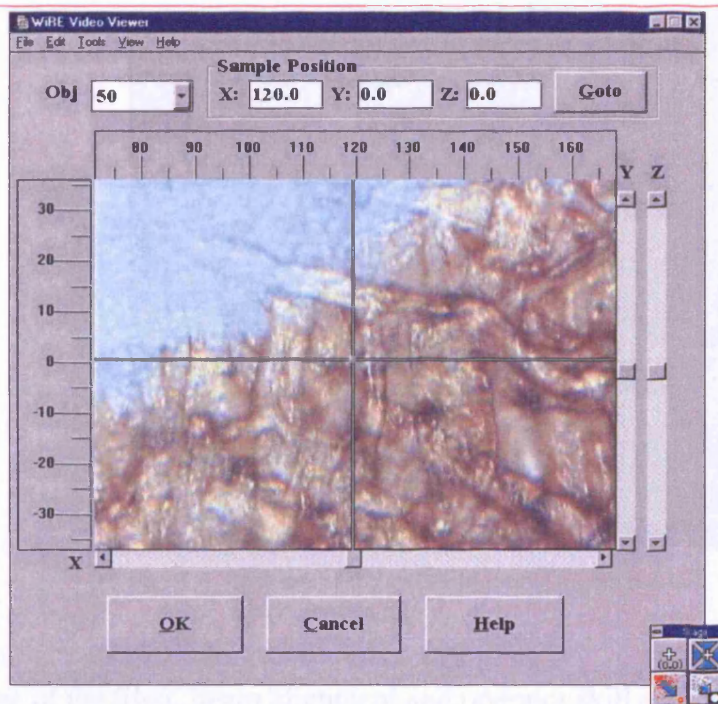


Fig. 3.3. An example of the computer monitor image recorded by the microscope camera.

This allows the effective toggling between the laser and white light (either incident or transmitted). The scattered signal passes up the ocular column and into the connecting tube. It then re-encounters the reflecting surface. For light of the excitation wavelength this component acts as a mirror and, ideally, all other wavelengths are transmitted. Commonly in visible excitation instruments this component and the next in the scattered light path are ‘holographic notch filters’, HNF (although other methods can be employed). Their roles are to reject all the intense Rayleigh scattered energy (i.e. with the same wavelength as the laser) as efficiently as possible. Briefly, the filter material consists of a sandwich of gelatinous polymers that has a hologram imprinted in it of a sine wave. The particular waveform used is very effective in interfering with the Rayleigh signal and reducing it. The notch filters are wavelength calibrated and mounted in matched pairs. The second filter is required to further reduce the intensity of the Rayleigh energy. Both are adjustable, aiding alignment, optimising the signal to noise ratio and how ‘close’ the Raman-shifted signal can be detected relative to the incident energy, the exciting or ‘laser’ line. For many materials Raman peaks may be located at a shift of only a few wavenumbers so the angular adjustment of the second filter can be crucial.



Fig. 3.4. Position of the switching mechanism below trinocular head.

The type and age of the filter, beam alignment and operator skill combine to determine this 'cut-off' value. In practice the minimum shift from the laser wavelength that can be realistically observed is around 100 cm^{-1} (refer to Section 2.3 and Figure 2.3). Although the rejection filters are effective in reducing the intensity of the Rayleigh signal they contribute significantly to the overall reduction in intensity of the Raman signal. In addition to notch filters, Renishaw also supply 'Super Notch Filters' that enable signal with Raman shifts from around 50 cm^{-1} to be detected. 'Edge' filters have the property of removing all scattered radiation, including the anti-Stokes scattered signal, below a certain frequency. This value is usually around a Raman shift of 200 cm^{-1} but maybe 400 cm^{-1} using UV excitation. Obviously this includes all the intense Rayleigh scattering. Although no spectral information can be recorded from the lower Raman shifts, edge filters can prove useful at much larger shifts since the filter material used contributes less fluorescence. Holographic notch filters are considerably more expensive than edge filters and are also susceptible to degradation caused by humidity. Edge filters are not affected by atmospheric moisture. Visible excitation instruments can be supplied with filters made of fused silica. These are formulated to absorb energy of the specific wavelength. They have the advantage of fluorescing less than notch filters and are not associated with 'ripple' effects observed with edge filters. Unfortunately, the great cost of this filter material precludes it for many users.

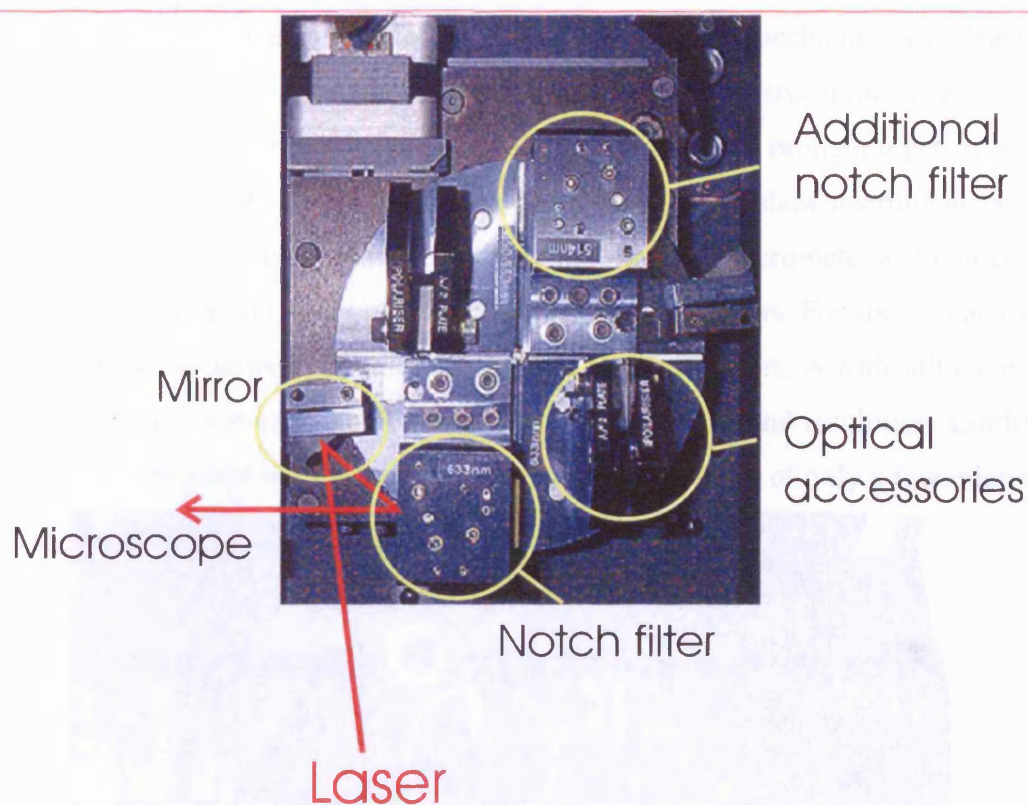


Fig. 3.5. Motorised kinematically mounted filters on rotary mount. A small circular mirror reflects the laser beam onto the first filter component from where it is reflected into the connecting tube.

During the course of this study some modification of the components occurred with technological developments by Renishaw. New and upgraded instruments used were fitted with rotary-mounted, fully motor-controlled filter units and are shown in Figure 3.5. These units replace the ‘plug and play’ filter units seen in the schematic in Figure 3.1. and there is a slight modification to the beam path, indicated in Figure 3.5. The rotary mount enables up to four kinematically-mounted filter units to be fitted (two are shown in Figure 3.5), expanding the potential for other lasers to be fitted and simplifying the switching between wavelengths. Any of the filter units can be selected from the software interface and the motor referencing ensures that each unit delivers a highly repeatable parfocal and parcentric spot to the sample.

For the RM series of Raman microprobes light throughput values are quoted at ‘greater than 30%’ (Renishaw technical literature) and this was determined to be accurate by measurement. This compares very favourably with the older single or double (or triple) monochromator instruments (briefly discussed later) offering much greater transmission (Wolverson **In:** Andrews and Demidov, 1995).

The filtered, Raman-only, signal is focussed by a lens onto the mechanical slit. The location of the slit is indicated in Figure 3.6. Ensuring that the light is focussed increases the signal quality. The slit consists of two parallel-edged plates that can be brought together by means of a vernier with an accuracy of less than micrometer. Newer Renishaw instruments are fitted with a slit vernier calibrated in ten micrometer units, not one micrometer as in older instruments. Accuracy can then only be stated at five micrometers. For spectral analysis the slit is typically set at between 15 micrometers and 50 micrometers. A wide slit increases signal strength but at the expense of background noise and spectral resolution. Confocal work (discussed later) requires the slit to be set with an opening width of only a few micrometers.

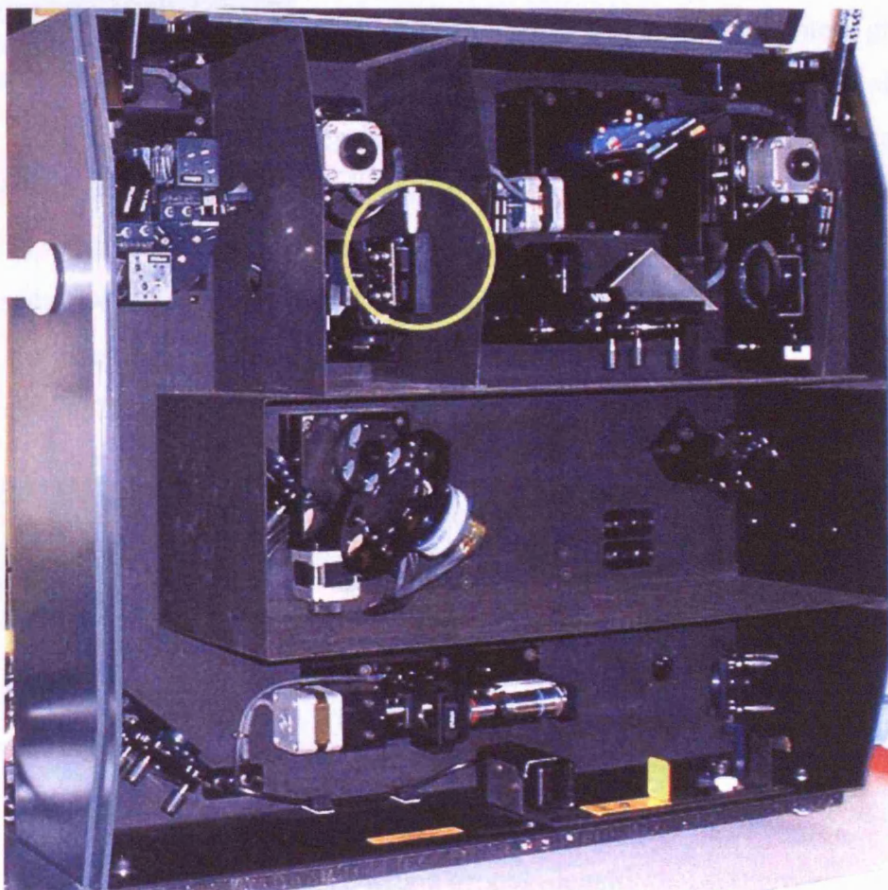


Fig. 3.6. Location of the mechanical slit within the instrument.

The 'spectral' beam is then directed through another lens and onto the triangular mirror where it is reflected onto the motor-controlled dispersion grating. A choice of gratings is available. Typically these have 1200 or 1800 grooves per mm for visible excitation. For high-resolution studies gratings with greater groove densities can be fitted, for example a system with visible excitation may have a 2400 groove per mm grating fitted. Kinematically-mounted gratings are available as an option and changed manually or a motorised double-sided grating can be opted

for. Figure 3.7 displays a double-sided dispersion grating mount with an 1800 groove mm^{-1} and 2400 groove mm^{-1} fitted.



Fig. 3.7. Software-controlled double-sided grating.

For a given excitation wavelength the greater number of grooves per unit permits greater spectral resolution but at the expense of spectral range and efficiency. From the grating the dispersed Raman signal is passed from the triangular mirror and focused by a lens onto the detector. The three lenses in the spectrometer are optimised for the excitation wavelength: either UV, visible or near IR.

Typically each is kinematically-mounted, greatly facilitating their removal and replacement should another

excitation be selected. Figure 3.8 demonstrates the easy removal of these optical components. A unique function of the Renishaw instrument is the patented Continuous Extended (CE) spectral scan, or latterly, 'SynchroScan'. This facility overcomes the spectrometer's inherent limited spectral 'window' when the gating is held in one position. This is a product of the wavelength of excitation and high dispersion gratings (Dyer *et al*, 1995). The user defines the spectral range in the experiment set-up (discussed later). For example, during a 'static' scan

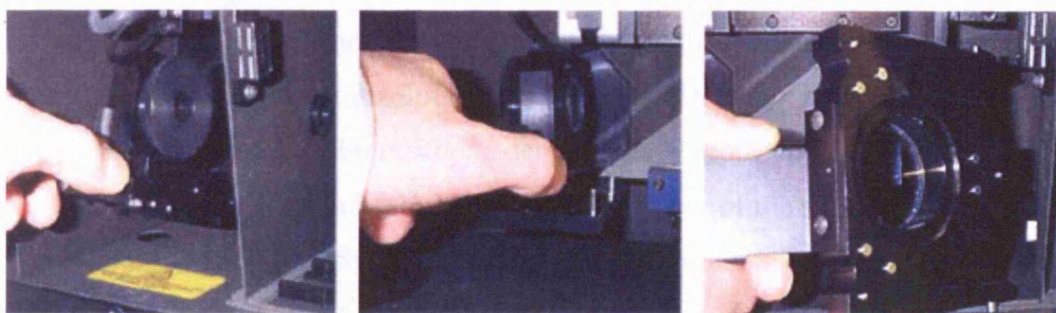


Fig. 3.8. Kinematic lenses: the lens-before-the-slit, pre-grating lens, pre-camera lens.

using 514 nm excitation and a grating with a groove density of 1800 grooves mm^{-1} the spectral range covered is around 600 wavenumbers about a central wavenumber. CE scans solve the problem by synchronising the rotation of the dispersion grating with the movement of charge across the detector. This allows spectral ranges covering the entire frequency response of the detector, several thousand wavenumbers, to be covered in a single acquisition. Other manufacturers achieve this by the so-called 'step and stitch' method. A spectrum is recorded in the static grating mode, the grating then 'steps' to a new position such that its new range has a minimum wavenumber equal to the maximum value of the first position range. Spectra are then 'stitched' together by the computer software. The effects of vignetting cause

errors to be introduced, particularly if the spectra exhibit marked fluorescence. Lens effects cause the intensity to be significantly reduced at either extreme of the static spectrum. Very high NA lenses are difficult to correct for, although the effect is rarely a problem in the RM series since the lenses are much thinner (I. Haywood, pers. comm.). Anomalous spikes or sharp troughs in the spectrum mark the errors (T. Smith, pers. comm.). The step and stitch method is an option on the Renishaw RM and RA (discussed only in section 14) series instruments. The method is of use because using the CE method the sample must be exposed for a minimum of ten seconds. For thermally sensitive samples this may induce damage. Step and stitch allows exposure times of fractions of seconds whilst still acquiring full spectral coverage.

CCD detector

The Renishaw family of Raman instruments use multi-channel Charge Coupled Device (CCD) detectors. The CCD detector is now commonly used to record spectroscopic data. It replaces the single-channel photomultiplier tube and multi-channel diode array detectors. Amongst the advantages of this type of detector are that it is far more efficient, stable and faster than older single channel detectors. CCD camera detectors have been used for some time in astronomy due to their sensitivity; the ability to record almost every photon that strikes. They possess a linear response over the spectral range they cover, have a good spectral range and greater resolution and quantum efficiency (QE) (Gardiner *et al*, 1989) than the photomultiplier and photocathode detectors they replaced. The QE is a measure of the detector's performance and is the ratio of the intensity of the signal to the number of photons received by the detector. Specialised CCD chip detectors have QE values approaching 70% (Williams *et al*, 1994). This compares with QE values of <20% for photocathode detectors. The largest problems faced by CCD chips are dark current and noise. Dark current is the signal that is generated in the absence of light by thermally excited electrons. This thermionic current is reduced by electronically (Peltier) cooling the chip to -70°C , resulting in very low dark current levels of typically $<0.01 \text{ e}^{-1} \text{ pixel}^{-1} \text{ s}^{-1}$ (Williams *et al*, 1994a). Electrically cooling the detector removes the need for expensive liquid coolant. CCD chips are inherently low-noise devices. The detector itself is a two-dimensional Si array of 400 x 600 pixels, each pixel measures 22 micrometer x 22 micrometer. For spectral applications typically a central vertical strip of 20 by 576 pixels is used to read the signal. The last 24 pixels (600-576) in the strip are used as the output register. The long axis, therefore, is used to record the spectral dimension and the short axis the image height (intensity or spatial dimension) (Williams *et al*,

1994a). This chip area depends upon the sample and type of study. The active portion of the detector is adjusted from the ‘Experiment Set-up’ window.

Methods to improve the signal at the detector include ‘binning’ and cosmic ray removal, CRR. Selecting the binning option via the software allows the addition of up to four consecutive readout values to provide a single data point. The signal to noise is improved, since noise is random, and the size of the dataset reduced, but at the expense of spectral resolution (Dyer *et al*, 1995). The nature of the CCD chip renders it very susceptible to Cosmic Ray Events, CRE’s, particularly during long experiment exposures. CRE’s are easily spotted in the spectrum. They are very intense compared to the Raman peaks and have very narrow half-width values, maybe only a few wavenumbers. The facility exists to remove these effects automatically using the software. Essentially, the scan is repeated three times and the spectra compared. If the software recognises any peaks that are present in only the first of the spectra it is removed. However, the process more than triples the total exposure time. If the experiment acquisition time was relatively short then the spectrum can be re-run. Alternatively, if the acquisition was long then the peak can be removed manually.

Spectral analysis experimental set-up

With the area of the sample selected and the laser spot focussed the experimental parameters can be set. Fig. 3.9 shows the set-up screen. The wavenumber range selected depends upon the sample and whether the CE or static scans are to be employed. An unknown mineral sample would usually be analysed initially using a range between 100 cm^{-1} and 2000 cm^{-1} .

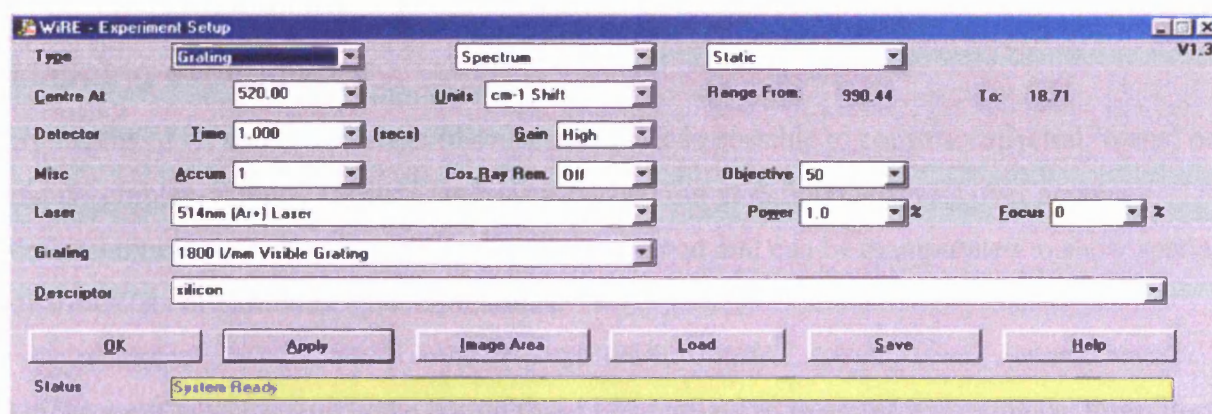


Fig. 3.9. Experiment parameters set-up ‘window’. Type of experiment, exposure time, laser power and wavenumber range may all be controlled.

Generally mineralogical samples contain no useful spectral information beyond these values and this range conforms well to the majority of the mineral spectra cited in the literature. A

static scan may provide the required information with the advantage that exposure times may be set at very short values (as low as 0.01 s for some species). Samples that are weak Raman scatterers may have their signals improved by increasing the exposure time. To illustrate, the Raman spectrum for diamond can be acquired in 0.5 s but the Raman spectrum of feldspar may require acquisition times of 30 s. However, long exposures increase the risk of Cosmic Ray Events (CRE's). Signals can be improved and noise reduced by accumulating spectra. Repeated, short exposure-time experiments also help to decrease the risk of CRE's. The number of identical repeat experiments can be set. The noisier the spectrum, the more accumulations are run and co-added, as explained in section 3.3. Since noise is a random event, by co-adding new spectra the signal to noise ratio (SNR also S/N ratio) is improved by the square root of the number of accumulations.

The required laser power can be selected from a drop-down menu in the experiment set-up window. Defocusing the laser spot can also reduce laser power density at the sample. The beam expander can be set, via drop-down menu, to defocus the spot by up to 100%. For routine spectral analysis a fully-focussed spot is used. A defocused spot or line focus attachment may be used to analyse thermally-sensitive samples since the power density of the laser is reduced. The choice is presented and selected from a menu. Once the parameters are set the experiment is set to proceed by clicking the 'get' button on the software interface. The recorded spectrum can then be saved to the computer, printed, manipulated or re-run with modifications to the set-up to optimise the signal.

Mapping experiments

By means of an automated stage (discussed later) it is possible to construct spectral 'maps' of many samples. Simply, spectral analysis is carried out at defined intervals over an area defined by the user. The data for each point are stored and can be manipulated to show spatial distributions of particular spectral features.

Under the 'Collect' menu is the option to set up a variety of mapping experiments. From the CCTV white-light image displayed on the monitor an area (or line) of the sample is selected by dragging a 'box' (or line) using the computer's mouse. The area is limited by the objective used and the maximum travel of the automated stage. It is then possible to define the array of analysis points recorded. This may be random or, more commonly, a regular distribution. The

distance between points (in x and y directions) controls the spatial resolution of the analysis. Step sizes of 0.1 micrometer are possible. Since the spot size is around 1 micrometer this value is usually selected as the step size interval. The need for greater resolution must be weighed against the increased analysis time. Each point is analysed using the parameters set in the experiment set-up 'window' before the sample is moved automatically to the next position. The acquisition parameters must be exactly the same for each point. Other options included a user-defined 'dwell' time. This function is used where photobleaching creates better quality data, for example. If a motorised z-drive is fitted it is possible to autofocus on the sample or to perform 'depth maps'. Although available for simple single point analysis the advantage for mapping surfaces with an uneven topography is clear. Autofocusing can be achieved either through the computer analysing the quality of the spot, i.e. the brightness, or by recording a Raman spectrum. In each case the stage height is moved incrementally through a defined range before assessment until the best position is achieved.

Upon completion of the mapping experiment the data is stored as a 'multifile'. This computer file contains the spectra for all the analysis points. These data can then be interrogated and manipulated collectively and a range of maps created displaying characteristics such as the intensity or width of a particular peak in a spatial context. The technique is powerful, if somewhat slow, and very detailed maps (experiments with thousands of analysis points are not unusual, e.g. Nasdala *et al*, 2001) with spatial resolutions as high as 1 micrometer can be created. There are several ways in which Raman mapping data may be used and presented. One of these is shown in Figure 3.10. The greyscale image in the upper left corner represents the intensity of the 520 cm^{-1} band of silicon over the mapped area of a computer Si chip with the letter 'B' etched into it. The dimensions are also indicated. The lower left corner displays the Raman spectrum recorded for any point on the map that is 'clicked' on using the mouse.

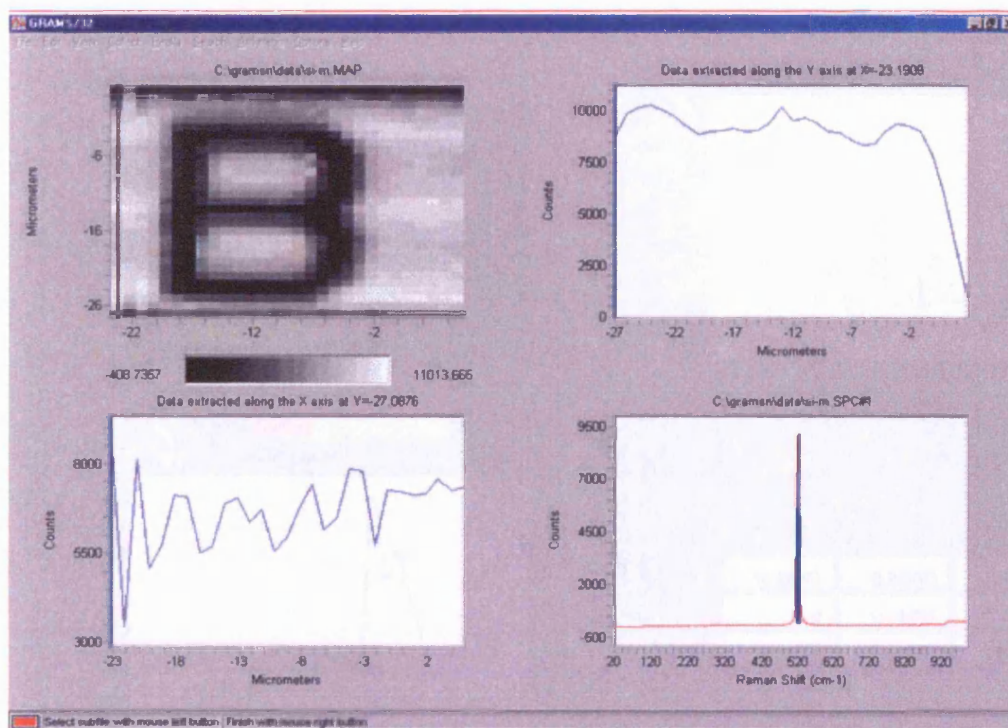


Fig. 3.10. Screen-grab of the results of Raman area mapping of an etched Si chip.

3.3 - Imaging Mode

In global Raman imaging mode a much larger area of interest on the sample is selected than in spectral mode. The selected region, up to around 100 micrometers in diameter depending on the objective, is illuminated with a defocused spot. Instead of the Raman spectrum being recorded the aim is to acquire a two dimensional spatial representation of the distribution of a particular species within the sample. For example, selecting to filter out all other information except that of a characteristic peak of clinopyroxene could image the distribution of exsolved clinopyroxene within orthopyroxene. Figure 3.11 shows an example of Raman imaging data recorded by the author. The selected Raman band belongs to pyrite and the image reflects the mineral's distribution (bright areas) within the quartz host. Images are saved to the computer and can be recalled independently of the experiment.

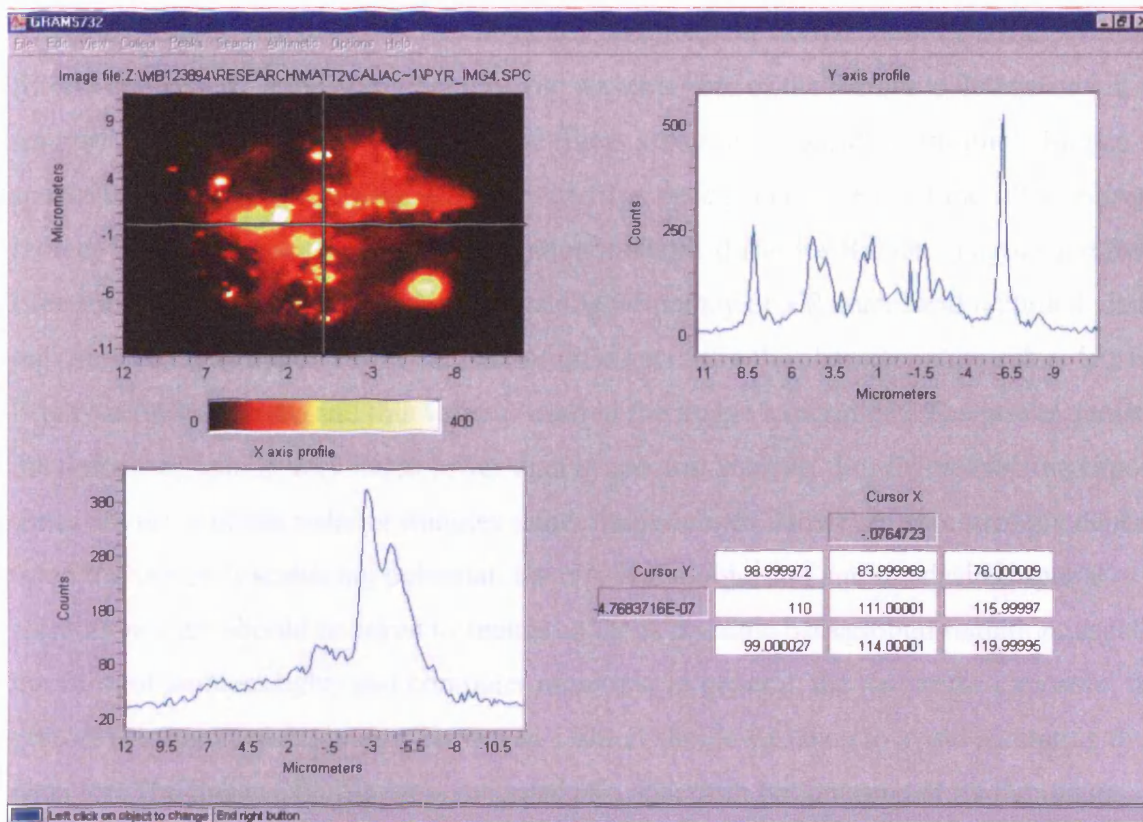


Fig. 3.11. Example of Raman global imaging results. Bright areas represent the spatial distribution of the species whose characteristic Raman peak was passed by the filters.

The beam path for imaging experiments follows the components coloured pink in figure 3.1. The scattered radiation passes through the HNF's as in the spectral mode to remove the Rayleigh scattering. Two 45° mirrors direct the signal through the image filter wheel (bottom left image of figure 3.1). This disc is controlled by a motor and can spin on its central axis so that any of the nine filters can be selected. The range of filters used is tuneable over the range 514 nm to over 900 nm with a bandpass (spectral resolution) of 20 cm^{-1} (Williams *et al*, 1994a). Another motor controls the narrow range of tilt angle the disc can be moved through on an axis perpendicular to the direction of beam propagation through the filter. This effectively controls the path length of the signal and thereby the cut-off wavelengths. The filtered Raman signal is then passed via two more mirrors then imaged onto the detector by a focusing lens.

Imaging analysis experimental set-up

Filter Image analysis is selected from the menu of options. This enables the motors that position the 45° mirrors so the beam travels in the imaging compartment of the instrument. It also optimises the detector settings. The wavelength of the characteristic feature, expressed in

wavenumbers, is selected. This automatically positions the correct filter (see fig. 3.1 Imaging filters) component at the correct angle. The wavenumber of the feature is determined in a separate, filter spectrum, experiment. The filters are used to record the sample's Raman spectrum instead of the grating. Running the filter spectrum ensures that the filter setting is correct for the image experiment. Calibration methods differ for Raman imaging and Raman spectrum acquisition and it is possible that the frequency of a Raman band recorded via the two methods may differ. From the filter Raman spectrum the characteristic peak is 'curve-fitted' to find its centre and this value is used in the image experiment. The power density of the defocused spot is very much lower than in spectral analysis. For this reason the exposure times are often of the order of minutes rather than seconds. However, this strongly depends upon the sample's scattering potential, the NA of the objective and the desired spatial resolution. Care should be taken to reduce as far as possible background radiation, usually in the form of ambient lights and computer monitors. In general, the longer the exposure, the greater resolution of the image. However, caution should be taken to avoid saturating the detector. The image experiment is recorded as a spectrum but interpreted by the image analysis software to produce a two dimensional image with bright areas corresponding to the intensity of the selected characteristic Raman feature.

Flat-fielding

The defocused laser spot can be shown to have a Gaussian profile, that is, a bell-shaped intensity. It is clear that increased excitation will occur towards the centre of the illuminated region. This may result in misleading Raman images unless corrected. The procedure for correcting the image computer files is termed flat-fielding. Before the image experiment of the sample is carried out an image is recorded in exactly the same way of a flat wafer of silicon, typically. The uniform image intensity file is stored and used in the flat-field calculation by the computer. The resulting file is an image corrected for uneven illumination.

3.4 - Confocal arrangement

It is possible to acquire the Raman spectrum in many cases from below the surface of the sample, i.e. the system can be enhanced in terms of its depth resolution. It can be shown that the lateral spatial resolution of the system is around half the diameter of the laser spot, i.e. ~1 micrometer, depending on the objective used. To reduce the signal received from scattering from the region outside the focus of the laser spot the Renishaw instrument employs two

spatial filters. The primary aperture is the mechanical slit and the second is the arrangement of the CCD detector. For confocal work the slit may be closed to 10 micrometers or less. Since the spectrograph is of on-axis design and with no astigmatism (Williams *et al* 1994a) the spatial dimension of the array can be reduced, typically to around 4 pixels in height, via the software such that the out-of-focus signal is discriminated against. This method is comparable with the 'pinhole' arrangement used by other manufacturers. Williams *et al* (1994b) discuss the two methods using a comparable experiment and describe the CCD plus mechanical slit confocal arrangement in more detail. They conclude that the slit and 'virtual slit' detector method provides a better depth resolution and light throughput, is less time consuming and more convenient than the pinhole arrangement. Depending on the sample the discrete sampling volume can be up to several mm below the surface. It has been widely used in the analysis of thin films, polymers and also fluid inclusions.

3.5 - Sampling

In contrast with many analytical techniques microRaman spectroscopy requires virtually no sample preparation, no matter what form the sample is in. Preferably, surfaces are flat and free of impurities. The microscope can operate in either transmitted or reflected light so most petrological and mineralogical samples are easily dealt with. Figure 3.12 illustrates how a thin section slide may be positioned beneath the microscope objective. The sample stage is either of the manual mechanical, metallurgical, type with adjustment wheels for the x and y directions or a motorised version equipped with encoders for accurate movement. The motorised version, often called the mapping stage, has much greater precision with a repeatability of ± 5 micrometers and is required for mapping experiments. A motor may also be used to control the z direction allowing depth profiling (in confocal arrangement) and the use of the autofocus facility.

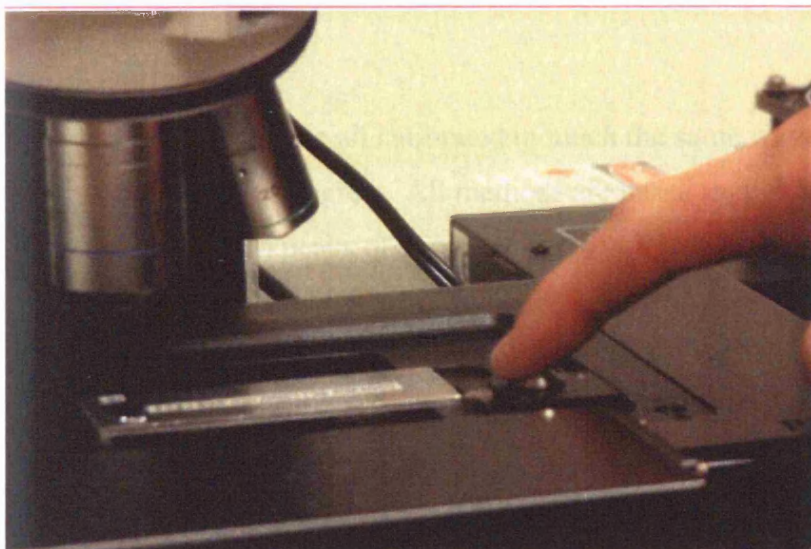


Fig. 3.12. Loading a slide on the mapping stage beneath the objective.

are many studies that successfully use high-pressure cells. Most commonly this is the diamond anvil cell (DAC). The very small sample is held between the points of two diamond crystals and pressure applied. The laser spot is focussed 'through' the cell and diamond to excite the sample. Calibration of the pressure attained is calculated by the Raman shift of a ruby crystal, a material that has a well-characterised response to increased hydrostatic pressure.

For samples too large to be mounted on the microscope's sample stage a 'macro kit' is available. An attachment screws into the nosepiece that deflects the light at 90° to the axis of the microscope. Objectives, usually with large working-distances, are screwed into the attachment and the large sample can be moved into focus. Alternatively, a fibre-optic can be attached. One end of the fibre-optic is held in a plate that attaches to the sample stage. The laser is then focussed in the usual way on the end of the fibre. Excitation and Raman radiation is carried along the fibre-optic efficiently up to many metres thus allowing points on very large objects to be studied.

Several sample cells are available and can be attached to the Renishaw instrument. A heating/freezing stage manufactured by Linkam can be attached allowing samples to be analysed between liquid nitrogen temperatures and several hundred degrees C. There

3.6 - Calibration

Raman spectrometers are all calibrated in much the same way and each instrument can be calibrated to different degrees. All methods are based on the fact that many substances have characteristic Raman peaks of very low full-width half maximum (FWHM) values. The spectrometer is calibrated depending on the laser excitation wavelength(s) used across the spectral range to 1080 nm. Simply, calibration involves recording the emission lines from a small Ne source and comparing the positions, as determined by automatically curve-fitting the spectrum, to the 45 or so reference peaks that occur in that region of the spectrum. A value for the residual error, expressed in terms of wavenumber, is determined upon completion. This type of full calibration is rarely required. A more routine calibration involves analysing the Raman shift from a flat Si wafer or diamond. Each has a very intense single characteristic peak. Again, curve-fitting calculations are performed to precisely determine the centre and minor adjustments to the positions of the grating can be performed through the software. Grating calibration of this sort is fast and routine and can be performed between samples or following the adjustment or replacement of any other component in the system, for example. It can also be used to determine whether any corrections need to be made due to thermal drift.

In addition to spectral calibration the response of the detector to the signal intensity (y axis) can also be calibrated. Any errors caused by filter ripple, an approximately sinusoidal pattern superimposed on the spectrum but rarely observed in the general collection of spectra, as well as vignetting can be corrected for and it also permits the responses of different systems to be compared (Smith, T. pers. comm.). A source of white light of known intensity is used for this type of calibration.

Referencing the positions of all the motors used in the instrument can provide an additional method of maintaining precision. This process is automatically carried out when the instrument control software is initiated. The 'Raman.ini' computer file is unique to each Renishaw Raman instrument and contains vital information about its set-up. The file is updated automatically. The data it contains is used by the computer to instruct the instrument on the reference positions of each motorised component, i.e. the beam expander, grating and image filter wheel and rotary-mounted filters if applicable.

3.7 - Optimisation

While the recording of Raman spectra is a largely trivial matter there are some methods that can be employed to optimise the signal. For example, in many cases the selection of an alternative excitation wavelength may produce a spectrum with reduced fluorescence. Experimentation with the power density at the sample, acquisition times and accumulations can often yield spectra of higher quality. Great care taken with the choice of objective and accuracy in focussing the laser can usually increase the signal strength. In many cases only a small portion of the Raman spectra may be required and better results may be achieved if this region is concentrated upon. Many of these adjustments are based on user experience, knowledge of the Raman response of the sample and a clear idea of what is required of the analysis.

3.8 - Data manipulation

The GRAMS[®] software package supplied with the Renishaw RM instruments provides a very powerful means of spectral data manipulation. It is used by other manufacturers of spectroscopic equipment, not just Raman instruments. Its most basic function is to interpret the information from the detector and produce a spectrum on the computer monitor. It is useful to mention here some of the more common data manipulation functions.

Baseline correction

Figure 2.6 displays the Raman spectrum of emerald recorded by the author using 514 nm excitation. The spectrum is seen to be imposed a gently climbing fluorescence background. In this example the background does not mask the Raman bands, as it does with the longer, 785 nm excitation, also shown in figure 2.6. It is possible to artificially remove the background using the software. Several options are available, including 'Auto' and various mathematical algorithms such as polynomial and quadratic functions. In practice, good results can be obtained using the Auto option or by manually inserting the shape of the background to be removed. An example of a manual 'multi point' baseline correction applied to the 514 nm emerald Raman spectrum of figure 2.6 is displayed in figure 3.13. In the case of the emerald spectrum, a baseline correction is probably not required. Manual corrections should be applied with great caution since it is easy to inadvertently add spurious peaks, alter the relative ratios of real bands or to remove bands.

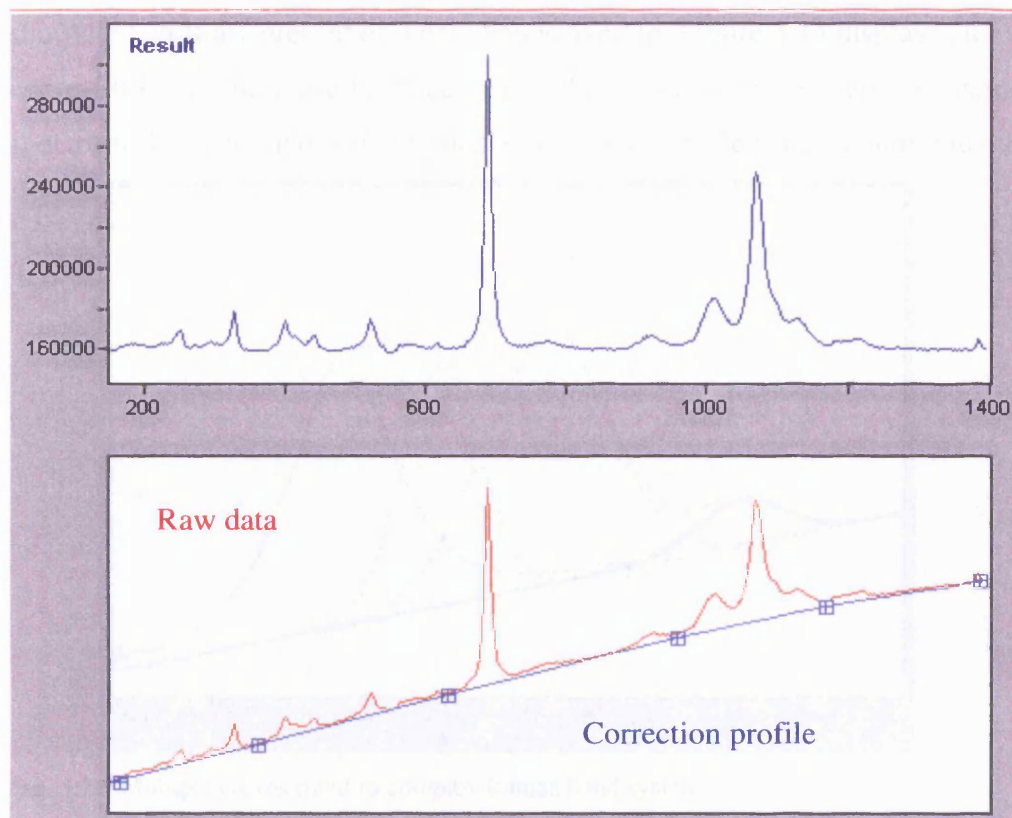


Fig. 3.13. Manual multi point baseline correction of emerald Raman spectrum recorded using 514 nm excitation.

Smoothing

The signal to noise ratio has already been discussed. It is possible to artificially improve the ratio by applying various algorithms and functions. The GRAMS[®] software allows the user to use either a Fourier, Binomial or Savitsky-Golay method. The author favours the latter since it appears to offer a reduction in the mean noise signal without the loss of spectral resolution (i.e. band broadening) observed with the two other methods. Ideally, noise would be reduced by re-running the experiment using either increased incident energy, longer acquisition times or greater accumulations or a combination of all these.

Curve-fitting

Because the RM instrument employs a CCD detector with only 600 pixels (effectively 576) in the spectral axis, there are relatively few data points that define the bands. Other manufacturers may have close to twice the number of pixels. To accurately determine the position, shape, FWHM, intensity and area of a band, users of Renishaw instruments use a curve-fitting routine. This has been alluded to in 2.3. The example of fitting a mixed Gaussian-Lorentzian profile to a band was demonstrated in figure 2.5. The method can be applied to more complex band shapes, for example, where band splitting has occurred,

shoulder bands are present or where bands overlap. Figure 3.14 displays an example where curve-fitting has been used to ‘deconvolute’ a system of three bands in a garnet Raman spectrum. The parameters mentioned above are available for each individual band.

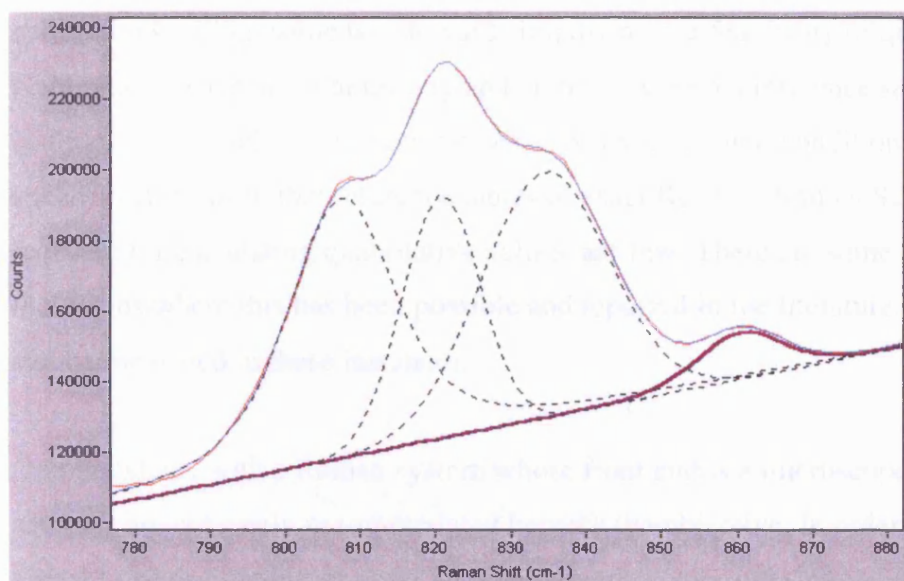


Fig. 3.14. Multiple curves fitted to complex Raman band system.

Curve-fitting is also often employed in the creation of Raman maps with the RM instrument. The Si chip map in figure 3.10 could have been created by applying a stored ‘curve-fit file’ to each of the Raman spectra that made up the experiment ‘multifile’. In this way, maps can be created of the FWHM, intensity, position and area parameters calculated by the curve-fitting routine.

3.9 - Limitations and drawbacks of the technique and instrument

With recent technological developments Raman spectroscopy has become an extremely useful addition to the analyst’s laboratory. The method is rapid and is complimentary to IR spectroscopy, a technique far more established in terms of routine analysis. Raman spectroscopy does have limitations. As mentioned elsewhere the inherent fluorescence of many samples proves to be the largest problem. Methods of overcoming or reducing the effects have been covered in 2.4.

Whilst analysis by Raman spectroscopy serves as an excellent qualitative method it has only rarely been used to provide quantitative information. Theoretically, the spectrum can be used to provide quantitative information since the area under a peak is proportional to the molecular species or structural unit it corresponds to (Janz and Wait **In:** Szymanski, 1967),

the basis of the Beer-Lambert Law. The fundamental problem is based in not being able to define the exact volume from which the scattering occurs and in characterising the exact laser power density at the sample (McMillan and Hoffmeister, 1988). Recent advances in intensity calibrations will go some way towards improving the feasibility of quantitative studies. Calibration by means of analysing and comparing with a reference sample is difficult since it is almost impossible to reproduce exactly the experimental conditions. Differences between spectrometers mean that reference tables of exact Relative Raman Scattering Cross-Sections required for calculating quantitative values, are few. There are some analyses of fluid inclusions where this has been possible and reported in the literature. The discrete volumes can be measured in these instances.

One drawback with a Raman system whose front end is a microscope is that very rough samples are not easily accommodated beneath the objective. In order for collection of the signal to be as efficient as possible high numerical aperture (NA) objectives (also called 'fast' lenses) are used. In most cases the working distance, i.e. that distance between the sample and objective, is very small. For objectives with magnifications of x50 this distance is around 350 micrometer. To accommodate lenses with such high NA's (e.g. 0.75 with a x50 objective) the body of the objective must be very wide. This naturally limits how close the objective may approach the sample surface. Ideally, therefore, sample surfaces are flat. Long-working distance objectives, up to several mm, are available but the greater working distance allows more stray light to be collected.

The RM series of instruments are, technically speaking, spectrographs or spectroscopes. Their arrangement of relatively wide aperture slit, single dispersion grating, multichannel detector and use of filters to block the laser differs from spectrometers. Spectrometers used for Raman studies usually consist of two or three ('double' and 'triple') monochromators. As the name suggests, monochromators transmit only one wavelength to the detector at any one time. Rotation of the gratings allows a continuously changing wavelength to be presented to the detector and a spectrum is slowly built up. Double and triple 'additive mode' monochromators use two or three gratings respectively, to disperse the light. Two apertures are used in the triple and one in the double monochromator to remove the excitation wavelength, the elastically scattered light, and stray light. A single channel detector, for example, a photomultiplier tube, receives this signal. Triple monochromators operating in the subtractive mode operate in a similar manner but the second grating recombines the light

before it is re-dispersed by the third on to the detector. Overall, the resolution is less than that achieved by a double monochromator (Gerrard and Bowley, 1989). In this way, the RM series is similar but employs filters to block the excitation wavelength instead of two gratings and an aperture. Monochromators have the advantage that they are able to operate much closer to the laser 'line' than filter-based spectrographs. In general, the greater the groove density of the grating, the greater the spectral resolution. However, this is achieved at the expense of throughput. Since the Raman signal is inherently very weak double and triple monochromator spectrometers are inferior to spectrographs of comparable spectral resolution.

Almost all materials may be analysed using Raman spectroscopy. Samples in solid and liquid form can all be studied non-destructively (except in some cases where the sample is very thermally-sensitive). With the advent of stable high-powered lasers and sensitive detectors the previously intractable gaseous samples now no longer present a problem. Black and strongly-coloured substances and those with high Fe content may present difficulties but these may, in some cases, be overcome with an alternative excitation wavelength. It has been shown that the type of bonding affects the Raman scattering ability of a substance. For this reason metals, or those substances with strongly metallic bonding, are not amenable to Raman analysis.

3.10 - Other manufacturers

Worldwide, Renishaw, plc is one of a small but growing number of Raman spectroscopic instrument manufacturers. The popularity of the technique lies in the diversity of possible applications and the success in the development of easy-to-use, reliable instruments. Instrumentation costs are decreasing with increasing technological knowledge in the fields of lasers, detectors and optics.

Whilst the principle of analysis remains the same, the various manufacturers achieve results in slightly different ways. Some of these differences stem from the fact that some manufacturers target different market sectors. For example, concentrating on process-line applications might lead an instrument's design to be based around fast spectral analysis of a bulk sample via fibre-probe. To compare the Renishaw RM series instruments other laboratory research grade microRaman designs should be selected. Amongst these is the French company ISA, which markets the T64000. The spectrometer can function as a single, double or triple in subtractive or additive modes. Spectrometers of this kind employ a different configuration of

spectrometer components than are found in 'notch filter'-based instruments. Rayleigh rejection is achieved via mechanical slits with gratings used to disperse and recombine the Raman light. The basic design of this type of spectrometer can be found in Wolverson (**In:** Andrews & Demidov, 1995), for example. Mono- and/or multichannel detectors can be fitted to the instrument. Spectral resolution with the triple arrangement is quoted at 0.15 cm^{-1} and signals as close as 1 cm^{-1} shift from the excitation wavelength is given in the technical literature. These figures highlight the spectral advantages of this type of spectrometer, however, signal throughput might be expected to be low. This instrument and others from ISA employs a pinhole in the optic axis. As a consequence the system is always in confocal arrangement. The pinhole diameter can range in size between 100 micrometers and 300 micrometers and is placed in the back focal plane of the microscope. Adjustment in the optical plane and along the optical plane was traditionally controlled by means of manual vernier. Modern instruments use a motorised version controlled by the user software. Arguments against the pinhole method of achieving confocality are that it is difficult and time-consuming to maximise the position and less signal throughput results.

InPhotonics of the USA manufactures a Raman instrument with an echelle-equipped spectrograph. This type of grating has a relatively few number of ruled lines per mm and a broad groove. The spectral range is compromised but resolution of less than 1 micrometer is easily achievable. Although not a microtechnique in terms of selecting and defining the sample spot, this instrument used a narrow fibre to limit the spatial dimension.

The ability to record the spatial distribution of characteristic Raman peaks from a region of the sample is described in 3.3. This powerful facility is only available to those instruments that use a two-dimensional array multichannel detector, such as a CCD. The Renishaw instrument is able to preserve the spatial characteristics of the Raman scattered signal through both the notch filters and narrow bandpass filters and project the information onto the detector and record a Raman image. Only the Renishaw instrument offers this technique of Raman analysis.

4 – Aims of the project and outline

The purpose of this section is to describe the aim of the project, to discuss why certain application areas were chosen and the format of the rest of the work.

4.1 – Introduction

The preceding chapters have briefly introduced the origin of the project, the basic principles of the underlying theory and the Renishaw Raman instrument on which the following analytical investigations will be performed.

It is clear that the technique and the instrumentation has some limitations but appears to have much to offer the mineralogist and petrologist. Given the limitations of the instrument, the theoretical considerations and the scope of published work, some parameters could be determined for suitable materials that could form the basis of the research project.

It has been stated that Raman spectroscopy is not yet a routine technique in mineralogical studies. The well-understood methods based upon X-ray interactions (and the derivatives of these methods) hold a pre-eminent position in this regard. From the preceding sections it is apparent that Raman spectroscopy has much to offer to compliment these traditional techniques.

The fundamental aim of the project, then, is to *apply microRaman spectroscopy to a variety of materials of interest to the mineralogist, petrologist or crystallographer and to assess the applicability and usefulness of the technique in the context of the analytical instrumentation widely used in the Earth sciences.*

4.2 – Possible areas of exploration

The application potential for Raman spectroscopy in mineralogy and related areas is vast. Its use thus far has predominantly been in mineral characterisation, investigations of crystal structure and the qualitative analysis of fluid inclusions. It was decided that a series of ‘case studies’ focussing on mineral identification, the structural study of minerals, the ability to create maps

based on spectral data and Raman imaging would be the best way of approaching the research project. Collectively, these are the key areas in which microRaman spectroscopy offers advantages over techniques traditionally used in the Earth sciences.

Mineral identification

Traditionally, mineralogists and petrologists have relied on physical and optical properties to identify minerals. A technological solution was provided by the X-ray diffraction technique. The method enabled the accurate distinction between many polymorphs and minerals of identical physical and optical properties, as well as facilitating the study of very small minerals. The method does have limitations. Data can be ambiguous and difficult to interpret; significant sample preparation is usually required and may require that a sample of rock be reduced to a fine powder. MicroRaman spectroscopy appears to a comparable method of mineral identification to X-ray diffraction but with fewer limitations.

There are many possible potential areas for exploring this facet of the technique in petrology. The study of fluid inclusions and daughter minerals is one of the more obvious but this was rejected for this study since it was decided that there has been considerable research in this area. Further developments must entail the advancement of quantitative analyses, which is beyond the scope of this work.

Many of the Fe- and Mn-rich minerals are difficult to distinguish and it was thought that Raman spectroscopy might be able to address this issue. A set of samples was acquired but the minerals proved rather intractable to the technique and this aspect was not explored further.

Sections of this work that explore the method's ability for the discrimination between minerals are sections 5, where the existing Renishaw database of mineral spectra is reviewed, and section 6 that describes the analysis of a possible coesite inclusion; a key indicator mineral for ultra-high pressure metamorphism that is difficult to accurately identify optically. Mineral identification also forms aspects of sections 11 and 12 in studies of 'industrial' rocks and minerals. In these situations, the technique is applied in an attempt to solve existing problems that could not be addressed by other techniques and where microRaman spectroscopy has a significant potential

analytical advantage. Technique developments are described in sections 14 and 15 that facilitate the ability for mineral identification using the technique. These sections address theoretical and practical considerations, respectively.

Crystal structure

Characterising new minerals based on their Raman spectra, in combination with other techniques, is likely to become increasingly common practice. It provides information that is comparable to XRD but without the limitations described above. However, due to the difficulties in acquiring potentially new minerals, none have been attempted in this work.

There is great scope for studying various aspects of crystal structure and crystallography using Raman spectroscopy. These include calculating the orientation of functional groups and commenting on the bonding environments. In this work, changes in the structure of some minerals have been studied by how these changes are reflected in the Raman spectra. Biotite, zircon and quartz are the focus of sections 7, 9 and 10, respectively.

Mapping

The ability to create maps spatially detailing the distribution of key components of Raman bands on a micrometer scale is potentially one of the major advantages that the technique offers. One could, for example, study the zoning in magmatic feldspars that might not be apparent from optical microscopy. Because the technique is applied over a micrometer scale reaction rims and diffusion processes could be studied.

Section 10 describes the use of mapping in a study of the strain thought to be stored in undulose quartz. Mineral structure changes are mapped in studies of biotite and zircon in sections 7 and 9.

Imaging

As mentioned, the ability to project an image of a selected Raman feature from a large illuminated area to highlight its distribution is a function not offered by any other microRaman manufacturer. To this end there are few published accounts of this technique applied to minerals.

Global Raman imaging has been applied in this study to zircon and limestones, in sections 9 and 13.

As a rapid alternative to some types of Raman mapping experiments, the technique could have been applied to many other samples. Imaging of exsolution lamellae, overgrowths, inclusions, textures and symplectite intergrowths would all make interesting areas of petrographic study that would be difficult or time-consuming to study by other methods.

4.3 – Format of the project

The following chapters of this work have been grouped loosely by the headings above, i.e mapping or by sample type, since often the different approaches described can be used on the same sample. It also allows each sample to be considered as a separate ‘case study’; a complete entity that describes the use of the technique in only that region of study. Each is introduced and placed in context, the experimental work discussed and concluded. The common threads of microRaman spectroscopy and the analysis of materials relevant to the Earth scientist run throughout. The underlying theory has been briefly presented in section 2 and a description of the instrumentation given in section 3.

Chapter 2 deals with the main fingerprint applications, sections 5 and 6, although mineral identification is a strong theme throughout this work. Chapter 3 covers the most significant crystal structure investigations. Chapter 4 is concerned primarily with rocks and minerals used for structural purposes and the processes and transformations that can affect these and other rocks. For each case, previous analytical methods have not been able to solve the issues highlighted and it was thought that different approaches offered by Raman spectroscopy might be able to add to the existing techniques used in these areas. Three developments to the technique are described in Chapter 5 that arose during the course of this work. Since each section is discussed and concluded, general conclusions appear in Chapter 6 along with suggestions for further work.

Chapter 2 – Fingerprint applications

This chapter comprises sections 5 and 6 of the current work. A discussion of the use of databases of mineral Raman spectra is followed by an account of the work undertaken to improve an existing database with suggestions for further development.

A case study is presented where an attempt is made at the identification of a mineral polymorph. The findings are discussed with the implications for the petrogenetic history of the rock sample.

5- Inorganic database development

The use of reference databases is pivotal to the success of Raman spectroscopy in the qualitative analyses of unknown materials. The following describes the use of one of the proprietary Renishaw databases and makes some suggestions for development.

5.1 – Introduction

The pre-eminence of microRaman spectroscopy as a fingerprinting tool cannot be denied. IR spectroscopy is inferior due to the naturally broad absorption bands, and sampling constraints hampers XRD analyses. However, the ability to accurately determine the exact species of a sample must, in the absence of any other information, be limited by the reference database. Renishaw, plc market several databases including those of polymeric materials, substances of interest in forensic science and inorganic materials. The databases are supplied on a single CD with access to each provided by a password that is sold to the customer.

5.2 – The Renishaw Raman Database of Minerals and Inorganic Materials

Renishaw's collection of approximately one thousand gem, mineral and inorganic materials spectra in the form of a searchable database has been in existence since around 1996. Although the concept was for a gemmological tool it had the potential to be a very useful tool to the mineralogist or petrologist. There exist a number of other similar, significantly smaller databases of mineral Raman spectra and generally these contain spectra that are freely available on internet websites. These are largely limited collections of spectra collated by researches at academic institutions, for example, the database of some 150 spectra at the University of Parma assembled by Dr Danilo Bersani. Others, for example, that held by the CalTech Institute, consist not only of spectra recorded by researches at that institution but the facility exists for anyone to contribute a mineral spectrum. Because there are many different models and designs of Raman spectrometer, and from the discussions of spectral resolution and calibration, these spectra should be approached with caution.

To the author's knowledge, the Renishaw mineral database remains the largest single collection of mineral Raman spectra. Those databases that exist in the public domain are merely collections of spectra, i.e. a spectrum of an unknown mineral cannot be directly searched against them.

Using any of the Renishaw databases is a very simple process. The sample of interest is analysed using the Raman instrument using whichever configuration of parameters provides the best quality spectrum. This may involve selecting a different laser or acquiring many accumulations to provide a good SNR. From the GRAMS software the 'Search' option is selected. A new window appears that allows the user to select the appropriate database and the type of search required. Within the categories of 'Text', 'Peak match', 'Full spectrum' and 'Custom' there are further options to refine the search. The 'Text' search is a useful option when the sample is not completely unknown. Typically, the 'Peak match' is selected or in combination with the 'Full spectrum' search using a first derivative least squares correlation. After initiating the search the computer applies the algorithms to the sample spectrum and the contents of the database. Within a few seconds the matches are presented as a list of hits. An example of the resulting computer screen is depicted in figure 5.1.

From the first use of the Renishaw Raman Database of Minerals and Inorganic Materials it was clear that it had serious shortcomings. Running a search resulted in the generation of a 'hit' list of 20 reference spectra that most closely matched the sample spectra using the search parameters and mathematical functions. On screen the information for each 'hit' comprised only the species name and positions of the three most intense peaks in wavenumber shift. Selecting the 'Hit info' button and 'Text' screen for any of these reference spectra yielded no further useful information. Other areas that raised concern were the several spurious entries and the use of old terms used in the gem trade and not the recognised mineralogical term for that species. It was felt that entries such as 'slate' should be deleted. Clearly, a rock type such as slate is an assemblage of different minerals and could not be represented by a single spectrum derived by a technique with a spatial resolution as high as one micrometer.

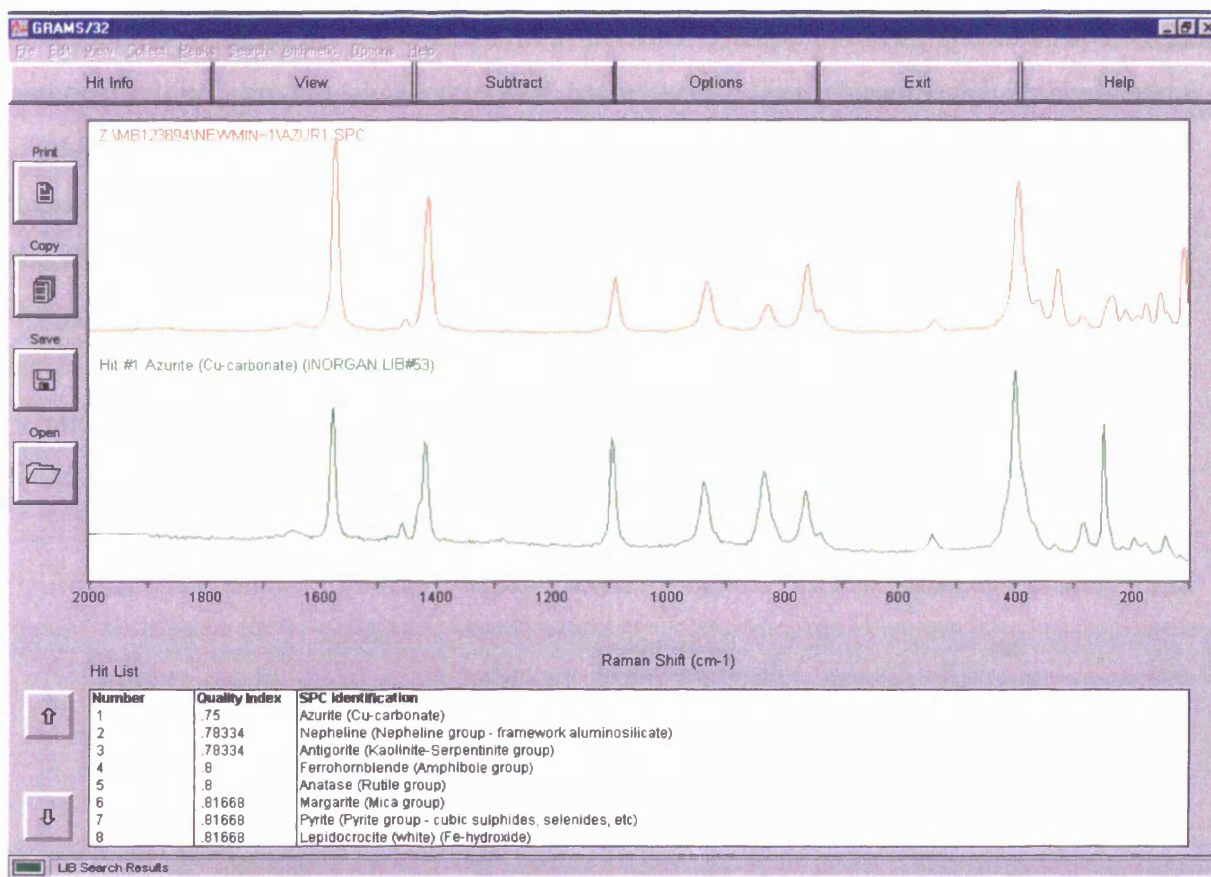


Fig. 5.1. Example of library search showing sample spectrum in red and reference spectrum in green.

There were many entries for species that belonged to solid solution series' but listed by their family name. It was felt that because of the way in which the Raman effect responds to solid solution in minerals it was appropriate to leave these spectra in the database because even though the term applied was broad they still provided useful information.

5.3 – Database development

It was decided that to make the database a far more useful tool it would need to be extensively re-edited. The most useful addition to the database would be to add chemical formulae. Ideally, quantitative chemical compositions for each entry would be provided but this level of information does not exist for the reference spectra. Raman spectroscopy applied to mineralogy is at best semi-quantitative so the absence of chemical data was deemed to be not too great a criticism.

The Inorganic Database, originally supplied to customers on a 3 ½ inch disk, was also accompanied by two hardcopy volumes. They contained some additional information, for

instance, the positions of all the peaks for a specimen and copies of raw specimen spectra i.e. without their background signals removed. More usefully, some specimens had their general chemical formulae listed. However, some of these were erroneous and the majority were missing. Cross-referencing between sample spectra and the hard-copy library information was time-consuming. To provide immediate on-screen information for each 'hit' to aid the non-mineralogist a brief descriptor was determined for each species. This took the form of either the group or family the species belongs to and in many cases a chemical and structural summary. In figure 5.1 this new information is located in the hit table column labelled 'SPC Identification'. From the results screen of the search it is possible to view a text screen for each of the 'hits'. An example of the 'Hit info' now available for all entries can be seen in figure 5.2.

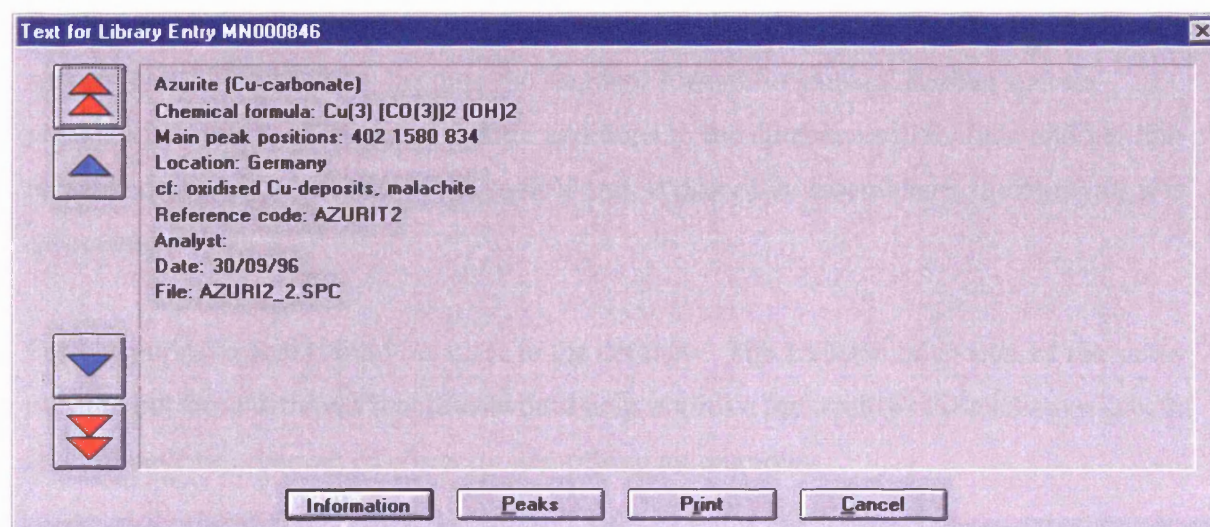


Fig. 5.2. 'Hit' text available for search matches.

For each reference species the chemical formula was added. In some cases this was quite general. Other information added includes a line of key word text that gives the analyst information on topics such as which rock types the mineral is commonly associated with, synonyms and minerals related either by chemistry or structure. Where the source location, or provenance, of the reference is known this was also added. All the reference samples are listed with a code so that the individual specimens can be reanalysed if there is any doubt about their nomenclature.

It was decided that mineralogical structure or crystallographic information was probably not of much importance to the analyst and so would not be included. The interested analyst could refer to reference literature for detailed information.

To accompany the revised version of Renishaw's software application a press release was drafted (see Appendix) and appeared in a Company newsletter distributed worldwide.

5.4 – New additions

The reference samples used to build the database belong to the private collection of Dr. J.B. Nelson. At the beginning of this project approximately 100 samples were presented to be analysed and added to the database. In preparation, information was recorded in a format so that it could be easily transferred to the database and be of the same standard as the re-edited spectral files. This has now become the standard format for mineral Raman spectra presentation used by Renishaw. Future additions to the database will include another line of text that describes the nature of the sample and, if part of an assemblage, the minerals it is associated with.

Further improvements could be made to the database. The addition of spectra of the same mineral but from different localities would help improve the quality of the existing spectra and improve the chances of correctly identifying an unknown.

Minerals commonly associated with particular geological settings, for example, hydrothermal ore deposits may prove useful. Often, the minerals are characteristic of a particular type of deposit and recognising the type from key minerals may help to predict the occurrence of minerals of economic importance.

Thorough chemical and Raman studies of suites of minerals comprising a solid solution series may help to quantify samples from those families. Figures 5.3 and 5.4 very simply depict the one- and two-mode behaviours exhibited by some minerals that form a solid solution series. One-mode systems are those in which the frequency of a Raman band changes between two end members along the solid solution. The change may not be linear nor very large (Figure 5.3 depicts a very large change for clarity). Two-mode behaviour, as displayed by the olivines forsterite, fayalite and montecellite, for example (Chopelas, 1991),

is described by two bands in the Raman spectrum that change in relative intensity along the solid solution. To a first approximation the ratios of the intensities of the two bands can be used to comment on the relative proportions of each member.

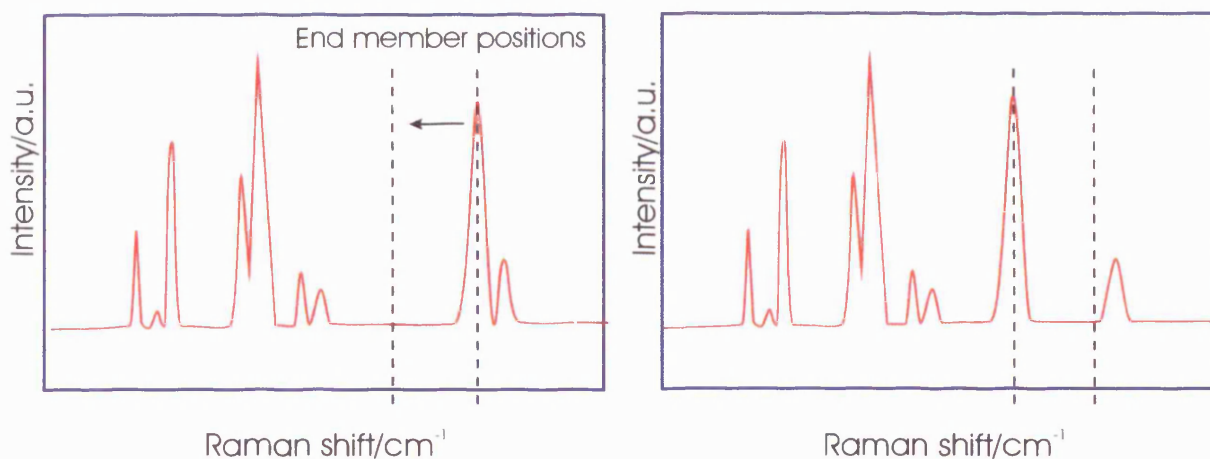


Fig. 5.3. Representation of one-mode behaviour in solid solution Raman spectra.

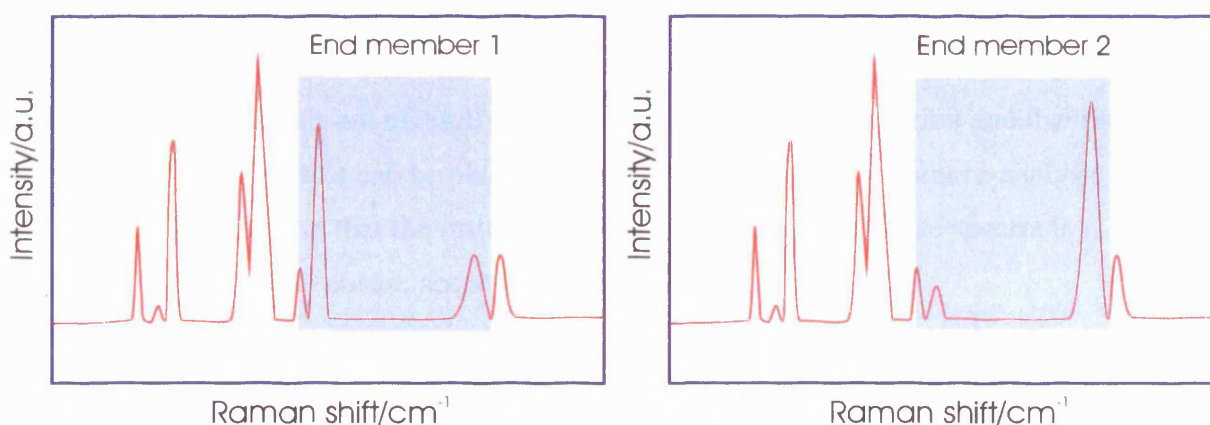


Fig. 5.4. Representation of two-mode behaviour in solid solution Raman spectra.

The acquisition of suitable solid solution series samples and their characterisation by quantifiable analytical techniques represents a significant program of study and was not undertaken as part of this work.

The Raman analysis of fluid inclusions has only been very briefly mentioned in this study. The very nature of the phenomenon presents difficulties in determining quantitative data for the species present in an inclusion. However, there are some published studies that have been able to achieve this. Increasingly, semi-quantitative analyses are appearing based on microRaman spectra. Whilst this is not the place to describe in detail the problems and proposed solutions it is pertinent to suggest that a database of fluid inclusion components would be of great benefit. MicroRaman spectroscopy remains an excellent qualitative tool.

Although generalisations are impossible, it is fair to say that many of the mineral inclusions studied, and those of greatest interest to the petrogenetic history, belong to the C-O-H-N-S system. Demonstrably, species belonging to this system, e.g. CO₂, SO₄, can be detected using Raman spectroscopy. It would be trivial to record the spectra of these species but of more use would be the response from synthetic samples that are made to a specific composition, both in liquid and vapour forms. Daughter crystal spectra could be gleaned from the existing database.

5.5 – Conclusion

The re-editing of the 1000 or so entries has led to a more useful database. For example, a text search for 'Feldspar' now responds with 49 'hits' representing the semi-precious and common varieties of this group as opposed to the three spectra returned in the unedited version. The database can only benefit from additional spectra. However, it is important that these reference materials are carefully characterised prior to their addition and that they remain as part of a set that can be obtained easily should their subsequent re-analysis be required. It is imperative that the instrument used to record the reference spectra is thoroughly calibrated to ensure accuracy and precision.

Whilst a general database of mineral spectra is very useful there is considerable scope for more specific databases to run in parallel. These could be rock type-, deposit-, geological setting-, or fluid inclusion-specific.

Other examples where specific databases could be useful are:

1. Economic deposits. Many of the minerals in these settings are opaque and analysis of these phases in polished block by reflected light microscopy can be ambiguous. An additional advantage is that polished blocks of this kind are ideally suited to microRaman spectroscopy. The deposits often host rare minerals and unusual compositions as a function of the highly evolved fluids involved. Such a database could also include fluid inclusion related compounds, for example, like those in the C-O-H-N-S system.
 2. Brick, cement and industrial minerals. Minerals in this field range from the common to unusual, like the 'cement minerals' that include C₃S, thaumasite and ettringite. Due
-

to their rarity they may be difficult to identify from petrography or XRD pattern.

Development of the database could lead towards quality control for some industrial minerals.

3. Environmental mineralogy. A database for this application area could also include biological compounds like lichens and soil.
4. Igneous, volcanogenic and metamorphic systems. Rocks from these settings often have unusual chemistry and may contain trapped fluids.

6 - Suspected coesite inclusion

The ability to successfully acquire Raman spectra from minerals in petrographic thin section is of paramount importance to the petrologist. The technique potentially offers an almost unique method of distinguishing between minerals of identical physical properties. This study aims to show how the ability to make this distinction using Raman spectroscopy can have ramifications for petrological study by analysing a suspected coesite inclusion.

6.1 – Introduction

Raman spectroscopy is an excellent method of distinguishing between mineral polymorphs. Traditionally, petrography and X-ray diffraction methods are used. However, these techniques cannot be applied in all situations and the results of the analyses may be ambiguous. Many common minerals are stable in more than one structure even though their chemical composition remains the same. Raman spectroscopy provides a simple and effective means of discriminating between polymorphs based on crystal structure. Frequently, the presence of a particular polymorph has bearing on the geological interpretation of the rock in which it occurs.

6.2 - Sample description

The suspected coesite sample used in this study comes from an omphacitite pod from the Glenelg inlier, NW Scotland. The suite is thought to have experienced eclogite facies metamorphism. Peak conditions are thought to have been 20 kbar at 750°C based on chemistry and petrology (C. Storey pers. comm.). The successful identification of a suspected inclusion as coesite essentially confirms minimum conditions of metamorphism. In addition, there have been no previous reports of coesite in the NW Highlands of Scotland (C. Storey, pers. comm.).

The omphacitite consists of essentially equigranular pyrope/jadeite garnet and omphacite pyroxene porphyroblasts. Triple junctions are common. The matrix is composed mainly of aggregates of polycrystalline quartz and feldspar. Some larger grains of feldspar exist and some of these show perthitic textures. The rock is relatively fresh and unaltered. In places minor clay minerals occur along grain boundaries. The inclusion is shown in Figure 6.1 using low magnification plane polarised light. The image was recorded from the closed circuit

television camera mounted to the Leica microscope attached to the RM instrument. Figure 6.3 appears to show a coesite inclusion surrounded by an α -quartz mantle, all within an omphacite grain. Note the high relief of the 'core', the radial fractures in the omphacite and the polycrystalline mosaic. The inclusion measures approximately 180 micrometers along its long axis.

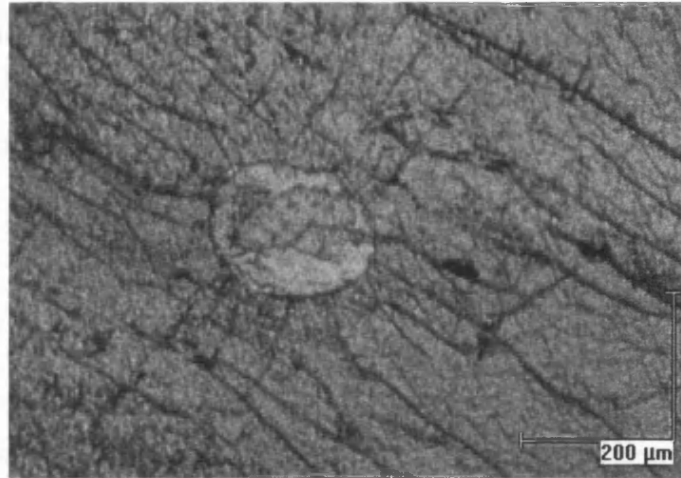


Fig. 6.1. PPL image of suspected coesite inclusion in omphacite.

Coesite has a slightly higher relief and lower birefringence than α -quartz. Despite these differences coesite is rather difficult to distinguish from α -quartz by optical petrography alone. As described later, the use of textural information can be useful in discriminating between the two polymorphs but these textures can be misleading. Obviously, the use of chemical methods does not aid the distinction between polymorphs.

Where single crystals of polymorphs are available, X-ray and electron diffraction techniques may be used. However, possible occurrences of coesite in the sample rock are expected to be extremely unusual and so no attempts were made to isolate single crystals. An approach using microRaman spectroscopy was deemed the most suitable method of determining if the inclusion was, indeed, coesite. If not, the spectra data derived might indicate the nature of the inclusion. Analyses can be performed non-destructively on the grain *in situ* in the thin section without the need for further preparation. Analysis spot sizes of the order of a micrometer permit highly specific, high spatial resolution analyses to be performed on any part of the inclusion or any other grain. As has been mentioned, the technique is an excellent means of discriminating between polymorphs because the Raman spectrum is influenced predominantly by atomic structure.

6.3 – Coesite

It is insightful to describe the structure of coesite; most of which has been learned through the study of synthetic specimens. A review of the limited occurrences of coesite and its petrogenetic significance highlights the importance of unambiguously detecting it. Of the few published accounts of the presence of coesite in an assemblage, many were by textural evidence; an adequate micro analytical technique was really not available before the advent of microRaman spectroscopy. Subsequently, there have been published descriptions of the mineral in rocks that have used this technique.

Chemistry and structure of coesite

Unlike quartz, coesite is pure SiO₂. The low temperature polymorph normally has a composition ‘very close to 100 per cent’ silica (Deer *et al* 1995). Impurities are present either as minute inclusions like rutile or as fluid inclusions and fluid-filled cavities. Substitution of Al³⁺ for Si⁴⁺ may occur; accompanied by either Li⁺ or Na⁺. Studies by Mosenfelder & Bohlen (1997) using synthetic coesite highlight the importance of H₂O in the kinetics of transformation to quartz. These authors point out that it is unknown if coesite incorporates H₂O to the same degree as quartz. They found no evidence of the presence of H₂O using FT-IR methods. Although their synthetic coesite contained significant quantities of hydrogen it was thought that this was mostly in the form of fluid inclusions.

Probably the most significant work on the structure of coesite was carried out not long after its discovery and synthesis in the late 1950’s (e.g. Zoltai & Buerger, 1959). Coesite is monoclinic with the *C2/c* space group. It has a ‘feldspar-like’ (Deer *et al op. cit.*) structure of the three-dimensional linkages of four-membered rings SiO₄ tetrahedra. Gibbs (1977) went on to describe the “corrugated layers” of cross-linked 4-membered rings to produce “crankshaft” chains that formed a much denser arrangement than seen in feldspars. The unit cell is hexagonal, as is its symmetry.

Occurrence

Coesite is a rare polymorph of silica that is stable at high pressure. The more common varieties are quartz, tridymite and cristobalite that are stable at surface conditions of pressure

and temperature. Coesite is commonly associated with ‘foreign’ rock inclusions, or xenoliths, in kimberlitic rock. These fragments are believed to represent material from beneath the Earth’s crust. Should free silica be present in the upper mantle it has been suggested that coesite is the stable phase (Chopin, 1984). Reported occurrences of coesite in xenoliths date back to the late 1970’s (Smyth & Hatton, 1977, and Ponomarenko & Spetsius, 1978, **In:** Wang *et al*, 1989). Other natural occurrences of coesite are, predominantly, in impact-related rocks. These include tektites and meteorite craters and are the result of impact-metamorphism transforming the impacted rock’s existing silica mineral to the high-density polymorph. Chopin (1984) was amongst the first to report naturally-occurring coesite in terrestrial rocks, believed to have formed under high pressure in the high-grade blueschists from the Western Alps. Subsequently, a handful of occurrences of coesite in eclogitic and other ultra high-pressure metamorphic (UHPM) rocks of varying ages have been reported (see, for example, Parkinson & Katayama, 1999 for references).

Petrographic significance

The presence of coesite in terrestrial rocks has great significance for petrologists. Indeed, as Parkinson & Katayama (1999) point out, it is the “primary indicator mineral” of ultra high-pressure metamorphism. Although it has been shown that coesite can grow from strained quartz at lower pressures (Chopin, 1984) its presence suggests that under static conditions, and depending on the temperature, the maximum pressure experienced typically by the coesite-bearing rocks was 25 kbar to 30 kbar. Furthermore, Gillet *et al* (1984) suggest in a seminal study that by calculating the volume of α -quartz associated with a coesite inclusion much of the possible P-T history of the same can be determined. Under these ultra-high pressure conditions the coesite would have existed in the matrix (e.g. Chopin, 1984). Since coesite is stable at pressures >29 kbar at 800° C (see Figure 6.2) (Mirwald & Massonne, 1980, in Enami *et al*, 1990) it requires that host rocks must have been subducted to depths of >90 km (e.g. Enami *et al*, 1990). These are very considerable depths for terrestrial crust to have been exhumed from and the tectonic interpretations and possible mechanisms that allow this present the structural geologist with a challenge

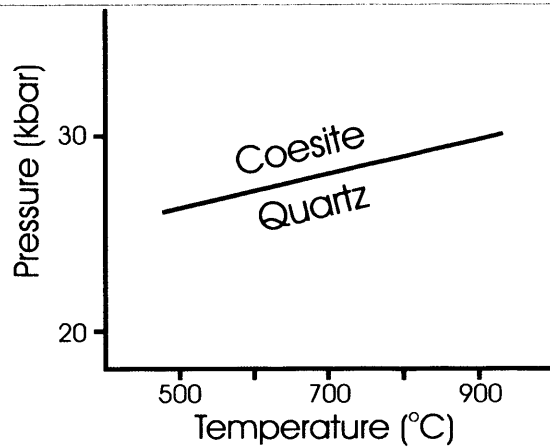


Fig. 6.2. Approximate stability field of coesite. After Mirwald and Massonne (1980) in Enami and Zang (1990).

Transformation of coesite to quartz

Rocks that experience UHPM conditions and are exhumed to the surface rarely *completely* preserve coesite inclusions. A strong ‘pressure vessel’ such as zircon or diamond appears to be required. Indeed, Hacker *et al* (1995) report that coesite can only survive exhumation, even partially, if present as an inclusion. Mosenfelder *et al* (op. cit.) suggest that a 100-micrometer matrix crystal of coesite would be completely transformed at moderate temperatures in less than 1 Ma¹.

Coesite contained inside a host crystal is one mechanism that accounts for the existence of natural examples in surface rocks. During decompression on the retrograde path, models suggest that the host can act to buffer the pressure on the silica system back to the equilibrium, limiting the transformation to between 25% to 30% at around 400°C (Mosenfelder *et al* op. cit.). The inclusion will remain in the coesite stability field even though the rock is within the quartz stability field. The kinetics of transformation from quartz are, however, poorly understood. From experiments using synthetic coesite, the transformation reaction, in the absence of fluids, is sluggish (Hacker *et al* op. cit.). When the inclusion pressure overcomes the mechanical strength of the host, cracking occurs. This has great effect on the rate of transformation. In addition to allowing fluid access to the inclusion, the cracks

¹ The study of Mosenfelder *et al*, and that of Hacker *et al* (1995), was based on synthetic coesite powders. Although the similarities between the experimental and natural samples were said to be ‘striking’ by the authors (and, therefore, thought to reflect the dominant mechanisms in natural samples), several assumptions were made regarding nucleation and growth rates. The powdered samples, in the presence of water, may provide useful upper limits on the transformation rates.

also provide nucleation sites for quartz (Mosenfelder *et al* op. cit.). The presence of hundreds to thousands of ~1-micrometer-wide elongate quartz grains that show no topotactic relationship to the inclusion radiating out from the core, suggests a very high ratio of nucleation rate to growth rate driven by a sudden change in the reaction driving potential (Chopin *et al*, 1995). Cracking allows a departure from the equilibrium conditions and the model of Mosenfelder *et al* (op. cit.) suggests that total ‘consumption’ of the coesite is inevitable. Cracks observed to appear in the coesite itself at high pressure also act as nucleation sites (Mosenfelder *et al* op. cit.). Boyer *et al* (1985) recorded the presence of optically undetectable incipient quartz along cleavages and throughout the coesite lattice. The rate of transformation is also thought to be ‘catalytically’ (Mosenfelder *et al* op. cit.) affected by the presence of fluids, both that fluid bound in the inclusion and that circulating around the rock. One possible mechanism proposed by Mosenfelder *et al* (op. cit.) is that H₂O present assists in strain relaxation; high elastic- and plastic-strain being one of the methods of inhibiting nucleation. The same workers also point out that H₂O aids diffusion in other silicates, maybe acting to reduce the activation energy of Si—O breaking.

Textures

Frequently, what are thought to be coesite grains in a rock exists as a pseudomorph after α -quartz, often completely replaced by α -quartz and, rarely, as tiny preserved relics in an α -quartz crystal. The inclusions are typically ovoid to subround in shape and 50 micrometer to 350 micrometer across (Ruyuan *et al*, 1996). Host mineral crystals in eclogites are Fe,Mg-rich garnets (typically almandine-pyrope series) and omphacite (a bright green pyroxene, (Ca,Na)(Mg,Fe²⁺,Fe³⁺,Al)[Si₂O₆]). More rarely relict coesite and its pseudomorphs have been discovered in jadeite, kyanite, dolomite, zircon, epidote, zoisite and diamond. Parkinson *et al* (1999) record the occurrence of completely untransformed coesite present as inclusions in zircon and garnet (Parkinson, 1999, in Parkinson *et al*, 1999) from the Kokchetav massif of Kazakhstan. Although this appears to be the first reported occurrence of coesite in this state of preservation the authors point out that this mode of occurrence in zircon may well be quite common and only the difficulty in recognising it, since characteristic textural features are absent, has prevented it from being more widely reported. Chopin *et al* (1995) also refer to a totally pristine coesite preserved within a diamond.

It was noted by workers early on that suspected coesite inclusions shared common textures and features. Most striking of these are the radial fractures observed in the host crystal. From

the bounding surface these persist into the host and are usually gently curved and may be associated with concentric cracks around the inclusion. It is widely thought that the cracks are the result of the ~10% volume increase upon transformation of coesite to quartz and is thought to be a low temperature event (Chopin, 1984) in the retrograde history of the rock. However, the presence of quartz within the cracks within synthetic samples suggests that the cracking must have formed at high pressure (Mosenfelder & Bohlen, 1997). Studies by Mosenfelder *et al* (1997) suggest that only around 25% to 30% transformation can occur before the inclusion pressure becomes three times greater than the outside pressure on the host crystal and cracks form. Cracks are not observed around inclusions of other species, for example, rutile and kyanite, in the same host minerals (e.g. Chopin, 1984). Crystals with good cleavage like dolomite tend not to show fracturing around the pseudomorph after coesite.

The presence of an inclusion of palisade quartz; a central mosaic of polycrystalline quartz surrounded by radial growth of fine-grained, feathery quartz aggregate within a radially-fractured host has been cited as evidence (Liou *et al*, 1996, Enami *et al*, 1990) of the former presence of coesite. Inclusions often comprise islands of relic coesite surrounded by identifiable α -quartz. Coesite has a higher relief than α -quartz and this feature has been used to aid the determination of a sample as coesite. In plane polarised light it often has a more yellowish colour than quartz (C. Storey pers. comm.). More typically the entire inclusion transforms completely to the low-pressure polymorph. Smith (1984) alluded to a crystallisation sequence of coesite to α -quartz based on the textural differences he observed in a single thin section. Liou *et al* (1996) defined a series of steps by which coesite transforms to quartz. They proposed a “reconstructive, interface-controlled” mechanism as opposed to a process of epitaxial overgrowth. The transformation steps from coesite are:

- 1 – growth inwards of thin, fine-grained palisade aggregates from the coesite-host boundary
- 2 – coarsening of palisade quartz into mosaic aggregate, and the transformation to quartz along coesite cleavages, creating islands of coesite
- 3 – total replacement of coesite by fibrous quartz aggregate with mosaic boundaries
- 4 – creation of coarse, polygonal quartz aggregates due to prolonged annealing
- 5 – recrystallisation of aggregates to a few granoblastic quartz crystals
- 6 – development of single quartz grains with either straight or undulating extinction.

Identifying coesite based on textural evidence

The former existence of coesite in some rocks has been determined on the basis of the presence of certain textural features alone. Smith (1984) cites the presence of radial fractures around an inclusion that shows no relic crystals as evidence of pre-existing coesite (and therefore UHPM conditions). Liou *et al* (1996) similarly attested that radial fractures associated with a palisade quartz inclusion as proof of the existence of coesite in a rock. Coleman *et al* (1995) argue that radial fractures around a quartz inclusion alone are insufficient evidence of former coesite. The authors point out that certain P-T conditions of decompression could cause inclusions of quartz in a garnet to ‘explode’ since the elastic properties of the two minerals are different. Differential volume changes between the two phases on decompression/cooling may have led to the inclusion exerting enough strain on the host to cause brittle failure. They suggest that only the texture of subparallel quartz subgrains of the inclusion itself provides ‘convincing evidence’. The majority of work concerning the presence of relic coesite proves the mineral’s existence by the use of microRaman spectroscopy. Spectral evidence provided by the technique of coesite is unambiguous.

6.4 - Vibrational spectroscopy of coesite

The vibrational spectrum of coesite is usually given when discussing those of all the silica polymorphs (for example Kingma & Hemley, 1994). Indeed, given the similarity of the spectra of the different polymorphs there is little published purely on coesite Raman spectra. Kingma & Hemley furthermore state that since the silica polymorphs do show common Raman spectral features then similar vibrational motions of Si and O must be responsible for those Raman bands. Boyer *et al* (1985) give the characteristic Raman band for coesite as 521 cm^{-1} . Three other bands, at 117 cm^{-1} , 177 cm^{-1} and 271 cm^{-1} may be used to characterise coesite and other bands that are attributed to coesite but may not be always be present, are found at 151 cm^{-1} , 355 cm^{-1} and 425 cm^{-1} . Figure 6.3 shows the coesite Raman spectrum recorded by the Cal Tech laboratory and the most important bands are indicated. The spectrum of α -quartz, recorded by the author is overlaid with the coesite spectrum for comparison. It is notable that there are significant differences between the spectra of the two polymorphs; particularly so in the case of the strongest bands, which for both polymorphs is the characteristic band of that form.

Liu *et al* (1997) note that although 33 Raman-active modes are predicted for coesite this figure does not match that of the number of observed bands. The complete set of fundamental vibrations has not been fully determined so it is possible that degeneracy, the coincidence of two or more Raman bands having exactly the same frequency, and very low intensity may account for some. The most intense peak is at 521 cm^{-1} and is assigned to the ν_s (Si—O—Si) symmetric stretching mode and is equivalent to the 464 cm^{-1} band in α -quartz. The difference between the frequencies between the A_1 mode in these two polymorphs is ascribed to the presence of 4- (coesite) and 6-membered rings (quartz) of silicate tetrahedra that form the structure (e.g. Liu *et al*, 1997).

McMillan *et al* (1982) grouped the bands of the silica polymorphs into three regions: the high frequency group (1000 cm^{-1} to 1250 cm^{-1}) corresponds to Si—O stretching vibrations; bands near 800 cm^{-1} are said to relate to vibrations of Si about the O atoms that bridge between tetrahedra and the low frequency region (400 cm^{-1} to 500 cm^{-1}) is the region of vibrations of the bridging O.

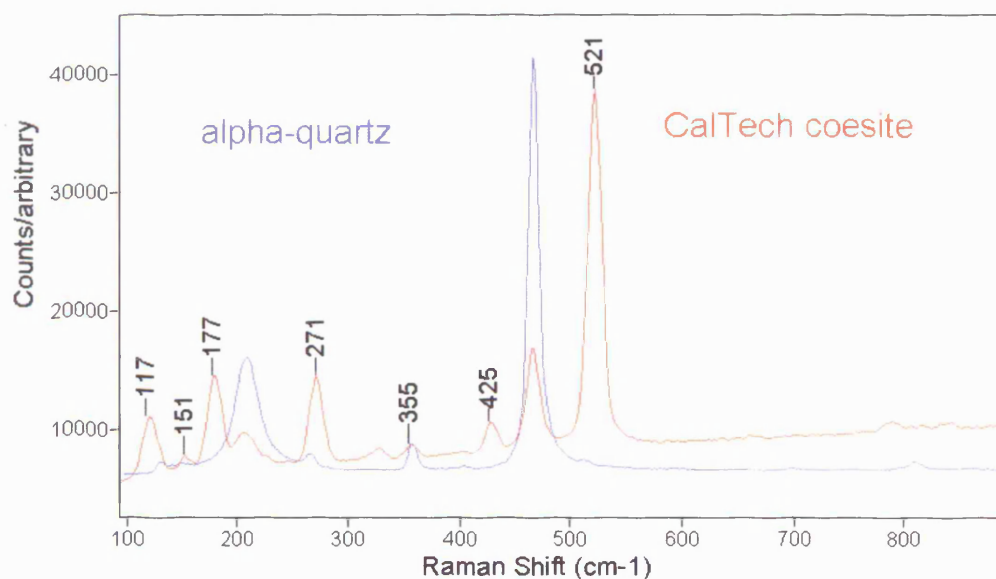


Fig. 6.3. CalTech coesite Raman spectrum. Characteristic bands only are indicated. α -quartz spectrum for comparison.

6.5 - Analysis and Results

Due to the nature of the inclusion, the analytical possibilities are limited to micro-techniques that allow *in situ* testing. Although several petrographic thin sections were produced from the rock sample, only one contained textural evidence suggesting the presence of coesite.

EMPA

The electron microprobe analyses were performed before analysis by Raman microscopy. The aim was to ensure that the inclusion had not been ‘plucked’ out during polishing of the thin section and that it was silica and not another mineral species.

The carbon-coated polished thin section was analysed using a JEOL 8600 Superprobe. The instrument comprises three spectrometers with both gas-flow and sealed chambers. Operating with an accelerating voltage of 15 kV and a filament current of 3×10^8 A, the 5 micrometer spot was used to record quantitative analyses from several points from the inclusion. All spots analysed returned compositions of pure SiO_2 , indicating that the inclusion was still present and that it was silica.

SEM

Images taken using the fore-scatter detector of an SEM can be used to highlight differences in subgrain orientation. Figure 6.4 was recorded from the inclusion in omphacite. The upper half of the image highlights the presence of α -quartz subgrains surrounding the central inclusion.

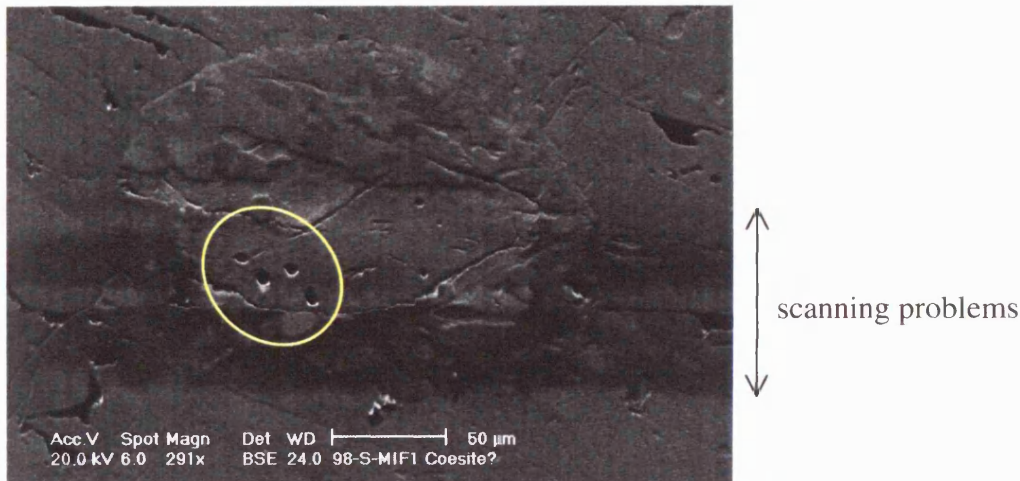


Fig. 6.4. Fore-scatter SEM image of suspected coesite inclusion. Note the differences in subgrain orientation. Lower portion of the image suffers from poor quality due to scanning problems. The four closely-spaced circles (highlighted) in the core are ablated pits from microanalysis.

The slight changes in contrast between subgrains underlines the differences in crystal orientation. In contrast to the ‘mantle’ of polycrystalline α -quartz, the core of the inclusion is notably completely free of features in the fore-scatter image.

MicroRaman Spectroscopy

Analyses of the inclusion were carried out on a Renishaw Raman System 2000 instrument coupled to a Leica DM LM microscope. Excitation was initially by the 514 nm line of a Spectra Physics Ar ion laser, delivering approximately 5 mW at the sample. This excitation has proved the most effective when recording the Raman spectra of minerals. The intense Rayleigh scattering was essentially removed using holographic notch filters and stray light removed by a mechanical slit set to 50 micrometers. The weak Raman signal was passed to the Peltier-cooled CCD camera detector by an 1800 grooves mm^{-1} grating. Calibration of the instrument was achieved using a Ne emission lamp and a Si-wafer was used during analysis sessions to check for spectrometer drift. Spectral resolution was better than 2 wavenumbers. Acquisition times were up to 60 seconds and scans co-added in an attempt to improve the signal to noise. No polarised measurements were recorded.

Approximately fifty points were selected across the inclusion for the automatic collection of Raman spectral analysis. All spectra returned were featureless and noisy, except one, which gave a weak peak at around 425 cm^{-1} . Typically, the spectra showed the constantly climbing response of luminescence obscuring any Raman features.

Further Raman analyses were carried out on the sample using the 785 nm line of a HeNe laser, supplying a maximum of approximately 6.3 mW at the sample. No polarised measurements were initially recorded. The longer excitation wavelength was selected in an attempt to avoid the electronic transitions that lead to luminescence. The Renishaw RM 1000 was coupled to a Leica DM LM microscope with automated mapping stage. Two area 'mapping' experiments were set up with a combined total of 1191 analysis points. The approximate area used for the mapping experiments is shown in Figure 6.5.

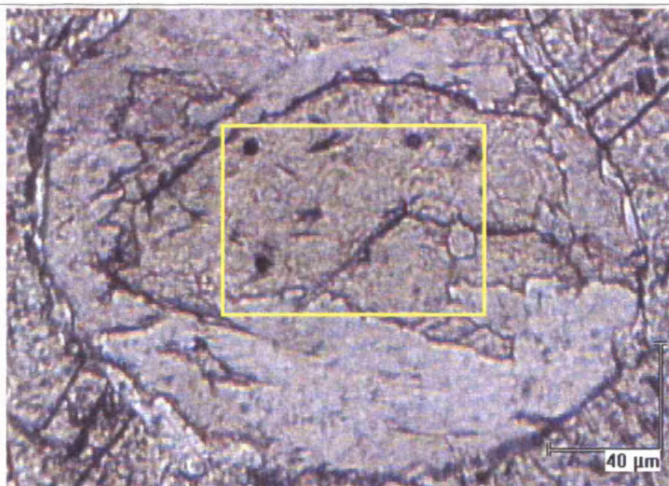


Fig. 6.5. Suspected coesite inclusion surrounded by α -quartz. Mapped area indicated.

The mapped area covered a region of 90 micrometer by 65 micrometer. For the first experiment analyses were recorded on a grid with points spaced at 5 micrometers. The second was a more detailed experiment with analyses recorded on a 2.5 micrometer grid, i.e. closer to the spot size. The spectrometer's slit width was set 50 micrometers and the grating had a density of 1200 grooves mm^{-1} .

Although providing reduced spectral resolution this instrument configuration enabled a much greater portion of the spectrum to be recorded in a static scan, i.e. with the grating remaining stationary during data acquisition. With the grating centred at 600 cm^{-1} a 'snapshot' of the response from 200 cm^{-1} to 820 cm^{-1} is recorded. The lower density grating would still be capable of resolving the peaks expected from crystalline coesite. Using the longer excitation wavelength more features were observed in the Raman spectrum. Fig 6.6 shows a representative spectrum recorded with 785 nm excitation. The features are broad and there is still significant noise.

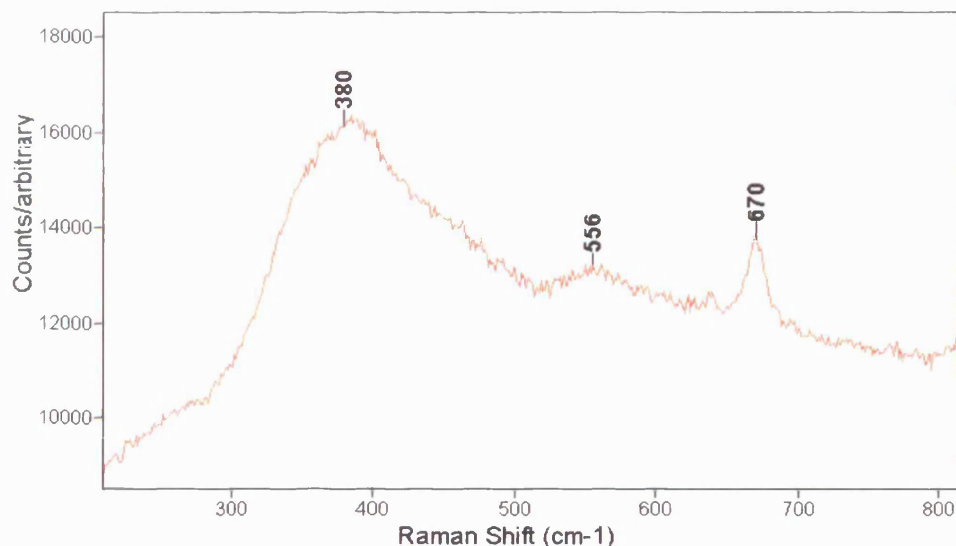


Fig. 6.6. Representative Raman spectrum from suspected coesite inclusion.

The spectrum rises sharply at the low frequency end of the range presenting an intense continuum centred at approximately 380 cm^{-1} . This is not a feature observed in the Raman spectra of crystalline materials. Another broad feature, centred at approximately 555 cm^{-1} is invariably present. Although quite weak in some spectra it becomes more defined in some of the mapping experiment analyses.

The most significant band in the spectrum is a moderately intense, asymmetric band centred at about 670 cm^{-1} . Analysis of both the mounting medium used and that of the omphacite in the thin section reveal bands in both material's Raman spectra that correspond with this frequency, as shown in Figure 6.7. However, if the mounting media were being excited by the laser a greater influence from the stronger Raman band at around 640 cm^{-1} and the band system above 740 cm^{-1} would be expected. This is not observed in the inclusion data. Similarly, given the high spatial resolution and high specificity of the laser spot it is highly unlikely that the omphacite is contributing to the Raman spectrum. Some of the sample spectra show low to moderate intensity, sharp bands occurring at 785 cm^{-1} and 738 cm^{-1} .

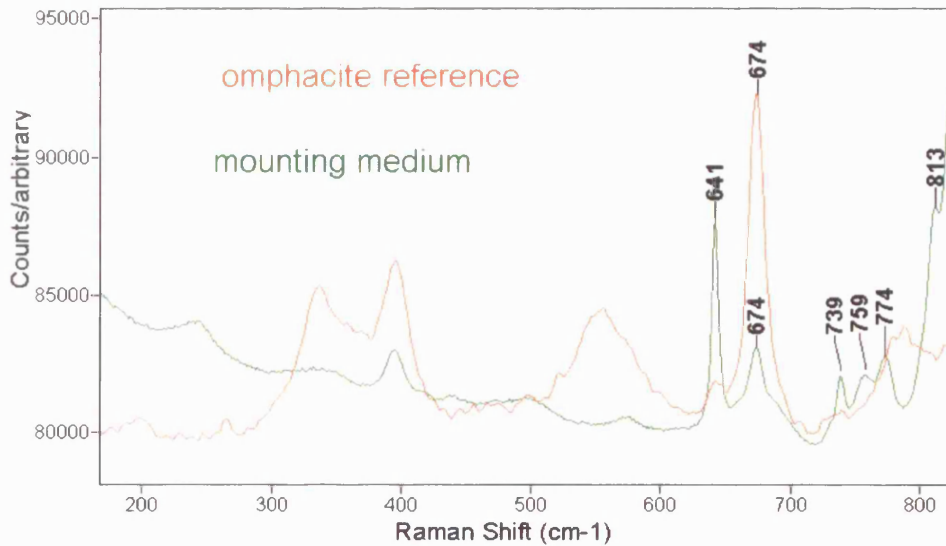


Fig. 6.7. Reference Raman spectra of omphacite and mounting medium.

Part of the mapped area includes regions of the mantle. These are easily identified as α -quartz from the Raman spectra by the intense 464 cm^{-1} band; characteristic of this polymorph, as shown in Figure 6.8. The band is seen to occur in some instances at the exclusion of the 670 cm^{-1} , 635 cm^{-1} and 560 cm^{-1} features and in some analyses a more positive correlation is observed.

The WiRE™ software used by the Renishaw instruments to process data allows maps showing the spatial distribution of selected data to be presented. Iterative curve-fitting to the multiframe (the entire set of spectra files) created by a mapping experiment is a rapid process using modern computers. The data file created can then be manipulated to show a range of maps. Figure 6.9 shows the spatial distribution of the area under the 670 cm^{-1} band for the higher spatial resolution map. For comparison, Figure 6.10 shows the distribution of α -quartz, calculated from the area under the 464 cm^{-1} band.

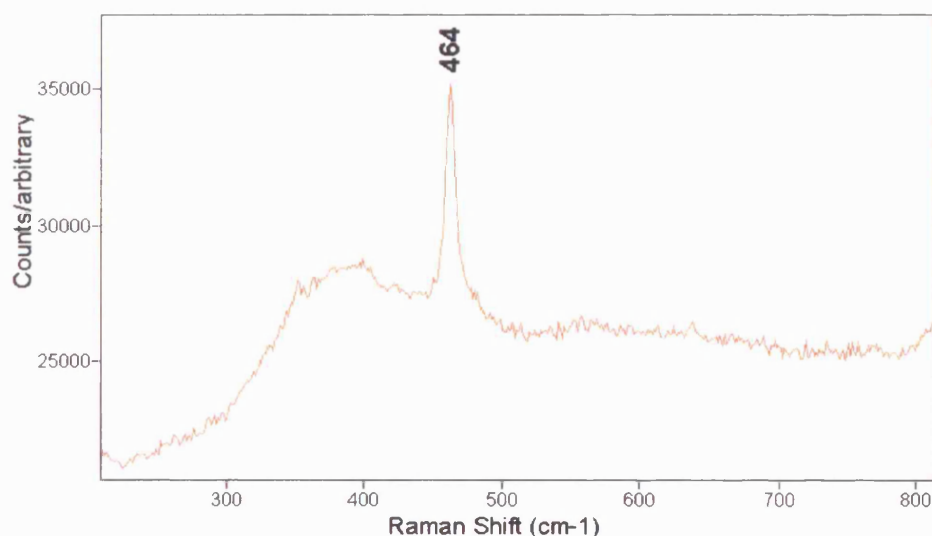


Fig. 6.8. Raman spectrum showing characteristic Raman band of α -quartz.

The results clearly show that, for this region of the inclusion transformation to α -quartz is most complete in the lower right corner and along the cracks that can be seen in plane transmitted light. By comparison with Figure 6.9 it can be seen that the 670 cm^{-1} feature is not correlated with α -quartz.

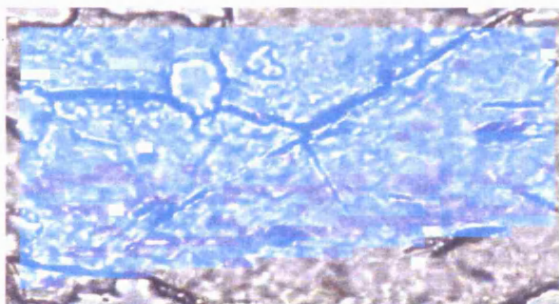


Fig. 6.9. Map showing area under 670 cm^{-1} band. Pale blue = highest intensity. Map dimensions 90 micrometers by 65 micrometers.

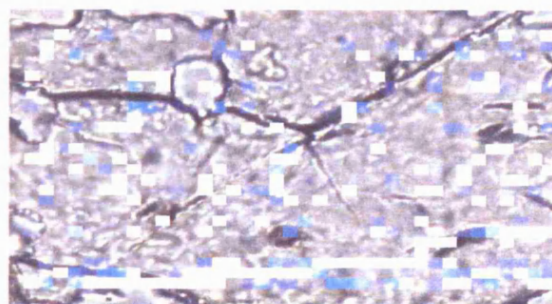


Fig. 6.10. Map showing area under 464 cm^{-1} band. White = highest intensity.

The spectra recorded from the inclusion suspected of being coesite do not correspond to that expected from coesite or from α -quartz. As expected, α -quartz is detected as forming the mantle to the inclusion. As discussed, the spectra also do not suggest that the mounting media underlying the inclusion is contributing to the recorded data. EMPA analyses indicate that a silica compound is present in the inclusion, i.e. it has not been removed during the polishing process. This is supported by optical petrography and the Raman data, which would show the numerous strong bands of the organic mounting medium.

The Raman spectra do show strong similarities with that of vitreous silica. Figure 6.11 shows the polarised Raman spectra of vitreous silica (after Galeenar, 1982a).

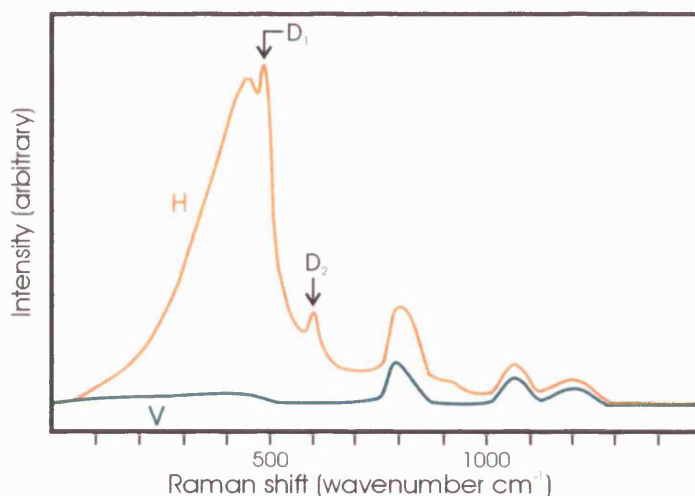


Fig. 6.11. Polarised Raman spectra of vitreous silica. Note the positions of the two “defect” bands commonly observed in this material. ‘H’ refers to parallel polarisation and ‘V’ to perpendicular polarisation. After Galeenar (1982a).

6.5 - Silica glasses (*vitreous silica*)

The strong similarities of the 785 nm Raman excitation spectra for the inclusion sample to that of silica glass warrants a review of the structure and spectra of vitreous silica.

Introduction

The molecular and vibrational structures of silicate liquids and their quenched glasses have been very successfully studied using spectroscopic methods, and Raman spectroscopy in particular (McMillan & Piriou, 1983). Although the vibrations in amorphous solids are not well understood (McMillan & Piriou, 1983) the spectra can be interpreted in a general way with the assignment of band groups to structural units and also allowing the comparison with models derived from other analytical or mathematical calculation models. McMillan (1984) provides a comprehensive tabulated summary of all the previous published Raman spectroscopic studies of silicate melts and glasses. He notes that for similar compositions the spectra are comparable, with the positions of bands agreeing to within five cm^{-1} . Many of the studies of silica glasses form a part of greater studies of silica ‘joins’ with alkali or alkaline earth silicate systems (e.g. Taylor & Brown, 1979, Sykes & Kubicki, 1996). Silicate glasses play an important role in many geologically-important melt systems and spectroscopic studies have led to advances in mantle science. The properties of density, viscosity and heat content of magmas are the goal of glass/melt studies in geology. Although melts and glasses of a

specific composition differ in their macroscopic properties, similarities in major spectroscopic features suggest that the vibrational structures are comparable (McMillan *et al* 1983) although some argue against the extrapolation of results. It is agreed upon that if the spectra of a glass and crystal are comparable then the molecular structures are also comparable (e.g. McMillan & Piriou, 1983) on a short and medium range scale (Calas & Petiua, 1983).

The structure of vitreous silica

Vitreous silica has been extensively studied in terms of its vibrational and molecular structure but is still not fully understood (McMillan, 1984). Numerous models have been proposed for a structure based on an interconnected network of corner-sharing SiO₄ tetrahedra (Sykes & Kubicki, 1996) as in the crystalline polymorphs; α -quartz (Bock & Su, 1970), β -quartz (Narten **In**: Wang & Angel, 1976), β -cristobalite (McMillan, 1984) and tridymite (Konnert & Karle, 1972, Dowty, 1987). Evidence from radial distribution curves and IR studies suggest that tridymite and silica glass share similar short-range order with up to 90% of the glass atoms forming tridymite-like regions (Konnert *et al* op. cit.). The same study points out that this supports a model of greater order than previously thought and that bonding between the regions differs from the crystalline form so that isotropic properties are created, probably by orientation differences and distortions.

The distinction between glassy or amorphous and crystalline states is the degree of ordering. Amorphous structures lack long-range order but possess short-range order. There is some disagreement over the degree of mid-range order possessed by glassy structures (Sykes & Kubicki, 1996). Short-range order could be in the form of small regions of crystalline-like ordered entities that are randomly bonded together or a random network of connected tetrahedra with Si—O bond distances that reflect those of their crystalline counterparts. Figure 6.12 depicts highly simplified models of long-range and short-range structural order. Long range ordered structures have infinitely extending arrays of repeated structural units. Short range structure has been shown here as a random array of the same repeat units. Bond angles and bond lengths between structural units are highly varied. Medium range structural order can be considered as a state between long- and short-range order.

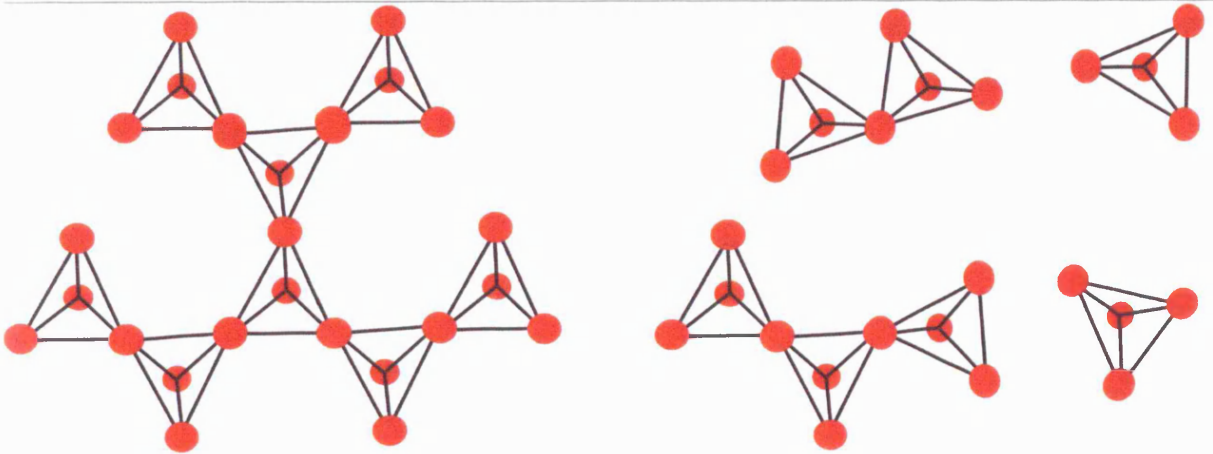


Fig. 6.12. Simplified diagram showing difference between long- (left) and short-range order (right).

There is great controversy and disagreement over the nature of rings in silica glass. As Dowty (1987) attests, there have been ‘many arguments... for and against almost any conceivable structure using many different techniques’. The SiO_4 rings in silica and silicate glasses have been extensively studied, both experimentally and from *ab initio* calculations (e.g. Galeener, 1982a, 1982b, Uchino *et al*, 1998, Sykes & Kubicki, 1996, Sharma *et al*, 1981). Recent studies by Uchino *et al* (1998) support the earlier work of Galeener (1982b) who identified a structure incorporating planar 3- and 4-membered rings. Based on energy considerations the 4- and higher-membered rings model of Sharma *et al* (1981) was shown to be unlikely. Dowty (1987) advances the tridymite-like crystallite-based model of 6-membered interlocking rings with partially disordered intertetrahedral configurations. The structure of α -quartz is based on 6-membered rings and it will be recounted that coesite has a 4-membered ring structure.

The spectrum of vitreous silica and band assignments

The spectrum of vitreous silica appears in Figure 6.11. There is excellent agreement in the literature between observed and calculated silica and silicate glass spectra of comparable composition.

The relatively sharp bands marked ‘D₁’ and ‘D₂’ in Figure 6.11 have caused much discussion regarding their structural significance. The bands were not predicted by model calculations based on ideal structures (Bock & Su, 1970). It was only when structural ‘defects’ like broken bonds were considered that the predicted spectra incorporated these features. Hence the commonly used term ‘defect bands’ is used when discussing these features. The bands only

appear in the spectrum of vitreous silica (i.e. they are not present when alkali or alkaline earth oxides are added to the composition) and are considered to be a characteristic feature (McMillan, 1984).

McMillan (1984) in a comprehensive review of the study of silicate melts briefly summarised the controversy to that date. Originally some considered the bands to reflect structural defects, and then the lower frequency, broad feature was related to the 430 cm^{-1} band. Both bands were in turn ascribed to motions of small siloxane ring structures within the glass although the broken bond concept was invariably retained. Later defect models invoke doubly bonded Si—O linkages as the cause. More recent work has revived the 4- and 3-membered rings model to account for the 490 cm^{-1} and 606 cm^{-1} bands. Uchino *et al* (1998) suggest that the D_1 band may in fact be composed of 490 cm^{-1} and 495 cm^{-1} features relating to vibrations of $\text{O}_3\text{—SiOH}$ and the “breathing mode”² of 4-membered rings. Sykes & Kubicki (1996) similarly propose that the D_2 peak may be the response of the breathing mode of the bridging oxygen (often referred to as O_{br} and as opposed to the non-bridging oxygen atoms O_{nbr}) between silica tetrahedra in 3-membered rings although a ‘defect’ model of broken Si—O bonds and over-coordination of Si and O is still retained. The relatively narrow width and symmetry of the D_1 and D_2 peaks suggests that the modes responsible are symmetric vibrations of regular structural units.

Discounting the ‘defect’ bands the vitreous silica Raman spectrum can conveniently be divided into three regions. McMillan (1984) defines the high frequency region as that between 800 cm^{-1} and 1200 cm^{-1} , mid frequency as 700 cm^{-1} to 800 cm^{-1} and low frequency as between 400 cm^{-1} and 700 cm^{-1} . Much of McMillan’s work on silica glass is derived from studies of the joins with alkali and alkaline earth silicate glasses and assignments are based on the positions, symmetries and changes with glass composition and the corresponding crystal spectra.

High frequency region

It is widely noted that vitreous silica has two depolarised bands in this region, at 1060 cm^{-1} and 1200 cm^{-1} . It has been suggested (e.g. McMillan, 1984) that the latter represents two bands, at 1160 cm^{-1} and 1209 cm^{-1} . The bands are usually ascribed to asymmetric vibrations

of Si—O stretching within the framework, although all the assignments are controversial. Other proposed models are that the bands represent two different structural units with different average Si—O—Si bond angles (Mysen *et al* **In**: McMillan, 1984), or that they are TO (transverse optic) and LO (longitudinal optic) components, which arise from symmetry considerations (Galeener & Lucovsky, 1976), or different Si—O stretching modes of the same structural unit. Although HyperRaman experiments support the existence of TO and LO waves in the glass it is commonly felt that more understanding of the dynamics of vitreous silica is required since the bands in this region are probably the key to understanding depolymerisation (McMillan, 1984).

Mid frequency region

Vitreous silica shows a weak, asymmetric band close to 800 cm^{-1} . It is not highly polarised and may consist of two bands at 790 cm^{-1} and 830 cm^{-1} (McMillan, 1984). Isotope studies may confirm that the band is the result of motion of the Si atom against the tetrahedral ‘cage’ of possibly stationary O atoms (McMillan and Piriou, 1983). There appears to be some degree of agreement over this assignment.

Low frequency region

This region dominates the polarised spectrum shown in Figure 6.11. The band at about 430 cm^{-1} is broadened and made more intense due to thermal population of the vibrational density of states (McMillan & Piriou, 1983). The effect is thought (Hass, 1970) to be related to temperature effects and so does not form part of the ‘real’ spectrum. Further broadening of the highly polarised 430 cm^{-1} band is caused by further shoulders at 280 cm^{-1} and 380 cm^{-1} (McMillan and Piriou, 1983). This peak is assigned to the symmetric (since the band is strongly polarised) motion of O_{br} in a plane bisecting Si—O—Si with little or no motion of Si (McMillan and Piriou, 1983). Again, the vibrations are not well understood but it is believed

² The term “breathing mode” is applied to the symmetric stretching vibration when applied to ring structures since the motion of the ring of Si—O—Si—O—Si— etc. bonds can be likened to the ring ‘expanding and contracting’ as if it were breathing.

that the frequency is dependent on the Si—O—Si and so may be sensitive to the degree of polymerisation.

6.6 - Discussion

Petrographic studies and comparison with published accounts of coesite occurrence strongly indicates that coesite did exist as an inclusion in the omphacite grain shown above. Textural indicators including radiating cracks and palisade α -quartz in combination with the higher relief, size and shape of the inclusion suggest that the UHPM indicator did crystallise in this eclogitic suite. However, the spectroscopic evidence described above appears to indicate that if the inclusion did consist of the regular structural arrangement of crystalline coesite then some form of transformation to something other than α -quartz had occurred. The silica polymorphs are relative weak Raman scatterers but it usually possible to identify, at least, the symmetric stretching mode that falls between 400 cm^{-1} and 550 cm^{-1} even in microcrystalline samples or where there is strong contribution from a fluorescent species. None of the strong Raman bands indicative of the any of the silica polymorphs was detected in the inclusion.

If the inclusion sample were coesite we would have expected a strong band at 521 cm^{-1} and possibly other, weaker bands as described in the literature. None of the many hundreds of spectra recorded from the inclusion indicate a band that corresponds to that of coesite. On this basis and even with the textural features, the inclusion cannot be unambiguously identified as coesite.

Similarly, the sample is not believed to be completely α -quartz for the same reasons, i.e. the characteristic band of α -quartz is only detected in regions of the mantle surrounding the inclusion. Some workers have noted a total transformation from coesite to α -quartz and this would be expected from the textural features including radial fractures and palisade quartz. Certainly some regions within the inclusion are α -quartz as evidenced by the appearance of a weak feature at 465 cm^{-1} . α -quartz probably exists as very discrete islands within the inclusion; a conclusion also reached by Boyer *et al* (1985). Crystallite sizes may be smaller than the spot size since the $670/638\text{ cm}^{-1}$ bands do appear in the same analyses. Islands may be linked on a sub-microscopic level by fractures not resolvable by the microscope.

In a study of the stishovite polymorph from Meteor Crater, Skinner *et al* (1963) describe the rapid transformation to an amorphous silica phase that is a transition between the high-density polymorph and other crystalline forms (coesite and quartz in their example). The isotropic amorphous phase is described as resembling pure synthetic glass and silica glass ‘in all measurable ways’, with very close refractive index values and identical XRD patterns to silica glass. Quartz, cristobalite and tridymite are all known to invert upon heating to glass at different temperatures. It is also noted (Skinner *et al* op. cit.) that grinding can provide the activation energy required for this thermal degradation transformation. The glass from the Meteor Crater assemblage is thought to have been produced from the breakdown of stishovite. As the 360 kbar to 600 kbar stresses from the impact were relieved temperatures in the rock rose rapidly, melting some of the stishovite.

Other minerals are known to attain glassy states. Best known of these is zircon that is known to transform to glassy state via a mechanism of α -particle recoil damage to the lattice. This mechanism is not considered likely here since a source of radiation would have to be within about 50 micrometers thus restricting it to the omphacite host grain.

Considerable research has been carried out in to the vibrational spectroscopic features of synthesised silica and silicate glasses. Some of the work has been summarised above. The Raman spectroscopic data recorded from the inclusion appears to have more in common with the spectra of glasses than with crystalline solids. Deviation from the published spectroscopic data for silica glasses and the sample spectra, if indeed it is a silica glass, may be explained by the differences in the nature of the two sample sets: the inclusion sample was originally a naturally occurring crystalline solid and the published work on silica glasses are either purely theoretical or based on synthesised compounds.

It is difficult to draw many parallels with the published work on silica glasses since the current work does not include the high frequency region of the Raman spectrum, identified as the region of several distinctive glass Raman bands.

The mid frequency region does have weak asymmetric bands that could correspond to motions of the Si atoms against tetrahedral cage (McMillan & Piriou, 1983).

The low frequency region of the sample spectra may have contributions from fluorescence (i.e. from thermal emission). However, such fluorescence might be expected to be much stronger than the observed signal and the shape of the curve would be different. The design of the holographic notch filters employed as Rayleigh rejection components have a very steep profile close to the cut-off around 150 cm^{-1} . Furthermore, fluorescence often overwhelms the entire spectrum, masking all the features. In contrast to this, weak bands are noted in other parts of the spectra. The observed broad band is at lower frequency than that observed in vitreous silica. This may be a reflection on the Si—O—Si bond angles and lengths compared to those from synthesised silica glasses. The frequency of this broad band depends on the number of SiO_4 units in the ring structure. Rings with > 4 members have bands that lie below 430 cm^{-1} (Sykes & Kubicki, 1996) since their Si—O—Si bond angles are greater than lower order rings. The broad band observed could thus be explained by a highly disordered network of SiO_4 units with a range of ring structures with greater than four members. Although energetically unfavourable (Galeener, 1982b) the structure could be retained by ‘freezing’ the puckered state.

The lack of relatively sharp bands that might correspond to the D_1 and D_2 defect bands may be explained by the lack of regular structures, i.e. the 2, 3 or 4 membered rings thought to be responsible for these bands. However, the origin of these bands is not clear and highly debated.

In the present study the refractive index (RI) of the inclusion is significantly less than that of the surrounding α -quartz (1.54) from Becke line tests. Skinner *et al* (op. cit.) measured the RI of transition glass at 1.461.

Geological significance

For coesite to be preserved at the surface quite unique conditions must have been in operation. The inherent instability of the polymorph requires that the mechanism by which the parent rock is transferred from great depths, of the order of 100 km (e.g. Hacker *et al* In: Coleman and Wang, 1995), closely follows the equilibrium conditions shown in Figure 6.1. Where coesite has been preserved, in the published studies cited, the inclusion pressure has been buffered back to the equilibrium (or to the coesite stability field) by the competence of the host grain. At very elevated inclusion pressures, maybe three times that operating on the

whole rock, the integrity of the host is overcome and it fails. Cracks appear in the grain at the corners of the inclusion where pressure is greatest and extend into the host. Transformation to α -quartz ensues; quite rapidly at elevated temperatures and in the presence of fluids but more sluggishly at lower temperatures. The P-T path that is most favourable to the preservation of coesite, and is most plausible geologically, is one of steady decompression and cooling (Gillet *et al*, 1984). It is important that the exhumation process does not involve heating since even if the decompression was steady, an increase in the temperature, as models of denudation and erosion suggest (Gillet *et al*, 1984 and Hacker *et al op. cit.*), would force the system into the quartz stability field. A successful model must then invoke tectonics as the main exhumation driving force or a combination of erosional and tectonic processes (Hacker *et al op. cit.*). Thrusting and tectonic thinning due to extension has been proposed but the model of continued subduction beneath a detached eclogite unit is plausible. It allows exhumation to occur at relatively fast or slow rates and permits cooling by depressing the geotherms (Hacker *et al op. cit.*).

In the present study neither coesite nor α -quartz now constitutes the inclusion that the textural features and literature studies imply was once coesite. Studies by Raman spectroscopy indicate that the inclusion does not possess the long-range structure and fully depolymerised network of silica tetrahedra of coesite. Discrete islands of α -quartz appear to exist within a seemingly amorphous atomic arrangement, possibly consisting of 4-, 5-, 6- or higher membered siloxane rings. Revised geological conditions of exhumation for the eclogite parent rock should account for this.

Naturally occurring amorphous forms of silica exist. Lechatelierite is the name given to the glassy silica that occurs in fulgarites – preserved lightning strikes in quartz-rich soils. Libyan desert glass is the term used for amorphous silica formed by meteorite impact on Earth. Whilst chemically (i.e. high purity) and structurally the sample in the present study may be very similar to that of the mineraloid, it is not thought it formed under these forms of extreme temperature and pressure.

The silica polymorphs quartz, tridymite and cristobalite are known to invert to glass at various temperatures. An intermediate glass transition phase was shown to exist (Chaklader & Roberts **In:** Skinner & Fahey, 1963) between quartz and cristobalite. Stishovite has been shown to invert and it can be expected that all the silica polymorphs can similarly become

amorphous on heating. It is possible that the sample under study represents a quenched, partially-inverted coesite-to-quartz transformation; the discrete islands of α -quartz representing relics of an incomplete transformation as the coesite structure broke down upon incipient crack formation in the omphacite. Rapid, tectonically-driven uplift and erosion may have resulted in the rupture of the omphacite host at low temperatures and the 'freezing' of the possible transitory state observed in the rock.

Amorphous silica caused by the excessive heating and subsequent melting of pre-existing quartz is not favoured. Had this occurred we might expect to see more evidence of the amorphous state in other grains in the rock. However, the grinding of the sample may have provided the required energy to disturb the metastable coesite structure had it been preserved as a relic surrounded by the α -quartz mantle we observe. Nothing is known about the rates of this reaction although stishovite was shown to invert to glass due to grinding within hours (Skinner & Fahey, 1963).

6.7 - Conclusion

In situ micro-analytical methods provide the only means of analysing this inclusion sample. MicroRaman spectroscopy has been shown to add significantly to the knowledge of this inclusion than had only EMPA and SEM techniques been applied. Whilst somewhat inconclusive, the spectroscopic data suggest that neither the preservation of pristine coesite nor the transformation of coesite to α -quartz occurred, as might have been expected. This information could be useful in determining aspects of the geological history of the host rock suite.

Textural evidence presented strongly suggests that the inclusion was coesite when it formed at great depth. Detailed analysis suggests that the inclusion has attained a largely amorphous, structureless state although discrete islands of α -quartz, the energetically favoured polymorph at surface conditions, exist. The size of these islands is beyond the spatial resolution of the instrument, i.e. less than 2 micrometers and probably considerably smaller than this.

The inclusion may represent a transition phase between coesite and α -quartz. Assuming that the coesite originally had a regular network structure as described above, sudden decompression due to the incipient cracking in the host pyroxene may have brought about

polymerisation into rings of silicate tetrahedra with varying degrees of order (i.e. the number of Si members). Broken bonds may also contribute to the spectra. The system may have been quenched by rapid decompression and cooling, freezing the incomplete transition to quartz.

In light of the findings of this study it is possible that previously published ‘unambiguous’ identifications of coesite based on the presence of textural information alone may have been incorrect. Exhumation mechanisms for the rocks that contain these inclusions may need to be re-evaluated in light of this. Raman spectroscopy is the only unambiguous method by which similar inclusions may be analysed *in situ* and should always be used when attempting to unequivocally report the occurrence of coesite.

The molecular and vibrational structure of silicate glasses is not well understood. It is a complex arena with highly conflicting arguments for the various models. A greater understanding of the kinetics of silica transitions and more detailed analysis by spectroscopic and XRD methods would help greatly in understanding the mechanism by which coesite has attained a seemingly amorphous state.

6.8 – Further work

Evidently, further analysis is required to characterise the nature of the inclusion. The microRaman analyses in this study used a static scan for improved efficiency over continuous extended scans and also because of the time advantage offered. The spectral region was selected such that the region in which the A_1 for silica minerals would be well covered. From a review of the Raman spectra of silica glasses it would be insightful to study the region of the Raman spectrum beyond 800 cm^{-1} and also to perform polarisation measurements.

Raman spectroscopy has been selected for the determination of the nature of silica inclusions in many studies. It allows the non-destructive *in situ* analysis from a petrographic or polished thin section. The solution to the identification of the inclusion under study would almost certainly have been most effectively solved by XRD analysis. However, this requires that the sample be a single crystal or ground to a powder. Obviously, in this case XRD was not an applicable method. The following are other analytical methods that may have provided useful information:

TEM

Transmission Electron Microscopy also includes the related techniques EELS, HRTEM and Electron Diffraction. Based upon the sample's interaction with a tightly-focused beam of electrons, the methods permit the very high spatial resolution investigation on a nanometer scale. The techniques essentially record elemental information. The sample preparation requires electron-thinning to the order of nanometers. TEM analysis would provide information about lattice defects and the order of the atomic lattice. Spot size of around 1nm and magnifications of 10^6 possible. Information in the form of images can provide detail about defects and dislocations in crystalline materials.

SNOM, AFM, STM

These related techniques provide subwavelength resolution of the topographical features of the sample. The atomic-scale deflections of an extremely fine probe tip are used to map the positions of individual atoms. The method could provide useful data on the atomic order of the inclusion.

NMR

^{29}Si MAS- (Magic Angle Spinning) NMR is a technique that allows structural refinement of Si-bearing crystalline and amorphous compounds. Spectral information can be used to suggest local bonding environments, bond lengths and angles. An advanced analytical technique, it is widely available and it is not known in what format the sample must take.

IR spectroscopy

This vibrational spectroscopic technique is akin and somewhat complimentary to Raman spectroscopy. As with Raman spectroscopy, energy associated with the vibration of atoms in a molecule corresponds to the infrared region of the electromagnetic spectrum and is recorded. Since it is change in the dipole moment of the functional groups on excitation that give rise to the spectrum, the response might be expected to be similar, but not identical to that obtained by Raman spectroscopy. IR studies have proved useful in the assignment of bands to vibrational modes in both crystalline and non-crystalline materials. Calculated spectra agree well with experimental spectra in the study of the silica polymorphs and glasses. Characteristic absorption features are well known for both the silica polymorphs. Analysis by absorption IR and most reflectance experiments require the sample to be ground to a powder.

ESI (Electron Spectroscopy Imaging)

This chemical technique is used to provide elemental distribution maps of very high resolution, in the order of nanometers. It may be possible to interpret the data to provide structural information.

Chapter 3 – Crystal structure investigations

This chapter comprises sections 7, 8 and 9 of the current work. MicroRaman spectroscopy is a highly sensitive technique for studying the structure of crystalline materials.

Case studies are presented in which the Raman spectra of biotite, cubic zirconia and zircon are used to comment on structures and defects that arise in samples used.

The different approaches to using Raman spectroscopy that are available using this instrument are employed.

7 – Inclusion haloes in biotite

This is the first case study to investigate the use of Raman spectroscopy in the elucidation of crystal structural changes on a micro scale. By offering a non-destructive analysis on a petrographic thin section it may present a powerful analytical tool. The common pleochroic ‘haloes’ observed in biotite grains appeared to present an accessible example.

7.1 - Introduction

Biotite is a ubiquitous component of intermediate and acid igneous plutonic rocks and may in some cases may be the chief ferromagnesian mineral. Additionally, it also occurs in some basic igneous plutonic rocks and is a common constituent of metamorphic rocks formed over a wide range of temperature and pressure conditions. Biotite is one member of a group whose members show “considerable variation in chemical and physical properties” and, by nature of their structure, all members exhibit a “platy morphology and perfect basal cleavage” (Deer *et al*, 1962).

Inclusion haloes

Diffuse black haloes surrounding inclusions in biotite are a common feature, often attributed to inclusions of zircon or other minerals containing elements in the U-Ra and Th-Ac series’. Until very recently they had received very little attention within the published literature; the unchallenged view was that the inclusions were zircons, rich in radioactive elements and that this was the cause of the haloes. MicroRaman spectroscopy appeared to be the only way to simply characterise both the nature of the inclusions and the structure of the surrounding biotite grain. A thorough literature review revealed no published work on the subject and so samples were gathered and experimental work carried out. Unbeknown to the author, it appears that a similar but more extensive study was under way by Lutz Nasdala at the Institute of Geosciences, Johannes Gutenberg University in Mainz, Germany. The results of the study were published in 2001, during the course of the present investigation.

Biotite chemistry and structure

The general chemical formula for micas is $X_2Y_{4-6}Z_8O_{20}(OH,F)_4$. The structure is capable of supporting many different elements in the X, Y and Z sites. Common X species are K, Na and Ca but also Ba, Rb and Cs may be present. Al, Mg and Fe are usually found in the Y site although Li and transition elements like Mn, Cr and Ti can satisfy the charge balance. Ti

and Fe^{3+} may substitute for Si and Al in the Z site. The general formula of biotite is given as $\text{K}_2(\text{Fe}^{2+}, \text{Mg})_{4-6}(\text{Fe}^{3+}, \text{Al}, \text{Ti})_{0-2}(\text{Si}_{6-5}, \text{Al}_{2-3})\text{O}_{20-22}(\text{OH}, \text{F})_{4-2}$ (Deer *et al op. cit.*). It is important to note that biotite is an Fe-rich mica. Deer *et al* (1962) collated many chemical analyses displaying varied compositions and list total Fe wt % values between 15% and 35% (biotites may be subdivided on their Fe_{tot} and Mg content. The most Fe rich are called lepidomelanes). Fe plays a significant role in the body colour of biotite. Where the ratio of $\text{Fe}_2\text{O}_3/(\text{Fe}_2\text{O}_3+\text{FeO})$ to TiO_2 is high, a greenish colour is observed and reddish brown where the ratio is low (Deer *et al op. cit.*).

The structure of biotite, and the monoclinic mica family of minerals, is based on a composite sheet. Identical layers of sheets are repeated and stacked on top of each other perpendicular to the z-axis. Each composite sheet comprises of a layer of octahedrally coordinated cations, the X-site K ions, bonded to the apical oxygen atoms of two facing (Si,Al) O_4 tetrahedra. The tetrahedra are linked by the three bridging O atoms to form a hexagonal mesh parallel to the cleavage. It is this feature that is responsible for the perfect cleavage. Each tetrahedron is linked to form a six-membered ring, each of which is connected to another six symmetrically equivalent six-membered rings (Tlili *et al*, 1989). Figure 7.1 shows the plan of the hexagonal mesh structure, looking down the z-axis.

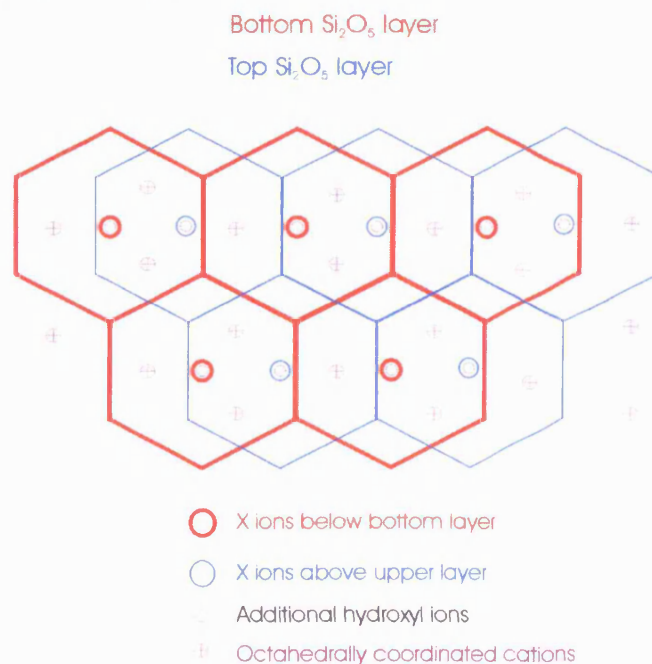


Fig. 7.1. Plan view of phyllosilicate structure. Reproduced from Deer *et al* (1962).

Y cations (Fe,Mg,Al) are located in the two octahedral sites between the composite sheets. They form a tri-octahedral layer with each cation coordinated to apical, non-bridging O atoms and two OH (F may be included) groups that substitute for O. Figure 7.2 depicts the structure looking along the y-axis. Chemical data in Deer *et al* (1962) suggests that $(\text{OH,F})_{\text{tot}}$ may comprise up to 5 wt% (by difference).

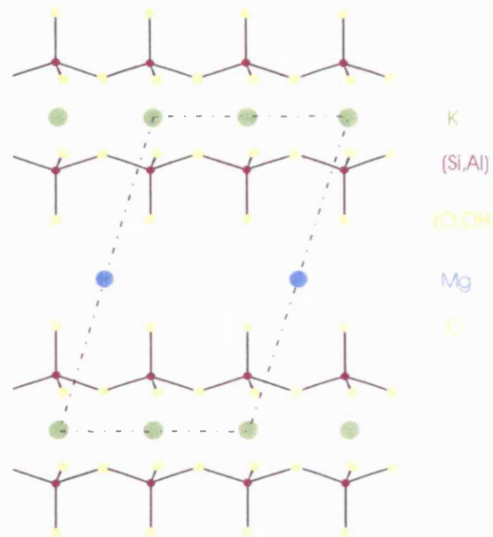


Fig. 7.2. y-axis view of biotite structure. The simplest unit cell is indicated. Reproduced from Deer *et al* (1962).

Raman and vibrational spectroscopy of layer silicates

The lattice-layer silicates have not received a great deal of attention within the field of vibrational spectroscopy, particularly so with Raman spectroscopy. Silicate minerals in general are poor Raman scatterers (Griffith 1974) and it was recorded by White (1986 in Tlili *et al* 1989) that of the silicate minerals, micas gave poor Raman responses; an opinion recently emphasised by Nasdala *et al* (2001). Tlili *et al* (1989) used visible excitation in a systematic microRaman study of the tri-octahedral micas (although notably this did not include biotite). These workers cited the few previous Raman studies of phyllosilicates to date. These include Rosasco and Blaha (1980) on talc and Haley *et al* (1982) on muscovite and vermiculite. Considerably more work has been done using IR methods and references for these studies can be found in Tlili *et al* (1989).

McKeown *et al* (1999a,b) presented thorough vibrational analyses of phlogopite and muscovite. Bands observed in their polarised FT-Raman spectra were correlated to those calculated using FGA and force constants, with good agreement. Their calculations on

phlogopite structure are most relevant to this study. They calculate 27 Raman-active fundamental modes for phlogopite and *clearly* observed 18 of these. Eight of the predicted modes were calculated to be common to both A_g and B_g modes and some were beyond the spectral range of the instrument. Despite reportedly using FGA to calculate the expected frequencies of the molecular vibrations, Tlili *et al* (1989) interpreted their spectra on the basis of crystal chemical features and the spectral variation with composition. McKeown *et al* (1999a) were more rigorous in their approach. Lattice dynamics and force constants were used to compute the expected frequency of the Raman-active fundamental modes. The results are quite detailed and are not fully reproduced here. McKeown *et al* (1999a) categorised the Raman bands in to three groups of ‘eigenmodes’ as those:

- above 850 cm^{-1} - localised T—O stretching and O—T—O bending that are internal to the sheets
- 350 cm^{-1} to 850 cm^{-1} – T_4O_{10} and M2 octahedra bond stretching and bending
- below 350 cm^{-1} – dominated by lattice modes where long-range motions of the T_4O_{10} sheet mix with M2 and (OH,F) displacements.

(where T is the tetrahedral site within the sheets occupied by Si or Al and M2 is one of the octahedral sites between the sheets occupied by Mg in phlogopite). In the absence of a similar detailed study of biotite, the work on phlogopite serves as a good proxy. The chief difference between the minerals lies in the Mg:Fe ratio so Raman spectra can be expected to differ only slightly. This observation was found by Nasdala *et al* (2001). ‘Moderate’ shift differences were accompanied by a significant splitting of a major band around 680 cm^{-1} in the phlogopite Raman spectrum into three separate bands in the biotite spectrum. The explanation offered was the diverse occupation of octahedral sites in the biotite structure compared to that of the phlogopite structure.

It might be said that the Raman spectra of biotites are difficult to interpret because there is considerable mixing of internal sheet vibrations with octahedral site displacements in the 350 cm^{-1} to 850 cm^{-1} range. McKeown *et al* (1999a) interpret the resulting broad and clearly overlapping bands as reflecting the coupling between the tetrahedral sheets and their surrounding environment. Accordingly, these workers do not attempt to assign any empirical bands to vibrations in the lattice mode region.

Biotite presents certain analytical difficulties when Raman spectroscopy is used. Nasdala *et al* (2001) described it as a “challenging task”. In their comprehensive study of the vibrational spectra of tri-octahedral micas, Tlili *et al* (1989) did not include biotite. Considering the widespread occurrence of this mineral in many igneous and metamorphic rocks, this omission provides an insight into the analytical difficulties. From the nearly Fe-free micas that were studied, they noted high background noise, high fluorescence and strong absorption as elements that affected the quality of the spectra. The acquisition of Raman spectra from coloured micas led these workers to suggest that it is the total absorption that is important, not the colour. Amongst the comprehensive list of analytical tools used to study radiohaloes in biotite (confocal microRaman, EMPA, HRTEM, X-ray diffraction and Mössbauer spectroscopy) Nasdala *et al* (2001) compared the optical absorption spectra of both unaltered biotite and that from the radiohaloes. They found that both the unaltered biotite and the regions in the haloes exhibited very strong absorption that increased towards shorter wavelengths. This accounts for the noted difficulty in using visible excitation for microRaman spectroscopy of these materials. In addition, the halo region was observed to be more strongly absorbing than the unaltered crystal. In the studies by McKeown *et al* (1999a) the workers failed to record sufficient quality Raman spectra from phlogopite using 514 nm excitation. Despite using a Nd:YAG delivering 600 mW to the instrument, these workers had to co-add 640 fluorescence-free scans to achieve the desired quality of data. Similarly, using 30 μ W of 514 nm excitation, Nasdala *et al* (2001) spent many hours acquiring single point spectra from the samples.

7.2 – Sample

The leucocratic Bodmin granite is a two-mica granite, with muscovite the other sheet silicate, indicating a peraluminous bulk chemistry (Deer *et al*, 1992). In thin section the micas are easily distinguished. The biotite flakes are strongly pleochroic with maximum light absorption occurring parallel to the (001) plane. Many of the grains display diffuse pleochroic haloes.

The microinclusions show no preferred mode of distribution in the biotite. They are not always present and rarely appear to attain sizes greater than 50 micrometers. Haloes typically seem to show a maximum radial extent of around 40 micrometers around the inclusion. This observation was also made by Nasdala *et al* (2001) in biotites from stuarolite gneiss

(Spessart, Germany), quartz diorite (Bavarian Fichtelgebirge, Germany) and in macrocrystals of biotite (Horní Slavkov, Czech Republic) who provide Monte Carlo simulations to explain the apparent constant width.

The biotite haloes in the Bodmin granite all appear to be identical in form. Larger inclusions appear to be surrounded by thicker, darker haloes than smaller inclusions. Nasdala *et al* (2001) further observed that the intensity of the halo was a function of the actinide content of the inclusions. The shape of the haloes is close to circular and they have no features within them. At the halo edge they become suddenly more diffuse and then grade very sharply to the unaltered host biotite. In some of the haloes it is impossible to distinguish the inclusion. Figure 7.3 displays the appearance of a typical biotite grain in the Bodmin Granite. In cross-polarised light the strong absorption of the biotite is noted. Nasdala *et al* (2001) recorded a variety of radiohaloes. Differences in intensity of the colouration, presence of zonation and distinct annular features were attributed to differences in actinide content.



Fig. 7.3. Image of typical biotite grain from Bodmin Granite. Note the pleochroic haloes. PPL.

7.3 – Experimental

Raman analyses were carried out on a Renishaw System 2000 instrument using uncovered petrographic thin sections. Experiments with visible excitation were carried out prior to the publication of the work of Nasdala *et al* (2001). A transmitted light source, condenser and polariser were fitted to the Leica DMLM microscope. This greatly facilitated the locating and selecting of suitable biotite grains and radiohaloes. Excitation was by a Spectra Physics 514.5

nm Ar⁺ laser, the 632.8 nm line of a Renishaw HeNe laser, a 782 nm Renishaw diode laser and also a Renishaw High Power diode laser operating at 785 nm. The visible excitation sources delivered a maximum of ~5 mW at the sample via a 50x objective. The maximum power available at the sample from the near-IR laser is around 60 mW. Rayleigh scattered radiation was removed using two holographic notch filters. The visible dispersive instrument used a grating with 1800 grooves per mm and 1200 grooves per mm with near-IR excitation. The system was calibrated using the 520 cm⁻¹ band of a Si wafer reference standard. The wafer was repeatedly analysed to monitor spectrometer drift. Acquisition times for the samples were typically thirty second scans over the range 100 cm⁻¹ to 2000 cm⁻¹ with the spectra co-added up to ten times to improve signal to noise. Despite the co-adding the spectra had poor ratios of signal to noise. However, as Bowie *et al* (2000a) point out, dark noise associated with the CCD detector is improved as the square root of the number of scans recorded. It is clear, then, that ten accumulations for a poor Raman scatterer is insufficient.

It has already been stated that of the silicates micas are poor Raman scatterers. Difficulties in analysing biotites are compounded by the problem of excessive fluorescence when using Raman spectroscopy. The strong red/brown body colour of the biotite and the dark colour of the haloes led to marked absorption and fluorescence, swamping much of the Raman signal. The effect was more so with red, 633 nm excitation than with the green, 514 nm excitation. Spectra can be baseline-corrected using the GRAMS® software package although this should be used with caution to avoid the introduction into the data of artificial features.

Some experiments were carried out using the 782 nm excitation provided by a solid-state laser. Theory suggests that longer wavelengths are preferable since they do not coincide with the electronic transitions that lead to fluorescence (Bowie *et al*, 2000a). Also, data presented by Nasdala *et al* (2001) suggest that absorption in biotites and their radiohaloes is dramatically reduced with longer excitation. However, the greater power density of the near-IR lasers is more likely to induce sample heating. No qualitative experiments were carried out but Nasdala *et al* (2001) and others, point out the readiness with which biotites are observed to degrade due to laser energy absorption. Spectral results obtained using confocal 782 nm excitation indicate that in the low wavenumber range the peaks were of comparable quality to those obtained using 514 nm excitation. However, the near-IR excitation is more sensitive to the glass used for the thin section. The glass Raman spectrum is characterised by a very

strong, broad and asymmetric spectral feature at around 1400 cm^{-1} with a FWHM of some 200 cm^{-1} . This feature is not seen using the 514 nm, partly because the shorter, visible excitation does not coincide with the long-range order of the glass structure and also because the penetration depth below the surface of the sample using visible excitation is less than that of the near-IR excitation. The spectra with the highest signal to noise and least fluorescence were obtained with 514 nm excitation.

Initially, continuous extended grating scans were run over randomly selected points on the biotite and within the radiohaloes. No polarising components were used. McKeown *et al* (1999a,b) note the negligible difference in the two configurations $z(y,y)z$ and $z(y,x)z$ in the analysis of phyllosilicates unless the crystal is oriented such that the laser is incident along the c-axis. In this instance, differences can be significant. Line-mapping scans were also run with equally spaced analysis points passing from unaffected regions of the biotite crystal through the halo to the inclusion. Haley *et al* (1982) note that when analysing sheet silicates by Raman spectroscopy diffraction of the incident light source may occur in the sample. Diffraction of this nature could lead to ambiguous spectra since Raman activity may be recorded from regions surrounding the point of interest. Good spatial resolution is required since the Raman spectra from selected points in the biotite radiohaloes appear to show extensive heterogeneity on a micrometer scale. To ensure that the Raman signal was recorded from a discrete volume only, the instrument was set-up in confocal mode with visible excitation. This optical arrangement is commonly used when analysing fluid inclusions in mineralogical samples and is discussed elsewhere in this study. Despite Raman signal throughput being greatly reduced in this optical arrangement, this effect can be accounted for by increasing the exposure time of the analyses or by recording and co-adding more accumulations. Repeated line map experiments were run and analyses recorded at five micrometer steps from the unaffected biotite to an inclusion.

EMPA experiments were carried out on the same polished thin section used for Raman analyses. Where possible, the haloes used for EMPA analysis were also those used for MicroRaman analysis. A JEOL 8600 Superprobe consisting of three spectrometers, gas-flow and sealed chambers was used. The microprobe was operated at 15 kV accelerating voltage and a filament current of 30 nA. Only information derived from traverses through the biotite crystals of interest was recorded. The spot size was reduced to five micrometers diameter to

reduce overlap and the signal from the respective inclusions on each traverse. Typical traverse step sizes were five micrometers. Inclusions were located using the back-scattered image and their identities confirmed using the WDX facility.

7.4 - Results

MicroRaman spectroscopy

Inclusions analysed yielded spectra that most closely match those of monazite and apatite. Some zircons were also detected. Hutton (in Deer *et al* 1962) recorded that the commonest inclusions that lead to radiohaloes are monazite, xenotime and apatite. The monazite inclusion shown in figure 7.4 is approximately ten micrometers in its longest dimension. The intense peak close to 974 cm^{-1} is typical of the P—O stretching frequency of phosphates (also vanadates [V—O] and arsenates [As—O]). The spectrum recorded from this monazite is shown in figure 7.4. Monazites are rather rare accessory phases in granites and other acid igneous rocks. The chemical formula $(\text{Ce,La,Th})\text{PO}_4$ allows substitution of other rare earth elements of the Th-Ac series into the monoclinic structure. The numerous peaks in the spectrum are reasonably sharp and intense and suggest that the inclusion has not sustained any damage due to self-irradiation. The apatite group has the formula $\text{Ca}_5(\text{PO}_4)_3(\text{OH,F,Cl})$ and represents the most abundant P-bearing group of minerals. Substitutes for Ca have been found to include trace levels of Sr and the lighter Y group of rare earth elements (Deer *et al*, 1992). They are common accessory phases in igneous rocks. Neither spectrum is similar to that of zircon, a more common accessory phase than monazite in granites.

Several biotite grains from a single thin section were analysed with 514 nm excitation. Spectra recorded from radiohalo-bearing grains, and biotite showing no haloes, were identical. The representative biotite spectrum closely matches the reference biotite in the Renishaw Raman Database of Minerals and Inorganic Materials as seen figure 7.6. The major differences are in the relative intensity differences in the bands at around 187 cm^{-1} , 555 cm^{-1} and 675 cm^{-1} . The latter appears as a shoulder to the band at 725 cm^{-1} in the sample but appears more isolated in the reference spectrum. Rosasco and Blaha (1980) attribute this band in talc to the totally symmetric stretch of the SiO_4 tetrahedra, based on its coincidence with other silicates, e.g. pyroxenes. These differences can probably be ascribed to the relative orientations of the sample and reference crystals. Based on the work of Rosasco and Blaha (1980) the band at around 770 cm^{-1} may be associated with asymmetric stretching of the SiO_4

tetrahedra and the weak, broad feature just above 1000 cm^{-1} to asymmetric stretching of the Si—O—Si linkages. Two inclusions in biotite and their respective haloes and regions of unaffected biotite were also analysed.

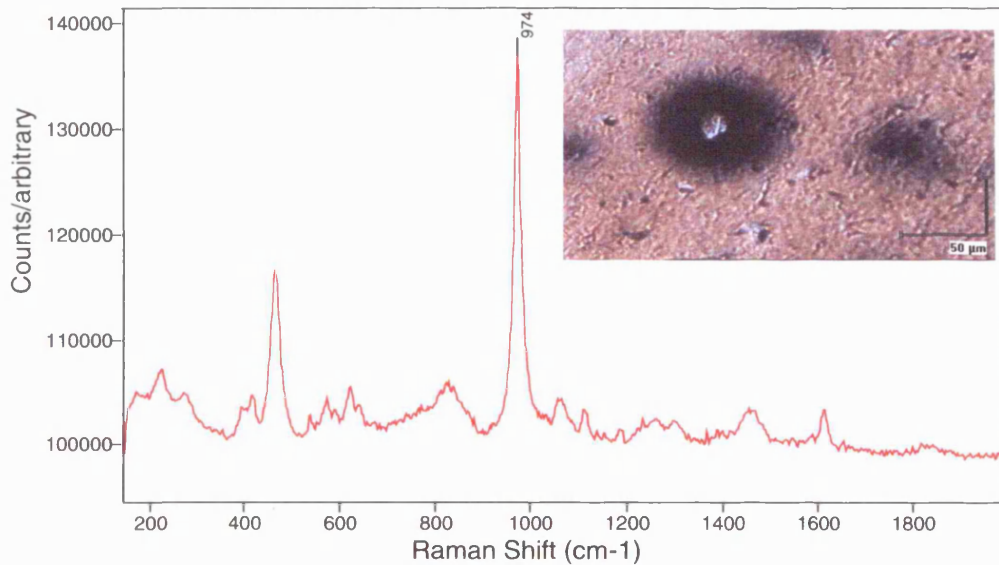


Fig. 7.4. Raman spectrum of monazite microinclusion. Inset: white light image of inclusion and halo.

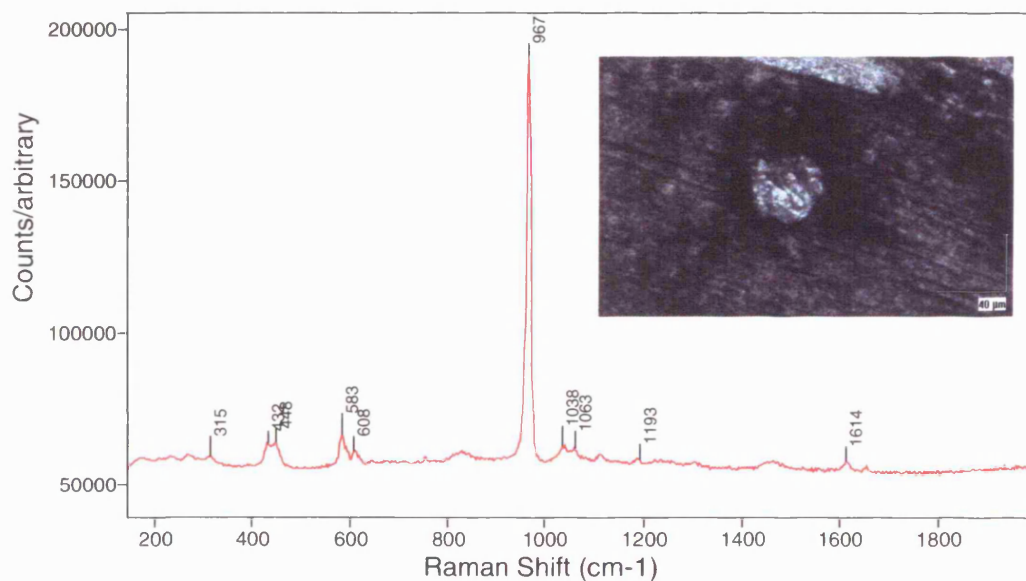


Fig. 7.5 Raman spectrum of analysed apatite inclusion. The fluorescence has been subtracted for clarity. Note the dark halo around the inclusion in the inserted white light image.

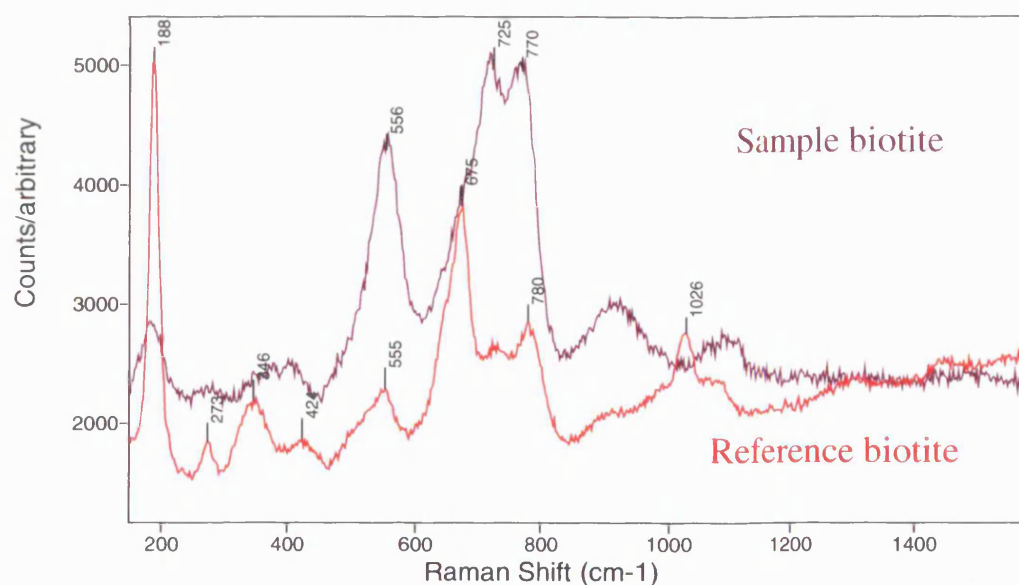


Fig. 7.6. Biotite Raman spectrum from sample (purple) and that from a biotite in the Database (red).

Several discrete points within the radiohaloes were analysed, again with 514 nm excitation. They gave markedly different spectra to those obtained from unaltered biotite. Figure 7.7 compares typical spectra recorded from the two separate regions. The radiohalo spectrum (lower spectrum in Fig. 7.7) has only weak, very broad Raman bands. This contrasts with that of the unaltered region (upper spectrum in Fig. 7.7) that has moderately strong, moderately sharp bands. This suggests that there has been significant modification of the biotite

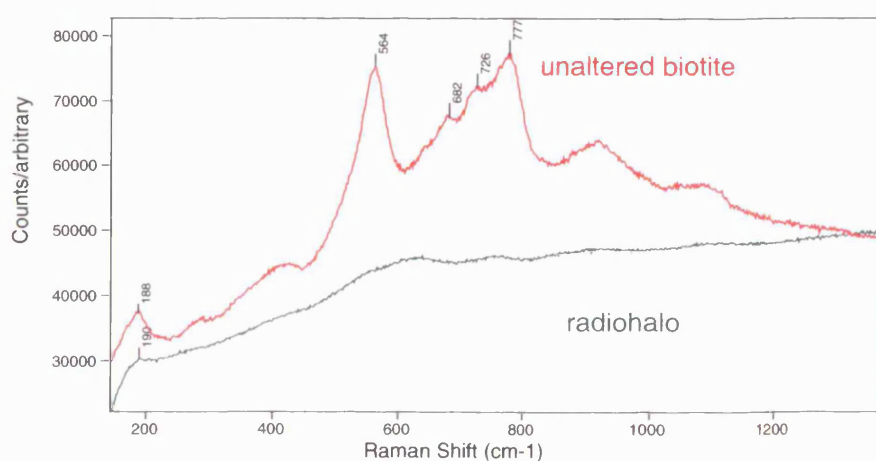


Fig. 7.7. Raman spectrum of normal biotite (upper trace, red) and the dark halo regions (lower trace, green). Neither spectrum has been baseline corrected for the effects of luminescence.

structure in the halo areas. The severe loss of intensity and spectral shape in the low wavenumber, ‘lattice region’ of the spectrum suggests a loss of order in the structure. As noted above, this portion of the Raman spectrum concerns the motions of the $(\text{Si,Al})_4\text{O}_{10}$ network, the M2 octahedra and the long-range lattice modes. Loss of intensity and Raman band shape is indicative of the metamictisation observed in some zircon crystals. The differences recorded above were repeated in other radiohaloes.

An integral part of the mica structure is the presence of inter-sheet hydroxyl ions. By analysing the OH-stretching regions using the technique we might expect to see further evidence of any crystal structural differences or modifications between the normal and halo biotite. In recent work, Nasdala *et al* (2001) pursued the same rationale. Figure 7.8 shows the Raman shifts of the normal biotite in the O-H stretching range 3500 cm^{-1} to 3800 cm^{-1} . Figure 7.8 clearly shows moderately intense bands attributable to the OH-stretching mode at approximately 3655 cm^{-1} and at 3601 cm^{-1} , recorded with 514 nm excitation. The peaks are broad which may suggest a composite of multiple bands. This might reflect a range of bond angles and bond lengths. The positions of these two bands are in close agreement with those observed recently by Nasdala *et al* (2001). Additional weak peaks may be hidden by the noise. The signal to noise is low due to the confocal arrangement and the inherent weakness of OH as a Raman scatterer. The spectrum shown is the result of ten co-added 45 second exposures. OH groups occur in different positions and orientations within the phyllosilicate structure (e.g. Haley *et al* 1982) and it might be expected that other bands would be present in a more extended portion of the spectrum.

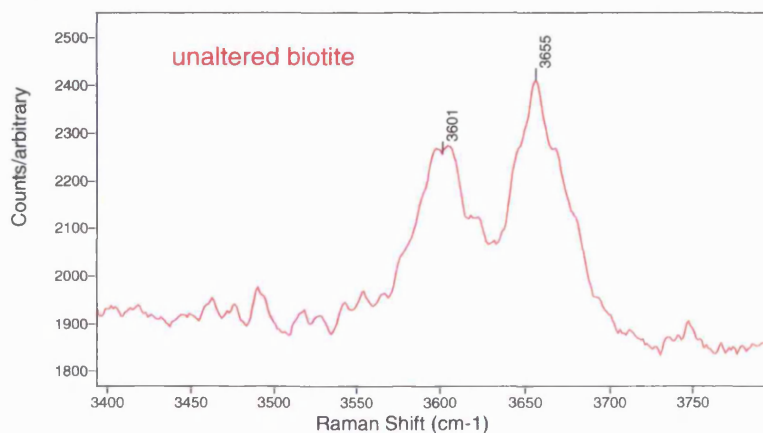


Fig. 7.8. Raman spectrum of the OH stretching region of normal biotite grain (confocal mode).

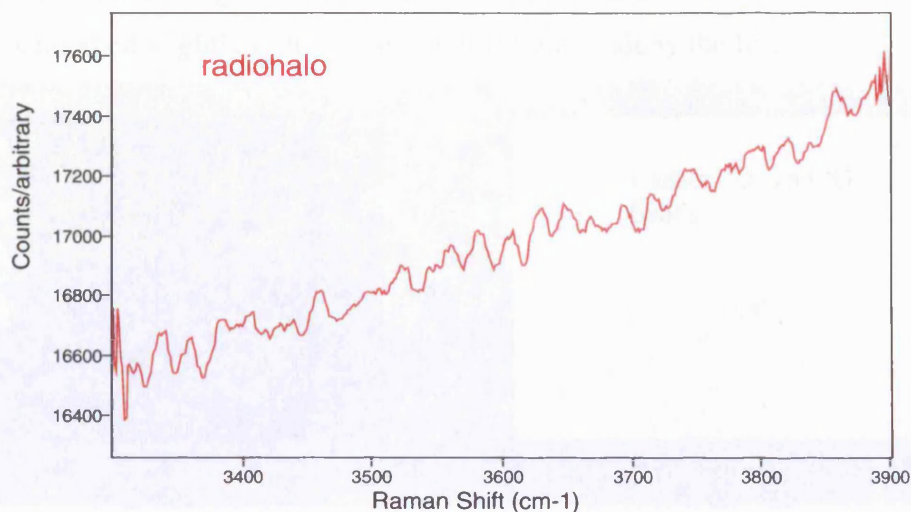


Fig. 7.9. Raman spectrum of the OH-stretching region of the dark halo region (confocal mode).

Figure 7.9, recorded from the halo, shows none of the features of figure 7.8. Experimental conditions were identical between the respective experiments and the results seen in figure 7.9 are typical of the radiohaloes in the thin section. The spectrum clearly indicates the absence of interlayer hydroxyls in the halo.

Several Raman line maps were attempted to record spectra from successive points between the inclusion and the unaltered biotite with 514 nm excitation. The experiments were hampered by very low signal. Despite using relatively large step sizes of five micrometers, acquisitions of three or five accumulations of twenty-second exposures per analysis point resulted in impractically long experiments. Of these limited experiments, some data sets were seen to be overwhelmed by fluorescence or a very strong signal from surface carbon where the EMPA section was used. An example of the surface carbon spectrum obscuring the biotite spectrum is shown in figure 7.10. Some of the line maps produced some adequate results.

Figure 7.11 is an image of a biotite grain recorded in reflected light with the inclusion clearly observable in the centre. Generally, the inclusions (and therefore the haloes) were selected in transmitted light since this illumination makes them easier to distinguish than in transmitted light. Unfortunately, it is difficult to identify the halo with this illumination. The line along which confocal measurements were made at 1.5 micrometer spacing is marked in white. The

data for the lattice mode and the $(\text{Si,Al})_4\text{O}_{10}$ vibrations regions are shown in figure 7.12 and the OH-stretching region in figure 7.13. In each case, the data has had to be baseline-corrected and smoothed slightly to highlight the differences along the line.

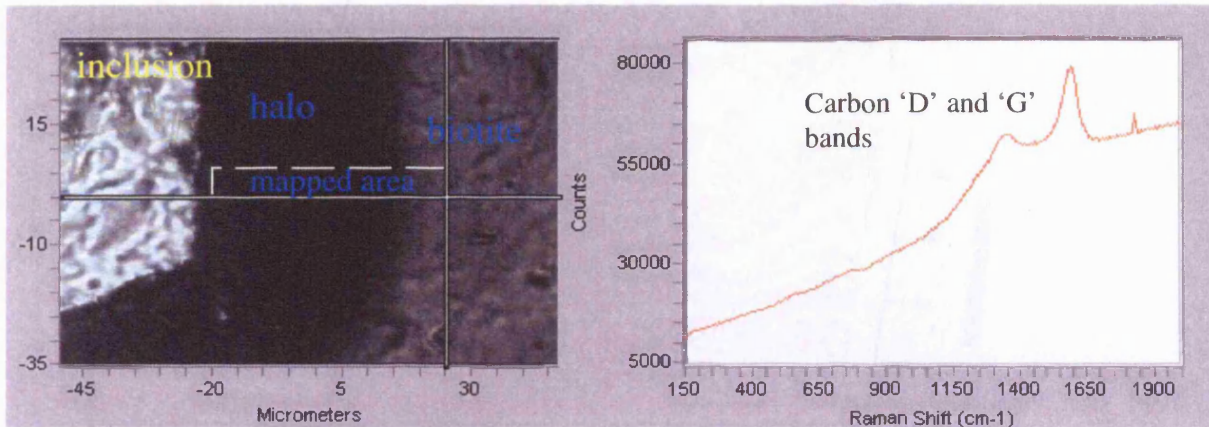


Fig. 7.10. Example area map showing prismatic inclusion, halo and unaltered biotite. Right: carbon spectrum.

Figure 7.12 shows broad, undefined nature of the bands in the mid-wavenumber region within the halo graduating towards sharper and more distinct and intense bands in the unaltered biotite. Of particular note is the band around 550 cm^{-1} , which shows this most clearly. The effect is repeated in the OH-stretching region, as highlighted in figure 7.12. Although suffering from low signal to noise ratio the absence of the OH band is notable in the halo before gradually appearing and becoming more intense in the unaltered biotite.

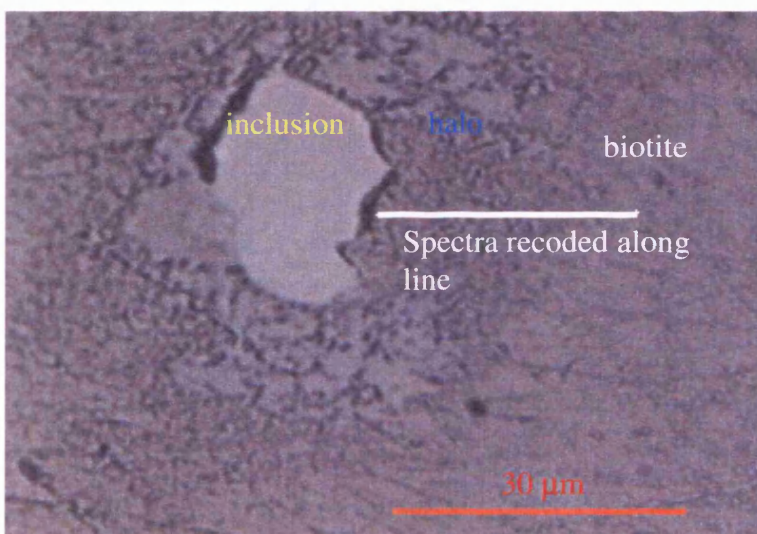


Fig. 7.11. Reflected light image of an inclusion and halo region analysed.

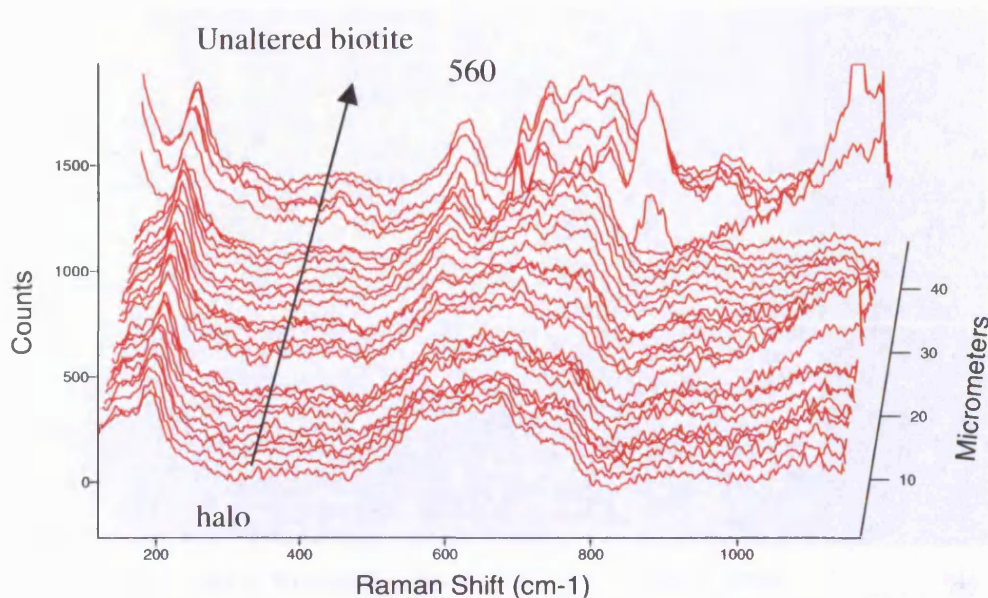


Fig. 7.12. Line map from inclusion to unaltered region of biotite. Note 550 – 800 cm^{-1} region.

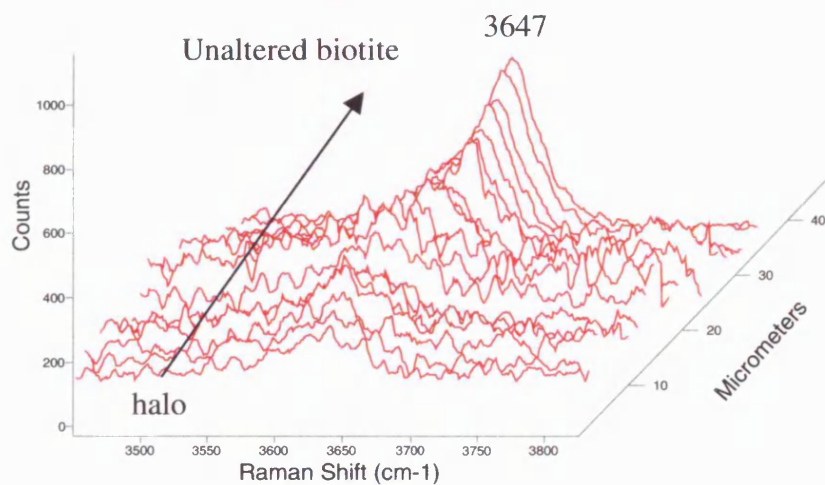


Figure 7.13. Line map showing portion of OH-stretching region.

Another inclusion was analysed in confocal mode using 514 nm excitation. The cross-polarised, transmitted light image is shown in figure 7.14 with the line indicated in white. The step size used was three micrometers. From the spectra in figure 7.15 the gradual increase in the biotite bands, both in the mid-wavenumber and OH-stretching regions is observed.

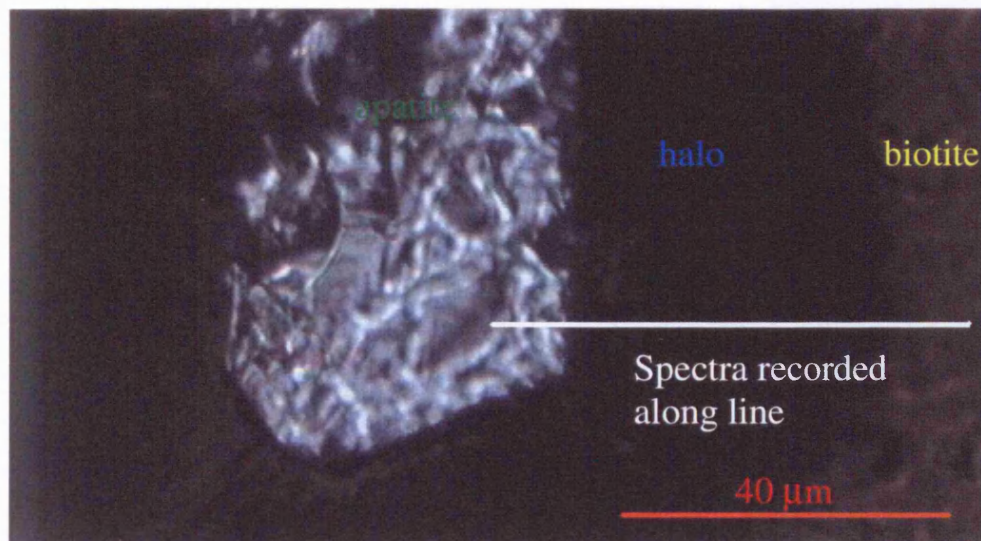


Fig. 7.14. CPL image of a prismatic apatite inclusion with halo in biotite.

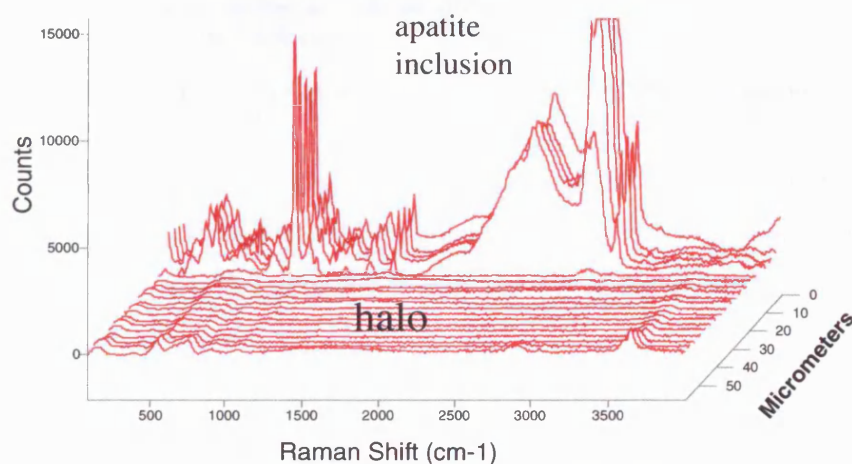


Fig. 7.15. Line map from apatite inclusion through halo to unaltered biotite.

It was apparent that analysis with visible excitation induced excessive fluorescence. Early analysis using confocal near-IR excitation suggested that the line experiments could be run with this longer excitation. A line mapping experiment employing 785 nm excitation was set up to just analyse the OH-stretching region, since this could be achieved within a practical timescale. The laser used projects a line of light on the sample instead of a spot, as used with the 514 nm laser. A confocal arrangement was not used for this experiment. The laser is significantly more powerful than the visible laser used. However, since the laser is spread into a line the power density is similar. The results of a line map are shown in figure 7.16.

Whilst the differences between the spectra in the biotite, halo and inclusion are striking the bands displayed cannot be ascribed to OH ions with confidence. The positions of the main band just below 3300 cm^{-1} do not agree with the positions of OH bands for phyllosilicates in the literature or those shown in the preceding figures.

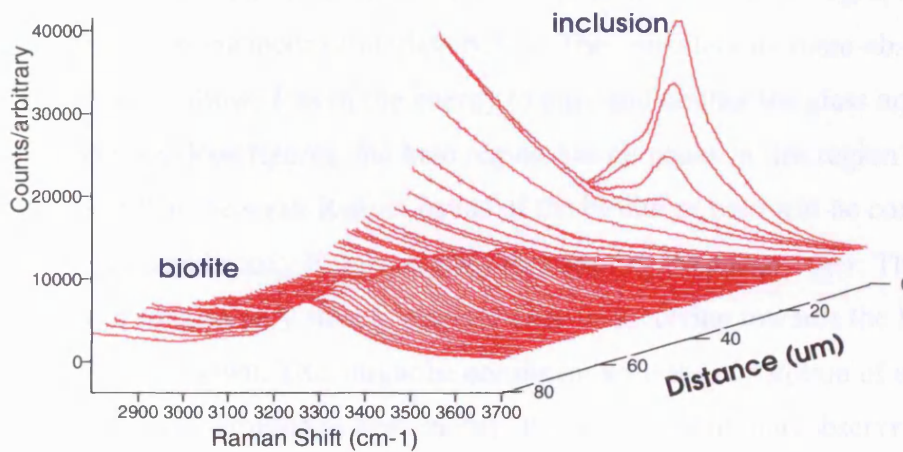


Fig. 7.16. Line map from inclusion to unaltered biotite using 785 nm excitation.

Raman spectra were recorded from the thin section glass and from the epoxy mounting medium on the glass slide for comparison with the spectrum from the near-IR line map. The positions of the main band centre is very similar in each case. Figure 7.17 displays the three spectra overlaid.

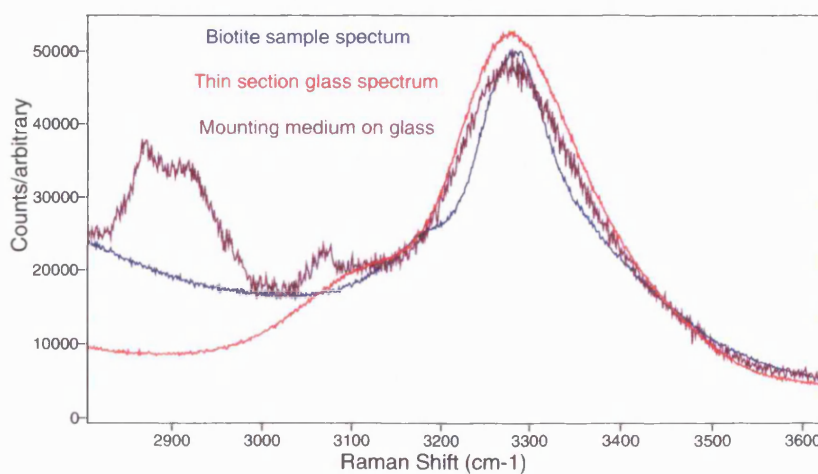


Fig. 7.17. Raman spectra from the near-IR line map, glass and mounting medium.

Whilst it is doubtful that the bands shown in figure 7.16 represent OH-stretching from the inclusion and biotite, the disappearance of the band in the hole is not explained if the bands are simply ascribed to the epoxy, or more likely, the glass. One possible explanation is suggested from the absorption spectra presented by Nasdala *et al* (2001) for biotites and their haloes. The inclusion (from the near-IR Raman spectrum, not shown, probably a self-irradiated, metamict zircon) and unaltered biotite have sufficient refractive indices to cause the incident, non-confocal, laser energy to pass through the petrographic section and interact with the mounting media and glass below. The considerably more-absorbing and lower RI halo material allows less of the energy to pass and neither the glass nor epoxy is excited. As shown in previous figures, the halo region has no peaks in this region of the spectrum. It is suspected that the weak Raman bands of the biotite or halo will be completely overwhelmed by the glass and epoxy Raman signals that are very much stronger. The halo region in figure 7.17 does suggest very strong luminescence is occurring towards the lower wavenumber side of the region shown. This might be consistent with the absorption of energy being subsequently re-emitted as heat energy. It was not possible to observe any thermal damage to the region of the sample analysed.

EMPA

In order to ascertain if there are any major chemical differences between halo regions and unaltered regions, analysis by Electron MicroProbe was carried out on the sample. In addition to the major element oxides, the oxides of Ca, Th, La, Ba, Ce and were also analysed for. In the recent multi-technique approach of Nasdala *et al* (2001) the authors followed the same route. The quantitative chemical analysis aimed to determine if compositional differences might account for the strong absorption. A search of the literature did not yield any published information regarding this issue.

Three inclusions (two identified as monazite by WDX and one unidentified) surrounded by radiohaloes were selected for analysis. For each, an approximately radial traverse from inclusion to unaltered biotite, or vice versa, was carried out both approximately parallel and perpendicular to the cleavage. The points were spaced at approximately five micrometer intervals. The EMPA results are tabulated and appear in the Appendix in Tables A7.1 to A7.6.

The quantitative analysis results indicate negligible differences in the major element oxides within the radiohalo. The value of [100 minus total wt% element oxides] was determined for each analysis point. This value can be assumed to be representative of the OH (as H₂O) and F content. Any oxides that are present in the sample not included in the EMPA analysis must be present at levels below the detection limit and thus negligibly impacting on the 'H₂O' value. A 2 θ scan should be performed to prove this, however. Figures 7.18 and 7.19 show the results of traverses perpendicular and parallel to the cleavage through the radiohalo shown in figure 7.14 and can be considered to be representative.

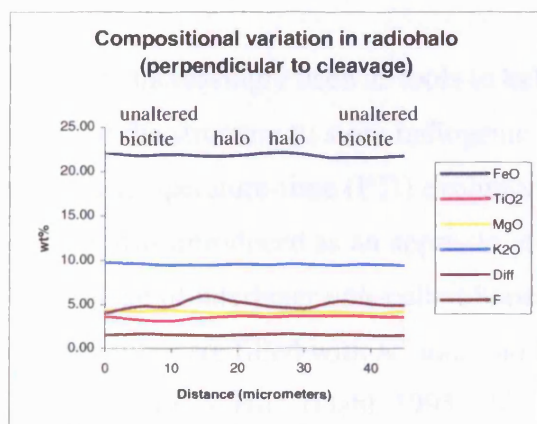


Fig. 7.18. EMPA results from biotite and halo.

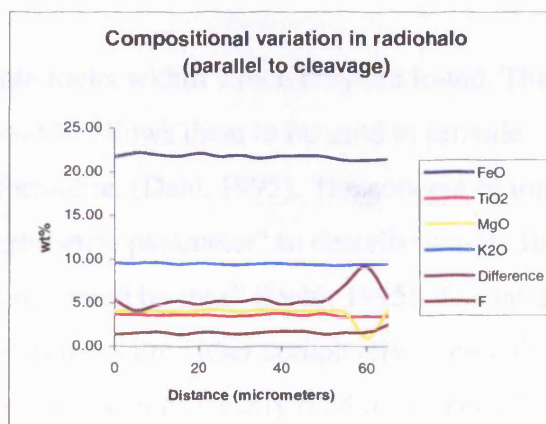


Fig. 7.19. EMPA results from biotite and halo.

Figures 7.18 and 7.19 indicate that there are no compositional gradients within the halo passing into the unaltered biotite. There are fluctuations in some of the oxide concentrations but these are probably within the error of the instrument. Figure 7.19 shows a significant anomaly in the MgO content, resulting in a low total and therefore increased 'difference' value. The 'blip' occurs at some 60 micrometers from the inclusion and so is beyond the extent of the radiohalo.

7.5 - Discussion

Despite rather poor signal to noise in the spectra presented above, it is clear from the Raman data that there might be significant modification to the biotite structure within the haloes. The broad, 'triple' band system around 680 cm⁻¹ and the band around 560 cm⁻¹, weaken and broaden in the halo region to become one, very broad and indistinct band. These bands have been ascribed only generally to motions of the M2 octahedral sites and T₄O₁₀ network in previous studies. Similarly, the lattice modes and low wavenumber bands ascribed to the OH

modes become weaker and broader in the halo. As recorded in many other studies, weakening and broadening of Raman bands can be attributed to variations in bond angles and bond lengths within and between atoms and molecules. Differences are also observed in the OH stretching region in the samples. The lack of observable OH activity must point to an absence of OH in any position and orientation. It is noted that some of the OH-stretching modes are crystal orientation-dependant, however, the $\sim 3655\text{ cm}^{-1}$ band is observed in both E_{⊥c} and E//c (Nasdala *et al* 2001). The bands are restored as the diffuse halo graduates into unaltered biotite.

Micas are increasingly used as tools to help date rocks within which they are found. The ability of the structure to store radiogenic Ar and Sr allows them to be used to provide pressure-temperature-time (PTt) evolution information (Dahl, 1995). The concept of ionic porosity was introduced as an approximate “geometric parameter” to describe simply the “percentage of interlayer unit-cell volume not occupied by ions” (Dahl, 1995). The interlayer sites in biotite are filled with K⁺ ions and the vacancies are either completely or partially filled with H₂O or H₃O⁺ (Dahl, 1995). The interlayer K⁺ ions weakly bind the linked (Si,Al)O₄ tetrahedral layers that sandwich octahedrally coordinated cations to form composite sheets. Dahl (1995) states that the ionic porosity is inversely proportional to the strength of the already relatively weak K—O bond (which, along with K⁺—H⁺ repulsion, explains the ease by which mica sheets are so easily cleaved). The Raman spectra of the halo region suggests the absence of water in the structure and this would have the effect of increasing the ionic porosity, thus further decreasing the K—O bond strength. Substitution of stable cations by radiogenic isotopes occurs in both apatite and monazite; a mineral that commonly contains 4-12 mol% of Th (Deer *et al*, 1992). With their low lattice binding energies (Dahl, 1995) it is easy to envisage a model whereby the emitted radiation from the decaying isotopes, or more likely the recoil of the nucleus upon emission, ‘knocks’ the weakly bonded H₂O and H₃O⁺ from the structure. Were this to occur it might be expected that interlayer separation would be greatly reduced; the relatively large H₂O and H₃O⁺ molecules between the composite sheets have been removed, as has the K⁺—H⁺ repulsion. Bond re-ordering may take place to account for the vacancies created.

There is potential, then, for errors in the radiogenic dating and PTt-evolution studies if this model is correct. The model describes the collapse of the interlayer partitioning upon the loss

of interlayer H₂O and H₃O⁺ molecules. Since this is the region where ⁸⁷Sr²⁺ and ⁴⁰Ar formed by the radioactive decay of other species they, particularly Ar, may be more susceptible to loss by diffusion or by weathering, alteration or recrystallisation. If quantitative ⁴⁰Ar/³⁹Ar measurements are made by microanalysis of discrete 'spots' then regions without radiohaloes might yield more accurate ages than from haloes.

Crystal structure damage leading to partial or complete amorphisation with the loss of medium- and long-range order is a feature observed in some zircons. The process by which this is thought to occur is by the emission of radiation by the decay of U and Th (and Pb) isotopes. These elements substitute for Zr in the zircon lattice. Wopenka *et al* (1996) record that in addition to the high energy α -particles producing displacements with a range of 10 micrometers, the recoil of the nucleus from which the α -particles were emitted is responsible for an order of magnitude more displacements over a 20 micrometer range. Recent work by Salje *et al* (2000) appears to confirm that the damage observed is the result of direct impacts caused by alpha-recoil nuclei. The Raman spectra of affected regions of the zircon crystals exhibit peak-broadening, i.e. increase in the FWHM value and shifts in the positions of the antisymmetric stretching peak of the SiO₄ tetrahedra to lower wavenumbers. Loss of intensity and increase in peak width increases with the degree of structural damage (metamictisation) in zircons (Wopenka *et al*, 1996). The observations of the changes in the biotite Raman spectra close to the inclusion correspond quite closely to those observed in metamict zircons.

Wirth (1985) described the effects on phengite, a layer silicate similar to muscovite in structure, of dehydration. Bombarding the sample with electrons in the TEM was found to induce dehydration, the removal of H₂O, with the loss of lattice spacings but without structural rearrangement. The energy in the TEM was thought to be too low to raise the temperature sufficiently to 'boil' off the H₂O molecules but was enough to delocalise protons from structural OH⁻ ions. The protons could subsequently recombine with other OH⁻ ions to form H₂O in the octahedral layers. The large water molecule formed in the hexagonal cavity buckles the layer, distorting the lattice. The Raman spectra recorded from the haloes indicate the loss of OH, which may have occurred by the interaction of α -recoil nuclei from decaying species within the microinclusions. Further, the weak, broad bands may indicate a wide variation in bond angles and bond lengths consistent with the buckling envisaged by Wirth.

Heating caused by irradiation by energetic neutrons and γ -rays was found to occur in gypsum by Patel & Raju (1970). The rupturing of OH bonds dissipated the energy. Dissociation of the OH groups and dehydration led to lattice distortion that was determined by streaks on the X-ray Laue patterns in the irradiated samples.

Raman spectroscopy using confocal near-IR 785 nm in this study appeared to provide comparable data obtained with visible excitation. Major differences were observed in the OH-stretching region between the two sets of experiments. The exact origin of the bands in the high wavenumber region determined with non-confocal 785 nm excitation are unexplained but are probably ascribable to the glass beneath the section. The confocal arrangement discriminates against any signal beyond a certain excitation volume. In this instance, the height of this volume is less than the thickness of the section. The success at recording bands in the low and mid-wavenumber region can probably be attributed to this wavelength lying at the weaker end of the strong absorption band of biotite. It could be for this reason that McKeown (1999a,b) favoured FT-Raman at 1064 nm over the visible alternative.

The EMPA data adds very little to the investigation into biotite radiohaloes. The increased absorption of the haloes may have been caused by increased levels of Fe (Nasdala *et al* 2001) but the chemical analyses indicate no enrichment and it is difficult to see where this may have been derived. The 'difference' value was calculated as it was hoped it might provide a measure of the OH. However, if OH is lost (as H₂O) then it will create a vacancy rather than the wt% total increasing, since the oxides are present in finite concentrations.

Contemporaneous studies – Nasdala *et al*

The current work hoped to provide an assessment of the use of microRaman spectroscopy to analyse *in situ* mineral structures. A novel approach was taken, using the little-studied radiohaloes surrounding micro inclusions in biotite. During the course of the investigation a remarkably similar investigation was published by Nasdala *et al* (2001). These workers recognised the effectiveness that microRaman spectroscopy would have on such an investigation. Some of their findings have been alluded to in the preceding work.

Interestingly, they indicate that the radius of the halo is dependant on the radioactively decaying species; the largest haloes correspond to the α -particles with the highest energy.

The penetration depths of various α -particles in biotite were calculated and an excellent agreement found with the empirically measured halo radii.

The microRaman studies by Nasdala *et al* revealed similar results to the current work. Band broadening, shifting and loss in intensity were recorded in the radiohaloes. However, these workers were able to detect significantly stronger Raman bands in the halo, particularly in the OH-stretching region, than was found in the current study. This, in conjunction with data obtained from TEM studies and Monte Carlo simulations, enabled them to reach a different conclusion. The model invoked suggests the creation of a low density of point defects in the halo with a disturbance in the short-range order. The model is strongly supported by TEM analysis indicating that the lattice remains relatively undisturbed in the halo.

Nasdala *et al* also showed that the other techniques, whilst supporting some of their arguments, with the exception, perhaps of TEM, could not provide the same level of information about the radiohaloes as microRaman spectroscopy.

7.5 – Conclusion

From studying the Raman spectra recorded from both the affected and unaffected regions of biotite it would appear that the structure has been severely modified from the original sheet silicate structure. Whilst biotite does not produce a particularly strong spectrum of well-defined peaks, the loss of structure between relatively fresh biotite and the inclusion, throughout the halo, is apparent from the spectrum. The loss of OH ions from the structure caused by α -recoil bombardment is seen as leading to incipient localised collapse of the structure. Significant bond-re-ordering is suggested, with concomitant variations in bond lengths and angles, reflected in the marked loss of intensity and band broadening observed in the Raman spectra.

No other technique could perform high spatial resolution crystal structure analysis *in situ* and with so much ease. TEM studies clearly aided other workers in their analysis. However, this technique is neither as simple to interpret or as non-destructive as MicroRaman spectroscopy. With the latter, textural relations are preserved, as is the specimen, enabling repeat analyses by Raman or other techniques.

EMPA added little to the analysis in this case. The technique is relatively common and has similar spatial resolution to MicroRaman and its possible to perform both studies on the sample micro areas of the sample, either uncovered thin section or polished block. However, it is advantageous to perform Raman spectroscopy initially because carbon coating typically has a much stronger Raman response than the inorganic minerals.

The results presented here would clearly have benefited from a revised analytical strategy. It is apparent from this work, and the work of others, that very many accumulations with long exposures for each analysis point are required. It may be that greater activity in the OH region would have been detected with a more considered experiment regimen. Absorption curves suggest that deep visible or UV excitation Raman would be of little use in recording good Raman spectra from the haloes. It is possible that water or oil immersion techniques with confocal near-IR excitation may help. This method could improve signal collection by minimising the effects of refraction at the objective/air/sample interface and may also allow higher incident energy at the sample.

8 – Investigation of Cubic Zirconia

Zirconia, ZrO_2 , can be stabilised at room temperature in its cubic form only by doping with different cations. In this form zirconia has desirable physical properties for technical ceramics and semi-conductor uses. Colourless cubic zirconias were popular as low cost imitation gem diamonds. Experimentation with various cation species enabled zirconias of almost any colour to be created, thus simulating many other gemstones. This section represents the second case study using microRaman spectroscopy for the analysis of crystal structure. The aim is to present a study of coloured cubic zirconia crystals doped with various trivalent cations and comment on the results in terms of the relationship between the dopant chemistry and colour mechanisms to the Raman spectra.

8.1 – Introduction

The high price of both coloured and colourless precious gemstones has led to an expanding industry in the manufacture of imitations. These man-made ‘crystals’ have become increasingly difficult to distinguish from the natural stones they emulate. One of these synthetic substances, cubic zirconia (CZ), was an early popular alternative to natural stones. It was tough, could be faceted and was available in large range of colours. Most importantly, it had optical and physical properties that made it an attractive, low cost alternative to diamond. With the advent of more advanced synthesising processes more realistic imitations, for example moissanite, have become available and the popularity of CZ has reduced.

Despite being supplanted as an imitation gemstone it is still of considerable interest to study doped cubic zirconia to elucidate the mechanisms by which colour is imparted to a crystal. This would be of direct relevance to gemmologists who endeavour to unravel the processes used by unscrupulous synthesisers and detect treated stones. Also, spectroscopic methods may help us understand better the mechanical and physical properties of zirconia’s used in industry.

The origin of this chapter has its roots in the 1999 International Jewellery London exhibition held in Earl’s Court, London. During the Raman spectroscopic analysis and identification of various natural and synthetic semi-precious crystals it was noted that different cubic zirconia crystals

produced different Raman spectra. Given that the Raman spectra of cubic crystalline materials is not orientation-dependent then another mechanism was thought to be responsible.

Due to zirconia's mechanical properties of very high melting point and ability to be made tough through work-hardening, there is much interest in zirconia for engineering ceramics purposes (Bowden, *et al* 1993). In this respect a "cutting edge" application is in the manufacture of false teeth. Cubic zirconia is an important material in many contemporary technological and commercial applications where its chemical resistivity and ability to be grown epitaxially (Cai *et al* 1993) are amongst its many valuable properties. Other industrial applications of zirconia include refractories, abrasives, piezo-electronics and capacitors, the manufacture of glasses and enamels, in fuel cells and catalytic converters and as a white pigment (Lopez *et al* 2000).

8.2 - Crystal structure of cubic zirconia

The naturally-occurring form of zirconia, ZrO_2 , is the monoclinic mineral baddelyite. A rare accessory mineral, it is often found in rocks derived from highly evolved parent magmas.

Synthetically-grown ZrO_2 exists in three states. Below about 1170 °C it has a monoclinic structure. Above this temperature it transforms to the tetragonal structure and then again to the cubic form above 2370 °C (Ostanin *et al* 2000). The tetragonal phase, desired for its physical properties for ceramic uses, can be stabilised at room temperature by using various binary oxides (Bowden *et al* 1993). Cubic zirconia (CZ) has the property of isotropic brilliance that makes it desirable as a gemstone. In its cubic form it dominated the synthetic diamond market during the 1980's (Huong, 1992). However, below the cubic phase transformation temperature the structure transforms to lower symmetry and the brilliance is lost (Huong 1992). As with the stabilised tetragonal form the cubic structure can be retained at room temperatures only by 'doping' the composition. Typical dopants used are yttria (Y_2O_3), MgO, CaO (Bowden *et al* op. cit.) and La_2O_3 (Ostanin *et al* 2000). Doping is the process by which Zr^{4+} ions are randomly replaced by the dopant ions and enough oxygen vacancies, or defects, are created to ensure charge compensation (Weller *et al* 2000, Cai *et al* 1993). Ostanin *et al* (2000) report that 'to date, no full quantitative description of the stabilization mechanism of YSZ has been reported'. There is much commercial interest in the yttria-doped variety, often referred to as YSZ. The concentration of

dopant in gem-simulant CZ's is not known; only qualitative 2θ scans were performed on the samples. Ishigame and Yoshida (1987) state that YSZ used as conducting thin films may contain up to 12 mol% Y_2O_3 , equivalent to 20 wt% (Cai *et al* 1993) and we might assume that the gemstone varieties contain comparable quantities.

The monoclinic, tetragonal and cubic phases of pure ZrO_2 have the Zr^+ ion located in seven-fold, distorted eight-fold and regular eight-fold co-ordination with the O^{2-} ions, respectively (Ostani *et al* 2000). The structure of cubic CZ is a distorted CaF_2 -type with the point group O_h^5 (Cai *et al* 1993).

8.3 - Samples

Dr. J.B. Nelson (Nelson Gemmological Instruments, Hampstead, London) kindly supplied a suite of CZ crystals for analysis. The ten samples used were selected to represent the range of dopant cations used. Dopants thought to be present are some of the trivalent REE and Cr. Where possible two crystals thought to have the same dopant element but with a different colour were used. Figure 8.1 shows the ten cubic zirconia submitted for XRF and Raman spectroscopic analysis.

8.4 - Review of colour theory

The study of colour centres, a term coined by Pohl to describe the special electronic configuration in a solid that gives rise to optical absorption, is a distinct branch of solid state physics. A brief review of the relevant aspects of colour theory to the current study is warranted in this assessment of synthetic, coloured crystals. The vast majority of the studies of colour mechanisms have been performed on the alkali halides, principally chlorides and bromides of Na and K. This is because they are easily grown, have a simple FCC structure and are optically transparent between the deep UV and the far IR. Studies based on these substances, thought to be chemically pure, revealed the importance and effect of impurities on the ease of colouration and on the nature of the colour centres (Schulman & Compton, 1962).



Fig. 8.1. Cubic zirconia crystals. Scales vary slightly. Largest crystal is V, diameter 10.7 mm.

Crystalline solids are regular structures with highly ordered atomic arrangements. However, some of their physical properties, including colour, can only be explained by the presence of imperfections or defects. The important examples are interstitial ions, vacant lattice sites, impurities and dislocations. Some of these defects can be combined and aggregated. Of these, the Frenkel and Schottky defects are well studied. Respectively, they relate to an interstitial (a cation or anion removed from its regular site to a region between regular atomic sites) plus the corresponding vacancy, and the vacancy created when a cation or anion is removed from the lattice site to the surface to form a new layer (Schulman & Compton, 1962). Other defects arise through impurities. Figure 8.2 shows how a divalent cation impurity in a lattice of monovalent

atoms is charge-balanced by a positive ion vacancy (an additional negatively-charged ion would also achieve this). Similarly, Figure 8.3 shows some of the various methods by which charge compensation can be attained in a lattice of divalent ions in the presence of a substitutional monovalent impurity. Either a monovalent cation is incorporated interstitially; a trivalent cation

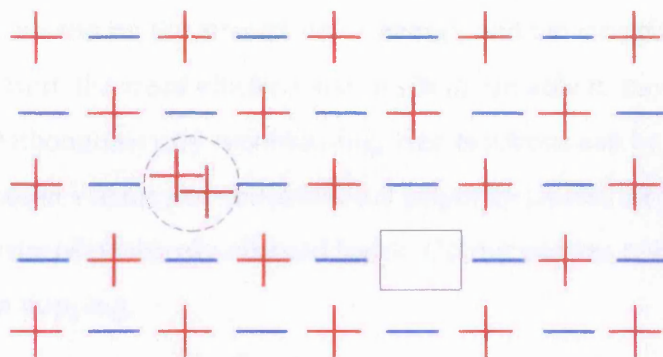
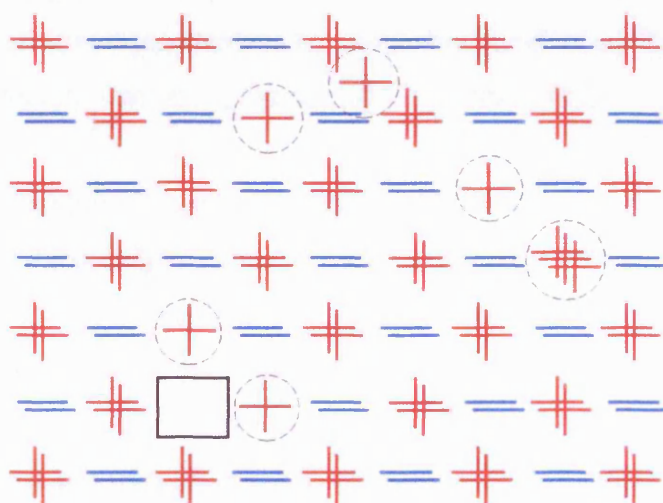


Fig. 8.2. Divalent cation impurity in monovalent ion lattice (after Schulman & Compton, 1962).



 Monovalent cation impurity

 Trivalent cation impurity

Fig. 8.3. Monovalent cation impurity in divalent ion lattice (after Schulman & Compton, 1962).

substitutes for a divalent cation; or a negative ion vacancy is incorporated for every two monovalent impurity cations. Schulman & Compton (1962) notes that impurity related defects tend to be associated into complexes of the impurity ion with the vacancy on adjacent sites. Such

associations are found in diamonds. Smith *et al* (2000) describe the various point defects involving nitrogen and vacancies in the diamond lattice, each of which gives rise to a characteristic absorption band.

Electron 'holes' can arise by the absorption of energy and the stripping of an electron from either a cation or anion. Both the freed electron and the hole are able to move, thus the hole differs from a vacancy. Although mostly recombining, free electrons can be trapped by wandering close to an interstitial, anion vacancy or substitutional impurity cation; all positively charged defects. The reciprocal is true of positively charged holes. Colour centres result from the interstitial 'atoms' created on trapping.

Deviation from stoichiometry with an excess of the electropositive ion is balanced either with the excess ion substituting at a cation site (with an associated vacancy) or as interstitial atoms. Excess electronegative components can be charge balanced by additional holes trapped at cation vacancies or as interstitial anions (Schulman & Compton, 1962).

The concept of dislocations in the crystal lattice enabled some of the mechanical properties of minerals to be explained. Edge and screw dislocations are relevant to colour centres since they can lead to the creation of vacancies and interstitial atoms. High-energy environments such as deformation at elevated temperatures are more favourable to the creation of these defects. Dislocations act as a source of vacancies and interstitials, as well as low energy 'sinks' for impurities, vacancies and interstitial atoms (Schulman & Compton, 1962). Collins *et al* (2000) in their study of natural brown diamonds noted that some samples had much stronger colouration along 'striations' and also in the 'tatami' pattern.

The most immediately relevant aspect of colour centre creation to this study appears to be the presence of impurities in the zirconia lattice, i.e. the doping cations. Schulman & Compton (op. cit.) list the important effects of impurities on colouration. Although based on the alkali halides, the points are valid, not least because the structures are similar to those of the zirconias used in this study. Differences may arise between the effects in the alkali halides and zirconia because of differences in the bonding strength and degree of covalency.

-
1. Impurity ions themselves behave as absorbing and luminescing centres
 2. Lattice constant changes arise due to differences in the ionic sizes of the 'host' ion and the impurity, creating localised regions of increased strain. This creates an energy shift and broadening of the colour centre bands already present
 3. Ionic charge differences between host and impurity promote a change in the concentration of positive and negative ion vacancies/defects, thereby enhancing or reducing the 'colourability'
 4. Impurity-vacancy 'complexes' can form as a result of ionic charge differences between host and impurity. These complexes can trap electrons or holes to create new types of colour centre that the pure crystal did not possess
 5. Differences in the ionisation potentials or electron affinities between the host and impurity may make it easier to trap electrons or holes, again, potentially forming colour centres not present in the pure crystal.

The effects on the physical properties of incorporating divalent cations, alkaline earth and monovalent heavy metal impurities into the alkali halide structure is said by Schulman & Compton to be 'marked'. In particular, monovalent heavy metal impurities were found to have characteristic emission bands. Of the divalent cations studied, only Pb had significant absorption features. No trivalent cations were discussed in the work of Schulman & Compton. Emission bands associated with these impurities were ascribed to transfer of electrons between the anion and cation. It was found that the coordination of the defect, hole or trapped electron determined the type of colour centre and the location of the absorption band (Schulman & Compton *op. cit.*). Impurities can also give rise to colour in a crystal by the selective scattering. The Tyndall scattering of colloids, impurities present on scale much larger than the atomic level previously discussed, causes light to be reflected to be of a different wavelength to that transmitted by the crystal. The zirconias studied do not exhibit Tyndall scattering.

The presence of impurity ions and colour centres described above lead to localised energy levels in the 'band gap' between the valence and conduction bands. Transitions between these states and the conduction or valence bands occur when a photon excites the colour centre. The centre loses the energy by the emission of a quantum of light. The spectrum obtained, when excited by a monochromatic source, corresponds to the different colour centres. Furthermore, Schulman &

Compton (op. cit.) state that the use of polarised light can be used to give information about the symmetry and position within the lattice of the defects.

8.5 - Analysis

Each of the CZ's supplied had had their dopant chemistry qualitatively analysed by Dr. J.B. Nelson using a spectroscope. Briefly, the hand-held device collects the light transmitted from an illuminated faceted stone. Passing through a narrow slit the light is dispersed either by a grating or prism and projected onto the eye. The spectrum observed is that of the light source minus those wavelengths that correspond to the energies of the electronic transitions occurring in the stone. The doping ions have characteristic absorption band positions in the visible spectrum.

Table 8.1 lists the samples used, their dopant based on this assessment, their colour and description.

Sample	Dopant determined by light spectroscopy	Colour	Description
V	Y ³⁺	Colourless	6.83 carats
JL	Probably Cr ³⁺	Olive green	Peridot/Alexandrite simulant 0.74 carats brilliant cut
JI	Eu ³⁺	Pale pink/lavender	0.88 carats brilliant cut h=3.1mm
ZK	Er ³⁺	Pale pink/lavender	brilliant cut 0.88 carats h=3.3mm
YR	Er ³⁺	Very pale lavender/lilac	Kunzite simulant 3.45 carats h=5.0mm
ZP	Pr ³⁺	Deep golden yellow	brilliant cut 3.91 carats h= 5.4mm
FA	Pr ³⁺	Deep golden yellow	brilliant cut 3.51 carats h=5.2mm
ZO	Nd ³⁺	Ruby red	brilliant cut 3.47 carats h=5.0mm
ZN	Nd ³⁺	Very pale lavender/ almost colourless	kunzite simulant 3.36 carats h=4.95mm
ZR	Nd ³⁺	Yellow/green	low-Fe peridot simulant brilliant cut 3.00 carats h=4.7

Table 8.1. Cubic zirconia samples. 'h' is the height of the crystal in mm. 1 carat = 0.2 g.

XRF

Quantitative analysis of the dopant chemistry was attempted using X-Ray Fluorescence (XRF) analysis. Some concern was expressed that the interaction of the incident X-rays would modify the colour of the crystals. This factor is a significant limitation to the analysis of crystalline materials whose desired property is their colour. Each crystal was formed into a separate powder pellet using boric acid under a ten-tonne hydraulic load. The samples were mounted such that the tables were presented to the incident X-rays. The analysis was deemed not to have affected the colour.

Raman spectroscopy

Each CZ was analysed using 514 nm excitation. Unfortunately, samples ZK, ZN and JL could not be analysed during the same session as the other seven samples. Single spectra were recorded from the samples with the laser spot focused on the table surface in each case. The crystals are very strong Raman scatterers; a function of the strongly covalent nature of the Zr—O bonding and the ease of deformation of the polarisability ellipsoid. Generally, low excitation power densities had to be used, or the entrance slit reduced, to avoid saturating the sensitive CCD detector, such was the strength of the Raman signal. This intense signal is in stark contrast to many minerals of interest in mineralogy where, typically, relatively long scans and many accumulations of spectra are required for a spectrum of good signal to noise.

8.6 - Results

XRF and spectroscopy

Results of the XRF 2θ scans for the ten crystals are summarised in Table 8.2 and the raw data appear in the Appendix figures A8.1 to A8.10.

There is poor agreement between the XRF 2θ data and the qualitative assignment made using the spectroscopy. Indeed, only the analyses of samples ZN, V and JL agree. The assessment of the doping agent elements made by Dr. Nelson were made with the benefit of many years using this technique in the study of gemstones. The light spectroscopy is quite simple to use but frequently the absorption bands are very weak or diffuse, making their assignment difficult.

Sample	XRF analysis	Lines
V	Y	K_{α}
JL	Cr?	$K_{\alpha}?$
JI	Nd	$L_{\alpha 1,2} L_{\beta 1,2,3,4}$
ZK	Not assigned	
YR	Nd	$L_{\alpha 1,2} L_{\beta 1,2,3,4}$
ZP	Cr	K_{α}
	Ca	$K_{\alpha} K_{\beta}$
FA	Y	$K_{\alpha 1,2} K_{\beta}$
ZO	Y	$K_{\alpha 1,2} K_{\beta}$
ZN	Nd	$L_{\alpha 1,2} L_{\beta 1,3,4}$
ZR	Cr	K_{α}

Table 8.2. XRF analysis of CZ crystals.

No reference material was available at the time of the analyses to check the assignments made. Similarly, the electron decay lines listed in Table 8.2 (XRF data) for the elements under investigation are closely spaced and given the similarity of their chemical properties, significant overlap is expected. The XRF data are also noisy, making assignment difficult. In light of these issues it is difficult to know which method has provided the more accurate determinations of the dopants.

The presence of Mn in the XRF analyses is attributed to the boric acid flux. However, the Ca-bearing CZ (sample ZP) has Mn in addition to that from the boric acid.

Raman spectroscopy

The spectra recorded from the samples are displayed in Figure 8.4. The positions of each band are listed in Table 8.3 were determined using the iterative curve-fitting routine in the GRAMS software. The spectra can be regarded as comprising three main systems of Raman bands – a region between 250 cm^{-1} and 450 cm^{-1} , an asymmetric band close to 600 cm^{-1} and a complex band system between 900 cm^{-1} and 1250 cm^{-1} . For each of the three systems the number and

positions of the component bands were approximated and modified until a precise match was made with the data. Figure 8.5 shows the intricate array of bands fitted in each region.

Sample	Suspected dopant		Low wavenumber region	Mid wavenumber region	High wavenumber region
	Spectroscopy	XRF			
V	Y	Y	Not fitted	593, 617	952, 1012, 1076, 1194
FA	Pr	Y	277, 321, 345, 369	544, 588, 609	952, 1012, 1078, 1188
JI	Eu	Nd	270, 283, 312, 344, 370, 387, 405	No band	952, 1031, 1083, 1192
JL	Cr	Cr	282, 350, 373, 395	578, 613	958, 1019, 1089, 1190
YR	Er	Nd	272, 283, 335, 344, 369, 386, 405	No band observed	951, 1014, 1086, 1196
ZK	Er	Not assigned	286, 320, 349, 373, 391	567, 604, 623	958, 1018, 1084, 1192
ZN	Nd	Nd	320, 350, 374, 391, 410	566, 606	958, 1019, 1089, 1195
ZO	Nd	Y	277, 349	548, 587, 610	951, 1012, 1078, 1189
ZP	Pr	Cr, Ca	275, 277, 341, 372	586, 612	952, 1014, 1078, 1188
ZR	Nd	Cr	279, 317, 342, 371, 399	547, 586, 607	952, 1012, 1082, 1188

Table 8.3. Positions of bands by curve fitting (where possible).

Lopez *et al* (2000) used the correlation method (see 2.2) to determine the irreducible representations of the monoclinic, tetragonal and cubic forms of ZrO_2 . Part of their Table 2 is reproduced here in Table 8.4. N_B and Z_B are the number of atoms and formulae units in the Bravais cell, respectively. Table 8.4 shows that only one fundamental Raman band is expected in the spectra of cubic ZrO_2 . Similar calculations for the monoclinic and tetragonal forms confirm that with the decrease in symmetry many more fundamental modes are expected. Lopez *et al* (2000) show only a single Raman spectrum from a cubic sample.

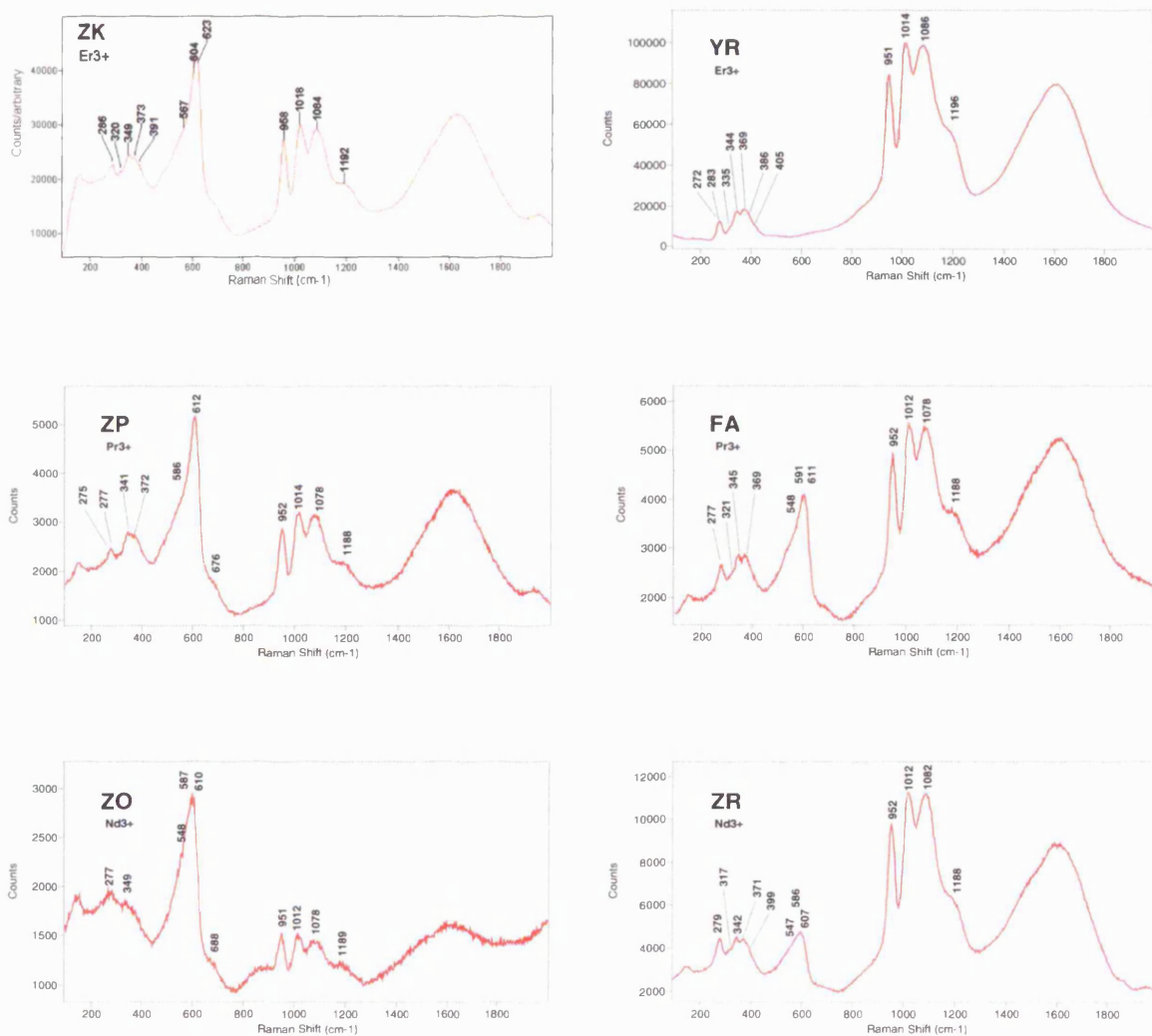
ZrO ₂ Cubic, space group <i>Fm3mw</i> O_h^5 $Z=4$, $Z_B=1$			
Atom	N _B	Site symmetry	
Zr	1	O_h	F_{1u}
O	2	T_d	$F_{1u} + F_{2g}$
Total			$2F_{1u} + F_{2g}$
Acoustic			F_{1u}
Optical		Raman active	F_{2g} (1 band expected)
		Infra red active	F_{1u} (1 band expected)

Table 8.4. Irreducible representations for cubic zirconia (reproduced from Lopez *et al* 2000)

The strong, broad, asymmetric Raman band at 616 cm^{-1} is assigned by Lopez *et al* (2000) to the triply degenerate F_{2g} mode, in keeping with other published work (e.g. Gogotsi 1997). These workers ascribe the broadness and asymmetry to a “one phonon density of states” which arises as a result of the oxygen vacancies (defects) created in REE-doped zirconias. Table 8.4 also indicates that the band corresponds to the three equivalent motions of the O atoms along mutually perpendicular axes. Lopez *et al* (2000) continue, stating that the mode can be regarded as the symmetric vibration of O—Zr—O. The spectrum shown by Lopez *et al* (2000) ends at 800 cm^{-1} (since the fundamental modes appear below this frequency) so no comparisons can be made with the bands in the upper region of the spectra in Figure 8.4. Also, the data of Lopez *et al* (2000) show only weak, broad bands ascribed to discrete regions of tetragonal zirconia in the low wavenumber region which is in striking contrast to the well-defined band system in the current work. Comparisons between the data presented in the current work can be made with the spectrum shown by Gogotsi (1997) for a sample of Y-FSZ-C (possibly an acronym for Yttria-Fully Stabilised Zirconia-Cubic). The published spectrum extends to just over 1600 cm^{-1} and shows a strong agreement with the present work in the low and upper regions i.e. below 400 cm^{-1} and between 900 cm^{-1} and 1250 cm^{-1} . Unfortunately, Gogotsi presents no discussion of the bands in either of these regions.

In order to more directly assess whether the Raman technique is sensitive to the change in dopant chemistry, spectra are overlaid in figures A8.11 to A8.17 in the Appendix. Samples YR and ZK (figure A8.11), and samples ZN, ZO and ZR (figure A8.12) were identified, by spectroscopy, as

containing Er^{3+} and Nd^{3+} , respectively. Similarly, samples Z and FA (figure A8.13); JI, YR and ZN (figure A8.14); JL, ZP and ZR (figure A8.15) were established to contain Y^{3+} , Nd^{3+} and Cr^{3+} , respectively by XRF analysis. Spectra from similarly coloured stones are also overlaid to determine whether determination of dopant is incorrect and that the stones contain a common dopant responsible for the same colour in each stone. The spectra of the pale pink/lavender/lilac stones are displayed in figure A8.16 and the golden yellow stones in figure A8.17.



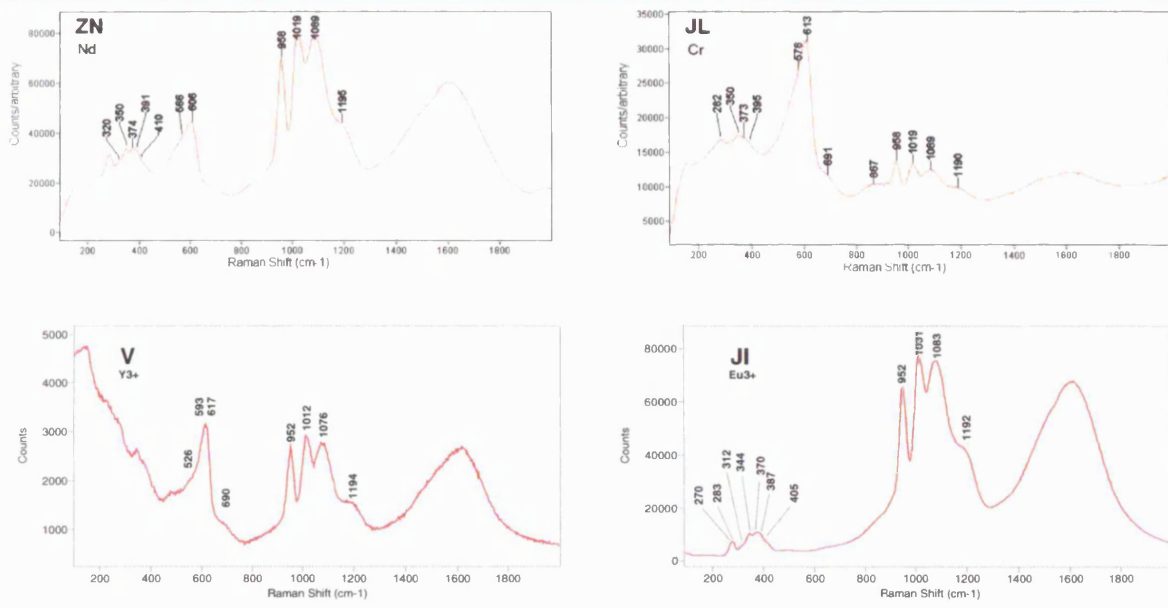


Fig. 8.4. Raman spectra of sample cubic zirconia. Band positions and suspected dopant (from spectroscopie) are indicated.

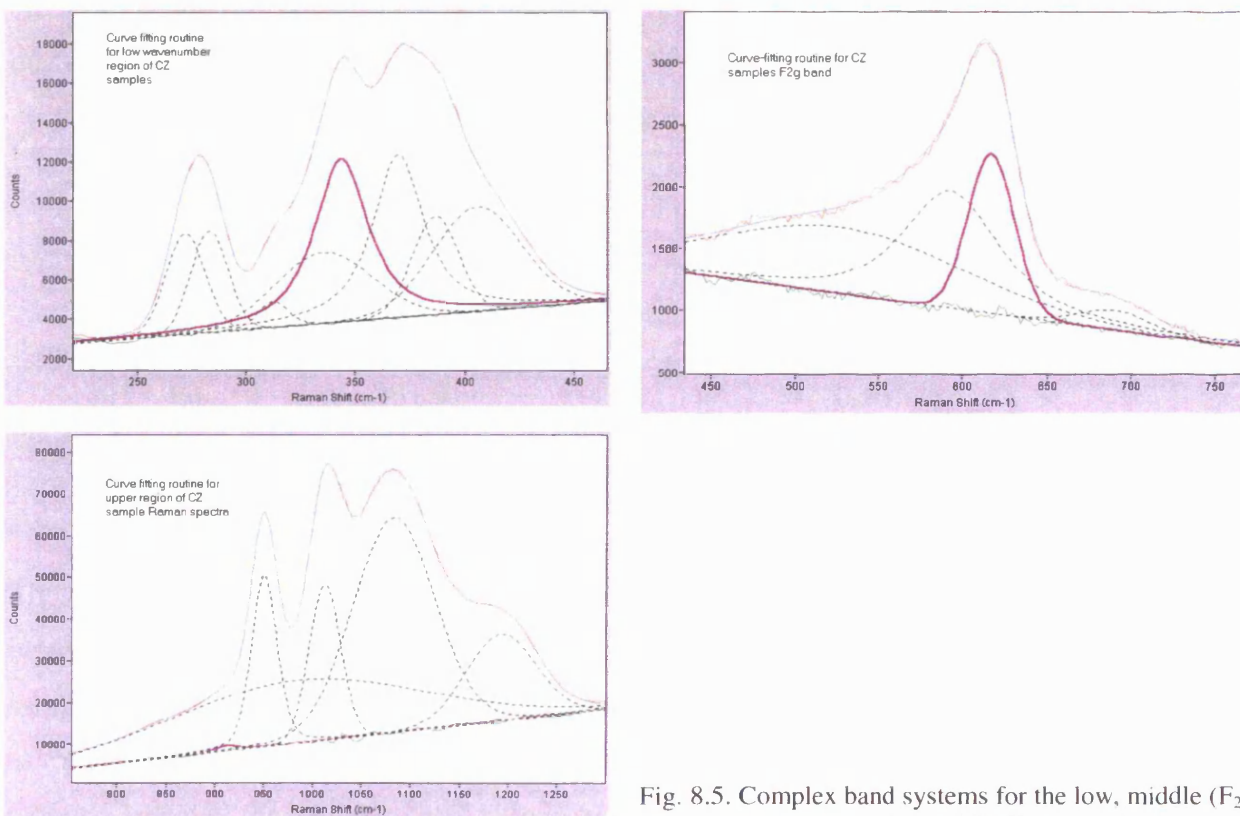


Fig. 8.5. Complex band systems for the low, middle (F_{2g}) and upper regions of the Raman spectra.

8.7 – Discussion

The major differences between the dopant chemistry determined by the spectroscopy and the XRF analyses have been briefly discussed. In light of the lack of agreement between the two methods it is difficult to confidently make any correlations between the chemical data and the vibrational analyses.

Analysis of Figure 8.4 indicates that the Raman spectra for the samples analysed are all very similar. It was noted that the spectra from samples ZK, ZN and JL that were analysed some time later and separately from the rest of the suite displayed a consistent, significant offset in band positions, particularly apparent from the 952 cm^{-1} band. To this end, the data from these three samples were adjusted by 6 cm^{-1} for the following discussion.

The spectra may be similar because only trivalent ions were used as dopants. Consideration of the REE^{3+} cations, listed in Table 8.5, thought to be present reveals a wide range of atomic masses and ionic radii.

Element	Atomic mass/a.m.u.	Ionic radius/nm (coordination number 8)
Pr	140.9	0.114
Nd	144.2	0.112
Y	88.9	0.1015
Er	167.3	0.1
Eu	151.9	0.107
Cr	52.9	

Table 8.5. Atomic masses and ionic radii of the REE^{3+} suspected to be dopants in sample CZs.

The relative atomic mass of Er is twice that of Y. Even if Y is not considered, the range in mass between is considerable and significant differences in band positions might be expected between samples containing these ions. One possibility is that the dopants are in such low concentration as to not affect the Raman scattering. However, from comparison with data and references by Gogotsi, much of the data presented here indicates that the zirconia probably contains greater than 10% REE_2O_3 and so the effect on the spectra of changing the dopant cation is expected to be large.

It is convenient to consider the spectra as three regions and discuss them separately.

Low wavenumber region

In the region below 400 cm^{-1} , when resolvable above the noise, there is a band around 275 cm^{-1} and a doublet around 350 cm^{-1} . Figure 8.5 reveals that this system probably consists of eight bands. The profile of this region is consistent with Gogotsi (1997) but differs from the data published in other studies (e.g. Ishigame & Yoshida, 1987, Huong, 1992, Lopez *et al*, 2000). Gogotsi (1997) does not explain the origin of the band system. Other studies of doped zirconia show broad, moderate bands in this region that are ascribed to A_{1g} and E_g modes. These studies found that the irreducible representations of Y-substituted zirconia contained these symmetries in addition to the F_{2g} mode of the fluorite structure. Ishigame (*op. cit.*) found that the defects, consisting of an octahedrally coordinated vacancy surrounded by six oxygen ions, gave rise to their own Raman bands due to changes in the electronic coupling effects. Lopez *et al* (*op. cit.*) assign the broad band at $\sim 270\text{ cm}^{-1}$ in their spectra of cubic zirconia to the presence of discrete domains of the tetragonal phase. This seems to be unlikely given that the band appears at a significantly lower frequency than it does in the pure tetragonal form, and that there appears to be no contribution from the other strong characteristic bands of the tetragonal phase to the spectrum.

In the present study, however, the bands in this region are more highly resolved than those in the cited published studies. This may be explained by significant, increased ordering of the defects within the lattice, perhaps the result of the manufacturing process, or that the bands are attributable to external, lattice modes. NaCl, also a cubic structure crystal, has no first order fundamental Raman bands yet published spectra (e.g. Wilkinson **In:** Anderson, 1973) reveal weak yet distinct features in the low wavenumber region that must be attributed to lattice modes.

A further proposed origin for the bands in the low wavenumber region is suggested from the work of Ostanin *et al* (2000). Depending upon the dopant cation concentration, the average cation coordination can be expected to lie between seven- and eight-fold due to the presence of O vacancies in YSZ. These workers imagine a 'relaxation of the ions away from their regular

lattice sites' as the coordination changes, resulting in local coordination environments that are similar to those found in monoclinic zirconia. From data presented by Lopez *et al*, the Raman spectra of monoclinic zirconia have bands between 300 cm^{-1} and 400 cm^{-1} that appear to show good correlation with the data of the present study of cubic zirconia. Specifically, the profile of a closely-spaced pair of bands at 335 cm^{-1} and 349 cm^{-1} and a band at 384 cm^{-1} in the data of Lopez *et al* (op. cit.) matches closely with a two-band system at 344 cm^{-1} and 370 cm^{-1} (actually comprising of an additional significant contributions from a weak band at 387 cm^{-1}) and a weak band at 406 cm^{-1} in the current study, although offset to slightly higher frequencies. However, the two strongest monoclinic bands in low region shown by Lopez *et al* (op. cit.) that lie between 170 cm^{-1} and 190 cm^{-1} do not appear in the current work. Lopez *et al* (op. cit.) do not include a full assignment of the Raman bands of monoclinic zirconia but it can be inferred from their work that these bands may be attributed to the vibrations of trigonally-coordinated and distorted tetrahedrally-coordinated oxygen. However, the Raman spectrum of Y-FSZ-C published by Gogotsi (1997) is identical to much of the data presented in the current work. In this work, he states that none of the monoclinic zirconia bands were detected.

Overlaying all the sample spectra, there appears to be no dependence of the position of these low wavenumber bands upon the dopant chemistry.

Mid wavenumber region

In the mid-wavenumber region there is the strong, asymmetric band associated to the F_{2g} mode, which has been previously discussed. Of note is the broadness of the band. Curve-fitting indicates that this band has typical FWHM of 30 cm^{-1} to 40 cm^{-1} Ishigame & Yoshida (1987) record that the F_{2g} mode in isomorphous thorite, ThO_2 , the FWHM of the band is only 7 cm^{-1} . The broadness in the CZ Raman spectrum has been ascribed to disorder due to doping (Lopez *et al*, 2000), contribution from A_{1g} and E_g modes (Ishigame & Yoshida, 1987, Cai *et al*, 1993) and because the band consists of the F_{2g} components of both the $q\approx 0$ and $q\neq 0$ Raman-active optical phonon (Cai *et al* op. cit.). Ishigame & Yoshida (op. cit.) suggested two origins for the broad nature of the F_{2g} band. The first model was that the broadness is related to a defect-induced first order Raman effect. The second model suggested that the second order Raman effect of the two-phonon process is responsible. Experiments at liquid He temperatures suggested to this group

that the broad band is the first order effect due to crystal defects created upon the random replacement of Zr by Y and oxygen by vacancies. In the defect the six oxygen ions surrounding the vacancy shift significantly towards the centre of the vacancy and the four metal ions surrounding the vacancy also shift, but by a smaller amount. The defect space, consisting of a vacancy and surrounding six O^{2-} ions contributes much to the Raman spectrum (Ishigame & Yoshida, *op. cit.*). These workers go on to state that appreciable changes in electronic coupling coefficients in the defect leads to changes in polarisability (and the dipole moment), itself leading to induced Raman scattering from the defect space. Calculations and representations of expected spectra using this model show that the F_{2g} , A_{1g} and E_g fundamental modes all produce very broad bands (hundreds of cm^{-1}) with features that are more intense but still quite broad (many tens of cm^{-1}). The discrepancy between the observed and calculated frequencies for the E_g modes shown by Ishigame & Yoshida (*op. cit.*) may be explained by the effect of the four metal cations surrounding the vacancy lowering the crystal symmetry. Their calculated A_{1g} modes have frequency distributions around 600 cm^{-1} and other similar values to those of the F_{2g} fundamental. Experimentally they found E_g modes concentrated in a broad band between 100 cm^{-1} and 300 cm^{-1} and some more at 600 cm^{-1} although this didn't agree with calculated positions.

Figure 8.4 reveals that the F_{2g} band is not always present or that the intensity of the band, relative to the low and high wavenumber band systems, is reduced. Repeat analyses of those crystals that did not produce an F_{2g} band (YR and JI) did subsequently produce a band consistent with the other samples, during a later analysis session. These results are consistent with samples that show orientation-dependent Raman spectra. This behaviour is unexpected in samples of cubic zirconia. Crystals that belong to the cubic system are not expected to show such dependence because the structure is isotropic and the vibrations are symmetrical along three mutually perpendicular axes. Huong (1992) notes that cubic BN is strongly Raman anisotropic. The Raman spectra of BN show TO and LO modes because it has the zincblende cubic structure that lacks an inversion centre. Polarisation studies of oriented doped cubic zirconia may reveal Raman anisotropy and deviation from the perfect cubic structure brought about by the lattice defects.

Overlaying the sample spectra showing this band suggests that it may be sensitive to the dopant used. Figure 8.6 and Table 8.3 indicate that the higher frequency component of the intense band (see Fig. 8.5) varies between 606 cm^{-1} and 623 cm^{-1} .

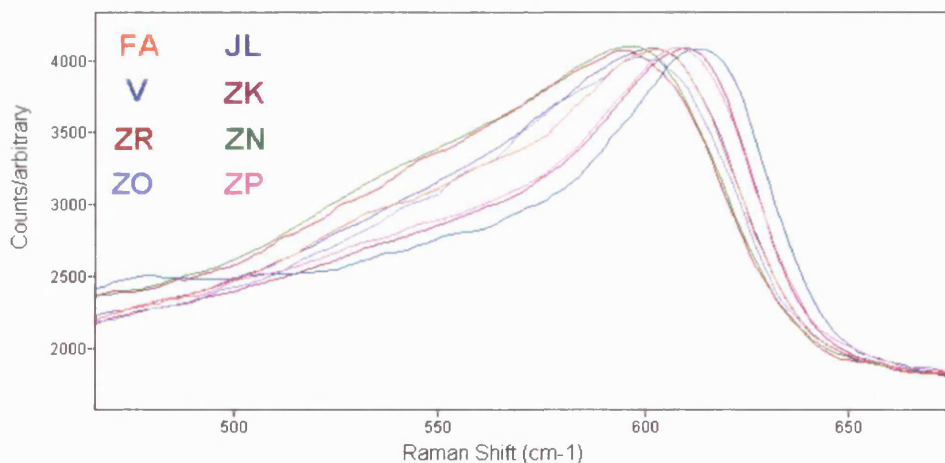


Fig. 8.6. Position of the F_{2g} band for the samples highlighted.

In order to test the possibility of a relationship to the dopant element, the position of the F_{2g} band determined for the samples were plotted against the value of the atomic mass unit of the cation thought to be present based on light spectroscopy and XRF determination. The results of this analysis are displayed in Figure 8.7.

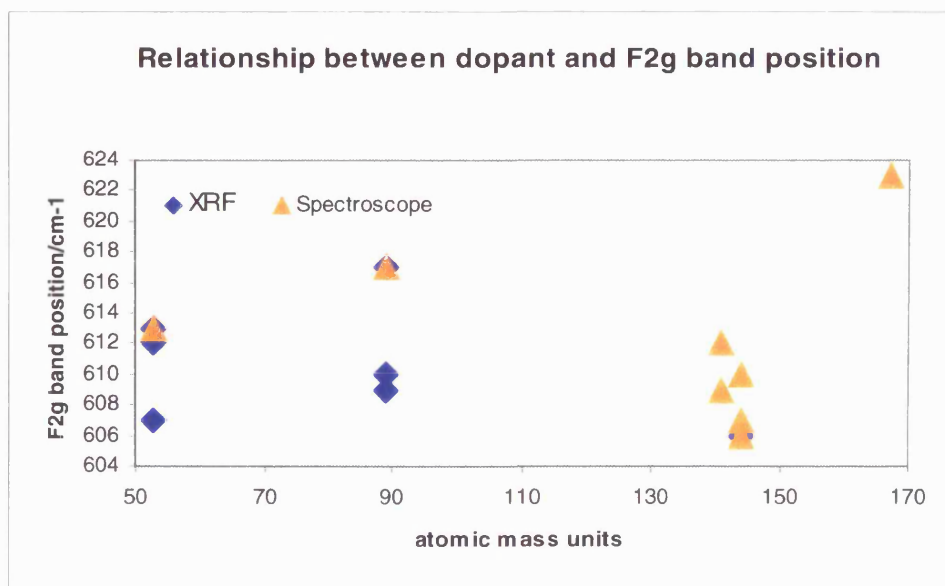


Fig. 8.7. Relationship between F_{2g} band and dopant by XRF and light spectroscopy.

Figure 8.7 clearly indicates that there appears to be no clear relationship between dopant chemistry and position of the F_{2g} band. From the published findings of many studies (e.g. Chopelas, 1991), this is somewhat surprising since the considerable differences in mass (see Table 8.5) should affect the O—T—O (where T is either Zr or the trivalent dopant cation) bond force constants, i.e. changing the vibrational energy of the bond. The samples with Nd as the dopant do seem to give lower values for the position of the F_{2g} band. And, if the Nd values are ignored, the few remaining data points (spectroscopy determination) do suggest a possible linear relationship between dopant atomic mass and band position. These factors might suggest that Nd has a considerably different effect on the structure of cubic zirconia, and in particular, on O—T—O.

The most obvious explanation for the lack of strong relationship is found in the large degree of disagreement between the dopant identifications of the two techniques. Figure 8.8 shows the relationship of the F_{2g} band position to dopant cation for those three samples (V, JL and ZN) where XRF and light spectroscopy *do* agree.

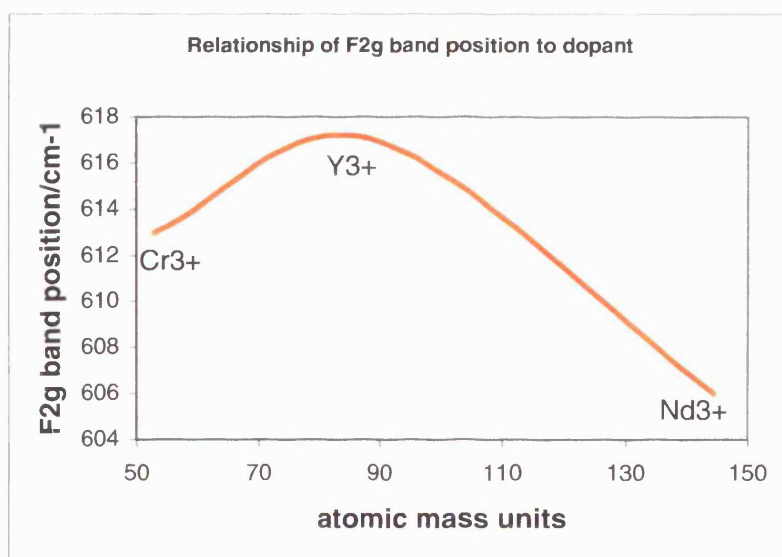


Fig. 8.8. Relationship between F_{2g} band and Y, Cr and Nd dopants determined by XRF and spectroscopy.

As there are only three data points in Figure 8.8 the suggestion of a trend is misleading. Again, the low wavenumber value for the Nd-doped sample is indicative of a modified role of this cation in the structure when compared to the other dopants.

High wavenumber region

The band system in the high-wavenumber region is consistent with that shown by Gogotsi (1997) but inconsistent with that published by Huong (1992). The system comprises a moderately sharp, intense band at 952 cm^{-1} , an equally intense doublet/two closely-spaced bands ($\sim 1013\text{ cm}^{-1}$ and $\sim 1080\text{ cm}^{-1}$) and a strong shoulder at about 1189 cm^{-1} . Huong (1992) published a spectrum of Y^{3+} -doped cubic zirconia with an intense, broad band centred around 1100 cm^{-1} that is probably associated to a two-phonon process in addition to the one-phonon mode at $\sim 600\text{ cm}^{-1}$. The region between these two band systems is free of spectral features. Gogotsi (1997) does not expand on the origin of the complex band system in the range 900 cm^{-1} to 1250 cm^{-1} .

Figures 8.8 and 8.10 display this region of the spectra with data from all the samples overlaid. The band at 952 cm^{-1} is shown separately from the ‘doublet’ for clarity. The bands appear to be completely insensitive to changes in the dopant chemistry.

None of the published work on zirconia collated during this study has described the origin (or even mentioned) the bands that occur in this portion of the Raman spectrum. In light of this some suggestions are made. One possibility is that the bands are attributed to a resonant enhancement occurring as a result of using an excitation that coincides with an electronic transition. Whilst this might be possible in samples JL and ZR (since a green excitation wavelength was used) all spectra display the same band system.

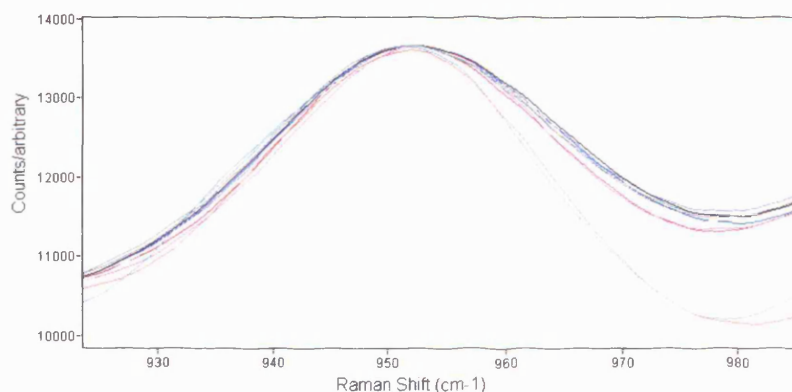


Fig. 8.9. The 952 cm^{-1} band. All sample spectra shown but not identified to illustrate the identical positions.

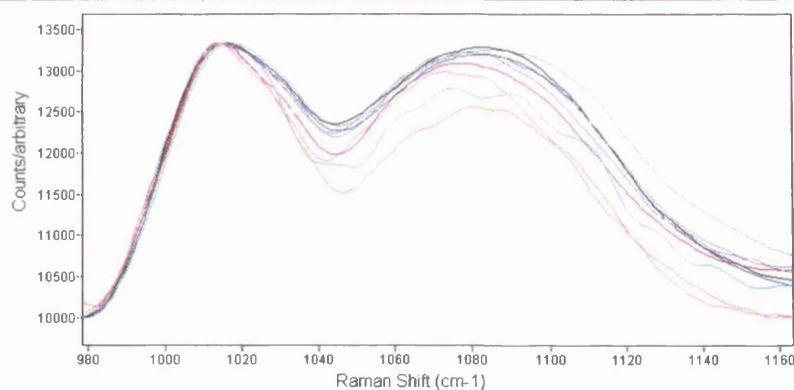


Fig. 8.10. The high wavenumber 'doublet' feature. All sample spectra shown but not identified to illustrate the identical positions.

A further possibility is that the bands are luminescence features from the excited REE cations. Naturally-occurring zircon enriched in REE has several bands above 1000 cm^{-1} (when a 514 nm laser is used) in their 'Raman' spectra that have been ascribed to laser-excited photoluminescence of the REE (Dr. Lutz Nasdala, pers. comm.). Furthermore, the complex band system between 950 cm^{-1} and 1250 cm^{-1} in these results corresponds to the range 542 nm to 549 nm . Burruss *et al* (1992) note from their study of laser-excited fluorescence in fluorite that this region of the visible spectrum contains some of the allowed electronic $4f$ orbital transitions of the RE elements Sm, Eu, Er, Ho, Pr, Eu and Tb. Those transitions of Nd appear to occur most strongly at longer wavelengths, however. If the bands observed are PL features of different REE, we might expect them to differ between samples. The constant position of the bands could be explained if they were PL features of Zr ions. Since PL features occur at fixed wavelengths the simplest method to test if the bands are related to PL would be to repeat the analyses with a different wavelength and compare the positions of the bands in absolute wavenumbers, or in nm.

Comparison of the spectra

As previously mentioned, the Raman spectra for the samples supposedly of the same dopant, either by spectroscopy or XRF determination, and by colour, are shown overlaid in the Appendix figures A8.11 to A8.17. In the preceding discussion, the bands in the low- and high-wavenumber positions appear to show no dependence upon dopant chemistry. The summary of the spectral comparisons in Table 8.6 therefore concentrates upon the F_{2g} band.

Samples	Relationship	Spectral comparison
ZK, YR	Er ³⁺ by spectroscope	F _{2g} present only in ZK.
ZO, ZR, ZN	Nd ³⁺ by spectroscope	ZR and ZN almost identical F _{2g} position, ZO approx. three cm ⁻¹ higher.
V, FA	Y ³⁺ by XRF	Significant difference in F _{2g} band position. V _{F_{2g}} 617 cm ⁻¹ , FA _{F_{2g}} 611 cm ⁻¹ .
ZN, JI, YR	Nd ³⁺ by XRF	JI and YR identical spectra in low and F _{2g} regions, Hard to compare ZN but may have very similar positions in low cm ⁻¹ region.
JL, ZP, ZR	Cr ³⁺ by XRF	Differences in the low wavenumber region but similarities may be hidden by low signal to noise. F _{2g} significantly different ZR _{F_{2g}} 606 cm ⁻¹ , JL _{F_{2g}} 608 cm ⁻¹ , ZP _{F_{2g}} 612 cm ⁻¹ .
ZK, ZN, JI, YR	Similar colour	All very similar in low cm ⁻¹ region, although ZK has one band slightly different (may be due to low signal). Only ZK and ZN gave F _{2g} bands. These have very different positions; ZK _{F_{2g}} 617 cm ⁻¹ , ZN _{F_{2g}} 600 cm ⁻¹ .
ZP, FA	Similar colour	Similar spectra in low cm ⁻¹ region. Significant differences in mid cm ⁻¹ region ZP _{F_{2g}} 612.5 cm ⁻¹ , FA _{F_{2g}} 609.7 cm ⁻¹ .

Table 8.6. Summary of spectral comparisons for related samples, either by suspected dopant chemistry or colour.

Assuming that the position of the F_{2g} band is related to the dopant, there are few conclusions to be drawn from the data. Some agreement can be seen between Nd determined by both spectroscope and XRF, however, the dataset is limited. Also, similar colours of zirconias almost certainly can be attained using different trivalent dopants. When spectra are compared, the position of the F_{2g} band strongly suggests that FA and JL (and possibly also ZO) have the same dopant, as do ZP and ZK, and also ZR and ZN. Further comments could be made if all sample spectra contained the F_{2g} band.

Raman spectra and colour centres

A very brief outline was given for some of the mechanisms for creating colour centres in crystals in 8.4. It is clear that substitutional impurity, i.e. the dopant trivalent REE cations, leads to the creation of colour centres by the generation of lattice defects. From the discussion of the F_{2g} Raman band of the samples studied, it is apparent that the Raman spectrum is sensitive to certain point defects. However, it is not possible from these data to distinguish between the colour centres or to comment more accurately.

Much more could be learned about the colour mechanisms and defect systems by studying the laser-induced photoluminescence and absorption spectra. For example, the technique of UV laser-excited PL has proved invaluable in the study of high-pressure, high-temperature treated natural brown diamonds (Smith *et al*, 2000). Analysis of the PL bands associated with the different defect systems (H3, H4 and N3) before and after treatment to reduce colour has elucidated on the structural changes within the lattice that occur on treatment and contributed much to the understanding of the colour mechanisms within diamond. The technique was proved to be far more sensitive than IR, CL and X-ray topography. The colour differences in the zirconias probably correspond to emission bands of different cations. Table 8.5 lists the ionic radii of the REE thought to be present as dopant ions. Schulman & Compton cite differences in this value as an important factor in the 'colourability' of crystals. Where the same dopant is thought to be responsible for producing different colours in the zirconias studied, the effect may be explained by concentration differences, or by the presence of different colour centres. These may result from different 'growing' conditions, e.g. temperature, or subsequent treatment, e.g. X-ray irradiation.

8.8 – Conclusion

There appear to be no other systematic Raman spectroscopic studies of 'gem' cubic zirconia where the different doping agents are thought to be known. Other vibrational studies have centered on those zirconias used in industry where the dopants are generally limited to Y^{3+} and Ce^{3+} .

Because there was little agreement between the spectroscopy and XRF determinations of the dopant it has not been possible to correlate changes in the Raman spectra with chemical changes. Under these conditions, the Raman spectra have proved inconclusive in correlating chemical dopants with chemical determinations. Plotting the position of the F_{2g} band against the mass of the dopant determined by spectroscopy suggests a possible relationship, although the dataset is extremely small. The role of Nd^{3+} in the structure appears to differ from that of the other trivalent cations based on the deviation from this possible linear trend and the fact that, what appear to be, Nd-doped samples have markedly lower values for the position of the F_{2g} band.

Similarly, the Raman spectra of stones of the same colour do not correlate. This supports the well-known fact that different ions can be used to impart the same colour on certain crystals. However, the F_{2g} band may be sensitive to the dopant used and some samples have been related on the basis of this feature.

The differences noted in the study of the CZ's at the jewellery trade show must have been due to orientation-dependence of the crystal during analysis. The cubic structure must be sufficiently perturbed by the presence of localised, ordered defects for the selection rules to break down, or, as with 'cubic' BN there is Raman anisotropy due to the lack of an inversion centre. Sufficient 'cubicity' must be retained, however, since the samples are brilliant and ultra-hard. The data suggest no evidence for the presence of the tetragonal phase although the situation with monoclinic bands is less clear. Based on the similarity of the sample spectra in the low wavenumber region with those published of monoclinic zirconia, the data may indicate discrete regions of monoclinic zirconia that results from the local decrease in coordination due to defects. However, the absence of the strong, characteristic 'monoclinic bands' and the increased frequency of the band system are unexplained and so the assessment is tentative.

MicroRaman is an excellent method for distinguishing cubic zirconia from other substances. Also, as many other studies into ceramics and engineering have shown, it is an excellent method for discriminating between the polymorphs of zirconia. However, it does not appear to be a sensitive technique for elucidating on the colour mechanisms. The instrument can be used, however, to record laser-excited luminescence. Photoluminescence is more sensitive to changes in dopant chemistry.

8.9 – Further work

There is clearly much scope for further work in this area. Of primary importance would be to acquire more published literature on the vibrational spectroscopy of zirconias, and in particular, cubic zirconia. Predominantly the subject of ceramic and engineering journals, the gemmological references should also be searched. The literature used in this study failed to account for many of the observed bands and little agreement was found between sources for the origin of the bands.

The Renishaw RM instrument can also be used to record the absorption spectra, in addition to Raman and PL spectra. This could be an excellent way of rapidly and accurately obtaining the wavelengths of absorption of the dopant ions. The light spectroscopy appears to be a rather subjective means of identifying the species.

Photoluminescence (both at room and LN₂ temperatures) studies should also be carried out using the RM. If the observed band system between 900 cm⁻¹ and 1250 cm⁻¹ is associated with REE emission then laser-excited fluorescence is an excellent means to determine the nature of the REE. As with fluorite, the dominant 1st order Raman band of cubic zirconia (the F_{2g} mode at about 600 cm⁻¹) is well-removed from the possible 'emission' region. Shorter, 'deep' visible excitation, probably around 400 nm, would be successful in exciting the electronic emissions. In addition, much could be learned about the dopant ions by using excitation wavelengths toward the red end of the spectrum. This is because many of the strongly-allowed transitions of the REE ions occur between 580 nm and 680 nm (Burruss *et al* 1992). The application of this method to the study of diamonds is well known.

MicroRaman analyses at LN₂ temperatures might allow the collection of much sharper Raman bands. If the change in dopant causes very small changes in band position the enhanced spectral resolution offered by this type of analysis may make the shifts easier to quantify. Polarisation studies should also be carried out on oriented crystals to elucidate on the structure as it clearly deviates from true cubic.

Since heavy atoms will have lattice vibrations at low frequencies, analysis close to the excitation, either with double or triple spectrometer or with Renishaw NExT filter, may be more sensitive to changes in mass than the spectral region obtainable from notch filter-based instruments. There do not appear to be any published studies of the low wavenumber shift Raman spectra of doped cubic zirconia.

A larger sample set of known origin and REE/dopant would be useful in continued Raman analysis. As the spectroscopy and XRF techniques are inconclusive, other techniques such as

ELNES (Electron Energy-Loss Near-Edge Structure) or cathodoluminescence (CL) should be used to confirm the dopant chemistry. It would be interesting to determine which band(s) are sensitive to change in dopant and plot band position against ionic radius or the atomic mass of dopant.

9 – Applications of Raman spectroscopy to geochronological zircon

Zircons are widely used in geochronology. However, the accuracy of the dating can be dependent on the detection of radiation-damaged grains, which may have lost radiogenic Pb. In this, the third application of microRaman spectroscopy to the study of crystal structure, the aim is to discuss the importance of 'metamict' zircons and assess different methods of using MicroRaman spectroscopy to assist geochronologists in the selection of crystalline zircons.

9.1 - Introduction

The importance of crystals of zircon for the dating of rocks in which they are found has long been recognized. Since the 1960's experimental methods based on mass spectrometry (MS) have been used to help constrain rock histories, from formation and cooling to subsequent periods of metamorphic activity and structural events. Modifications to the MS technique and the development of new analytical methods to probe the structure and chemistry of zircon grains have seen enormous strides in the precision and accuracy of the dates determined as well as into the understanding of geological processes. Amongst the latest additions to the geochronologist's arsenal is Raman spectroscopy. The technique compliments existing methods but has yet to be applied routinely.

In this study, Raman mapping and imaging are used to aid the detection of zircons grains suitable for geochronological analysis.

9.2 - Geochronology/Isotopic dating

Zircon is a relatively common accessory mineral in sedimentary, igneous and metamorphic rocks. Its primacy as a dating tool is attributed to its high melting temperature and resistance to chemical and physical agents. Zircon has the formula $ZrSiO_4$. U and Th plus other trace elements of similar ionic radii substitute quite readily for Zr^{4+} (0.72-0.84 Angstrom). Typical U contents of magmatic zircons range between 10 ppm and 4000 ppm although contents of up to a few wt% have been recorded (Nasdala, *et al*, 2001). Wopenka *et al* (1996) expand on the chemical complexity of zircon stating that Hf may account for more than 7 wt% and up to 50 elements

may be present, substituting for both Zr and Si. Dating techniques exploit the natural decay of radioactive U to stable isotopes of Pb. Since the zircon structure largely precludes the large Pb isotopes during initial crystallization, all the Pb present in the structure is radiogenic Pb. Kober (1986) states that the common Pb content of crystalline zircon is $<2 \times 10^{-12}$ mol.

Data from experiments on zircon populations are plotted on so-called concordia or isochron diagrams. Common Pb corrected values of $^{206}\text{Pb}/^{238}\text{U}$ are plotted against $^{207}\text{Pb}/^{235}\text{U}$. The natural decay curve of U acts a reference line: the 'concordia' (Wetherill, 1956 **In**: Dickin, 1995). Concordant isotopic values measured from the zircons fall on a linear array with upper and lower intercepts on the concordia. The regression line through these points represents the natural evolution of the U-Pb system if the system remains closed. For a simple magmatic system the upper intercept represents the age of crystallization; the age of closure of the U-Pb system. This is inferred as the age of the rock. The lower, younger intercept may represent a thermal event such as metamorphism, if supported by other geological evidence (Dickin, 1995). Open U-Pb systems produce discordant points and reflect a disturbance in the U-Pb systematics. The principal cause of discordant data is Pb and U loss; the closed system has become open. Processes that could account for this are metamorphic and structural events.

Further complications to the dating of zircon arise if the crystals become overgrown by much younger zircon material, for example, during metasomatic episodes. Nasdala *et al* (1996) note that overgrowths and metamorphically-recrystallised zircon are more robust and have not lost Pb. Rather, these areas are Pb-free since the structure excludes large common Pb atoms. Inheriting 'ancestral' zircons may contaminate young granite bodies; dating such cores will lead to erroneously old ages.

9.3 - Pb loss in zircon

It is readily seen from the above that Pb loss is the limiting factor in the isotopic dating of zircon. It was identified as such by Holmes in 1954 and leads to discordia scatter, particularly at lower ages (Dickin 1995). Pb loss due to geological process or radiation damage will lead to ambiguity in dating (Högdahl *et al* 2001). Dickin (1995) provides a useful summary of the history of the Pb-loss models developed. A continuous diffusional process had wide support but more recent

investigations (e.g. Meldrum *et al* 1998, Connelly 2000, Cherniak and Watson 2000) suggest that the process is so slow for crystalline zircon that the effects are negligible. Indeed, Cherniak and Watson (2000) state that it would take 10^8 or 10^9 years for 1% Pb loss to occur in a 10 micrometer grain at $>750^\circ\text{C}$. At higher temperatures Pb loss would be more significant but complete resetting of the 'U-Pb' clock would not always occur. It is for this reason that primary magmatic zonation commonly observed in even extremely old zircons is preserved (Connelly 2000).

Various workers, invoking microfissures and networks of capillaries and fluids to enable Pb to be escorted away from the host zircon, modified the diffusional model (references **In**: Dickin 1995). It is widely reported from studies on natural and synthetic zircons that radiation damaged grains exhibit dramatically faster rates of Pb loss (Nasdala *et al* 1996, Meldrum *et al* 1998, Cherniak and Watson 2000, Connelly 2000). Zircon altered by internal damage caused by the radioactive decay of elements in the structure loses Pb very rapidly while unaltered zircon loses no Pb under normal crustal conditions (Mezger and Krogstad in Connelly 2000). The altered state also shows a marked decrease in stability against dissolution (Nasdala *et al* 1996, Davis and Krogh 2000) The exact process by which Pb is lost in zircon is complex and likely to be different in each case and probably the result of several processes (Dickin, 1995). Temperature and fluids play a vital role. It has been shown that Pb loss by diffusion and leaching is far more rapid at low temperatures (Cherniak and Watson 2000). Experiments by Davis and Krogh (2000) on the acids used to prepare zircons for isotopic analysis show that leaching occurs from radiation damaged areas and has implications for the dating process.

9.4 - Mass Spectrometry techniques

Several analytical techniques based on mass spectrometry exist. A favoured method is Thermal Ionisation Mass Spectrometry (TIMS), a single crystal evaporation technique providing high precision data. As the name implies individual grains are annihilated by a controlled thermal source (usually a rhenium filament) and the resulting 'vapour' analysed for its isotopic content. With this technique Kober (1986) claims sub micrometer spatial resolution from individual grains because different temperatures are used to drive off the weakly-held Pb associated with damaged sites (Ansdell and Kyser 1993, Davis and Krogh 2000). Ansdell and Kyser (1993) point

out that the technique would struggle to provide accurate data in the presence of intergrowths and other structures.

Inductively-Coupled Plasma Optical Emission Spectrometry (ICP-OES) also requires the use of whole grains. Generally, separated grains are dissolved very slowly in acid (HCl, HNO₃ and H₂SO₄) and the solution passed in aerosol form to the plasma 'torch' where it is atomised. The spectral emission is analysed by the spectrometer; the wavelengths and intensity of signal corresponding the elements present in the sample. Although a more accessible technique, there are problems with spectral interference and practical difficulties associated with digestion. Crystalline grains may take days to go into solution at high P and elevated T (220°C) in Teflon 'bombs'. Kober (1986) states further that the technique fails if the zircons are structurally complicated.

Clearly, the quantitative analysis of a discrete region offers advantages over whole grain methods. Secondary Ion Mass Spectrometry (SIMS) uses an O₂⁻ beam approximately 15 micrometers in diameter to continuously excavate a flat-bottomed pit in a polished zircon grain section. A secondary beam of Pb ions is generated and analysed by a double focusing mass spectrometer (Dickin, 1995). Nasdala *et al* (1998) note an almost constant pit size for both crystalline and radiation-damaged grains. Given the complexity of the instrumentation and expense, ion probes are not widely available. Their principal drawback is interference from molecules of similar mass to Pb isotopes (Dickin 1995). A further restriction is raised by Davis and Krogh (2000); the aggressive nature of the spot sampling precludes the use of cracked grains. This effect is circumvented by a related 'spot' technique, Laser Ablation –ICP-MS. Vapourised material ejected from a pit is carried in a stream of Ar gas to the plasma torch where it is atomised then passed to the mass spectrometer. Connelly (2000) suggests the technique is of limited elemental precision and Dickin (1995) cites applications where it has advantages as a 'reconnaissance' tool.

Grain selection for MS

Aftalion *et al* (1987) describe a typical sample preparation required for analysis of zircons by MS techniques. Initially the rock sample is crushed in a jaw crusher or fly-press. Secondary

crushing is provided by a disc mill or TEMA. Heavy minerals such as zircon are separated from the lighter mineral constituents by using a Wilfley table and heavy liquids that exploit density differences. Magnetic separation discriminates the required low-Fe non-magnetic zircon, which is then sieved into size fractions. Handpicking can produce 99% zircon purity. Acid washing removes any surface impurities such as pyrite. Connelly (2000) describes how reflected light microscopy using an 80x objective allows the first order selection of suitable grains by the classification by colour, morphology and large inclusions. Higher magnification tools using transmitted light are used to characterise populations further based on inclusions, cores and the observance of magmatic zoning. Despite the thorough optical investigation Connelly observes that discordant data persists and he is one of a number of workers that call for a reliable method to identify suitable i.e. concordant, grains. It is here that MicroRaman has been identified as a potential analytical solution.

9.5 - Metamictisation

Zircon becomes metamict as a result of accumulated damage to the crystal structure caused by radioactive decay of U and Th substituted for Zr during initial crystallization (Woodhead *et al* 1991b). With prolonged damage the structure attains a glass-like, amorphous state. It had been thought that bulk unmixing to the component oxides might result from the process of metamictisation but several recent studies (e.g. Salje *et al* 1999, Zhang *et al* 2000a) suggest there is no evidence for this.

The mechanism by which zircons become metamict is still not well understood (Weber *et al* 1994) despite the vast amount of attention the subject has received. In 1914 Hamberg suggested that radiation damage was key (Murakami *et al* 1991). During the 1950's a model relating the degree of damage to the age of the zircon was expounded and received more attention in the 1970's. Given the number of uncertainties recently highlighted (Nasdala *et al* 1995) this method cannot be considered reliable. Unsurprisingly, a variety of models have been developed to account for the catastrophic structural collapse of zircon to the amorphous state.

Processes that lead to metamictisation and an understanding of chemical diffusion and the structural change in zircon have implications for nuclear waste storage (Chakoumakos *et al* 1987). Salje *et al* (1999) discuss some of the previously favoured models. Three radioactive decay processes contribute to the amorphisation of zircon. Emissions of high-energy α -particles (~ 4 MeV to 6 MeV) from U and Th atoms were originally thought to account for zircon lattice damage. This energy is now thought to be associated with ionization with only a small proportion of elastic collisions with other particles. The number of ensuing atomic displacements from elastic collisions, causing incipient amorphisation, is thought to be of the order of 10^2 (Weber *et al* 1994) over their path length of $\sim 10\,000$ nm. The isolated defects created by the α -decay particles are called Frenkel pairs (Ríos and Salje, 1999). Nasdala *et al* (1996) note that if the main cause of structural damage was α -radiation or spontaneous fission fragments then diffuse haloes, as observed in many biotites (and discussed in section 7), should be present. No studies have observed these diffuse zones in zircon.

It has been stated that the nucleus from which the α -particle is emitted has a recoil energy of ~ 0.1 MeV and a path length of ~ 20 nm (Weber *et al* 1994). Unlike α -particle emission, all this energy is dissipated in elastic collisions, leading to 10^3 atomic collisions and resulting in considerable localized damage (Weber *et al* 1994, Ríos and Salje, 1999). This process is thought to be the principal source of radiation damage in zircons (Davis and Krogh, 2000), biotites, monazites and titanites (Nasdala *et al*, 2001). Local amorphisation occurs as a result of the spontaneous local collapse of the crystal structure due to the high concentration of the local defects. Eventually, the accumulation of structural defects and amorphous nanoregions leads to a loss of long-range structural order (Weber *et al* 1994). With increasing α -recoil damage the defect regions overlap. Murakami *et al* (1991) used XRD and HRTEM to define three stages in the amorphisation of zircon, based on the relative proportions of crystalline to amorphous regions. By the third stage the XRD pattern is a diffuse halo and represents an absence of long-range periodicity, i.e. the substance has become X-ray amorphous. However, Salje *et al* (1999) note that XRD can give misleading or erroneous determinations of metamictisation. They point out that some glasses may have a diffraction pattern very close to that of related crystal structures. Ríos and Salje (1999) observe the limitations of using XRD to study metamict grains.

Firstly, the powder pattern reflects the average of a range of grain sizes and grain orientations and secondly, that grinding may introduce defects that were not intrinsic to the original grain.

Nasdala *et al* (1996, 2001 for an excellent, brief discussion of the origin of radiation damage) note that zircons may be heterogeneously metamict, since the distribution of U and Th within a crystal is similarly heterogeneous. Consequently, techniques used to probe the distribution of crystallinity or metamict zones must be capable of high spatial resolution.

The third process, γ -decay causes negligible destruction.

In order to quantify the amount of radiation damage a crystal has experienced, the α -decay event dose was introduced. Murakami *et al* (1991) provides an equation to determine the dose and provides value ranges for the three stages in the amorphisation process. Workers in this field appear to agree that a dose rate of the order $\sim 0.5 \times 10^{16}$ α -decay events mg^{-1} is required for a crystal to attain the X-ray amorphous state (Chakoumakos *et al* 1987, Nasdala *et al* 1998, Weber *et al* 1994). Meldrum *et al* (1998) have shown that the older the crystal the higher the dose rate required for it to become metamict. Increasingly in the literature, the dose is expressed as displacements per atom, dpa; a dose of >0.7 dpa would lead to complete amorphisation (Meldrum *et al* 1999a).

Chakoumakos *et al* (1987) correlated birefringence with α -decay damage in an attempt to estimate the dose rate. Along with a change in the birefringence of zircon, Murakami *et al* (1991) list many other physical changes that occur upon metamictisation:

- Decreases in density (17%), RI and birefringence (until isotropy), intensities of optical and IR absorption signals (until isotropy) as well as diffraction maxima, elastic modulus, hardness and thermal conductivity
- Increases in thermoluminescence, adsorbed H_2O , susceptibility to dissolution and chemical diffusion and unit cell dimension (5%)
- A darkening in crystal colour

The changes in the diffraction lines have been attributed to interstitial defects and decreasing grain size as the volume of aperiodic, non-crystalline component increases. Differential strain experienced by remaining crystallites may contribute to the broadening (Murakami *et al* 1991).

Several workers have noted the occurrence of radiating macro fractures in zircons with metamict zones. The fractures are the result of expansion in metamict zones leading to internal stress and cracking in the crystalline portions on the grain. Nasdala *et al* (1996) suggest that they are characteristic of heterogeneous metamictisation. Chakoumakos *et al* (1987) report that the fractures do not penetrate through the metamict layers since these have a low elastic modulus compared to the crystalline zones. Fracturing leads to diffusive or heterogeneous redistribution of Pb and makes grains more susceptible to attack (Wopenka *et al* 1996) since the fractures provide additional pathways for element mobilisation (Chakoumakos *et al* 1987). Studies by Nasdala *et al* (1998) similarly report that metamict grains are more susceptible to Pb loss than crystalline grains but that metamictisation is not the cause of Pb loss.

It is not possible to distinguish metamict grains or metamict regions within grains using standard optical techniques. Nasdala *et al* (1995) note that any of the structural analytical techniques, typically NMR, X-ray absorption, X-ray diffraction and IR spectroscopy can be used to determine amorphisation in zircon. Woodhead *et al* (1991b) used IR to study the H₂O (as OH) content of crystalline and metamict zircons in an attempt to correlate OH content with degree of amorphisation. It was found that the structural disorder and disturbance in metamict zircons allowed a multitude of possible sites for OH with a range of hydrogen bond lengths and strengths and consequently, a wide range of possible OH contents. Woodhead *et al* (1991a) determined that OH is not essential to the metamictisation process but may stabilise the amorphous state. However, the role and effect of H₂O on the transformation is open to debate. XRD has proved a popular method although Nasdala *et al* (1997) suggest that the method is only good for crystalline to disordered but not amorphous grains. In many XRD studies a large whole grain is micronised, as a consequence only very general information can be learned (Nasdala *et al* 1995). HRTEM and Electron Diffraction patterns have been used to assess the degree of crystallinity (Murakami *et al* 1991).

Annealing

Whilst poorly understood, the processes of amorphisation are counter-acted in some instances by the annealing process. Synthetic and artificially-damaged natural zircons have been used to attempt to understand the damage accumulation and annealing processes. Many studies (e.g. Zhang 2000b, 2000c, Capitani *et al* 2000) suggest that thermally-driven annealing is a multistage process and may occur over a range of temperatures (600K to 1800K, Zhang 2000b) depending on the initial degree of damage. Some workers also suggest a possible intermediate phase but this has not received much support. Moreover, severely damaged grains are annealed at a much slower rate than only partially damaged grains, if at all (Murakami *et al* 1991). Indeed, grains that have only attained Stage 1 (some regions of aperiodicity and rare occurrences of misoriented crystallites) may anneal over geological time (Murakami *et al* 1991). Weber *et al* (1994) suggest that with even over the vast timescales involved, high activation energies preclude the recovery of the amorphous state under ambient conditions.

Recrystallisation refers to the regrowth of crystalline material. Annealing, on the other hand, requires simply the repair of disrupted bonds by the reordering of nearest-neighbour atoms. Colombo *et al* (1999) used XRD to study the recovery of the short-range structural order to transform metamict to crystalline zircon. They found that annealing changes the average Si—Zr and Si—O distances, while Zr—Zr distances are not affected. This fundamental difference implies that while recrystallisation leads to a ‘resetting’ of the U-Pb isotopic ‘clock’, since radiogenic Pb is mobilized, annealing is not necessarily associated with Pb loss (Nasdala *et al* 2001). Annealed zircons will have a structure strongly dependent on the initial state of radiation damage (Capitani *et al* 2000).

Studies into the temperature relationship of annealing have drawn conflicting conclusions. Davis and Krogh (2000) argue the annealing of α -recoil damage is neither spontaneous nor continuous and is influenced by thermal events. Cherniak and Watson (2000) proposed the concept of a ‘critical amorphisation temperature’ value (360°C to 380°C, depending on U content). If the system was raised above this temperature then annealing rate > metamictisation rate and no amorphisation would occur. Some workers argue for temperatures close to that of recrystallisation whilst others for far more moderate, even surface temperatures (Nasdala *et al*

2001 for references). This could well be due to the variety of competing thermal annealing mechanisms. Woodhead *et al* (1991a) point to the effect of H₂O on annealing. Fluids may play a role by lowering the temperature and increasing the rate of crystallization. Counter-acting this, the presence of impurities is thought to slow the annealing process (Meldrum *et al* 1998).

Given the above, it is apparent that the derivation of concordant zircon ages rests squarely on the selection of the correct grains, particularly for whole grain techniques. Davis and Krogh (2000) observed a clear link between radiation damage and enhanced solubility of ²³⁴U and radiogenic Pb, and that leaching from damaged, but not metamict, sites has implications for discordance of ancient zircons. The heterogeneous nature of U and Th distribution, and therefore degree of amorphisation, similarly requires that equally careful selection be made for the 'spot' analyses. The use of CL and BSE gives ~20 micrometer spatial resolution and aided by HF etching for zones/structures and this has proved useful in certain instances (e.g. Nasdala *et al* 1998).

9.6 - Raman spectroscopy of zircon

Zircon belongs to the tetragonal crystallographic system with the space group $I4_1/amd$ (D_{4h}^{19}) (Nasdala *et al* 1995). The structure consists of isolated SiO₄ tetrahedra with strong internal Si—O bonds linked by weaker M—O bonds where M=Zr⁴⁺ or others that substitute in 8-fold coordination. Alternatively, the structure can be considered as edge-sharing SiO₄ tetrahedra and ZrO₈ dodecahedrons (Nasdala *et al* 2001). The structure of metamict zircon, however, is debated (Woodhead *et al* 1991a).

Vibrational spectroscopy has proved to be highly effective in elucidating the process of metamictisation. Woodhead *et al* (1991a) used IR and FT-IR to study crystalline and metamict zircon. However, the techniques require extensive sample preparation. Carefully cut and orientated thin plates (sub mm) must be mounted in KBr pellets. Consequently, the method does not preserve the entire structure and precludes the grain from other analytical techniques.

Wopenka *et al* (1996) list the fundamental modes and their frequencies and these are reproduced in Table 9.1. Figure 9.1 shows a Raman spectrum recorded by the author from a single euhedral zircon crystal. Some of the bands have been assigned to vibrational modes.

Raman shift	Symmetry	Assignment
1008 cm^{-1}	E_g	ν_3 SiO ₄ anti-symmetric stretch
974 cm^{-1}	A_{1g}	ν_1 SiO ₄ symmetric stretch
439 cm^{-1}	A_{1g}	ν_2 SiO ₄ anti-symmetric bend
355 cm^{-1}	E_g	ν_4 SiO ₄ symmetric bend
224 cm^{-1}	External (lattice) modes	rotational
201 cm^{-1}	External (lattice) modes	translational

Table 9.1. Positions of the most intense Raman vibrational modes of zircon and their assignments (after Wopenka *et al* 1996)

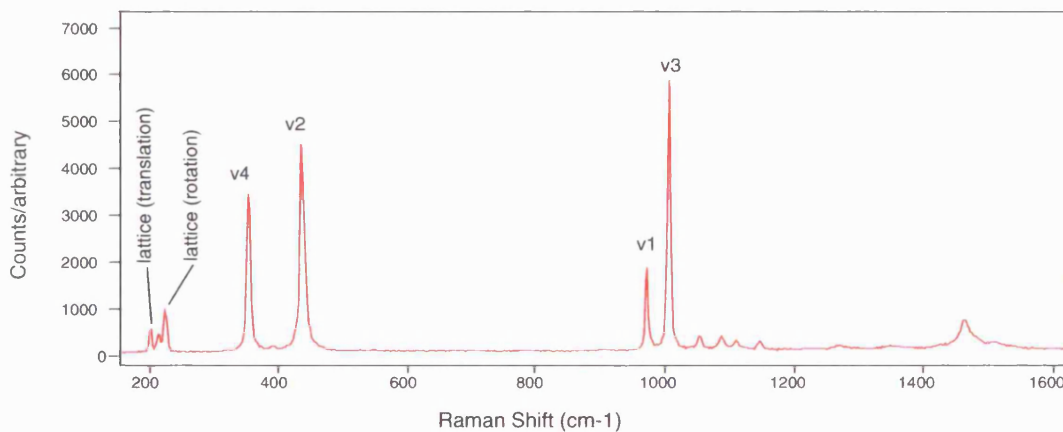


Fig. 9.1. Zircon Raman spectrum.

Other strong bands have been recorded in the literature between 200 cm^{-1} and 350 cm^{-1} that are also attributed to external vibrations; the translation and rotation of nearly rigid tetrahedra in relation to Zr atoms. It might be expected that the A_{1g} mode be the most intense spectral feature,

as is observed in the Raman spectra of other orthosilicates (Nasdala *et al* 1995). However, the spectrum is dominated by the $\nu_3(\text{SiO}_4)$ band (the B_{1g} mode of Nasdala *et al* e.g. 1995).

Nasdala *et al* in a series of papers (1995, 1996, 1998, 1999 and 2001) used the Raman spectrum to study the metamictisation of many zircons. Lutz Nasdala *et al* were the first to correlate the degree of metamictisation with changes in the Raman spectrum in the key study published in 1995. It has been widely reported since that initial study of Nasdala *et al* (1995) that with increasing metamictisation the Raman lines of zircon broaden and shift to lower frequencies (e.g. Nasdala *et al* 1995, Zhang *et al* 2000a); the so-called mode softening behaviour. Indeed, the external modes of medium to highly metamict grains degrade to a single broad feature $\sim 200\text{cm}^{-1}$. The estimation of crystallinity of polished grains is based on the FWHM of the $\nu_3(\text{SiO}_4)$ band, found to be most sensitive to structural change. The data of Nasdala *et al* (1995) correlating the FWHM to crystallinity is given in Table 9.2.

FWHM $_{\nu_3(\text{SiO}_4)}$	Degree of crystallisation
$<5\text{ cm}^{-1}$	very well crystallised
$\leq 10\text{ cm}^{-1}$	well crystallised
$10 - 20\text{ cm}^{-1}$	intermediate
$>20\text{ cm}^{-1}$	metamict
$>27\text{ cm}^{-1}$	highly metamict/amorphous

Table 9.2. Classification of the degree of metamictisation (after Nasdala *et al* 1998)

In a later study (Nasdala *et al* 1999) the FWHM $_{\nu_3(\text{SiO}_4)}$ was correlated with degree of discordance of U/Pb data. The shift in frequency of the $\nu_3(\text{SiO}_4)$ peak has been reported at up to $\sim 30\text{ cm}^{-1}$ (Högdahl *et al* 2001). Broadening of the external modes suggests that the lengths and angles become increasingly irregular (Nasdala *et al* 1995, Wopenka *et al* 1996). Internal vibrations of the SiO_4 tetrahedra remain throughout the metamictisation process (until a totally amorphous, glassy state is attained) suggesting SiO_4 tetrahedra remain stable but the lattice becomes disordered. Nasdala *et al* (1995) point to a continuous lattice decay with the environment of Zr^{4+} ions becoming increasingly disordered until no external Raman vibrations, i.e. vibrational activity of the Zr—O bonds.

From an IR study, Woodhead *et al* (1991a) suggested that broadening of fundamental and combination modes suggests that the D_{2d} symmetry of the SiO_4 tetrahedron is lost with metamictisation, possibly caused by rotating and tilting in response to Zr^{4+} displacements. A similar explanation was given by Nasdala *et al* (1995). Wopenka *et al* (1996) noted strong correlations between concentrations of REE elements and the position, intensity and FWHM of the $\nu_3(SiO_4)$ across a chemically-zoned lunar zircon and concluded that crystal structural damage was the cause. They recorded $FWHM_{\nu_3}$ values between 12.7 cm^{-1} and 23.3 cm^{-1} for U-poor and U-rich regions, respectively. Although increased REE content must lead to increased α -recoil damage, Nasdala *et al* (1995) suggest from annealing experiments that neither increased FWHM or peak position shifts are related to increased trace element content. The same annealing data also reveals that these spectral features cannot be attributed to the presence of water/hydroxyl groups. The shift in peak position of the mode has been explained by some workers (e.g. Wopenka *et al* 1996) by increased interatomic distances caused by the slight increase in lattice size and increased atomic distances that would occur as the lattice expands. These effects are observed in XRD patterns and density data from metamict zircons. Peaks can be further broadened if the analysed crystallites are very small in relation to the overall size of the grain or if the analysed region is a glass.

Crystalline zircon is a relatively strong Raman scatterer. Analysis of metamict zircon, however, is hindered by very low Raman scattering potential. Also, Nasdala *et al* (1998) found that brown/black zircons exhibited some thermal sensitivity when excited by the laser. The crystals were observed to change colour slightly unless the incident laser energy was below a ‘critical’ value of 5 to $10\text{ mW}/\mu\text{m}^3$. Nasdala *et al* (1998) cite instrument broadening (instrument function) and uneven background from fluorescence as limiting factors in the calculation of the FWHM values. The former can be avoided by ensuring that the instrument is capable of a spectral resolution of better than 3 cm^{-1} . In the same study, Nasdala *et al* explain the need for a confocal instrument arrangement, especially when the sample is mounted in an epoxy or other inherently Raman-active medium. As with many other Raman spectroscopy studies, ‘Raman background’ is commonly cited as a problem in the analysis of metamict zircons. Indeed, Nasdala *et al* (1995)

note that 'Raman background' can completely swamp the peaks. An increased background signal in the low wavenumber region of zircon analysis has been attributed to the vibrations of weakly-held water or related structural groups. Dehydration experiments appeared to reduce the background (Nasdala *et al* 1995).

The usefulness of the $\nu_3(\text{SiO}_4)$ peak for crystallinity estimations is enhanced by its frequency with respect to the exciting line. Laser-induced fluorescence of trivalent REE ions may cause additional peaks in the Raman spectrum and add to the background (Wopenka *et al* 1996).

Raman spectroscopy has also helped determine that the products of metamictisation are not oxides of Si and Zr, as was thought to be possible. These compounds would produce Raman bands of their own. Only one study has observed the predicted bands of ZrO_2 (e.g. Zhang *et al* 2000a), in a sample of unknown geological history, lending weight to the argument that metamictisation is a disorder phenomenon not a breakdown phenomenon. However, there is evidence for the presence of SiO_2 and ZrO_2 as intermediate phases in the recrystallisation of highly metamict zircon at high temperatures (Capitani *et al* 2000).

In the IR studies of Woodhead *et al* (1991a,b) a more extended region of the vibrational spectrum was analysed. Although ostensibly research into the nature of the hydrous species in zircon, they reported on several peaks not found in the Raman literature. These workers suggest that peaks at $\sim 3200 \text{ cm}^{-1}$, $\sim 3100 \text{ cm}^{-1}$ and $\sim 2750 \text{ cm}^{-1}$ could be used as sensitive measures of crystallinity. The latter of these is thought to be unrelated to trace element chemistry and therefore is of particular interest. Woodhead *et al* (1991b) did not go as far as attributing these bands to any vibrational behaviour.

The previous discussions have highlighted the importance of crystalline zircon grains in geochronology and the mechanisms by which crystal structure can be lost (and regained) and the system opened to chemical loss processes. Many workers have called for a reliable technique to discriminate crystalline zircons from metamict grains that lead to discordia and geologically-meaningless data. Whilst CL and BSE have proved useful in some instances Cherniak and Watson (2000) note that there are differences in the diffusion rates of the REE and Pb in zircon.

This could render useless the more ‘accurate’ locating of ‘spot’ analyses on the basis of defined, chemically zoned layers. Nasdala *et al* (1996) were the first to suggest Raman for screening grains for age determination candidates. The aim of this crystal structure investigation is to assess Raman spectroscopy, using different approaches, in an attempt to solve some of the common problems associated with grain or ‘spot’ selection in the analysis of geochronological zircon.

Samples

Obtaining samples for use in this study proved to be difficult. Ideally, well-characterised zircons from well-studied suites and displaying a range of crystallinities would be used. Prof. R.R. Parrish, Director of the NERC Isotope Geosciences Laboratory (NIGL), Keyworth, Nottinghamshire, supplied zircon grains from very different provenances and of very different ages and geological histories. An indication of the concentration of U was given. The four suites were to be mounted in epoxy and polished flat by C.D. Storey to aid analysis under the microscope. Unfortunately, a problem arose during the mounting and polishing process that resulted in most of the grains being lost during polishing. Analysis using MicroRaman spectroscopy of the surviving grains revealed them to be extremely well crystallised and unzoned and of little use in this study. Dr. J.B. Nelson supplied a large (approximately 1.5 cm), zoned Sri Lankan crystal, polished on two parallel sides and around one hundred grams of very high purity zircon sand. Some of this sand was prepared as a grain mount on a glass slide. Dr. G. Foster supplied a polished block containing several zircon grains that had been analysed using a LA-ICP-MS technique. Bi-directional ablation tracks on the grain surfaces can clearly be seen under the microscope.

9.7 - Global Raman imaging

Introduction

The use of global Raman imaging has found applications in many areas. It permits the spatial distribution of substances with different Raman spectra to be rapidly determined. Spatial resolution can be as high as 1 micrometer. The method is described previously in this study (section 3.3). By means of illuminating a large area of polished zircon grain it should be possible

to distinguish between crystalline and metamict regions by selecting a narrow pass-band for a characteristic Raman band of either species. Where a polished grain section is to be used for quantitative analysis, e.g. by ion probe, the method ought to offer advantages of increased speed, accuracy and no requirement for sample preparation over CL and BSE methods. The latter techniques require the use of a conductive coating and often HF is employed to highlight any structures that exist in the grain.

Samples

Microscopic analysis using transmitted light revealed a minute percentage of the crystals in the grain mount to contain distinct cores. These were generally light brown compared to the colourless overgrowths. The grains occupy a fairly narrow particle size distribution; typical grain sizes are around 100 micrometers across. A grain was selected that clearly contained a core and overgrowth so that imaging experiments would be simpler to interpret.

Experimental

In order for flat fielding to be performed on images of the zircon grain it was necessary to acquire Raman images from the Si wafer. The procedure is outlined elsewhere. Briefly, the frequency of the strong, symmetric first order Raman band of Si was determined using the imaging filters. The active 'Image Area' of the CCD detector chip was optimized for the defocused laser spot and images recorded with the 10x, 20x and 50x objectives. Exposure times of 200 seconds, 100 seconds and 100 seconds were used, respectively.

With the selected grain under the microscope, the frequency of the $\nu_3(\text{SiO}_4)$ band was determined using the Raman imaging filters. Curve-fitting of the spectrum indicated that a value of 1003 cm^{-1} should be used with the imaging path. Images were captured from two grains using the 10x objective since this allowed the entire grain to be illuminated in each case. Exposure times were varied; 200 seconds, 100 seconds and 50 seconds were used.

Results and Discussion

Figure 9.2 shows the white light image of an analysed grain and the uncorrected Raman image. Cracks in the grain (bottom left of the images), which may have been induced by expansion of

the core, can clearly be identified as dark lines in the Raman image. The core appears as a darker region on the image. This corresponds to a frequency position of the core $\nu_3(\text{SiO}_4)$ that differs from the centre of the band pass selected, i.e. 1003 cm^{-1} . It is not possible from the imaging experiment to determine whether the frequency is higher or lower than the centre. The overgrowth surrounding the core is brighter in colour. A very bright region appears at the top of the image. This area may correspond to a later overgrowth.

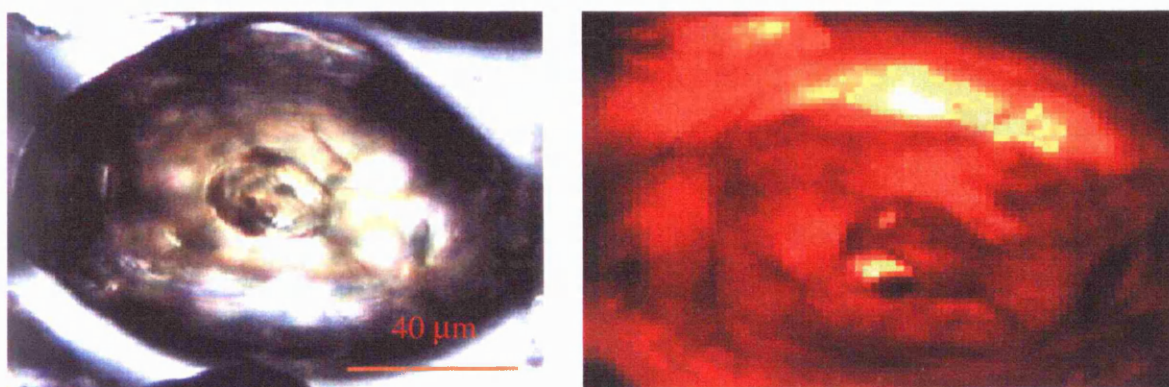


Fig. 9.2. PPL white light image (right) and Raman image (1003 cm^{-1}) of zircon grain. Uncorrected for illumination.

The differences in the colour scale between the core and overgrowth are small. This is because the band pass of the filter is some twenty wavenumbers and the change in the band position is only around five wavenumbers. To check that the Raman image was correct, standard Raman spectra were recorded from numerous ‘spots’ on the sample surface. Figure 9.3 shows the Raman spectra recorded and overlaid. The analyses from the core are indicated as lying to the high frequency side of an arbitrary centre value.

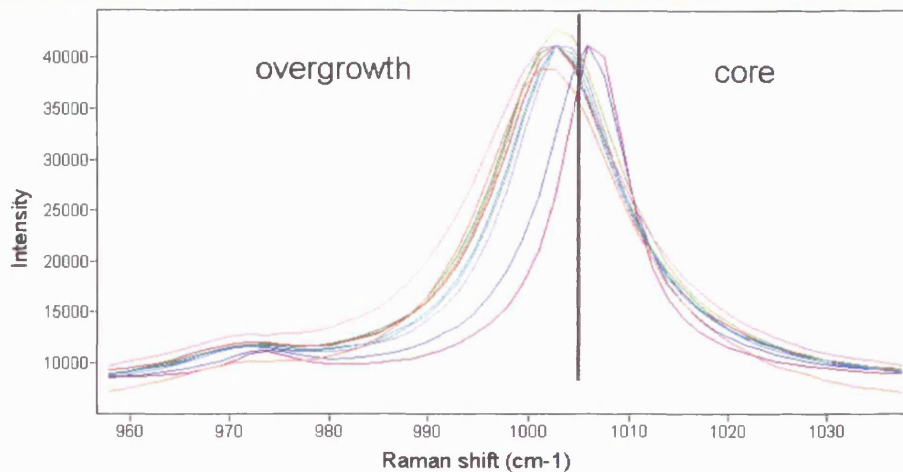


Fig. 9.3. Detail of Raman spectra from regions of grain shown in Figure 9.2.

The data presented suggest that whole zircon grains can be analysed with imaging using the 10x objective in as little as 50 seconds. Using the technique, grains selected for either whole grain or 'spot' MS analyses could be quickly screened. Raman imaging appears to be sensitive to the change in frequency of the band despite the position changing by only a few wavenumbers.

9.8 - Depth profiling

Introduction

No method exists for the reliable discrimination between mixed populations of crystalline and metamict zircons. High-flux magnetic separation and hand-picking can produce high yields but contamination is still problematic, leading to discordant age results. The ability to determine, non-destructively, the crystallinity of the core of a grain could be beneficial to the subsequent quantitative analysis of zircon grains.

Depth profiling ("optical sectioning", "z-scanning") is an invaluable technique available to research Raman Microprobes. This method makes use of the microscope's motorised z-drive. Raman spectra can be recorded from each successive interval and the data compared. The sample stage can be controlled in the axis of the microscope, i.e. the focusing axis, via the software with a movement precision of one micrometer.

Although the Renishaw RM instrument is inherently confocal (Dr. K.P.J. Williams pers. comm.), slight adjustments to the instrument's optical configuration offers tighter confocality. This allows Raman spectra to be recorded from a discrete 'scattering volume' (Baldwin *et al* 2001) that is smaller than the 'focal volume'. Where crystalline samples are required for whole grain evaporation or digestion methods, Raman spectroscopy should be able to confirm the degree of crystallinity of the core. The need for a tight confocal arrangement is highlighted by Nasdala *et al* (1998) who state that the effect of zircon's high RI is to increase the laser-excited volume from $<5 \text{ micrometer}^3$ to around 80 micrometer^3 .

Samples

The grain mount was again used to identify a suitable zircon crystal for depth profiling analysis. Although the experiment is, in this study, carried out on polished grains the principal of the method would be applied to separated whole grains to distinguish them *without* the need for polishing or any other sample preparation. Grains could, for example, be mounted temporarily in parafilm for the purpose of analysis.

Experimental

The focal volume created by a laser spot incident perpendicular to the surface is transformed from a cylindrical (Baldwin *et al* 2001) shape in the sample due to RI effects. The size and shape of the cone is dependent upon the NA of the objective and the RI of the sample. Nasdala *et al* (1998) attempted to describe the shape of the analysed volume in a sample during Raman measurements. Their estimations of the 'truncated cone' excited in transparent samples were estimated as 'far above $10^4 \mu\text{m}^3$ '. Nasdala *et al* (1996, 1998) estimated that with the use of confocal optics (in their arrangement a 100 micrometer pinhole placed in the beam path) the excited volume is $\leq 5 \text{ micrometer}^3$. Refraction at the air/crystal interface can be decreased, i.e. the exciting volume tends towards a cylinder rather than a truncated cone, by using a medium other than air between the objective and the sample that has an RI closer to that of the sample. Experiments on polymer laminates (unpublished data) confirms that depth resolution, the ability to discriminate between different layers in this example, is greatly improved with the use of an oil objective and RI matched oil.

The instrument was set up in confocal mode with a 100x objective. The slit was closed to 10 micrometers and the CCD height reduced from 20 pixels to 4. A Si wafer sample was used for preliminary alignment. For the depth profiling of the zircon grain an oil of RI 1.518, supplied by Leica, was used in conjunction with a Leica 100x NPlan OIL objective. The amount of oil used is critical; if too much oil is deposited on the surface it becomes impossible to view the sample. In practice, applying the smallest bead possible is ideal.

Confocal measurements are carried out to maintain the high specificity of Raman experiments. They are, however, rather less efficient; the entrance slit is reduced and the CCD area has a smaller active region. Under typical microRaman collection conditions the inherent volume resolution is generally adequate and the collection efficiency becomes more important

Results and Discussion

A depth profile was recorded of the Si wafer to test the confocality and provide a measure of the depth resolution. The profile consisted of a Raman spectrum recorded at 1 micrometer intervals ± 10 micrometers either side of the focus position using 514 nm excitation. Figure 9.4 shows the results of the Si depth profile. A curve-fitting file was created for the main 520 cm^{-1} Raman band of Si and then applied to the multifile, the collation of the twenty-one spectra comprising the experiment. The software allows maps to be created either from the raw data or from the results of the curve-fitting. Figure 9.5 shows results of the intensity of the Si band from the curve-fit against z-value.

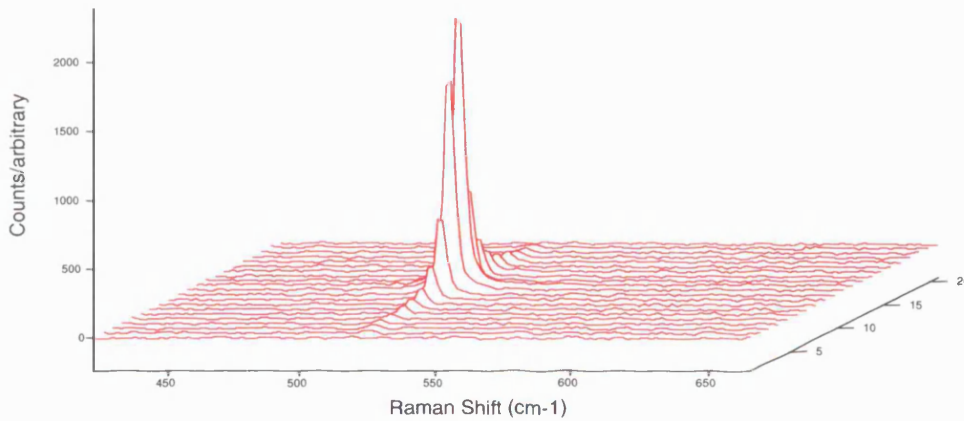


Fig. 9.4. Depth profile of Si.

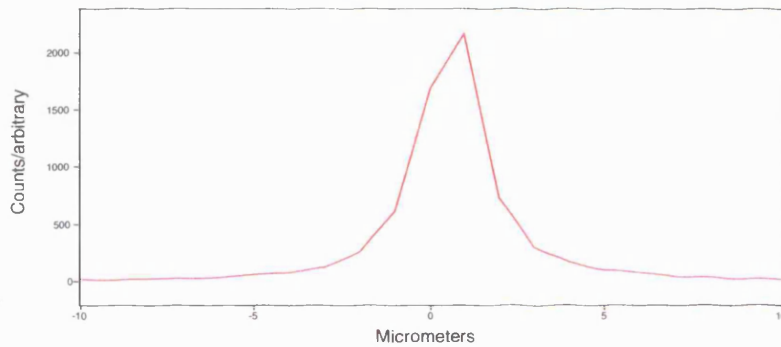


Fig. 9.5. Intensity profile of Si depth map.

A curve-fit was then applied to the intensity profile. Since the Si wafer approaches an infinitely thin layer (Ge is a better sample for this purpose Dr. I.P. Hayward, pers. comm.) then the FWHM of this curve is a measure of the depth resolution. Figure 9.6 is a screen capture of the curve-fit of the intensity profile. The FWHM value is 1.8 micrometers, i.e. the height of the sampling volume in this confocal experiment. With pre- and post-slit lenses optimized, the slit closed further and the CCD height lower, the confocal volume ‘height’ has been measured at one micrometer. However, this results in significantly lower throughput. The value determined was felt to be adequate for this experiment.

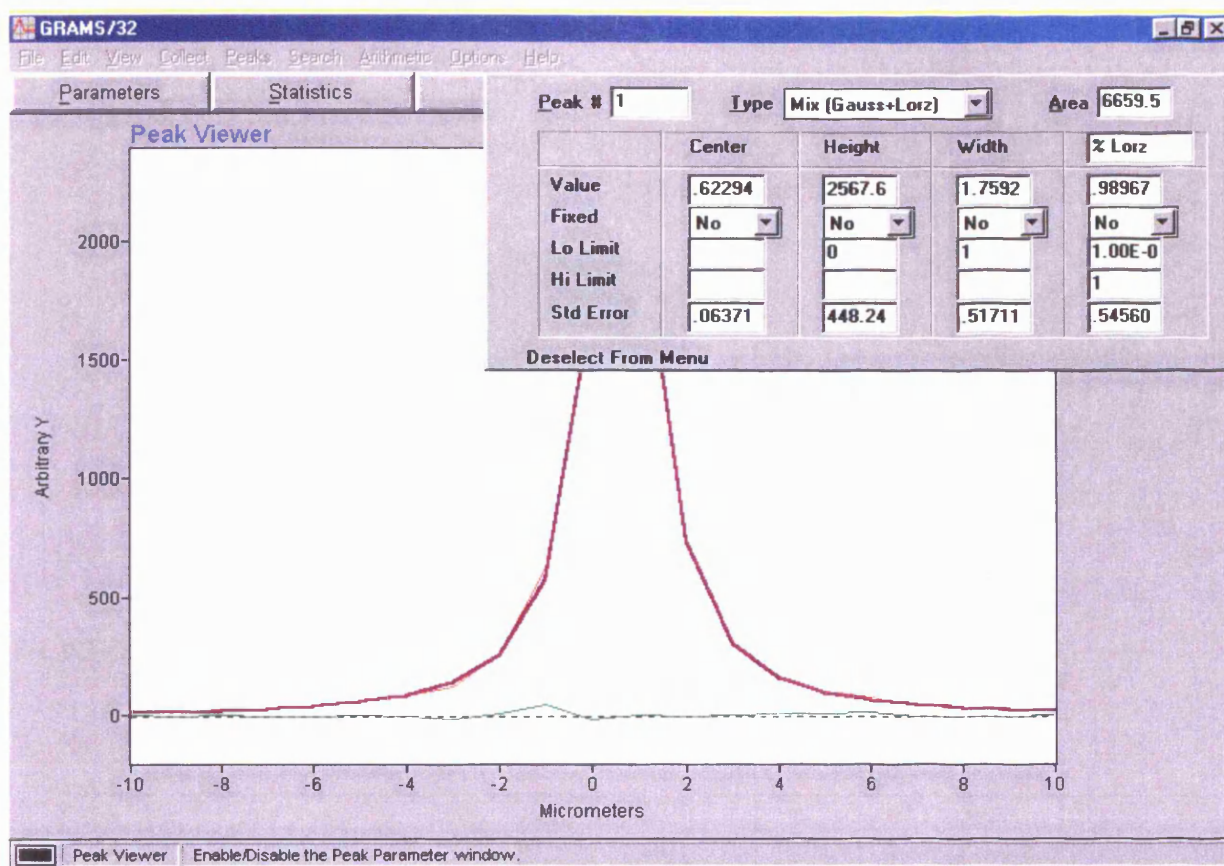


Fig. 9.6. Screen capture showing results of Si intensity profile with depth. Note 'Width' value of 1.7 micrometers.

For the zircon depth profile experiment a step size of two micrometers was selected on the basis of the Si wafer sample confocal performance. Sixteen steps were used to record the Raman spectra from the sample to a depth of 30 micrometers with the axis of analysis passing through the centre of the core and into the overgrowth beneath as indicated by Figure 9.7. A static scan centred at 1000 cm^{-1} was used because the band of interest is the $\nu_3(\text{SiO}_4)$ mode close to this frequency. Acquisition times at each interval were three accumulations of thirty seconds. The confocal arrangement significantly reduces the signal throughput, necessitating relatively long exposures.

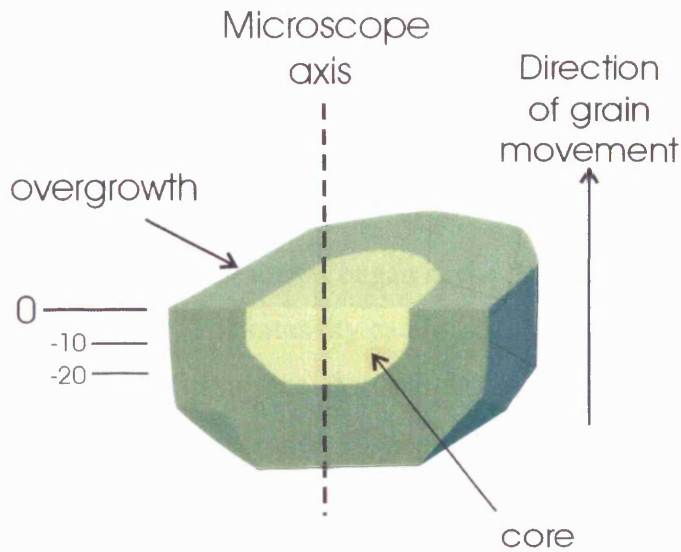


Fig. 9.7. Depth mapping experiment through zircon. Depths shown for illustration only.

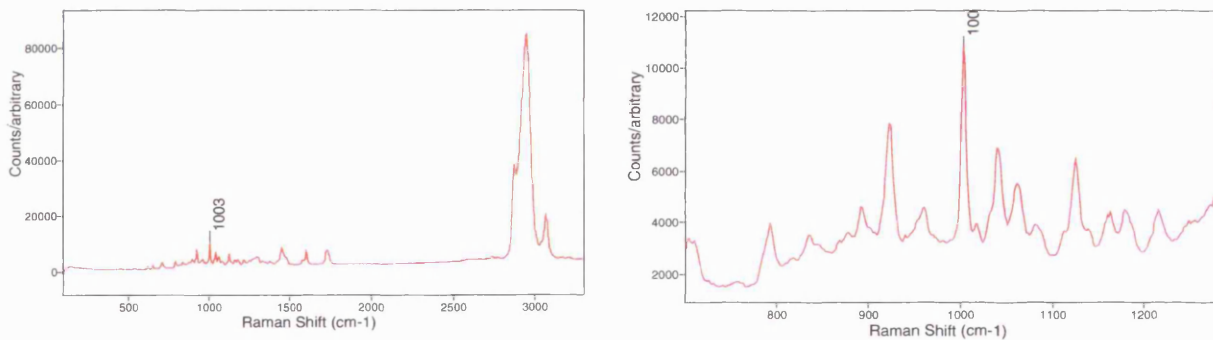


Fig. 9.8. Raman spectrum of immersion oil and expanded portion to show mid-wavenumber range.

The oil used has a strong Raman spectrum dominated by strong bands in the C—H stretching region around 3000 cm^{-1} . The spectrum is reproduced in Figure 9.8. There are many bands in the mid-wavenumber region of the spectrum. The spectra recorded from the zircon depth profile all show bands belonging to the oil. Figure 9.9 shows one of the depth experiment spectra and a reference spectrum from a very well crystallised zircon recorded dry. It is interesting to note the difference in position of the $\text{V}_3(\text{SiO}_4)$ band in the two spectra. The sample grain has a peak position of 999.5 cm^{-1} and the reference crystal a position of 1006 cm^{-1} .

The FWHM values are 8.0 cm^{-1} and 5.3 cm^{-1} , respectively. The trend towards lower wavenumbers with increase in FWHM is well documented (e.g. Wopenka *et al* 1996).

Figure 9.10 shows the depth profile spectra overlaid and offset. For clarity only the 1000 cm^{-1} region is displayed. The experiment began at the deepest position, i.e. 30 micrometer apparent depth below the surface. The intensity can be seen to increase as the focus position moves towards the polished grain surface. A curve-fit file was created for the $\nu_3(\text{SiO}_4)$ band and applied to the multiframe to allow the creation of maps and analysis of the results.

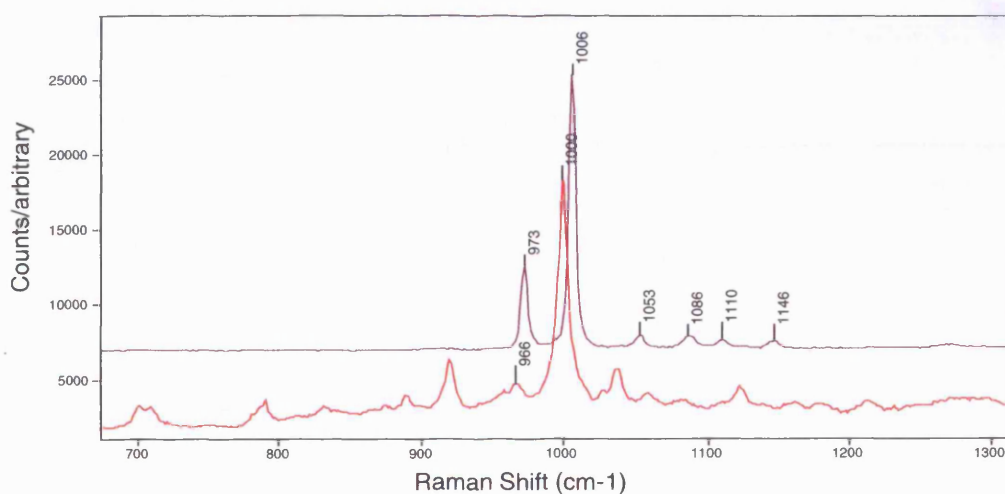


Fig. 9.9. Zircon sample spectrum (lower, red) and reference zircon spectrum (upper, purple). Offset only in intensity for clarity. Note difference in positions of the $\nu_3(\text{SiO}_4)$ mode.

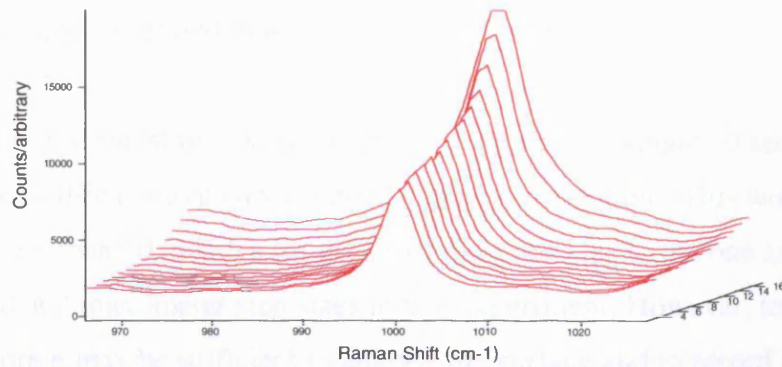


Fig. 9.10. $v_3(\text{SiO}_4)$ band through zircon core. The surface (core) is represented by the 'deepest' trace (no. 16).

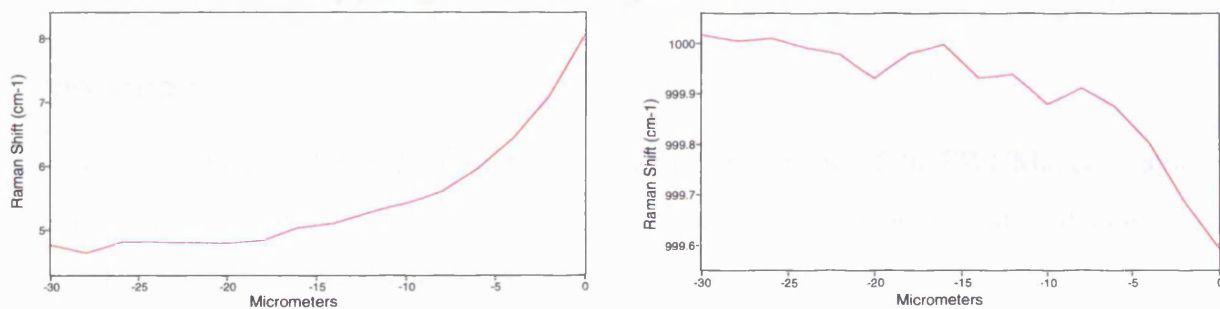


Fig. 9.11. FWHM (left) and position (right) of zircon $v_3(\text{SiO}_4)$ band with depth. 0 micrometers represents surface.

Figure 9.11 are plots of the FWHM and position of the $v_3(\text{SiO}_4)$ band against depth. At the surface, i.e. in the exposed core, the band has a FWHM of around 8 cm^{-1} and sharpens to $<5 \text{ cm}^{-1}$ in the overgrowth. The change in position is negligible; the change is around 0.5 cm^{-1} and may reflect a contribution at the surface of the immersion oil Raman band close to 1000 cm^{-1} .

The results strongly suggest that depth profiling using visible excitation, a highly confocal optical arrangement and immersion oil to reduce RI effects can be used to determine the crystallinity below the surface of zircon grains.

Where whole grains are used for MS analyses the method may help to screen those grains that have metamict cores and thus lead to erroneous ages.

The total experiment time was less than 30 minutes. A single 30 second acquisition per interval should be sufficient to provide a good signal to noise ratio. This would reduce the experiment time to less than 10 minutes for grains of a similar size to the one analysed. Analyses were recorded at 2 micrometer step sizes in this experiment. However, to characterise the crystallinity of the core it may be sufficient to analyse the surface and to record a spectrum at the core. Where it is difficult to measure the thickness of the grain it may be beneficial to analyse in stepped intervals.

9.9 - Line focus mapping of zircon grains

Introduction

Nasdala *et al* (2001b) published an impressive ‘crystallinity map’ of the $\text{FWHM}_{\text{v}_3(\text{SiO}_4)}$ values from a zircon fragment over an area of some 500 micrometers³. The grain had moderately-damaged core region with a metamict outer zone. The data appears to be of high spatial resolution (quoted as 2.5 micrometers with a step size of 2 micrometers) although no indication of image manipulation is provided. Their Raman data correlates very well with images of the fragment recorded using BSE, CL and photomicrography using cross-polarised light to show the birefringence differences. The Raman analysis presented is the result of over 12,000 individual ‘spot’ analyses.

Although clearly desirable, this type of experiment is rarely practical; indeed these authors cite the time required as a major drawback. Metamict zircon is a very poor Raman scatterer and in conjunction with the low laser power densities involved long acquisition times are required. Metamict zircon is a very poor Raman scatterer. Nasdala *et al* (1998) used acquisition times of ‘10 accumulations per 30 seconds’ for well-crystallised zircons and ‘10 accumulations per 900 seconds’ for highly metamict regions. It is unclear whether the total acquisition times were 30 seconds and 900 seconds, respectively, or whether the authors were referring to ten

accumulations each of 30 seconds and 900 seconds, i.e. for total acquisition times of 300 seconds and 90,000 seconds (~ one day), respectively. Regardless, the large disparity in the required acquisitions for crystalline and metamict regions should be noted. In the absence of CL or BSE data the ‘mapped’ data presented by Nasdala *et al* (2001b) provides an excellent guide to the geochronologist for the locations at which to record MS ‘spot’ analyses for concordant data.

Line focus mapping

Point-, or spot-mapping, added a new dimension to microRaman spectroscopy. The ability to determine spatially the distribution of components with different Raman spectra caused a revolution in many surface and interface science applications. Mapping experiments have been covered elsewhere in this study. Point-mapping using a laser spot has become almost routine within the field of microRaman spectroscopy. The shortcoming with mapping is that for large areas or weak Raman scattering species analysis becomes too long to be practical. A reduced spatial resolution is the only method to map in realistic timescales *and* maintain good signal to noise. The matter is compounded in older Raman instruments employing photomultiplier tubes where sensitivity is poor. For example, CCD-equipped instruments can be used to record diamond Raman spectra in seconds that a PM-instrument may require twenty minutes to acquire. Experiments requiring thousands of analyses points only become possible with CCD instruments.

Recently, a technique was developed whereby a line of laser light can be used to acquire Raman data from a sample (see, for example, Wolverson, 1995). Here, it will be referred to as ‘line focus mapping’ (henceforth LFM). Rather than a spot, the line focus attachment, described elsewhere in this study, projects a line of laser light onto the sample. Essentially, the computer software treats a line of laser energy focused at the sample surface as approximately twenty adjacent ‘spots’. Each of these ‘spots’ is capable of recording Raman spectral information in the traditional manner. The area of the sample selected for mapping is automatically split into a whole number of ‘strips’, twenty-one micrometers wide. At each step interval of the automated stage twenty-one Raman spectra are recorded from adjacent spots. At the end of a ‘strip’ the stage moves, either in a raster or bi-directional fashion, to begin the next strip. Figure 9.12 illustrates the principle of LFM. Note the line of laser light used rather than a spot.

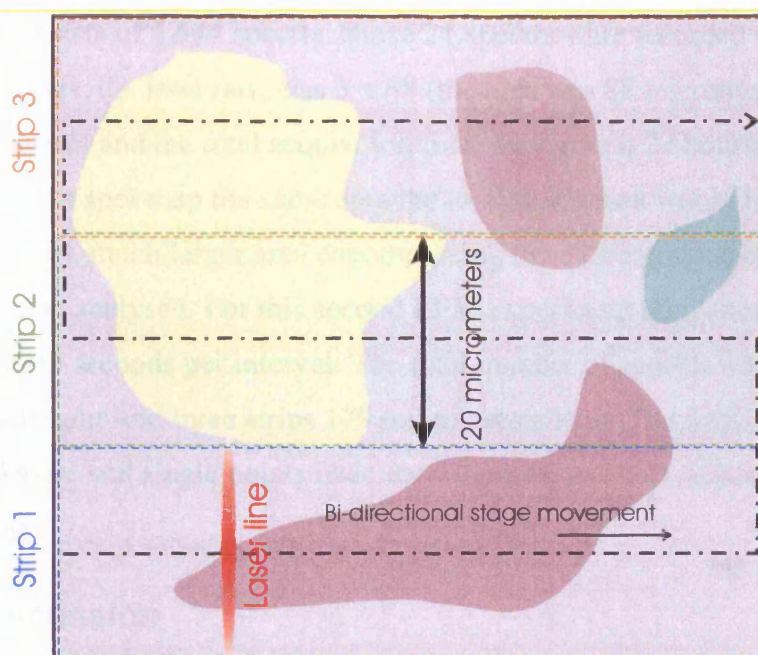


Fig. 9.12. Line focus mapping of large area with four different species.

The advantage of using a line focus for mapping is that some samples can be mapped approximately twenty times faster than a spot whilst retaining the spatial resolution. To account for any unevenness in laser power distribution across the line a correction function is recorded immediately before the mapping experiment is run. A single analysis is recorded from a Si wafer sample and the response is used in calculations by the software. The correction can be applied either during the experiment or at a later date. Simply, the correction multiplies the raw data by an amount that increases towards either end of the line.

Samples

Due to the limited availability of samples, grains from the grain mount used for depth mapping were used for LFM. The cores and outer zones were visibly different and it was thought that this would make correlation between 'white light' images and Raman maps simpler.

Experimental

For the first LFM experiment an area approximately 85 micrometers by 65 micrometers was selected that encompassed a portion of core and outer zone of a single grain. The first experiment used acquisition times of 10 accumulations of 30 seconds at each interval. The area was automatically divided into three strips by the software. A bi-directional scanning pattern was

used. The data set consists of 5,544 spectra. Since 21 spectra were recorded at each interval the total number of analyses, i.e. intervals, was 3×88 (the area was 88 micrometers long and 63 (3 strips of 21 micrometers) and the total acquisition time was around 22 hours. Had the experiment parameters been used to spot map the same area the total time taken would have been in the order of days. A second, much larger area encompassing the entire grain and mounting medium surrounding it was also analysed. For this second LFM experiment the parameters were five accumulations of thirty seconds per interval. The total number of spectra was in excess of 11,200. The area was split into three strips 179 micrometers long. The total experiment time was around 22 hours. Again, had single points been used the total analysis would have been of the order of several days.

Results and Discussion

A curve-fit file for the $\nu_3(\text{SiO}_4)$ band was applied to the data sets to enable maps of the FWHM and position to be created. The line profile correction was not applied to the first experiment but was to the second. The white light image and FWHM_{ν_3} map are displayed in Figure 9.13 for the first experiment and Figure 9.15 for the second LFM experiment.

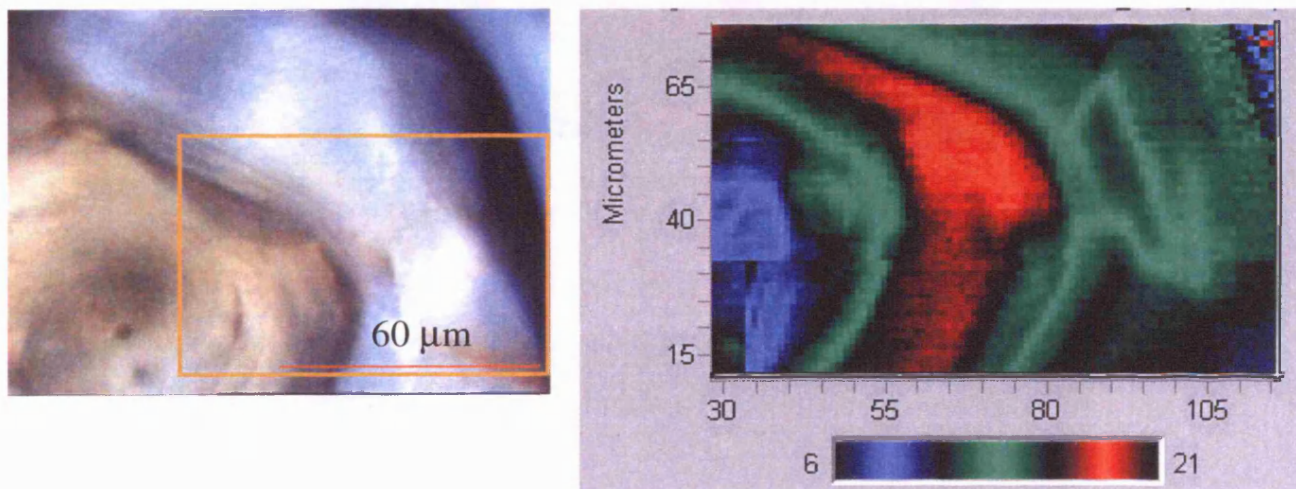


Fig. 9.13. White light image and FWHM map from Raman experiment using line focus attachment. The scale for the FWHM is given in cm^{-1} .

It is clear that although the two images do not exactly match the FWHM image gives a good indication of the degree of crystallinity of different regions. Errors can arise in various ways. There is a slight mismatch between the different strips of data. This has been attributed to the

Microscope Imaging Factor (MIF). This is a value applied to the data to account for the differences between the size of the same image on the video camera and CCD detector. Although a default value is adequate for most purposes, it becomes more critical in LFM applications. Calculating the MIF is not trivial. From Figure 9.13 it appears that the default value is adequate for reconnaissance purposes. In the upper right corner of the FWHM image it appears that the zircon is of good crystallinity. However, analysis of the raw data reveals this area to be epoxy mounting medium and not zircon. By coincidence, the epoxy has a weak spectral feature in the region of the zircon $\nu_3(\text{SiO}_4)$ band. Figure 9.14 shows an intensity map for the zircon ν_3 band in the mapped area (see Figure 9.13). The data clearly indicate of the shape of the grain. The results of the second LFM experiment, covering a much larger area, are shown in Figure 9.14 along with the white light image of the area mapped.

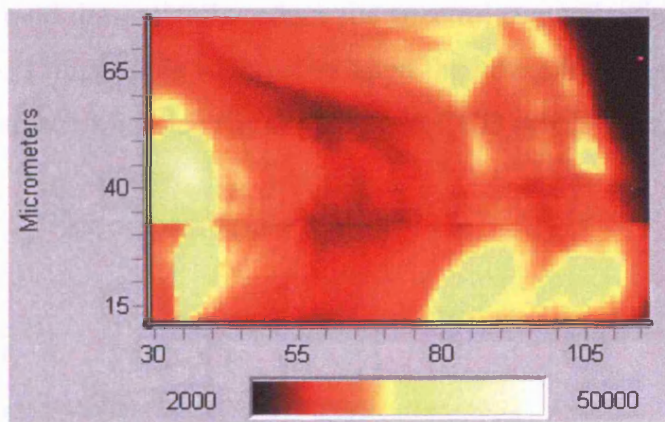


Fig. 9.14. Intensity map of the zircon ν_3 band for the first LFM experiment. Intensity scale in arbitrary units

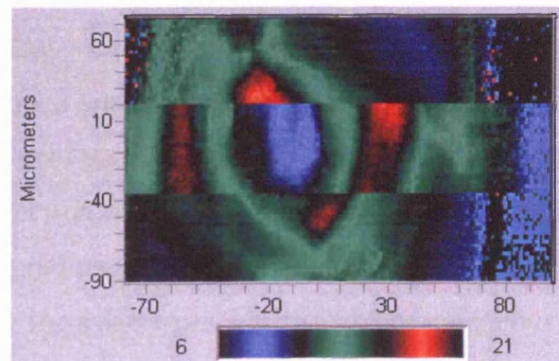
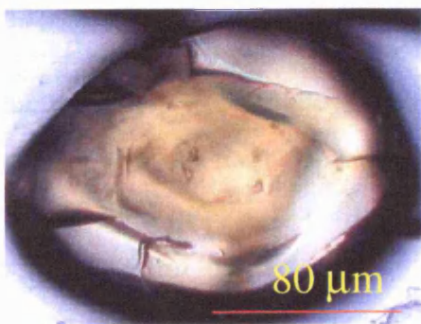


Fig. 9.15. White light image and FWHM map from second Raman experiment using line focus attachment. The scale for the FWHM is given in cm^{-1} .

There is a considerable mismatch between the strips of Raman data. This is attributed largely to the MIF. The disagreement is much larger than that seen in the Raman data of Figure 9.13. The main difference between the experiments is the application of correction function to the second map. Better precision may have been provided by not using the correction function. However, the data within the strips appears to have good precision and in good agreement with the data in Figure 9.13.

Other errors may arise if the grains in the grain mount are ‘domed’ in profile. Although nominally flat and adequate for petrographic analyses the surface profile is critical for MicroRaman mapping applications. Figure 9.16 shows how the beveled grain profile that can arise through polishing may cause epoxy to be analysed at the same analysis point as zircon. A confocal arrangement would dramatically reduce the spectral contamination. However, given the requirements for LFM it is impossible to improve upon the inherent confocality of the standard arrangement of 50 micrometer entrance slit and 20 pixel CCD detector height.



Fig. 9.16. Indication of the importance of truly flat zircon surface.

The initial, uncorrected, line focus map gave a very good indication of the regions of the mapped area that were of high crystallinity and that would be suitable for subsequent quantitative ‘spot’ analyses. The second map, covering a much larger area highlights the importance of setting the correct MIF for the MicroRaman instrument used. Similarly, the use of a robust correction file should be explored. In the example correction file used for the second LFM experiment the data recorded from the Si wafer had a low signal to noise ration. Instead of using a Si wafer it might prove prudent to use a correction profile recorded from a polished, homogeneous, crystalline zircon grain. This would account for the large differences in Raman scattering potential between the two substances. Careful setting of the limits (position, FWHM and intensity) used to generate

the curve-fit file would help to reduce the impact of epoxy mounting medium in the data set. Despite the poor matching of strips of line focus data the data within the strips appears good. The method has been shown to dramatically reduce the time required to produce crystallinity maps of zircon grains.

9.10 - Analysis of laser ablation ejecta

Introduction

The concordant analysis of crystalline zircon is achieved through the accurate measurement of the isotopic ratios of U and radiogenic Pb. The importance of selecting grains, or regions of grains, that have not experienced Pb loss was discussed previously.

Considering the extremely high power densities incident on samples during analysis by ion probe or laser ablation it was deemed possible that some chemical differentiation may occur upon excavation. If chemical differentiation were to occur then it is likely that the U/Pb ratio for that analysis would not be accurate. This prompted the question 'Does the analysis of zircon by ablation technique inherently produce inaccurate data?' In the inaugural investigation of Raman peak half-widths and degree of metamictisation Nasdala *et al* (1995) discovered from BSE and CL images that the EMPA beam had induced damage. Circles some ten micrometers in diameter with a central crater had been produced on the zircon surface. Similarly, Nasdala *et al* (1998) found alterations to zircons studied by the SHRIMP ion probe. Raman analysis of the zircon at the base of the pit was inconclusive. Some 'spots' appeared to be more crystalline, indicated by marginally sharper $\text{FWHM}_{\text{V}_3(\text{SiO}_4)}$ values. However, this result is counter-intuitive since the effect would be expected to be greater in the more metamict samples, yet no correlation was found.

A significant proportion of their Raman analyses from the base of the pits returned no Raman peaks whatsoever. The authors failed to adequately explain this. 'Raman background' swamping the Raman peaks was suggested as a possible cause. The 'slag flow-like' pit surface noted from their SEM investigations was attributed to either an amorphous zirconium silicate or a layer of the component oxides. The lack of data to support this was ascribed to the layer being too thin to analyse by the Raman microprobe. They concluded that ion probe studies are unlikely to cause

significant damage to the zircon but if Raman spectroscopy was to be used in addition to ion probe, the Raman analysis should be done first. Wopenka *et al* (1996) had obviously considered this in their study of lunar zircon using a troika of microprobe techniques. Raman microscopy was the first technique used in their study to preclude any damage by the ion probe.

Samples

A resin block comprising a small suite of polished zircons, some of which had been subjected to ablation techniques was supplied. Figure 9.17 is reflected white light image of a zircon from the block that has four ablation pits. Some ablation tracks and pits had discrete ejecta deposited on their margins. Optical microscopy at high magnification of the rims of the excavated pits and tracks revealed a slight topography estimated to be close to five micrometers above the 'base level' of the polished surface. The tracks themselves were generally around ten micrometers deep.

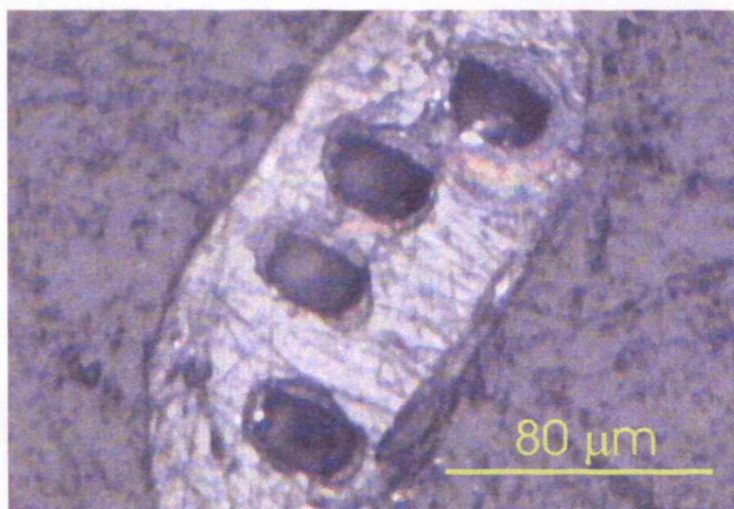


Fig. 9.17. Image of crystalline zircon with four ablation pits.

Experimental

Confocal Raman microscopy using 514 nm excitation was used to study the material in the ablated regions, the ejecta and the surrounding, undamaged crystal. As Nasdala *et al* (1998) found, it was often not possible to obtain good Raman spectra from the base of the tracks. Mapping experiments were conducted over regions of a zircon grain that comprised of unablated crystalline material and ablated track.

Results and Discussion

A curve-fitting routine was applied to the multifile data sets. Figure 9.18 compares the upper and lower values calculated for $\text{FWHM}_{\text{v}_3(\text{SiO}_4)}$ from one set of mapping data. There is considerable variation in the FWHM value of the band; between 4.1 cm^{-1} and 7.2 cm^{-1} . Maps were constructed from curve-fit results. A map of the $\text{FWHM}_{\text{v}_3(\text{SiO}_4)}$ in Figure 9.19 clearly shows that the band is slightly broader in and around the edges of the ablated track. The map indicates material with broader FWHM around the area where the ablation track changes direction. This might suggest that the laser energy is concentrated here slightly longer than along the straight paths of the track.

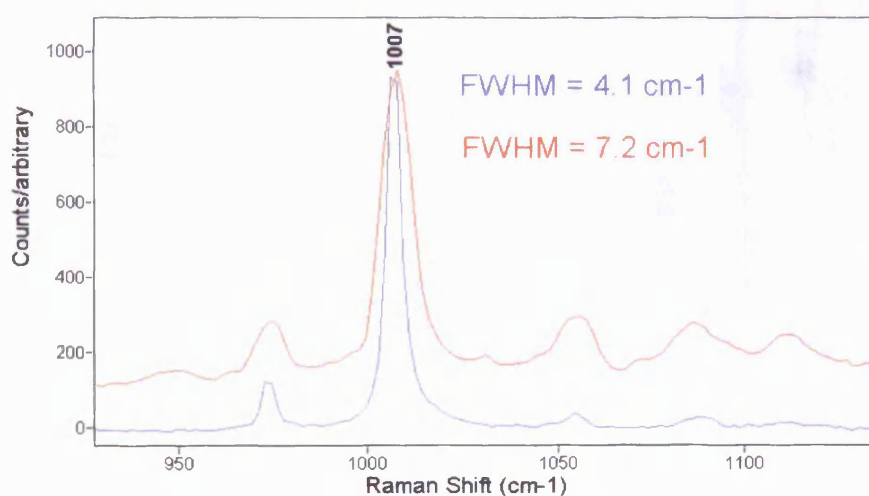


Fig. 9.18. Variation in FWHM for $\text{v}_3(\text{SiO}_4)$ in ablated zircon.

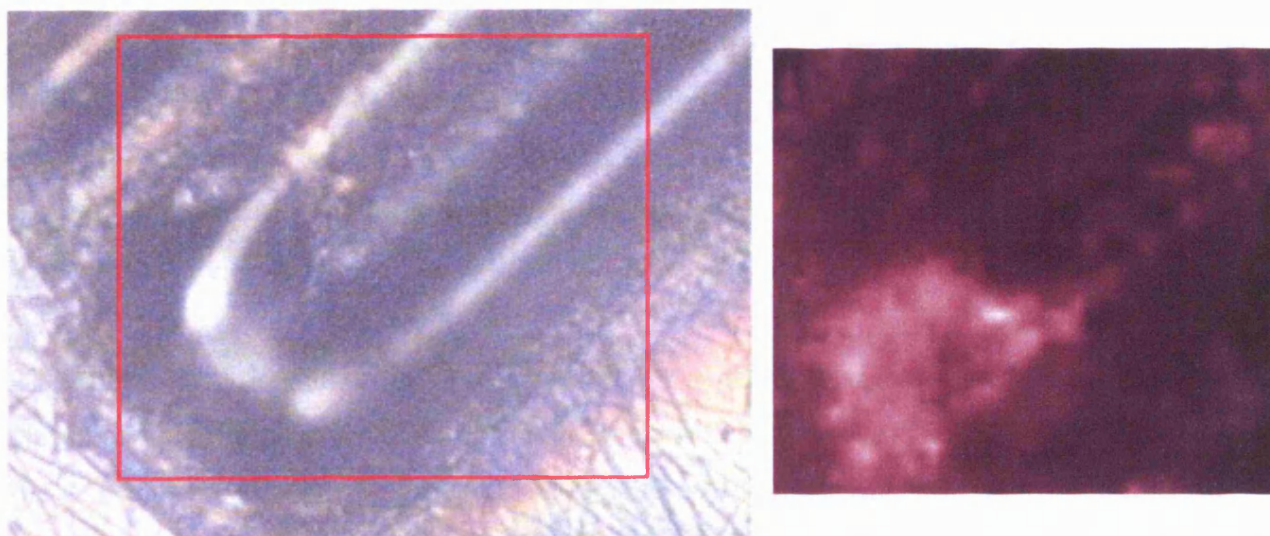


Fig. 9.19. Mapped area of ablated zircon and map of the FWHM of $\text{v}_3(\text{SiO}_4)$ (light areas have larger FWHM value).

Analysis of the data from mapping experiments yielded rare occurrences of spectra that indicated that the structure was being modified in some way other than a broadening of the ν_3 band. Figure 9.20 shows a comparison of a spectrum of crystalline zircon from an undamaged region with a spectrum from the same sample that has many additional bands. The bands that are not assigned to zircon are indicated. It has not been possible to ascribe these Raman bands to a compound or to locate the position on the sample at which they occurred, due to software problems.

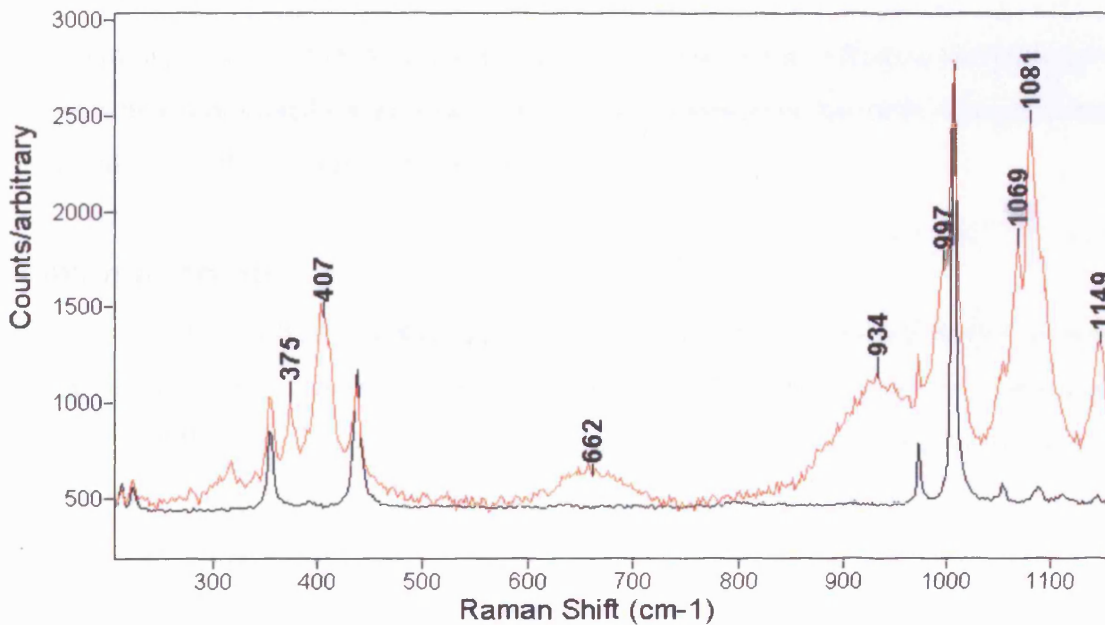


Fig. 9.20. Comparison of Raman spectra from regions within ablated sample. Crystalline sample in black, additional bands in red spectrum are unattributed to zircon.

The positions of the main bands of the polymorphs of zirconia are given by Lopez *et al* (2001). The non-zircon bands shown in Figure 9.20 do not correspond to any of the polymorphs or to any of the polymorphs of silica (Kingma *et al* 1994) or to that of baddelyite, the naturally-occurring mineral form of ZrO_2 . It would be of interest to repeat this mapping experiment to locate the region(s) that gave rise to these additional bands.

The Raman spectra from the mapping experiments appear to disagree with those found by Nasdala *et al* (1998) from studies of zircons analysed by ion probe. The differences observed in the values of FWHM_{ν_3} are significant; the band almost doubles in width. However, under the classification of Nasdala *et al* (1998), the material is still well crystallised and therefore probably not at risk of Pb loss. It would be of interest to produce maps of the ratios of the intensities of the

major Raman bands for a zircon with an ablated region. This may give a better indication of any change in composition as well as structure. Unfortunately, the data recorded in the mapping experiments described are of too low signal to noise ratio. A combined approach of microRaman spectroscopy and SEM may further add to understanding the processes occurring ablation.

9.11 - Conclusions

Different approaches have been used in an assessment of microRaman spectroscopy in the analysis of zircons used for geochronology. Each application has been discussed but it is pertinent to conclude each analysis here.

Raman imaging

The experiments with global Raman imaging were quite successful. It does take some time to set the experiment up and there is a need to use flat, polished grains. However, samples that would be used for MS analyses would be in this form. The data show that whole grains can be imaged in less than one minute using the 10x objective to reveal that regions of lower crystallinity can be defined.

Depth profiling

The experiments with depth profiling zircons with visible cores appeared to work quite well. However, the sample used was not ideal since there was little difference between FWHM of core and overgrowth. It would be advantageous to perform a 'spot' line map from core to rim to check the accuracy of the results. The data do indicate that changes in the crystallinity can be detected by mapping through the grain section in the vertical axis. The next stage in this analysis would be to perform depth mapping on an unpolished grain held in a temporary mount. Analysis of zircons by ICP and other whole grain digestion techniques require samples in this form.

Line focus mapping

The use of this technique offers a much faster means of analysing large areas of polished zircons than by spot mapping. The time advantage can be up to twenty, but due to considerations of laser power it is probably lower than this. The technique could become routine in the selection of

regions of grains used for MS analysis using points rather than whole grains. The approach is more practical than using BSE or CL methods. The process of correcting the data needs to be investigated method could be improved. A method based on principal component analysis may be more applicable (Dr. K.P.J. Williams). The experiments may benefit from using samples with truly flat grain profiles. The use of the autofocus function should be investigated. Furthermore, the microscope image factor (MIF) has been identified as of critical importance in LFM experiments where accurate spatial information is required (T. Smith, pers. comm.). A simple procedure for determining the correct value may result in more accurate data being collected and may negate the need for post-processing.

Analysis of ablated grain

Whilst the analyses detailed in sections 9.7, 9.8 and 9.9 were concerned with the detection of suitable grains or regions within grains, the experiments on ablated samples were of interest in analysing the zircon *after* MS analyses had been performed by LA-ICP-MS. The results were inconclusive but appeared to indicate that locally the zircon structure is modified by the aggressive analysis. Further work is needed, perhaps using a combination of optical and quantitative compositional techniques.

MicroRaman spectroscopy has been used in a limited number of investigations, principally by Lutz Nasdala, for investigating the structural changes that occur in zircons as a result of metamictisation. The current work describes the only known application of global Raman imaging, depth mapping and line focus mapping to zircon samples to describe how the methods could be used for the selection of grains and regions within grains for further mass spectrometry experiments.

Chapter 4 – Processes and transformations affecting natural materials

This chapter comprises sections 10, 11, 12 and 13 of the current work. Samples are predominantly taken from those that have an industrial application and that are affected by processes and transformations that are of interest.

Studies of α -quartz, marble dimension stone, clay bricks and limestone rich in organic matter are used to demonstrate the effectiveness of the microRaman technique by performing analyses not available using existing routine methods.

The focus is in the detection and identification of particles and of strain on a micrometer scale and the use of Raman imaging.

10 – Investigation of strained silica

The aim of this investigation, the first application of the technique to investigate processes and transformations that arise in natural materials with an industrial application, is to attempt to add further to the phenomenon of alkali silica reaction in concretes. MicroRaman spectroscopy offers a non-destructive *in situ* technique for sensitively analysing the structure in minerals in thin section. A method that could rapidly and simply quantify strain in silica, a principal requirement for the development of some alkali silica reactions, would be advantageous. The ability to screen out those aggregates containing silica exhibiting excessive strain might reduce the number of cases of alkali silica reaction.

10.1 – Introduction

Considerable analytical work has been applied to the Alkali Silica Reaction (ASR) in concrete bodies. This work has been concerned with the identification and possible means of preventing it. Concrete structures, for example, bridges and buildings could be liable to critical failure should ASR develop. The reaction was recorded in the late 1930's by Stanton (Smith, 1997). Its development leads to a breakdown in the strength of the concrete body and provides a route for other deleterious effects such as freeze-thaw damage, chloride attack and the corrosion of reinforcing agents (Smith, 1997).

The ASR reaction

The reaction is one between the aggregate particles, particularly silica but also carbonates and silicates, and the pore water in hydrating cement. The weak acid nature of disordered silica leads to an acid-alkali reaction with the pore fluids to form a hydrous silicate. OH ions are drawn into the silica and weaken the Si—O bonds. Water is attracted to the metal cations present in the concrete that are diffused to maintain electrical neutrality. The resulting alkali-metal ion hydrous silicate swells with water, exerting increased pressure on the surrounding concrete body (Smith, 1997).

Reactive silica

Silica grains displaying undulose or complex extinction contain greater dislocation densities and therefore more stored internal energy. They also possess greater surface area than silica grains with normal extinction. Small grains also have large surface areas and this is thought to be a key component in the formation of ASR since a greater reactive area is available. It is noted that other forms of naturally occurring disordered silica, for example, opal can also bring about ASR development in concrete. However, their identification by Raman spectroscopy, or simple petrography, is straightforward.

Historically strained quartz was thought to indicate a metamorphic origin of the rock. The presence of strained quartz is now known to be a very common feature of quartz-bearing rocks. Smith (1997) describes the various classification schemes based on the angle of undulosity exhibited by the strained quartz grains. He concludes that the only method of accurately measuring the angle is by the use of the universal stage. However, the method of measurement is not trivial by this technique and requires careful preparation of the sample.

Under the petrographic microscope strained quartz can be readily recognised by the sweeping motion of a zone of extinction across the grain as the stage is rotated. Undulose extinction can also be recognised as discrete zones of varying orientations within a crystal. These regions consequently extinguish at different degrees of stage rotation. Undulose extinction is a visual representation of the response of the quartz grain to the application of a differential stress system. The permanent strain is the result of ductile deformation carried out at relatively high temperatures at low strain rates over long periods and at relatively high hydrostatic pressure (Smith, 1997).

Samples

ASR development in concrete is associated with different forms of quartz. In this respect it is also the most studied reactive species. However, other reactions are also recognised. These are ACR, Alkali Carbonate Reaction, and the Alkali Silicate Reaction.

Samples of quartz-, carbonate-, and silicate-bearing aggregates were obtained from UK resources. Samples of granite have been collected from Cornwall (Bodmin Granite from the Luxulyan and Hantergantick quarries) and Carboniferous Limestone from Cauldon Lowe, Derbyshire. To try and minimise any complicating effects due to weathering the youngest samples have been obtained where possible. No samples have been collected for aggregate with a major single silicate phase.

10.2 – Stress measurement using Raman spectroscopy

Vlasov *et al* (1997) used confocal microRaman spectroscopy to study intrinsic stress variations in single crystals of CVD, chemical vapour deposited diamond, used as high quality thin film. They used the polarisation optical accessory components to show that the asymmetric line-broadening of the first-order optical phonon peak at 1332.5 cm^{-1} was due to splitting of this triply degenerate mode. The two components, separated by $\Delta\Omega$, are linearly dependent on stress. Their figure 2 is reproduced here as figure 10.1 that clearly displays the difference in polarisation of the scattered light.

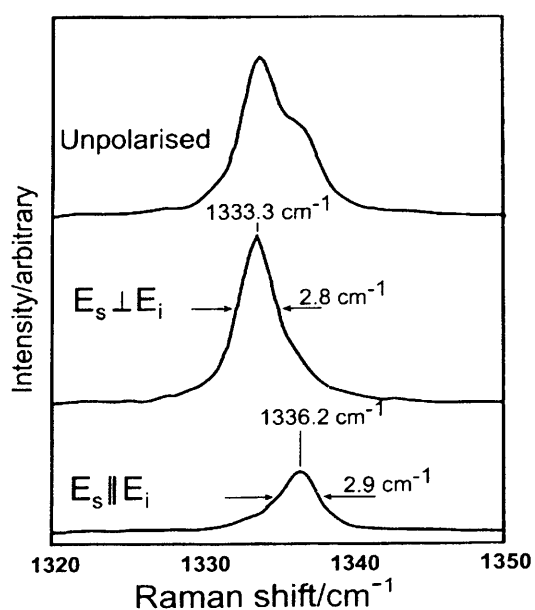


Fig. 10.1. Unpolarised and polarised Raman spectra of stressed CVD diamond. From Vlasov *et al* (1997).

Grimsditch, Anastassakis and Cardona (in Vlasov *et al*, 1997) determined that compressive stress systems in diamond induce a Raman band shift to higher wavenumbers and tensile systems a

shift to lower wavenumbers. Anisotropic stress measurements of up to 9 GPa (compressive and tensile) were calculated based on the magnitude of $\Delta\Omega$ for certain oriented crystallites measuring 100 micrometers to 200 micrometers. Mukaida *et al* (1987) reported on the stress induced in epitaxial layers of the 3C SiC polymorph deposited on a Si substrate. Difference in the coefficients of thermal expansion and lattice constants of the two materials causes the stress in the SiC crystals. Using the shifts in the peak positions of the longitudinal optical phonon mode of SiC grown by different methods they were able to calculate values of tensile stress. Similarly, Cai *et al* (1993) were able to relate shifts in the position of the F_{2g} band, relative to a Ne calibration source, to induced stress in yttria-stabilised zirconia. Bowden *et al* (1993) used the mapping facilities of modern microRaman instruments to reveal concentrations of stress-induced phase transformations in MgO-stabilised zirconia ceramic. These and other studies highlight the importance of grain boundaries in the distribution of stress. They can provide routes for stress relief and act as boundaries, limiting the effects of stress on the system.

It has been shown that Raman spectroscopy is an excellent technique for the analysis of stress in synthetic crystal systems. Studies on natural crystals are less well known. One such study relates to the stress field created within a diamond crystal around an olivine inclusion and, again, makes use of the shift in position (actually a splitting) of the first order optical phonon (Navan *et al* 2000). The advantage of using Raman spectroscopy over techniques such as XRD is that the high spatial resolution allows individual grains to be analysed, revealing spatial inhomogeneities and not an average result. The use of an encoded microscope stage for microRaman spectroscopic examination allows the accurate positioning of the sample with respect to the incident laser beam and for XY (and Z) mapping. Confocality, achieved either by mechanical or virtual pinhole methods, ensures that a tightly constrained sampling volume is analysed and any signal from outside this volume is discarded. The mathematical computations required for fitting functions to the Raman peaks allow precise determinations of the stress causing lattice disorder.

10.3 – Vibrational spectroscopy of quartz

Quartz was the focus of many Raman studies during the 1960's. It remains as probably the most widely studied mineral in this regard. This work is summarised by Wilkinson (1973) and

includes details of the polarisation assignments of the modes as well as the pressure and temperature dependence of the bands and the transformation between α and β quartz.

Kingma & Hemley (1994) provide a useful review of the vibrational motions that give rise to the silica polymorph Raman bands. Although rather generalised, these are tabulated in Table 10.2. Figure 10.2 displays an α -quartz Raman spectrum with the strongest A_1 and E mode frequencies indicated. The strongest band corresponds to the symmetric motion of the bridging oxygen along a line bisecting the Si—O—Si bond. The frequency of this vibration is sensitive to the Si—O bond length and bond angle (Sharma, 1981).

Band position/cm ⁻¹	Vibration	Mode symmetry	
129	Si—O—Si bending and twisting	$E_{(LO+TO)}$	
207		A_1	
265		$E_{(LO+TO)}$	
357	Torsional vibrations and O—Si—O bending modes	A_1	
402		$E_{(LO)}$	
465	Symmetric stretching-bending modes of O in Si—O—Si	A_1	
510	O—Si—O bending modes	$E_{(LO)}$	
696	Si—O stretching	$E_{(LO+TO)}$	
795		$E_{(TO)}$	
809		$E_{(LO)}$	
1083		A_1	
1160			$E_{(LO+TO)}$

Table 10.1. Summary of the vibrational modes of α -quartz.

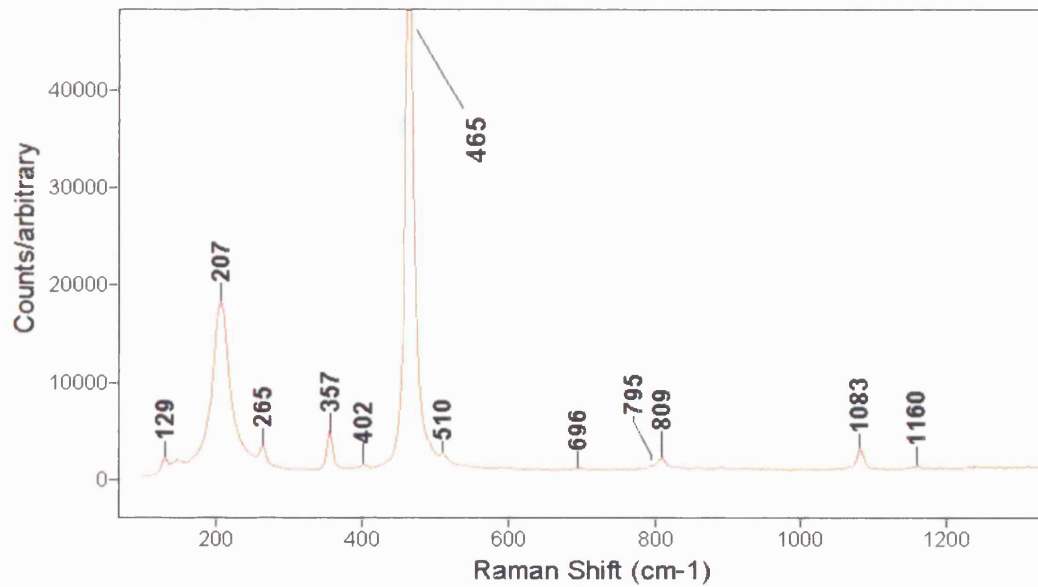


Fig. 10.2. α -quartz Raman spectrum.

10.4 – Experimental procedure

MicroRaman spectroscopy was carried out on quartz grains in the granite sample. Silica is by far the biggest contributor to the development of deleterious alkali reactions.

Uncovered petrographic thin sections of the Bodmin Granite were used for examination. This enabled the selection of suitable grains using a petrographic microscope and permitted microRaman spectroscopy without the interference of an additional glass layer and mounting medium present in covered thin sections. Suitable strained quartz grains were identified then marked on the reverse of the section to enable them to be recalled later.

For the Raman experiments visible excitation at 514 nm with a 2400 groove per mm grating was used. With this excitation crystalline quartz generally gives a fluorescence-free Raman spectrum (see Fig. 10.2) and the spectrograph arrangement provides a spectral resolution of around 1 cm^{-1} per pixel (e.g. Noons *et al* 2002). This factor is important since it might be expected that any differences in the spectra, i.e. FWHM or position, from strained crystals might be of this order or less.

After some preliminary, inconclusive single-point microRaman measurements of undulose quartz (M. Bloomfield, 1st year report) a line map across a relatively large quartz grain, shown in Figure 10.3, displaying undulose extinction was performed. The automated line map, consisting of 551 points at one-micrometer intervals was recorded. The points of the map lay along a straight line through the grain that was approximately perpendicular to the ‘band’ of extinction. The Renishaw RM instrument has a diffraction-limited spot approximately one micrometer in diameter with the x50 objective (for the simple equation see, for example, Baldwin *et al* 2001) thus essentially defining the spatial resolution of the instrument. The mapping stage has minimum step intervals of 0.1 micrometers in both X and Y.

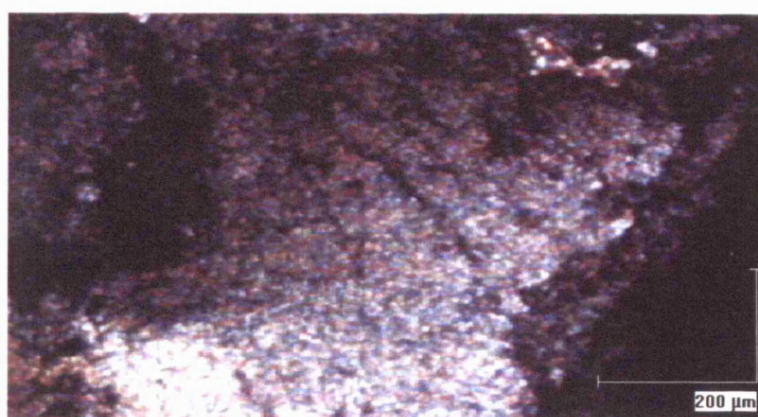


Fig. 10.3. Quartz grain showing undulose extinction. Upper part of the grain is passing into extinction.

Single acquisitions of thirty seconds per point provided adequate signal to noise. The grating was positioned such that efficient, static scans were recorded over the range 150 cm^{-1} to 830 cm^{-1} . From Figure 10.2 this spectral region covers the majority of the strongest quartz Raman bands. The data from the mapping experiment is stored as a multifile; the spectrum at each point along the line is saved. This facilitates the interrogation and manipulation of the dataset and permits the creation of ‘maps’ from the data. Curve fit routines were applied to the main Raman bands at 207 cm^{-1} and 465 cm^{-1} . These bands show the greatest frequency dependence on pressure and temperature (Wilkinson, 1973). Table 10.2 is reproduced from Wilkinson (*op. cit.*) and provides the empirical values of the frequency dependence. Figure 10.4 shows the curve-fit components that best match the data from the line mapping experiment.

Raman band frequency	128 cm ⁻¹	207 cm ⁻¹	265 cm ⁻¹	464 cm ⁻¹	697 cm ⁻¹	795 cm ⁻¹	807 cm ⁻¹
$dv/dP / \text{cm}^{-1} \text{ kbar}^{-1}$	0.6	1.8	0.5	0.9	0.8	0.8	0.8

Table 10.2. Pressure dependence of quartz Raman bands. Frequencies of other significant bands are almost independent of P (from Wilkinson **In**: Anderson, 1973).

Figure 10.4 reveals the very minor contribution to both band systems from weak shoulder bands. Fitting these bands is important to maintain high correlation values for the main band of interest. Also, as the shoulder bands have been fitted to the same extent as the main band in each system, they too can be studied in terms of their frequency, for example. This may provide further information a concerning the response of the crystal to strain.

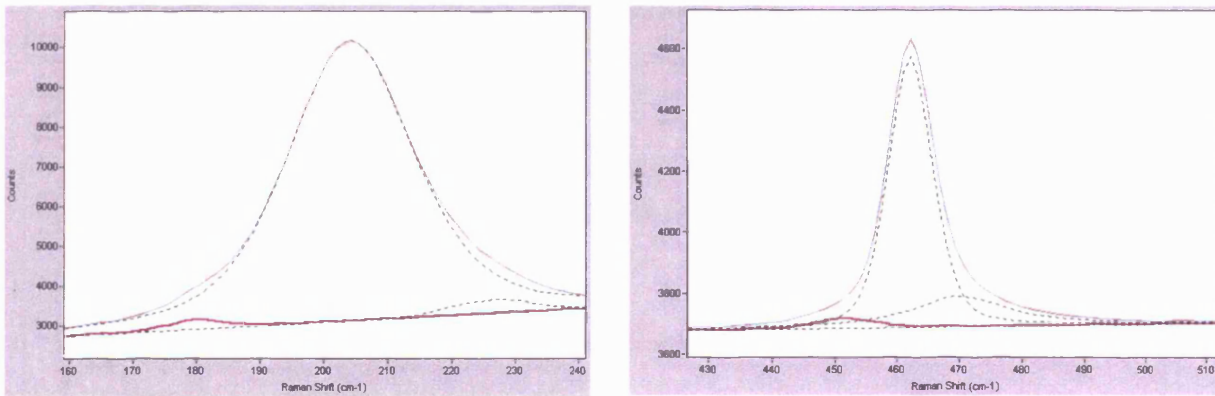


Fig. 10.4. Individual curves fitted to the complex band shapes of the A₁ modes at ~207 cm⁻¹ and ~464 cm⁻¹.

10.5 – Results

Only band positions were considered to be potentially affected by strain acting on the crystal. The measured parameters from the fit of intensity, FWHM and percentage contribution from the Lorentzian function were not regarded. Figure 10.5A displays the position of the 207 cm⁻¹ band of the quartz Raman spectrum along the line of the map. In Figure 10.5B the position of the three components of the 465 cm⁻¹ band are similarly shown along the length of the line. The main band has weak shoulders at ~456 cm⁻¹ and at ~472 cm⁻¹. Linear trendlines for each band are shown.

The sharp ‘spikes’ in the data of Figs 10.5 correspond with positions along the line where the analysis was contaminated by the excitation of small impurities; possibly feldspar or mica. At these positions along the line, superimposed on the quartz spectrum were additional bands

around 790 cm^{-1} . Weak features from the impurity species affected the curve-fitting of the bands of interest. This could possibly have been overcome by setting limits on the curve-fit parameters.

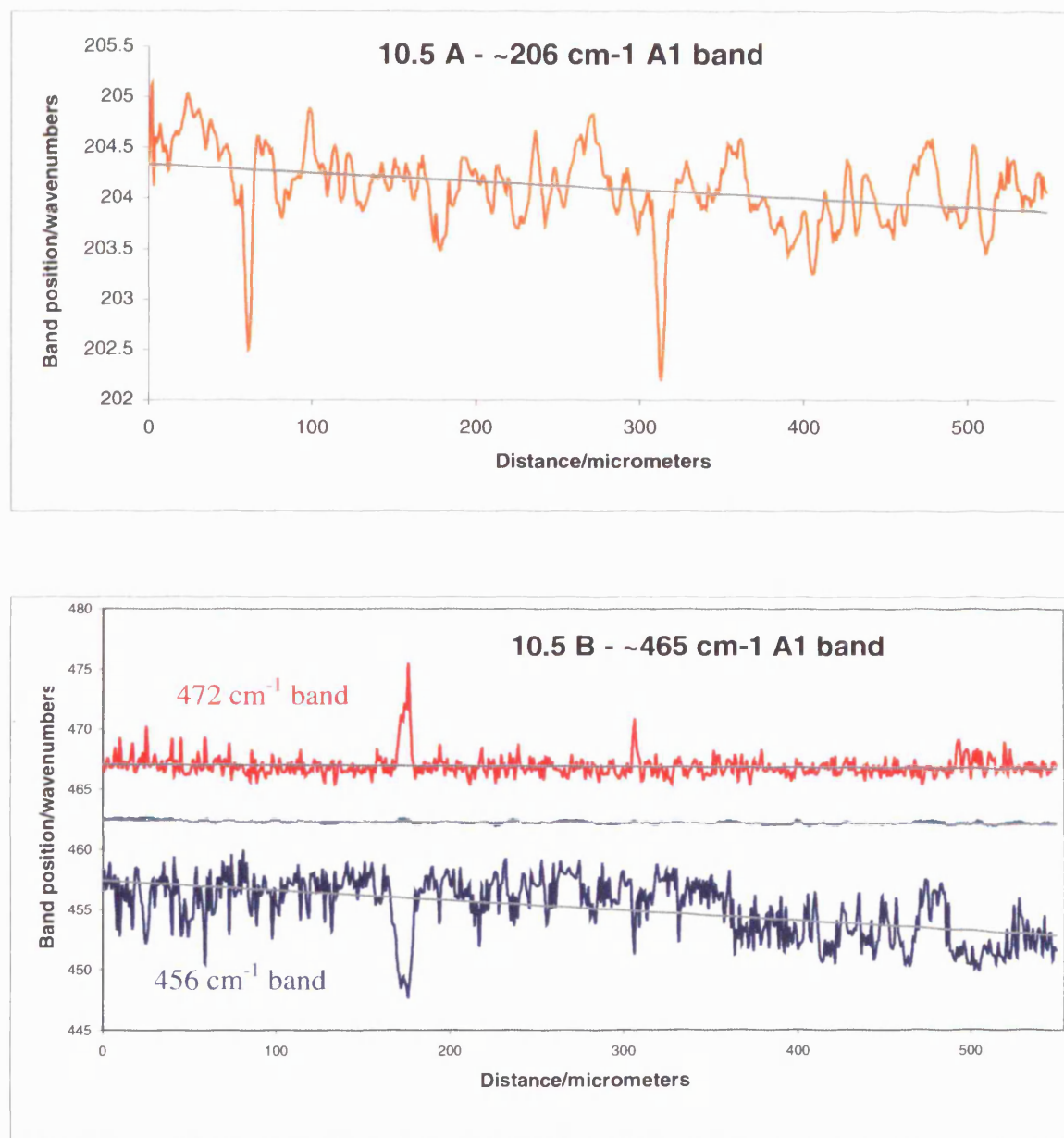


Fig. 10.5. Frequency positions of pressure and temperature dependent quartz Raman bands.

Closer inspection of the change in the intensity of the 207 cm^{-1} band reveals that the mapping technique may provide a way method of determining the crystallite size. A portion of the line map data is recast as a 3D projection in Figure 10.6. The intensity of this band fluctuates and may correspond to changes in the orientation of the crystallites. If each crystallite is considered

to lie only within a single orientation, then the size of the crystallites could be measured from this change.

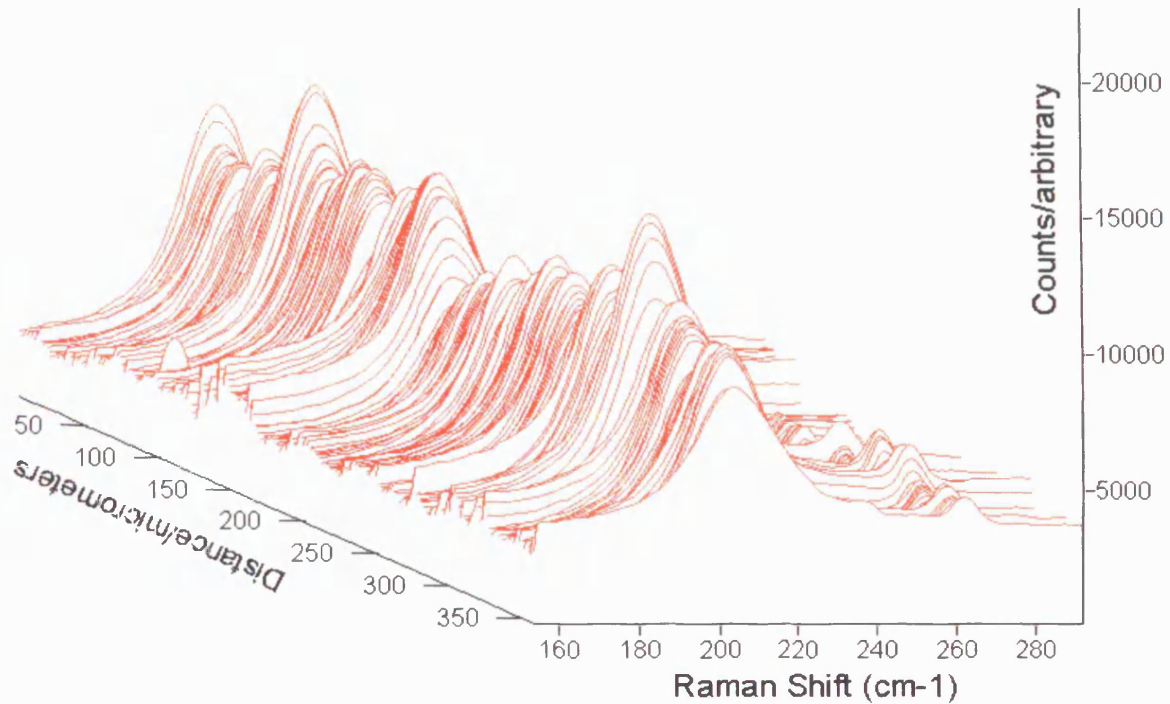


Fig. 10.6. Selected region of the quartz Raman line map experiment highlighting the change in intensity of the 207 cm^{-1} band.

10.6 – Discussion

Figure 10.5 reveals a very slight change in the position of the 207 cm^{-1} band over the length of the line. The trendline indicates a gradual lowering of the frequency of the band of around 0.5 cm^{-1} . Even with the spurious spikes ‘averaged out’ the trend is the same. The other A_1 band considered, at 465 cm^{-1} , varies less, as might be expected from Table 10.2. The change in frequency over the grain is only 0.3 cm^{-1} . A rather larger change in band frequency is expressed by the shoulder band at $\sim 456\text{ cm}^{-1}$. A total frequency change of some 4.5 cm^{-1} appears to have occurred. However, for the first 350 or so analyses, the band position is essentially unchanged. A step appears in the data around this point and the frequency of the centre of the band is lower for the remaining analyses. The origin of this shoulder is unknown and is not mentioned in the literature studied.

The small changes in the main A_1 bands at 207 cm^{-1} and 465 cm^{-1} could be attributed to residual strain in the crystallites as a response to deformation. However, the effect of sample heating should be considered as this factor could also account for the observed small shift. This effect is generally considered to be negligible in the microRaman analyses of minerals. A simple test might be to repeat the analysis. With the same grain used, and in the same orientation, the map should be re-run in the opposite direction. A small positive trend would indicate that sample heating has not occurred (the frequencies of the A_1 bands of quartz show a negative dependence with increasing temperature, e.g. Wilkinson, *op. cit.*). Another factor to consider is the spectral resolution of the spectrometer. Given that the overall change in the band positions is significantly less than this value, the figures may not be precise. Errors could also be introduced from the curve-fitting procedure. However, the calculated R^2 and reduced Chi^2 values suggest that errors from the fitting are negligible.

The undulatory extinction in quartz is clearly the optical expression of the grain to deformation. Experimentally, pressures of 138,000 atmospheres were used in the apparatus of Griggs & Bell (1938 **In:** Deer *et al* 1963) to induce undulose extinction in quartz. We might, then, expect the shift in the Raman band positions to be much greater than those observed. The lack of frequency change may be due to the method by which the quartz structure responds to deformation or that the quartz structure re-equilibrates at low temperature. Bailey *et al* (**In:** Deer *et al op. cit.*) considered that the undulose extinction occurs by bend-gliding and polygonisation. Perfect crystallites all mutually inclined to one another at small angles and separated by regions of atomic misfit were considered by these workers to be the result. In this scenario it would appear that undulose quartz grains are not repositories of energy. Similarly, a low temperature resetting of the strained structure can be envisaged based on the fast rates of reaction observed when studying the α to β phase transition of quartz.

This study has only been able to analyse, and therefore comment upon, a single quartz grain exhibiting undulose extinction. Very many more analyses of the type detailed above would provide more data upon which to draw conclusions. In addition to line map experiments, area maps would reveal far more about the distribution of strain in quartz. Low resolution maps, perhaps with ten micrometer steps, may be sufficient to cover large grains adequately. In

addition, high spatial resolution maps concentrating on grain boundaries should be studied. The spatial resolution of the microRaman technique can be considered to be limited by the laser spot size, down to the precision of movement of the encoded stage (0.1 micrometer in X and Y). Using a shorter excitation wavelength can reduce the spot size, which could then enable higher spatial resolution maps to be acquired.

Only quartz has been considered thus far in this investigation for the reason cited. 'Strained' quartz is visually very apparent in this section but the same cannot be said of carbonate minerals in thin sections of limestones. This may point to the fact that structural strain may be reset very easily in these minerals, perhaps indicated by the ease with which they go into solution.

10.7 – Conclusion

There is not a clear relationship between the degree of undulosity of a quartz grain and its Raman spectrum. In terms of the development of ASR it would appear that the presence of undulose quartz *per se* is not necessarily to be avoided in the selection of aggregates for cement. This study indicates that the subgrains, or crystallites, are not sites of stored energy. The subgrain orientational differences may be retained but the strain has been released. However, small crystallites, possibly associated with high strain rates, may be more important as they are sites of high dislocation density. There may be a relationship between dislocation density and the degree of undulosity (as measured by the universal stage).

The Raman spectrum can be used to quantify strain in some minerals, e.g. diamond but not in quartz. This may be because the structure is easily re-set by thermal events or that the deformation occurs by gliding and the energy released along planes.

MicroRaman spectroscopy has been used in this investigation of a quartz grain exhibiting undulose extinction in a petrographic thin section. Although it has not been possible to relate the degree of undulosity to changes in the Raman spectrum, it has been possible to comment upon the mechanism by which strain is stored and possibly released, from the data collected.

MicroRaman spectroscopy may be the only technique that allows the structure of minute grains to be analysed effectively *in situ* and with all textural associations preserved.

10.8 – Further work

This study has focused on the strained quartz that is the precursor to ASR development. It would also be interesting to study the gel itself. In particular, studying the boundaries between gel and silica to elucidate on the reaction and diffusional process. The gel is not likely to be a strong Raman scatterer and we might predict broad bands from the largely amorphous structure. The interactions of the OH (as H₂O) species with the silicate network may produce some interesting bands. MicroRaman is well suited to this task since the study of thin section samples is relatively straightforward.

Several other samples of Bodmin Granite were collected. These were from piles of material that had undergone differing degrees of the processing stream. The first stage is to blast the rock from the quarry face. The next phase is to pass this rock through the primary crusher. After more crushing and passing through the total processing stream, the final product is a coarse aggregate some 20 mm across. It would be interesting to assess how each of these process steps affects the strain stored in the quartz grains. The grains could be easily compared with those analysed in rock that had not been exposed to any form of blasting or processing. This material would have to be collected from outcrops in the area that had not experienced any blasting.

It has been proposed that quartz grains equilibrate readily in response to deformation. Other minerals may not adjust in such a manner and it may be possible for the technique described to be applied to many other petrographic conditions. The study of small-scale faults in thin sections, for example, has been limited by the paucity of microanalytical techniques that probe crystal structure.

11 - Investigation of stained dimension stone

MicroRaman spectroscopy has great potential as an analytical tool in the study of dimension stone and other Industrial Rock and Mineral applications. In this second investigation of an industrial material affected by a process the technique is applied to the study of a discoloured marble and aims to elucidate on the mechanisms involved.

11.1 - Introduction

The Buildings Research Establishment (BRE, Watford, England) supplied four samples for analysis. Three were recrystallised limestone rocks, or marbles, and the other a granite. Each was a sample of dimension stone used for tiling and had been polished to varying degrees. The samples were selected because they had developed a surface discolouration in service and so had failed to meet the requirements of the contractor. The cause of the discolouration is unknown and other methods employed by the BRE had failed to determine the origin.

Review of discolouration mechanisms

Although the staining problems are purely aesthetic and do not affect the structural performance of the dimension stone panel or tile, the development of a stain in the short term can be costly. There have been cases where the exterior cladding of large buildings (i.e. civic buildings and hotels) have developed unattractive stains and been in breach of the design specification. In these cases it is important to discover who is at fault since the replacement costs may run to millions of dollars.

Richardson (1993) argues that with the proper appreciation of the minerals and physical properties of a rock, many of the problems could have been avoided. He cites the following major causes of staining:

- The presence of organic matter in limestones derived from the decay of natural organisms. In the presence of alkaline solutions, for example from cement fixing, a reaction can occur to cause staining.

11 – Investigation of stained dimension stone

- Reactions between acidic cleaning agents and the trace content of iron sulphide minerals in some rocks. Bleach and other alkaline-rich solutions are known to adversely react with iron sulphides present in some marbles.
- Porosity and water absorption can affect the rate at which staining can occur. When the rate of water uptake and porosity are high then discolouration is rapid. This is noticeable where rainwater run-off is greater over some parts of a stone panel than other parts.
- The use of iron shot to texture the rock surface can lead to discolouration if the residue is not completely cleaned off. Remaining particles will quickly oxidise in the atmosphere and ‘rust’.
- Wooden crates are often used to transport dimension stone from the quarry. However, the wood may contain water-soluble organic substances like lignin, which have been seen to leach into stone under wet conditions. Similarly, hardboard laid over stone floor panels during construction can have the same effect.
- Sands used as screeds can be rich in iron oxide particles and it is possible that with the iron in solution migration to the surface could cause staining. The effect is particularly marked in light coloured porous stones.
- Silicone sealants are often used along the joints between stone panels. Whilst not directly the cause of staining, the use of hydrocarbons as extenders can cause problems. In addition, the highly water repellent silicone can lead to the deposition of dust and dirt held in water and is associated with characteristic stain migration and the development of ‘pattern’ staining.
- Welding over unprotected stone floors can lead to staining from the oxidation of molten metal.
- Biological sources of staining have been noted. Marble is particularly affected. There are reported cases of microorganisms on the surface and fractures in rock. These organisms may be the source of the colour or may lead to discoloration as a function of their biological activity.

Oils are commonly used to improve the physical appearance of a finished stone surface. Staining problems can arise later during service as the oil penetrates well below the surface and can discolour during polishing (Hunt & Miglio, 1992).

Atmospheric pollution also plays a part in the discolouration of facing stone. In a report written in 1931 (Schaffer, 1932) it appears that the effects of carbon dioxide and sulphur dioxide dissolved in rainwater on the weathering of stone were well understood. Sulphur compounds are known to be particularly deleterious. Coal contains a small percentage of sulphur, in the form of pyrite and in organic matter, which when combusted, oxidises chiefly to SO_2 and also SO_3 . In the presence of water, sulphurous and sulphuric acids are formed, respectively. There is, then, the potential to release millions of tons of these acids into the atmosphere each year.

Sulphurous acid, H_2SO_3 , combines with calcium carbonate from limestones and marbles to form the relatively insoluble calcium sulphite, CaSO_3 , which may then react with oxygen to form anhydrite, CaSO_4 . When crystallising from solution, the mineral gypsum, $\text{CaSO}_4 \cdot 2\text{H}_2\text{O}$ forms. The stronger sulphuric acid has the same end product as sulphurous acid but is present in less quantity. The reactions liberate carbon dioxide from the calcium carbonate, fuelling the deleterious creation of calcium bicarbonate. However, the effect on weathering of this compound is thought to be minor (Schaffer, 1932). No mention of staining is given in the report but the chemical reactions occurring at the stone surface are clear.

With the cause of the stain identified, methods of removal may be determined in most cases and, hopefully, the stain prevented from occurring in the future. Richardson (1993) describes the phased approach to stain identification. Organic sources are divided into biological and non-biological. The former are then analysed further using optical microscopy, SEM and culturing and the latter identified using solvent extraction and gas liquid chromatography techniques. Inorganic sources are usually identified using petrography. Other methods employed routinely are XRD, XRF, EMPA, XPS (X-ray photoelectron spectroscopy) and LIMA (Laser ionisation mass analysis spectroscopy).

11.2 - Samples

The samples had been selected for analysis because they displayed a discolouration. The 'Carrara' marble is highly desired because of its purity; manifested by being uniformly pure white in colour. The two very-fine grained Italian marbles from the Carrara region (but not necessarily the famous Carrara quarry) displayed different degrees of brown staining, irregularly

distributed over the surface. Of these, sample BRE 02, shown in Figure 11.1, displays the most intense discolouration. The staining is concentrated in fine, irregular veins and there are fine, pale silver-grey veins, thought to be related to sulphides in the rock (T. Yates, pers. comm.). The 21 mm thick samples did not show any discolouration on the lower surface; indeed, the brown staining appears to be wholly confined to the polished surface and to a minimal depth. Sample BRE 03 was sourced from Greece and is in contrast a much purer marble. The grain size is much coarser; individual grains measuring up to a few millimetres across. There is little evidence of sulphide in hand specimen. The sample was provided as a control.



Fig. 11.1. Left: photograph of sample BRE02. Note the large patches of brown staining, silver/grey veins and veinlets of orange brown staining. Right: detail of BRE02.

11.2 Experimental

Sample BRE02 was deemed to show the most intense discolouration and so analytical efforts were concentrated here. Uncovered petrographic thin sections were prepared from the surface as well as through the sample, perpendicular to the surface. Analysis with the petrographic microscope revealed a dense interlocking arrangement of equant, euhedral calcite grains. The grains are highly birefringent and many of them displayed two cleavage sets. Although largely colourless many appeared to have weak yellow brown hue in plane polarised light. Grains are equigranular and have a size of around 250 micrometer with random orientations. Low energy triple junctions are common; a typical texture of recrystallised rock. Pore spaces appeared to be negligible. There are rare occurrences of opaque grains, possibly sulphides and rutile, some 25

micrometer in diameter between carbonate grains. The region of discolouration is seemingly identified by thicker, darker grain boundaries and appears to extend to <500 micrometer from the surface of the tile.

XRD analysis

Two slices were cut from the polished BRE 02 tile. Each was approximately 3 cm x 1.5 cm x 0.1 cm thick. One was cut from the upper stained surface and the other from the lower, unstained surface. These slices were trimmed and placed into the aluminium sample holders used by the XRD instrument. Ordinarily with this technique, whole rock samples are reduced in a ball mill, or other grinding instrument, to a grain size of the order of micrometers. However, it was felt that the slices could be used directly and scanned by the beam without grinding. Samples were scanned between 5° and 65° 2θ by a Cu_{kα} X-ray in a Phillips PW 1729 instrument.

SEM analysis

SEM analysis of small (2 cm³ to 3 cm³), silver-coated specimens revealed no difference in the crystal textures over the surface or perpendicular to the surface to a depth of around 1 mm. An uncoated sample was also loaded in to the vacuum chamber to be studied. The operating current was reduced to 10 kV to avoid charge build-up on the surface. Some very small grains, approximately 10 micrometers to 20 micrometers across, could be distinguished as different to calcite. On the basis of morphology these were thought to be pyrite but in the absence of the EDX detector this could not be confirmed. The polished surface displayed a definite reaction to the electron beam. From the back-scattered image, the surface appeared to 'boil' in the same way that organic compounds behave in the instrument chamber when subjected to the electron beam (R. Branson, per. comm.). The Ag-coated specimens did not behave in this way and neither did the freshly-exposed surfaces roughly perpendicular to the polished surface of the uncoated sample. However, without a more detailed knowledge of the sample history, i.e. between extraction from the quarry, cutting and polishing the tile, the in-service history through to delivery as a sample, little else can be speculated as the cause of this 'boiling' effect.

Raman microprobe analysis

Raman microprobe analysis was carried out using a Renishaw Raman System 2000 with 514 nm excitation from a Spectra Physics Ar⁺ laser. Some analyses were also carried out with the 785 nm line from a Renishaw HPNIR diode laser. The polished tile was placed on the Leica DMLM microscope stage and areas identified by eye were studied. Numerous analyses were recorded, with particular attention paid to the deeply stained patches and veins, as well as the 'white' i.e. unstained areas. Since the carbonates are relatively strong scatterers analysis times were of the order of seconds. Accumulations of longer scans were required for other species in the sample. Spot analyses were combined with defocused spot analyses to cover greater areas of the sample.

Mineral separation

A 1 mm thick slice taken from the upper stained surface was reduced in an agate ball mill to a fine powder. Approximately 4 grams of the sample was mixed with bromoform, an organic halogen (specific gravity of 2.88) in order to separate the minute sulphide and oxide impurity grains from the carbonates. Rutile has a density of 4.23 g/cm³ to 5.5 g/cm³ and pyrite has a density of 4.95 g/cm³ to 5.03 g/cm³, calcite has a density of 2.715 g/cm³ (Deer *et al*, 1992). By mixing with the bromoform the particles with densities greater than that of 2.88 g/cm³ will sink and the lighter calcite will float. The dense grains were removed by pipette and retained.

11.3 - Results

XRD experiments were only able to resolve the presence of calcite in the sample owing to the high detection limits of the technique (Sasaki *et al*, 1998). A comparison between the upper and lower surfaces yielded no differences between the spectra; Figure 11.2 shows that peak positions, shapes and intensities were identical. The XRD spectra of the common carbonates are markedly different allowing unambiguous discrimination between the species.

Raman microprobe analyses of the opaque grains revealed them to include rutile and sulphides, probably pyrite. The concentration of these phases was too low to be detected by whole rock XRD analysis.

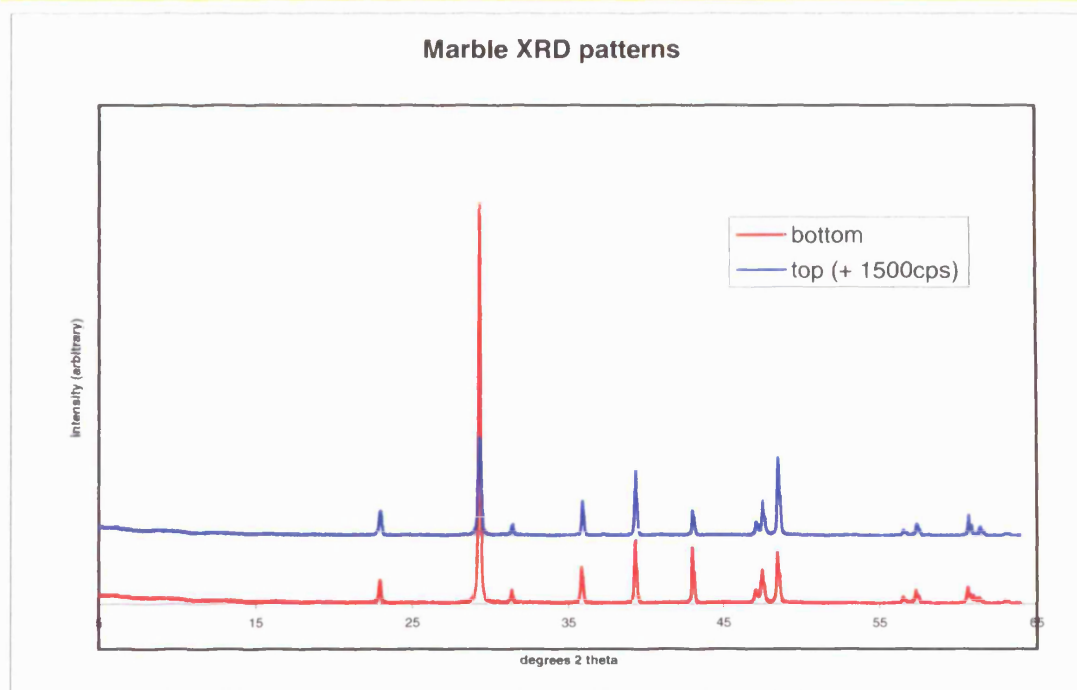


Fig. 11.2. Overlaid XRD spectra of the upper and lower surfaces of sample BRE 02.

Extensive Raman microprobe analyses using 514 nm excitation from an Ar⁺ laser source reveals the marble to be composed of predominantly calcite. The position of some of the Raman bands suggests the presence of other carbonates, probably dolomite. Table 11.1 details the frequency positions of the main Raman bands of calcite, dolomite and siderite as given by Herman *et al* (1997).

	external		ν_1	ν_3	ν_4	$\nu_1 + \nu_4$
Calcite, CaCO ₃	154	283	1087	1438	714	1750
Dolomite, CaMg(CO ₃) ₂	177	301	1099	1440	729	1745
Siderite, FeCO ₃	190	296	1090	1443	734	1736

Table 11.1. Raman band positions of calcite, dolomite and siderite (after Herman *et al*, 1997).

Figures 11.3 and 11.4 show the typical spectra recorded from areas immediately adjacent to sulphide grains. Figure 11.3 is the result of using the x100 objective lens with twenty accumulations of ten second scans. The analysis shown in Figure 11.3 suggests some overlap of the spot or interference from the pyrite grain. The pyrite peaks and calcite bands are indicated by 'py' and 'cal', respectively. Additional weak features indicated in Figure 11.3, centred at

approximately 1322 cm^{-1} , 610 cm^{-1} , 658 cm^{-1} , 407 cm^{-1} , 222 cm^{-1} probably relate to the brown staining and closely correspond to the Raman band positions of hematite, $\alpha\text{-Fe}_2\text{O}_3$. Subsequent analyses of particles within the BRE02 sample yielded Raman spectra of ‘pure’ hematite.

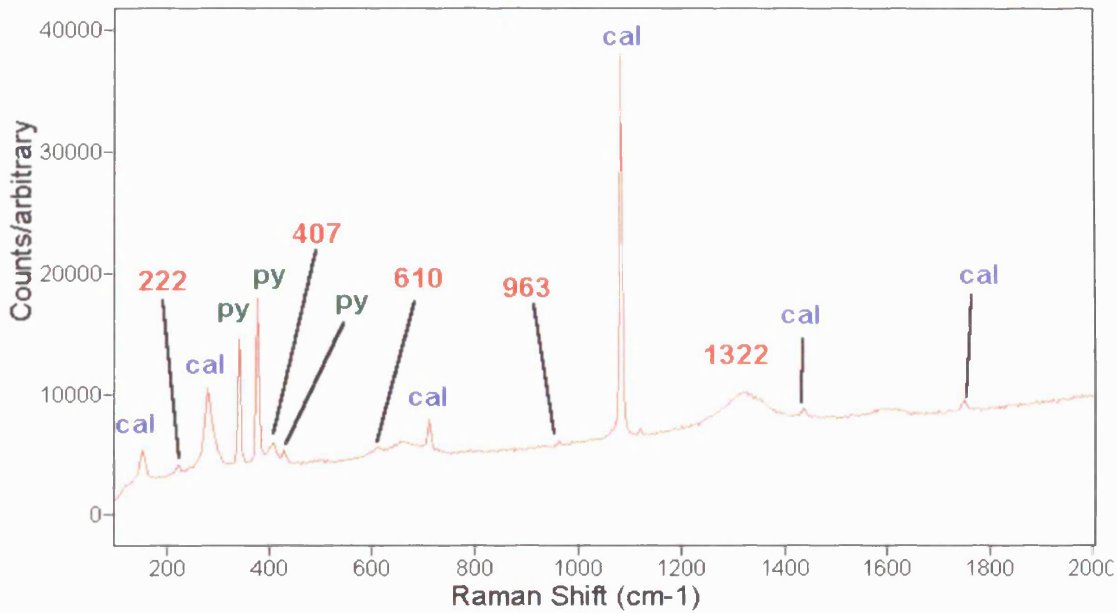


Fig. 11.3. Raman analysis of spot adjacent to pyrite grain.

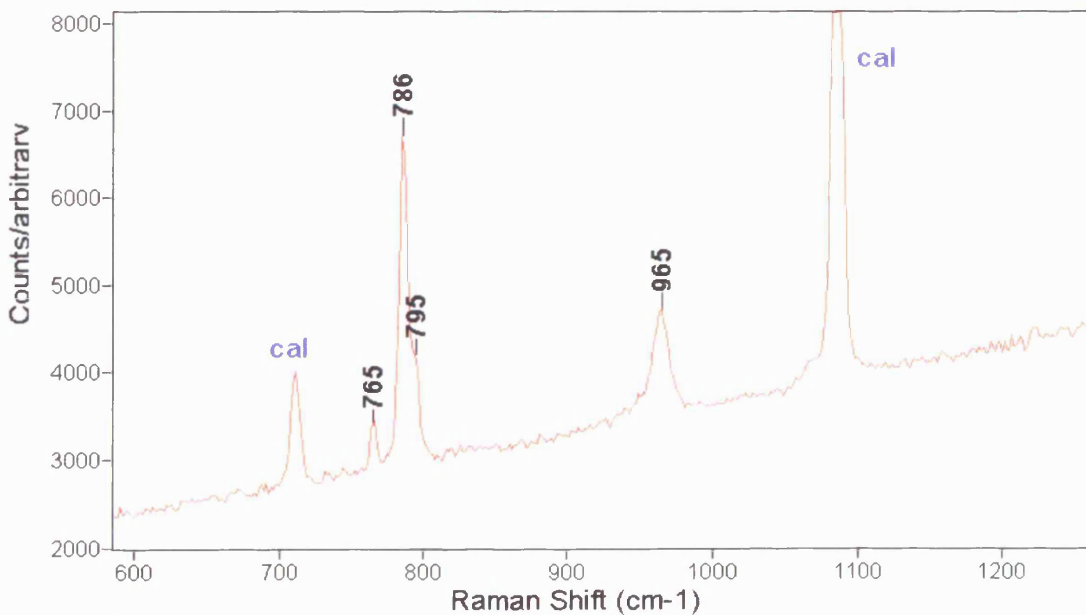


Fig. 11.4. Raman analysis of spot adjacent to pyrite grain.

The analysis in Figure 11.4 was acquired with the x50 objective and with three accumulations of ten seconds. Two of the calcite bands are indicated in this detailed region of the spectrum. Additional bands not corresponding to a carbonate species are indicated at 765 cm^{-1} , 786 cm^{-1} and 795 cm^{-1} . These bands may be attributed to SiC used in the grinding process. In comparison to Figure 11.3 the band at around 965 cm^{-1} is significantly stronger.

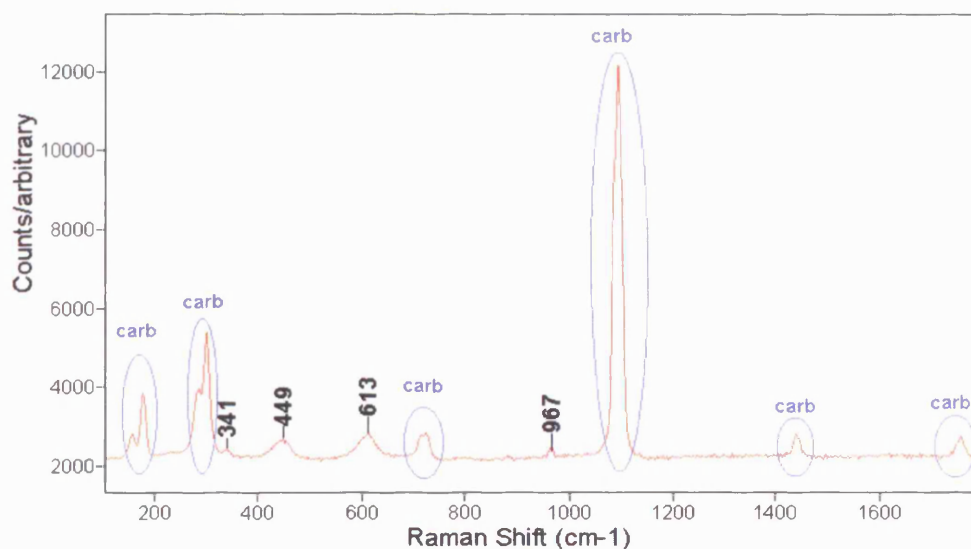


Fig. 11.5. Raman spectrum of stained area. Carbonate 'doublets' indicate two carbonate species.

Figure 11.5 displays the Raman spectrum recorded from a vein within a particularly stained area of the sample. The x20 objective lens was used and the spot was defocused by 20% to illuminate a larger area of the sample than with the x100 objective (several tens of micrometers²). Five accumulations of thirty-second scans were recorded. The spectrum has been multi-point baseline corrected for clarity. The predominant features of the spectrum belong to the carbonate in the sample. The presence of pairs of 'double peaks', indicated as 'carb', with subtle differences in position suggest that two carbonate species are present in the analysis region. Based on the study of carbonate discrimination using Raman by Herman *et al* (1987) the higher wavenumber peak in each of these pairs probably belongs to dolomite. Two broad, moderately weak features can be seen centred at 449 cm^{-1} and 613 cm^{-1} . The weak feature indicated at 341 cm^{-1} is probably ascribed to pyrite. As in Figures 11.3 and 11.4 there is an unattributed band at around 967 cm^{-1} .

Filter paper and residue analysis

The bromoform very efficiently retained the dense particles, which were analysed by Raman spectroscopy and found to be predominantly pyrite and rutile. It was noted that the paper used to filter the mixture had its outermost edge stained brown as the liquid evaporated. A Raman analysis of this staining was undertaken since as it was assumed that the same species responsible for the staining in the tile was responsible for this staining. Detailed optical microscopic examination of the outer edge of the filter paper revealed the presence of minute red brown crystals. One of these is displayed in Figure 11.6.

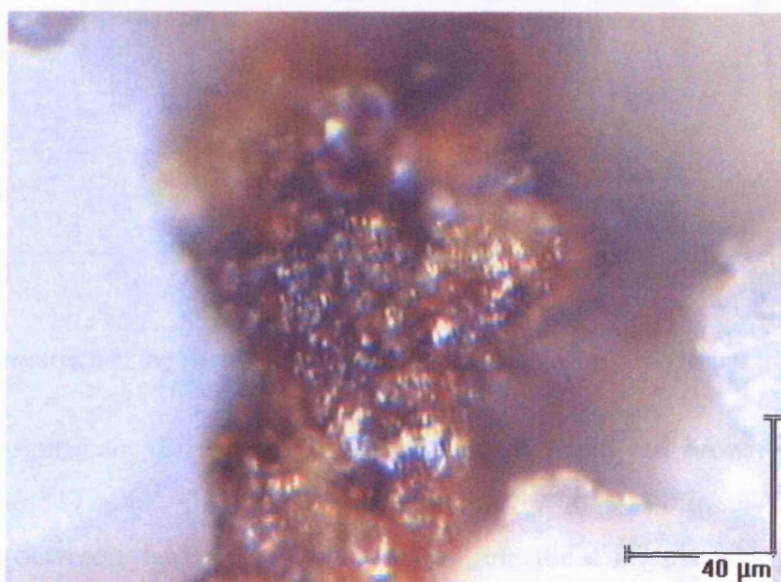


Fig. 11.6. Red brown crystal retained in filter paper.

The 785 nm laser was used in the analysis of the paper and residue. However, the spectra are still dominated by fluorescence, despite the selection of the longer excitation wavelength. Attempts were made at analysis and the spot size and laser power density were varied in order to obtain Raman bands above the fluorescence. Analyses were made of the inner, unstained area of the filter paper and also the brown edge and particles retained by the filter paper.

The brown edge, resembling liquid chromatography experiments, only gave Raman bands that matched those of the filter paper, analysed for reference. Figure 11.7 displays the overlaid spectra from a red crystal trapped by the filter and the reference paper spectrum. Both spectra have been baseline-corrected and smoothed for clarity. The red brown crystals in the filter paper

were found to be strongly absorbent in the red spectrum and some sample damage was observed at higher laser intensities.

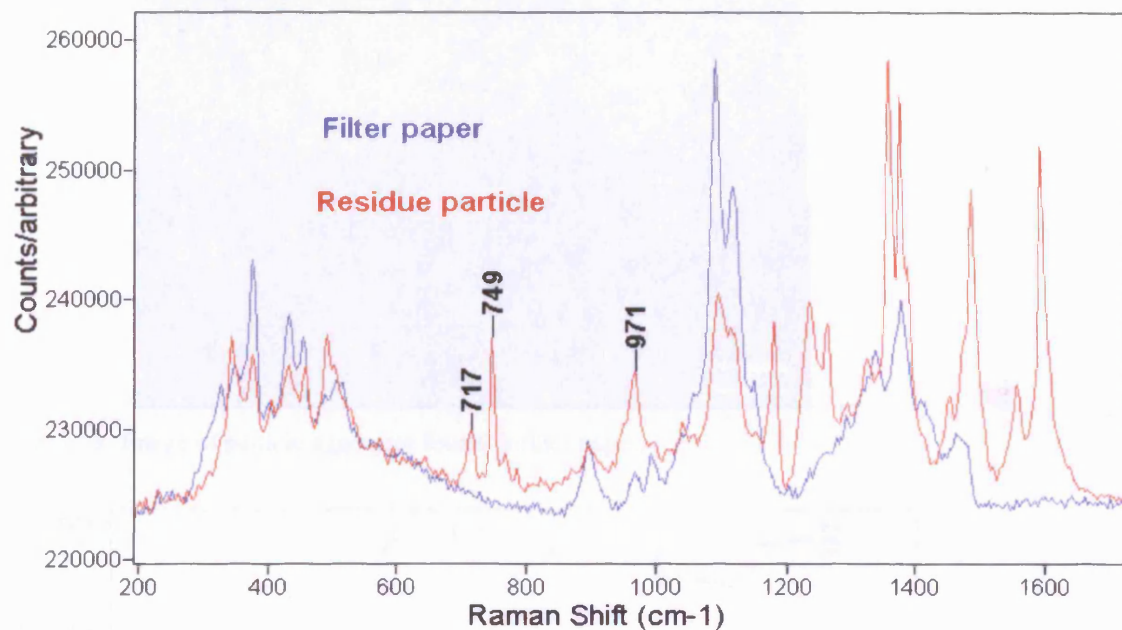


Fig. 11.7. Comparison of the Raman spectra of filter paper and red crystal trapped in the filter.

The most significant differences between the paper and red brown crystal Raman spectra are indicated at 717 cm^{-1} , 749 cm^{-1} and particularly at 971 cm^{-1} . Although there are several differences between the spectra above this region, these intense, sharp bands are not thought to belong to a pure mineral species. For example, the most intense Raman band of the carbonates is associated with the symmetric stretching vibration of the CO_3^{2-} anion and occurs, as has been shown, at around 1100 cm^{-1} . Given the nature of the bonding the masses of the elements involved, few functional groups in minerals are likely to have strong vibrations that occur above this frequency. The bands may belong, then, to the adsorbed organic species, for example, from the bromoform used.

The aggregate of crystalline particles shown in Figure 11.8 was analysed with 514 nm laser. Low laser power was used and a low magnifying objective used to illuminate many particles. Signal was built up by co-adding twenty-five accumulations of ten second scans. The spectrum from the sample, shown in Figure 11.9, is very different from any of the other analyses from this sample set. There are no contributions in the spectrum in Figure 11.8 from the filter paper.

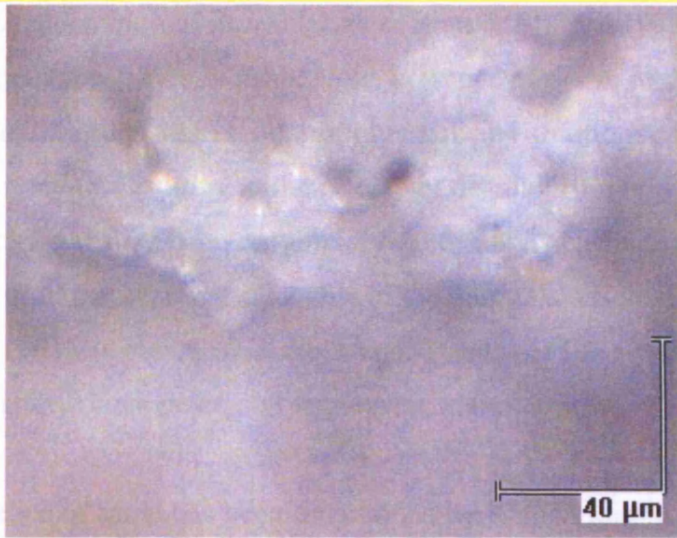


Fig. 11.8. Image of particle aggregate found in filter paper.

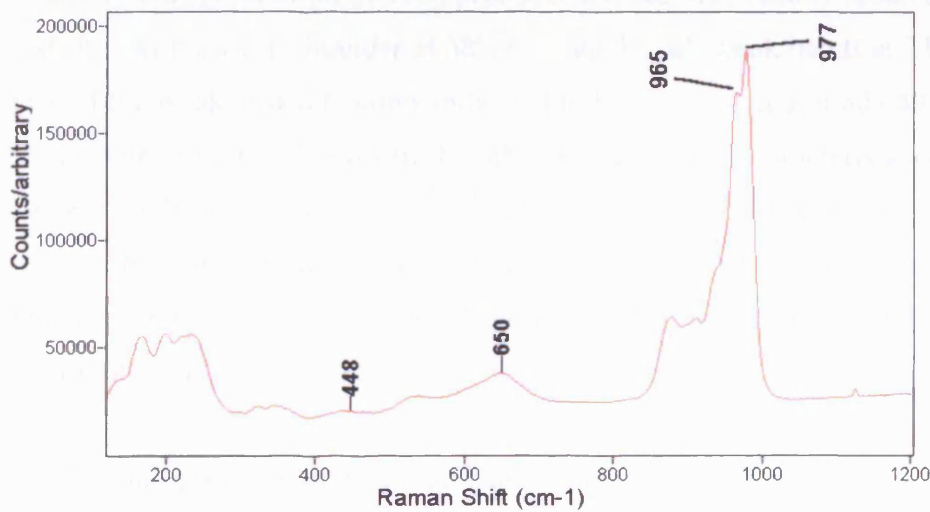


Fig. 11.9. Raman spectrum of aggregate shown in Figure 11.8.

The position of the most intense band, a doublet indicated at 965 cm^{-1} and 977 cm^{-1} is of interest. The frequency is very similar to bands displayed in Figures 11.3, 4, 5 and 7.

11.4 - Discussion

The presence of pyrite in marble is well known. The origin of the pyrite is probably the reduction of dissolved sulphate in the pore water of the original limestone reacting with Fe^{2+} in the pore water, itself derived from the reduction of iron hydroxides and oxides on clays and organic matter (Tucker, 1991). The Carrara marbles grade from pure white to shades of grey, depending

on their concentration of iron sulphides (Hunt & Miglio, 1992). It has been straightforward using microRaman spectroscopy to show the presence of pyrite in the BRE02 marble sample. The use of alkaline solutions, bleach or strongly oxidising solutions as cleaning agents are known to react with Fe sulphides resulting in the release of discolouring ferrous oxides. Highly variable discolouration results from ranging crystal density, size and permeability of the stone. The presence of hematite, the most stable of the many Fe oxide minerals under oxidising conditions (Tucker, 1991), is indicated in the Raman spectra of laser-excited regions of brown stain and also from the study of single crystal aggregates in the sample.

The presence of rutile has been determined by Raman microspectroscopy in sample BRE 02. Raman spectra recorded from grains in the sample are excellent matches with those of the database. This polymorph of TiO_2 produces intense, moderately broad Raman bands at 445 cm^{-1} , 610 cm^{-1} with a weak shoulder at 687 cm^{-1} , and broad, weak bands at 234 cm^{-1} and 805 cm^{-1} . Two of the weak, broad features indicated in Figure 11.4 at around 449 cm^{-1} and 613 cm^{-1} could be attributed to rutile. However, the other Raman bands characteristic of rutile are not present. The Raman bands are rather weak which would make these additional features difficult to resolve above the baseline. The calculated FWHM values for the 449 cm^{-1} and 613 cm^{-1} bands compare well with the values calculated from the rutile single crystal bands ($45\text{ cm}^{-1}/46\text{ cm}^{-1}$ and $41\text{ cm}^{-1}/35\text{ cm}^{-1}$, respectively).

Another interpretation of the broad bands around 449 cm^{-1} and between 610 cm^{-1} and 650 cm^{-1} is to ascribe these bands to the presence of a jarosite-group compound. This group, with the general formula $[\text{MFe}_3(\text{SO}_4)_2(\text{OH})_6]$ (where $\text{M}^+ = \text{K}^+, \text{NH}_4^+, \text{Na}^+, \text{Ag}^+$ and $\frac{1}{2}\text{Pb}^{2+}$), has been extensively studied with respect to the dissolution of pyrite (e.g. Sasaki, 1997 and Sasaki *et al*, 1998). Bands in these positions correspond very well to the $\nu_2(\text{SO}_4^{2-})$ and $\nu_4(\text{SO}_4^{2-})$ bending mode frequencies given by Sasaki *et al* (1998). If a jarosite-group mineral were detected in the BRE02 sample, we might expect the strong $\nu_1(\text{SO}_4^{2-})$ band at between 1000 cm^{-1} and 1015 cm^{-1} and the $\nu_3(\text{SO}_4^{2-})$ to occur at between 1090 cm^{-1} and 1115 cm^{-1} . However, the positions of the $\nu_1(\text{SO}_4^{2-})$ and $\nu_3(\text{SO}_4^{2-})$ bands are known to shift depending upon the species of the M^+ ion and the change in the c parameter that results (Sasaki *et al*, 1998). Figure 11.9 also reveals significant spectral activity in the region of the spectrum identified by Sasaki *et al* (op. cit.) where the vibrations of O—Fe

occur. The study of jarosite-group compounds is important in the study of acid mine drainage where iron-oxidising bacteria are known to dramatically increase the rate at which acids are produced from pyrite.

The phases known to be present in sample BRE02 do not account for all the Raman bands shown in the preceding spectra. The inference is, then, that they are associated with the orange brown staining. Typically, these additional bands are rather broad. Broad bands are hard to attribute to any particular functional group or vibrational mode since they cover a relatively large wavenumber range. One of the causes of broad bands is small crystallite size (Wopenka *et al*, 1996). Of these additional bands is one that occurs repeatedly at around 964 cm^{-1} and appears significantly sharper (see, for example, Figure 11.4) than the other non-carbonate bands. The band appears to be independent of the hematite, pyrite and rutile Raman bands.

mineral	Positions of main Raman bands/ cm^{-1}		
	ν_2	ν_4	ν_1
gypsum, $\text{CaSO}_4 \cdot 2\text{H}_2\text{O}$	412	619	1007
anhydrite, CaSO_4	418	677	1019
anglesite, PbSO_4	441	609	980
baryte, BaSO_4	453	617	988
glauberite, $\text{Na}_2\text{Ca}(\text{SO}_4)_2$	472	621	1008
linarite, PbCuSO_4	516	634	969
celestine, SrSO_4	463	641	1002
kalinite, $\text{KAl}(\text{SO}_4)_2 \cdot 11\text{H}_2\text{O}$	456	620	976/991
coquimbite, $\text{Fe}^{3+}(\text{SO}_4)_3 \cdot 9\text{H}_2\text{O}$	286	509	1026
polyhalite, $\text{K}_2\text{MgCa}_2(\text{SO}_4)_4 \cdot 2\text{H}_2\text{O}$	438	615	990/1015
apatite, $\text{Ca}_5(\text{PO}_4)_3(\text{OH}, \text{Cl}, \text{F})$	439	592	966

Table 11.2. Positions of some Raman bands in some sulphate minerals and apatite.

The Raman spectra of some sulphate minerals show their most intense band, corresponding to the symmetric stretching vibration of the (SO_4^{2-}) anion at around 980 cm^{-1} . The exact frequency depends upon the local bonding environment and chemical species. In single crystal gypsum it is centered at 1008 cm^{-1} (Prasad, 1999) and around 969 cm^{-1} in linarite. Anglesite and baryte share

many similarities in the positions of their peaks with those unattributed in the BRE 02 sample. Table 11.2 lists the positions of some of various sulphate minerals that have the sulphate anion in different structural configurations. The positions of the main bands in apatite, a phosphate mineral, are also given. Data are partly from the Renishaw Raman Database of Minerals and Inorganic Materials and partly measured by the author from samples.

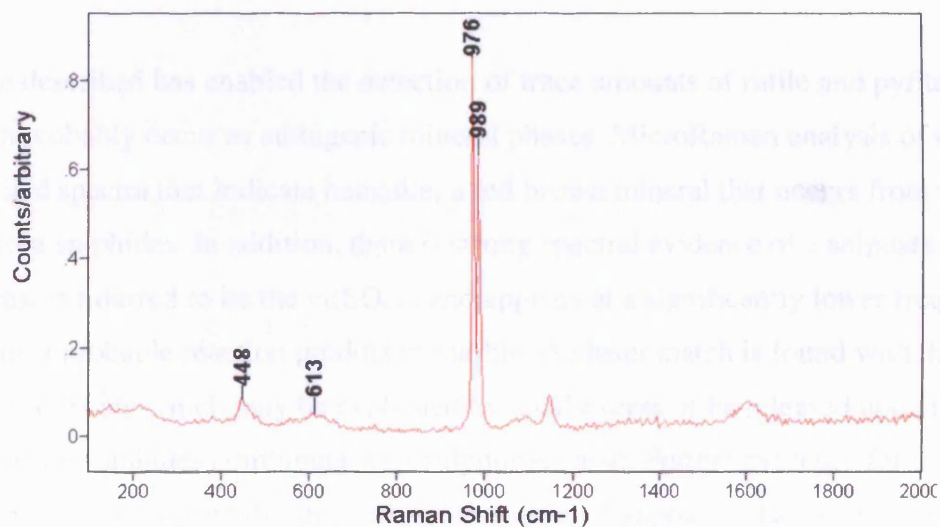


Fig. 11.10. Raman spectrum of melanterite, an Fe sulphate crystal.

Figure 11.10 shows the Raman spectrum recorded from a crystal of the Fe sulphate mineral melanterite, $\text{Fe}^{2+}\text{SO}_4 \cdot 7\text{H}_2\text{O}$. The band positions highlighted in the spectrum are a very close match with the positions of bands shown in the spectra from the discoloured regions of the BRE02 sample. The Fe sulphate shows two very sharp, very closely spaced bands at 976 cm^{-1} and 989 cm^{-1} . The presence of two bands may indicate two structural configurations of the SO_4^{2-} anion. It is not possible to resolve two bands in the BRE02 sample spectra shown. This may be explained by crystal size and orientation effects or by some deviation from the ideal structure.

The effect of using organic oils to improve the appearance of polished stone has been mentioned as a potential cause of staining. Although the main C—H stretching region of the spectrum was not routinely analysed there is no spectral evidence of organic matter in the region below 2000 cm^{-1} .

11.5 - Conclusion

Petrography remains the most useful tool in assessing the suitability of a stone for use in flooring and facades. However, when analysing stained stone, microRaman spectroscopy is probably the most effective tool. Sample preparation is minimal when compared to EMPA and SEM but it retains a sufficiently high spatial resolution and selectivity. For example, EMPA and SEM techniques are unable to determine the presence of organic matter.

The technique described has enabled the detection of trace amounts of rutile and pyrite in marble, which probably occur as authigenic mineral phases. MicroRaman analysis of stained regions can yield spectra that indicate hematite, a red brown mineral that occurs from the oxidation of iron sulphides. In addition, there is strong spectral evidence of a sulphate phase. The position of what is inferred to be the $\nu_1(\text{SO}_4)$ band appears at a significantly lower frequency than in free gypsum, a probable reaction product in marble. A closer match is found with the Raman spectrum of Fe sulphate which may be explained by local excess of Fe released upon the oxidation of the Fe sulphides combining with sulphurous acid. Further evidence for the presence of a sulphate phase comes from the study of jarosite-group compounds. However, it is not possible at this stage to comment upon the possible composition.

The samples provided for this study were not supplied with any additional information concerning the development of the staining. As Hunt & Miglio (1992) point out, staining and discolouration depends upon stone type can occur at every stage: at source, during the finishing process, packaging, transportation, storage, design, final usage and maintenance. The spectra indicate that oxidation of the authigenic pyrite has occurred. This may have been induced by the action of proprietary cleaning products or simply the action of atmospheric pollution.

This study has clearly demonstrated that microRaman spectroscopy can be more sensitive than X-ray diffraction in the determination of mineral species present in a rock. Not only were sulphides and oxides detected with the microRaman but it has also been possible to show the presence of other carbonates where XRD could not.

11.6 - Further work

This study has focussed on the analysis of one sample of stained marble dimension stone. Samples of unstained marble and also of a stained granite were also supplied but not analysed. It would be interesting to analyse these samples in the manner outlined above and to compare the Raman spectra. The granite would be particularly interesting because the staining could not have occurred as a result of reaction with calcite. Whilst pyrite could be present, it is not the likely major 'ferromagnesian' phase present.

The development of a field tool based on the technique of Raman spectroscopy could be highly advantageous in the study of discolouration of dimension stone. The preceding study has centred on the analysis of samples in the laboratory. However, it is entirely feasible that a optic fibre-based portable instrument could be used to determine the nature of discolouration components. This study has shown the advantages of using a large illumination area, which is technically easier to achieve than a micrometer-sized laser spot.

The recent development of Laser-Induced Breakdown Spectroscopy (LIBS) has enabled many detailed qualitative studies of pigments used in manuscripts and paintings. The method can be combined with Raman spectroscopy – the ablating laser is also used to induce the inelastic light scattering. The equipment is portable, provides sensitive measurement of elements and has adequate spatial resolution (Clark, 2002) for the analysis of stains on rock surfaces.

The other possible reaction products that could occur in this environment should also be investigated. For example, the presence of nitric acid could give rise to the development of nitrate minerals. Similarly, Table 11.1 lists the frequencies of the main Raman bands of apatite, which correspond quite closely with the observed positions of the Raman bands obtained from the marble sample. Phosphates of calcium and iron could arise as reaction products if a phosphoric acid were used as a cleaning agent, for example.

12 - Investigation of fired clay bodies

The aim of this preliminary investigation of brick-making material is to assess the suitability of microRaman spectroscopy in determining the phases present in a suite of fired clay samples. The study represents the third in the series using microRaman spectroscopy to study processes and transformations that can occur in natural materials.

12.1 – Introduction

This project was initiated because it was perceived that Raman spectroscopy could help elucidate the phase developments that occur upon firing clay materials. The ultimate aim of an investigation of this type would be to determine accurate time-temperature conditions that might lead to efficient firing programs and even provide *in situ* analyses, i.e. in the kiln, of the bricks as they are being fired.

Bricks have been manufactured for hundreds of years and the process is still largely unchanged. A comprehensive mineralogical review (Dunham, 1989) of the brick-clays used in the UK identified mineralogical techniques as key to understanding the mineralogical changes upon firing that produce a commercial product. This was taken a step further in a detailed chemical and mineralogical study of three important UK brick-clays (McKnight, 1991). With the aim of understanding the poorly studied phase changes, this study tried to ascertain if the time and temperature conditions used in the brick manufacturing industry could be altered to make the process more energy efficient whilst achieving the same quality of product. However, the chemical changes that accompany the phase changes (loss and nucleation of phases) identified were still largely qualitative since a technique that could allow one to measure the mineralogy during firing was not available.

Previous work

The DTA/TG analyses of Dunham (1989) were able to show the dehydroxylation and dehydration and collapse of the clay minerals and the loss of other volatiles. Other observations were semi-quantitative on the basis of chemical data only. Dunham (1989) suggested that the dehydration of the clay minerals and further heating caused a collapse in the structures to form

new, more compact and stable phases. For example, the transition of structureless (i.e. transparent to XRD) metakaolinite to mullite and cristobalite. The extensive XRD work of McKnight (1991) advanced the use of T-T-t diagrams by applying the method to the bulk mineralogy of pellets fired to a rigid range of conditions. The curves he produced were semi-quantitative in that the boundaries were placed between quite widely spaced data points that defined regions of either an occurrence or non-occurrence of a certain mineral species.

Initial searches the published literature exposed no studies where microRaman spectroscopy has been applied to the analysis of bricks. A later search, carried out towards the end of this study exposed a multi-analytical study of brick clays in Santa Cruz (Alia *et al* 1999). In it, FT-Raman spectroscopy was used, amongst other techniques, to characterise the mineralogical content of traditional bricks and make suggestions for starting materials to improve the properties of the fired brick.

12.2 – Sample material

As an initial assessment of the applicability of microRaman spectroscopy to this project some small briquettes were produced. The raw material selected was Etruria Marl from the Broomfleet Quarry, Humberside. This clay is very well studied and is one of the major brick clay resources in the UK; its composition leads to an almost ‘ideal’ brick (McKnight, 1991) composed of interlocking acicular mullite grains in a glass matrix that bonds the relic quartz grains. These are the mineralogical features that give rise to the desirable properties of high compressive strength, fracture toughness and durability.

Preparation of briquettes

The material available was ex-quarry, i.e. it was removed from the working stockpile. Grain sizes ranged from dust to fragments 4 mm across. In order to facilitate the briquette manufacture the clay was reduced in size using an agate TEMA mill. It was thought that the finer grain size would aid the homogenous mixing with water and reduce the likelihood of incorporating air pockets into the briquettes. Trapped air would expand in the kiln and lead to explosive disintegration of the briquettes.

Distilled water was gradually added to a quantity of the clay and mixed until a homogenous mixture close to its plastic limit was reached. This stage was defined by the clay mix being as stiff as possible but without crumbling upon moulding with the fingers. In this state the mixture contains slightly more water than that required for the plastic limit (Procedure for the Production and Firing of Clay Briquettes, Geology Department, University of Leicester). This was then placed in a Perspex mould whose internal dimensions were 12.5cm x 2 cm x 1.5 cm. The clay was carefully tamped down to eliminate air pockets. Excess material was removed and a code embedded in the surface. Briquettes were allowed to dry at room temperature before firing. A total of ten briquettes were made following this procedure.

Firing conditions

For this initial study firing times were selected as 500 °C, 750 °C, 850 °C, 950 °C and 1050 °C. Soak times were around one hour, with two briquettes fired at each temperature. Ramp parameters were 50 °C per minute with the kiln allowed to cool to room temperature naturally.

Petrography

Observations under plane-polarised and cross-polarised light (PPL and XPL) were carried out on samples fired to the lowest and highest temperatures. Sections were taken parallel to the 2 cm x 1.5 cm rectangular section towards the centre of the bricks.

500 °C

The deep red brown colour of the hand specimens is apparent in the PPL. The very fine grained nature of the matrix makes it difficult to distinguish individual particles. Larger matrix grains are estimated to be around 10 micrometers long and equant. The matrix is a strong red brown colour in PPL and under XPL the body colour masks any birefringence. Towards the outer edges of the sections the grain sizes are finer and there is less distinction between individual matrix grains. In addition, the body colour becomes more intense.

Around 25% of the volume of the brick is comprised of much larger grains. These range in size to a maximum of about 300 micrometers. Typical sizes are around 100 micrometers. Large grains have angular to sub-round shapes. They include lithic fragments and opaque grains. The

majority are a very deep red brown colour and are the coarse equivalent of the coloured matrix grains.

There is a relatively high proportion of pore spaces towards the middle of the sections. The sizes vary but are typically less than the average size of the large grains. Towards the edges of the sections the pore spaces become fewer and smaller.

Figures 12.1 and 12.2 display white light images in PPL of the 500 °C sample towards the middle and edges, respectively. Note the differences in matrix colour and concentration of pore spaces.

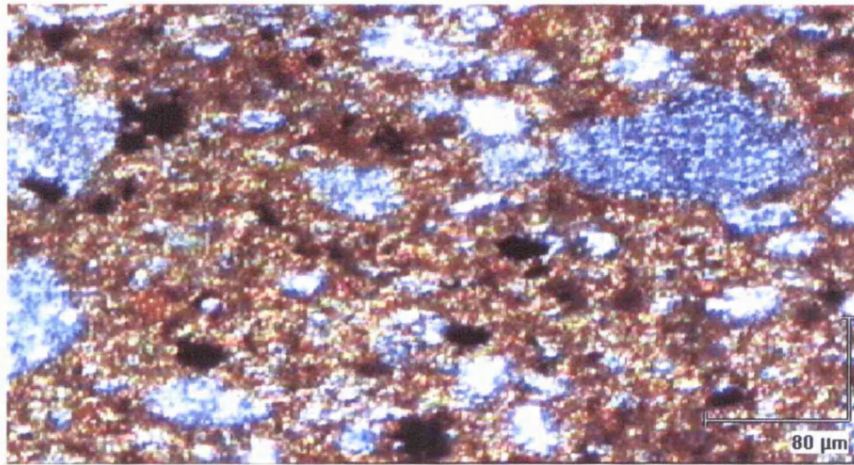


Fig. 12.1. White light image from section through middle of sample fired to 500° C.

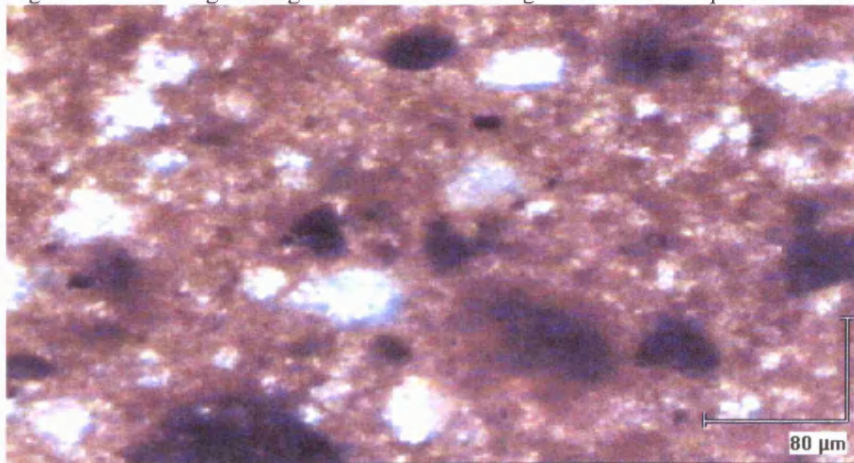


Fig. 12.2. White light image from section through outer edge of sample fired to 500°C.

1050 °C

The most striking difference between the high and low temperature-fired samples is that many of the large grains in the latter are surrounded by a thin pore space layer. The layer appears quite

uniform with a thickness of between 5 and 10 micrometers. It may be accounted for by differences between the coefficients of thermal expansion between the matrix and large grains and grain size (surface area). This pore space layer is clearly observed in figure 12.3 despite the low image resolution.

In comparison with the low temperature-fired sample, many of the large grains appear optically clearer; it is easier to identify individual angular quartz grains. In addition, there appears to be a lower concentration of pore spaces in the centre of the bricks and the matrix has a much less intense colour than in the 500 °C sample. However, there are much larger discrete areas of a dark red brown colour. The matrix appears to be more crystalline and with higher power objectives the presence of very small, colourless, acicular crystals with quite diffuse edges. These grains comprise only a tiny fraction of the total, perhaps only 1%. The image in figure 12.4 clearly shows one of these acicular grains.

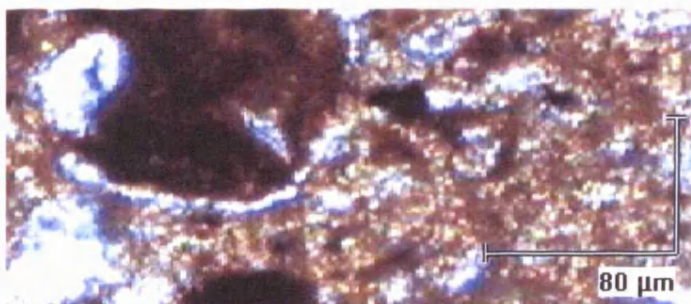


Fig. 12.3. PPL image from 1050 °C sample showing pore space layer.

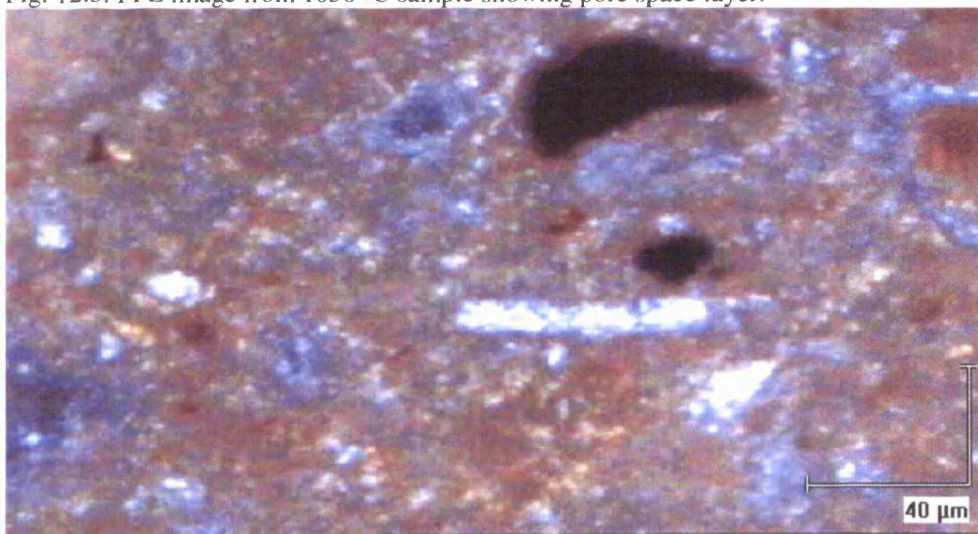


Fig. 12.4. PPL image from 1050 °C sample showing acicular crystal.

2.3 – Analysis and Results

Both powder X-ray diffraction, XRD, and microRaman spectroscopy are excellent means of mineral phase identification. The latter has the advantage of offering *in situ* analysis, i.e. in macro specimen and in thin section, and does not require samples to be ground to a fine powder. Both techniques offer similar spatial resolution; they are capable of analysing micrometer-sized particles.

The aim of using Raman spectroscopy in this study is to detect the various phases in samples and to elucidate on the conditions of phase changes during firing, including the nucleation of new phases, mineral structure changes and element partitioning, e.g. into the glass.

X-ray diffraction

Minerals detected	Samples and firing temperatures					
	Etruria Marl	1M 500 °C	2M 750 °C	3M 850 °C	4M 950 °C	5M 1050 °C
quartz	*	*	*	*	*	*
illite	*	*	*	*		
kaolinite	*	*				
goethite	*					
gypsum	*					
anatase	*		*		+	
chlorite	*					
hematite		*	*	*	*	*
pseudo-rutile				*	+	
mullite						*
rutile						*
crichtonite						*

Table 12.1. Results of XRD analyses. * indicates detection by XRD and + indicates possible presence.

XRD analyses were carried out on the dried raw material and on the briquettes fired to the five different temperatures. Pressed powder cavity mounts of the micronised materials were analysed by a Philips PW1710 instrument operating at 40kV and with a beam current of 30mA. A Cu target was used and the X-rays filtered to select the $\text{Cu}_{k\alpha}$ radiation. Analysis parameters were 4° to $65^\circ 2\theta$ with a step angle size of $0.02^\circ 2\theta$ and a scan rate of $1^\circ 2\theta$ per minute. The peak positions were run in μPDSM software against the JCPDS data set. The qualitative results are shown in Table 12.1.

MicroRaman spectroscopy

This initial assessment of the suitability of the technique was based around phase determination in the briquettes and the spatial resolution. The uncovered thin sections used for petrographic analyses were used for microRaman analysis.

A Renishaw RM 1000 was used throughout. The 782 nm line of a HeNe diode laser was used initially but excessive luminescence caused by the strong absorption of the incident energy by the sample masked the Raman signal. In order to reduce the effects of luminescence the 514 nm line of an Ar^+ laser was employed. Acquisition times used were typically single exposures of thirty seconds or five accumulations of 10 seconds.

The Raman instrument was used to try and determine the identity of the coarse grained particles. The fine grain sizes made it impossible to resolve the clay particles optically in the samples fired to lower temperatures (i.e. below 1050°C , samples 1M to 4M). The clay and other minerals proved to be intractable to analysis by this method. In addition the high Fe content made Raman analysis difficult due to the effects of luminescence on the Raman spectra.

MicroRaman analysis was based on sample 5M, fired to 1050°C . The grain sizes were significantly larger, facilitating their visual detection. Analysis of the Raman bands recorded and using the Renishaw Raman Database of Mineral and Inorganic Materials spectra, quartz, anatase, hematite and goethite were determined. Figure 12.5 displays a Raman spectrum recorded from a spot in the 5M sample and compares it to the reference hematite spectrum. There is an excellent agreement with the position of many of the main hematite bands.

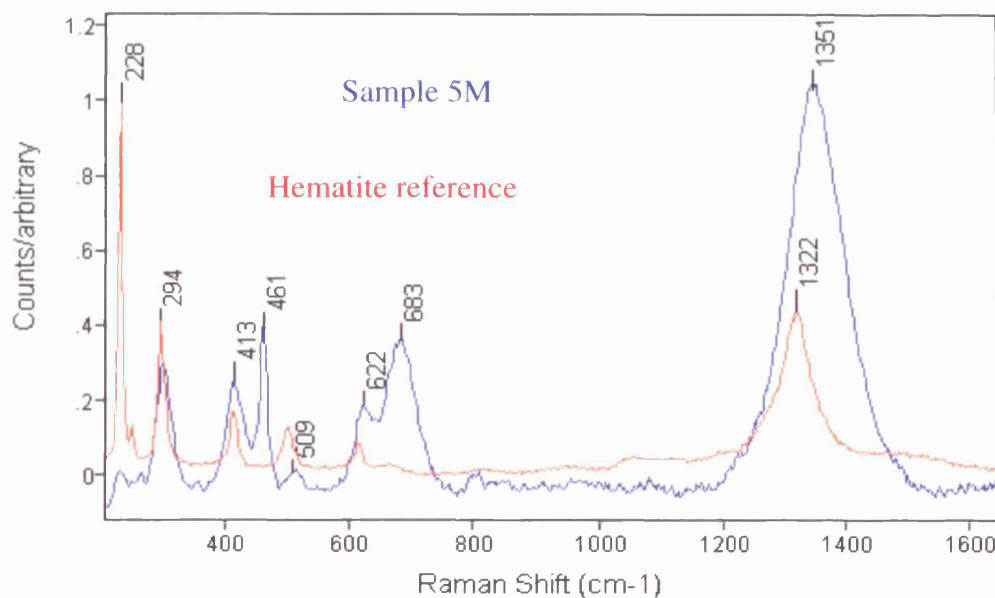


Fig. 12.5. Hematite reference spectrum (red) and hematite from sample 5M (blue).

Figure 12.6 displays a Raman spectrum recorded from sample 5M with a goethite reference spectrum. The sample spectrum shows quite poor signal to noise ratio, however, the strong agreement between the bands at 211 cm^{-1} , 277 cm^{-1} and 380 cm^{-1} is evident. The broad band in the reference spectrum at $\sim 1300\text{ cm}^{-1}$ is barely resolvable above the noise in the sample spectrum. Additional peaks in the 5M sample spectrum at 136 cm^{-1} and close to 600 cm^{-1} may be associated with anatase. A reference anatase spectrum is shown in figure 12.7. However, anatase was not detected with any certainty using XRD in samples fired to more than $750\text{ }^{\circ}\text{C}$. The two strong bands in the anatase spectrum at 393 cm^{-1} and 513 cm^{-1} are orientation dependent; at certain crystal orientations they are very weak relative to the 139 cm^{-1} band, which is always very intense.

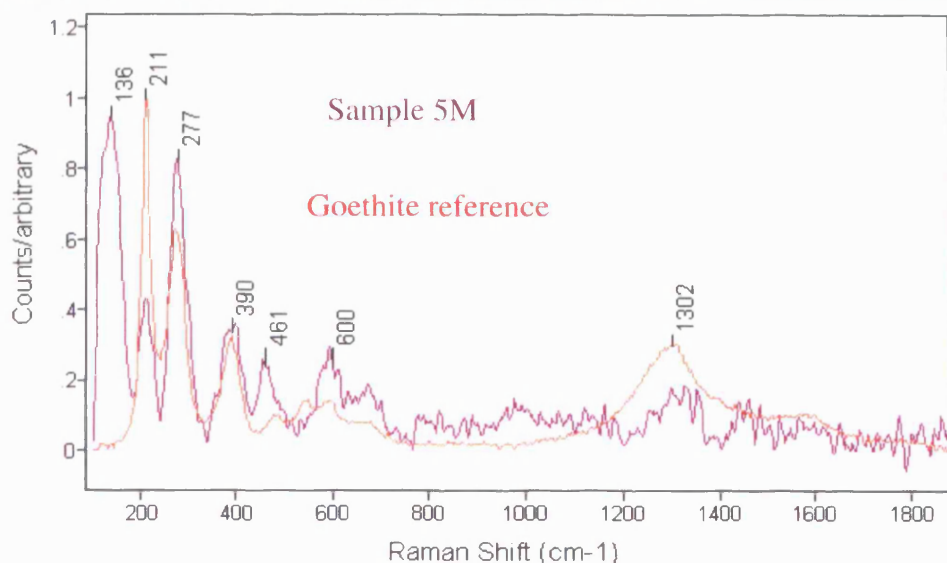


Fig. 12.6. Goethite reference spectrum (lower trace, red) and goethite from sample 5M (purple).

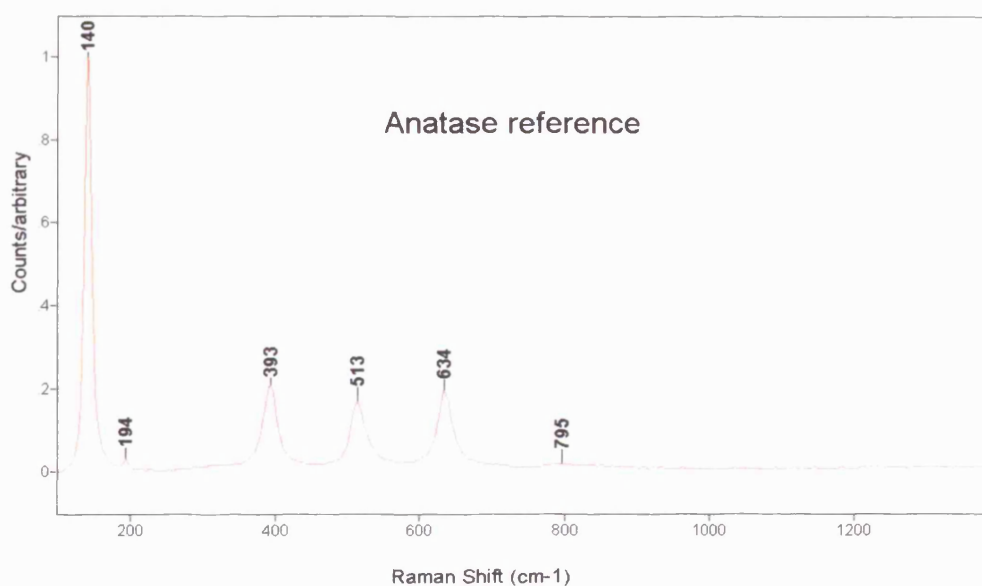


Fig. 12.7. Reference anatase spectrum.

Several of the colourless, low relief needles were analysed. In all cases, the Raman spectrum was identified as α -quartz. Some analyses returned spectra with bands attributable to hematite in addition to those of quartz. The Raman spectra of mullite and the high-temperature forms of SiO_2 are significantly different. A Raman spectrum recorded from a needle is shown in figure 12.8 with a reference spectrum of α -quartz. There is excellent agreement between the two spectra, apart from the additional band in the 5M sample spectrum at about 147 cm^{-1} . In the absence of

any other significant additional bands it is possible that the presence of the band is orientation-dependent.

It was not possible to positively identify any of the mullite, rutile and crichtonite, $(\text{Fe}^{2+}\text{Fe}^{3+}\text{Ti})_{1.71}\text{O}_3$, phases detected by powder XRD in sample 5M using microRaman spectroscopy.

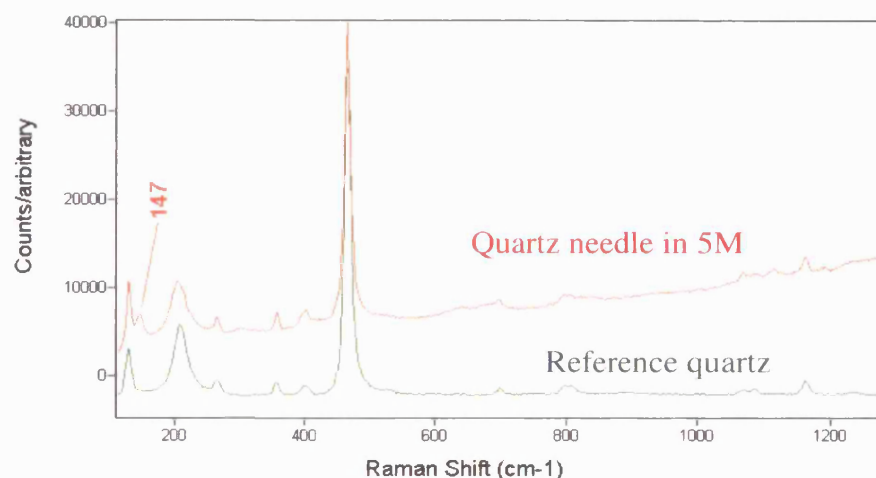


Fig. 12.8. α -quartz Raman spectrum from needle in sample 5M and reference sample.

2.4 – Discussion

The purpose of performing powder XRD analysis on these fired materials was to support identification of phases determined to be present using microRaman spectroscopy. However, the results do clearly display the phase changes; the gradual loss of clay minerals to form the K,Al-rich glass (and later mullite), the dehydroxylation transformation of goethite, $\alpha\text{-FeO.OH}$, to the high-temperature stable form hematite, $\alpha\text{-Fe}_2\text{O}_3$. As the temperature increases some of the Fe is combined with the Ti to form pseudorutile, $\text{Fe}^{2+}\text{Ti}_3\text{O}_9$, then crichtonite, $(\text{Fe}^{2+}\text{Fe}^{3+}\text{Ti})_{1.71}\text{O}_3$. Anatase is detected in the briquette fired to 950°C . The transformation of anatase, the low temperature polymorph of TiO_2 , occurs at temperatures greater than 730°C (Deer *et al*, 1992). The occurrence of anatase in sample 4M, fired to 950°C , could be explained by the dependence of this reaction upon the fineness of the material and the short soak time. Anatase shares very similar d-spacing reflections with pseudorutile and it is possible that the assignment of peaks to anatase is incorrect. Analysis by EMPA would help determine the chemical nature of this phase.

The extremely fine-grained nature of the material made any optical studies impossible. The XRD results for the bulk raw material are similar to that detected by McKnight (1991). He observed hematite additionally, but not chlorite or gypsum.

Due to problems of sample heating and subsequent excessive luminescence overwhelming the Raman spectra, few results from the Raman analysis of the samples are presented here. However, the experiments that were successful raise some interesting points. The strong band at 1351 cm^{-1} for the 5M sample in figure 12.5 is considerably broader than that in the reference hematite spectrum. This difference could be associated with the very fine particle size in the sample (the reference was almost certainly recorded from a single, euhedral crystal) or, possibly, due to disorder in the lattice.

White (In: Farmer, 1974) notes that a deviation from stoichiometry can result in large differences in Raman bandwidths and intensities. The effect is poorly studied but one study suggests that the bandwidth change can be used to measure the degree of non-stoichiometry in some compounds. All the hematite bands in sample 5M are broader than those of the reference which points to disorder differences. The differences in relative intensity between the bands around 294 cm^{-1} for the sample and reference spectra in figure 12.5 might be attributed to orientation effects. Additional bands in the sample spectrum could be assigned to quartz or ilmenite, FeTiO_2 , both of which also have a peak close to 461 cm^{-1} . The broad band around 683 cm^{-1} also suggests an ilmenitic component to this analysed region. Figure 12.9 shows a reference ilmenite spectrum.

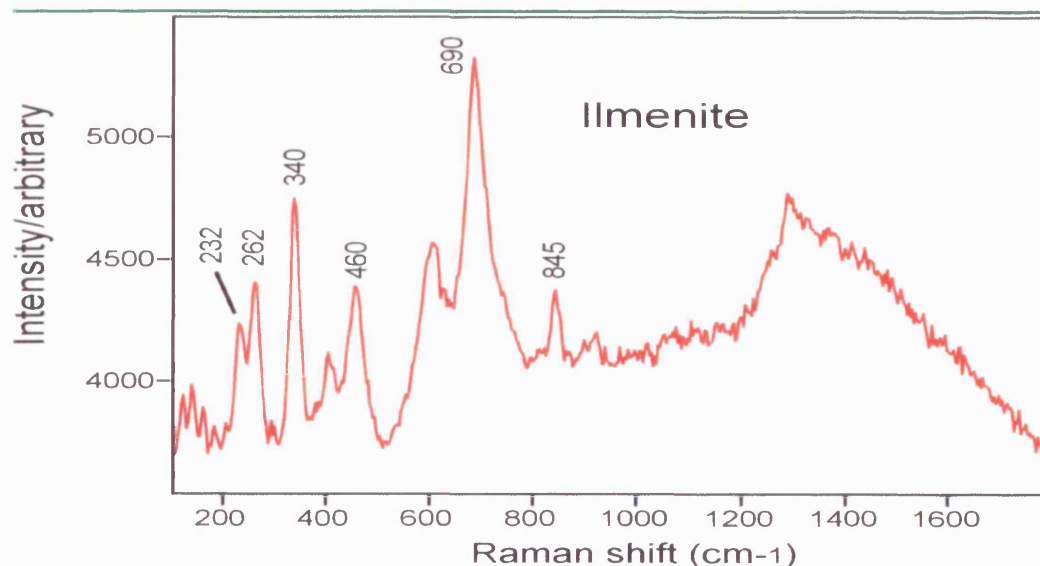


Fig. 12.9. Reference ilmenite spectrum.

The strongest band in the ilmenite spectrum is at approximately 690 cm^{-1} , close to the position of the 683 cm^{-1} band in figure 12.5. The ilmenite identification could be supported by the fact that at high temperatures a solid solution exists between hematite and ilmenite (Deer *et al*, 1992). The hematite-ilmenite series probably does not fit into either of the classic ‘one-mode’ or ‘two-mode’ behaviour models in terms of their Raman response. One-mode behaviour is characterised by a shift in band frequencies between the (very similar) end-member spectra. This model conforms to factor group analysis. Two-mode systems break the selection rules (White, *In*: Farmer, 1974) and intermediate compounds along the solid solution have Raman bands belonging to both end-members. As the percentage of each end member changes the relative intensities of the Raman bands change. The presence of both ilmenite and hematite bands could also be explained by the laser spot overlapping and exciting two or more grains. Given the very fine particle size and non-confocal instrument arrangement this might be a possibility. It should be noted that ilmenite was not detected in any of the samples analysed by the XRD method.

Figure 12.6 strongly suggests the presence of anatase in the 5M sample. This appears to support the interpretation of the XRD data that anatase is present in sample 4M. The XRD data for sample 5M did not suggest the presence of anatase. The identification of goethite is less sound, however. There are strong matches only with the 211 cm^{-1} and 277 cm^{-1} bands of the sample and reference goethite. Neither of these bands occurs in the hematite or ilmenite Raman spectra

(figures 12.5 and 12.8, respectively). From the XRD analyses, goethite is only detected in the raw material; none of the fired samples appear to contain this phase. It is possible that the XRD data was misinterpreted or that the Raman bands at 211 cm^{-1} and 277 cm^{-1} are common to mullite or crichtonite (or even pseudorutile). Mullite has the formula $3\text{Al}_2\text{O}_3 \cdot 2\text{SiO}_2$ with a structure similar to sillimanite consisting of Al octahedra cross-linked by Al and Si tetrahedra (Deer *et al op. cit.*). The Renishaw database of mineral spectra reveals a simple spectrum for mullite consisting of only two bands located at 440 cm^{-1} (actually a broad band centred at 441 cm^{-1} with a weak shoulder at 408 cm^{-1}) and 609 cm^{-1} (actually a band at 609 cm^{-1} with a weak shoulder at 577 cm^{-1}). The mullite reference Raman spectrum appears in figure 12.10. Poor signal to noise ratio makes it difficult to confidently determine additional bands at either higher or lower wavenumbers.

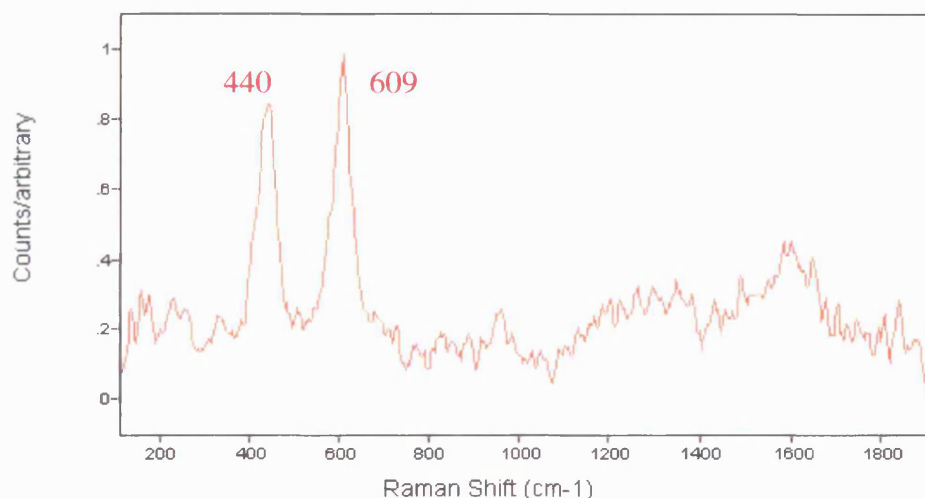


Fig. 12.10. Reference mullite spectrum.

Given the comparably simple structure, it appears logical to assign the lower frequency mode to the symmetric stretch of the Si tetrahedra (the band is located at 465 cm^{-1} in α -quartz) and the higher frequency mode to the identical motions of the Al tetrahedra. McMillan & Piriou (1982), however, assign aluminate-stretching frequencies in mullite to around 700 cm^{-1} from their work with glasses along the SiO_2 - MAIO_2 join. The structure of the glass can be considered in terms of isolated structural units. In crystals the interactions between the different structural units becomes important and this could lower the frequencies. Also, since the symmetric stretching motions of $(\text{Si,Al})\text{O}_x$ polyhedra are highly polarised the absence of strong bands around 700 cm^{-1}

in the reference mullite spectrum could be ascribed to polarisation. None of the bands listed for mullite are close to the 211 cm^{-1} and 277 cm^{-1} bands currently assigned to goethite.

Crichtonite and pseudorutile do not appear in the Renishaw database. With the formula $(\text{Fe}^{2+}\text{Fe}^{3+}\text{Ti})_{1.71}\text{O}_3$, crichtonite might be expected to have Raman bands at lower wavenumbers than mullite due the motions of the large, heavy Fe and Ti atoms. Similarly, the Raman spectrum of pseudorutile ($\text{Fe}^{2+}\text{Ti}_3\text{O}_9$) might also be expected to have its strongest Raman bands in the lower region of the spectrum, as is found for ilmenite, hematite and goethite. These are, of course, generalisations and the band positions will be highly dependent on the crystal structure, site symmetries and bond character.

It was hoped that at this early stage in the investigation that the presence of mullite could be firmly established using Raman spectroscopy. This is the phase identified by McKnight (1991) as the principal strength-providing component in bricks. Analysis of sample 5M by XRD confirms the presence of mullite above $1050\text{ }^\circ\text{C}$. The studies of McKnight (1991) suggest that sample 5M underwent firing that placed it only just within T-T-t space where the assemblage anatase + K-feldspar + hematite + quartz + mullite + ilmenite is stable. This, and the fact that the mullite crystals are likely to be of the order of five micrometers long (McKnight, 1991) and weak Raman scatterers, probably explains why mullite was not detected. McKnight found that for a four-day soak period at $1300\text{ }^\circ\text{C}$ mullite crystals attained typical dimensions of fifty micrometers by 0.5 micrometers.

It has not been possible to comment upon the formation, distribution or role of glass in the brick samples. Identified as the key matrix component binding mullite and other strength-forming grains together (C.A. Jeffrey pers. comm.), vitrification may occur at around $900\text{ }^\circ\text{C}$, depending on the starting composition, and in particular, carbonate content (Alia *et al* 1999). Raman spectroscopy is not suited to compositional studies of glasses although the method has been applied to synthetic glasses along relatively simple systems (see section 6 for a discussion of Raman spectroscopy in glass analysis). In the brick samples, it should be possible to identify regions of glass from crystalline material with the caveat that chemical analyses be performed by EMPA, for example. The major limitation to this aspect of study would be fluorescence and an

FT-Raman approach may be most suitable. Performing area maps could provide useful insight in to the abundance of glass that could then lead to optimisation of firing conditions or use of fluxes.

2.5 – High temperature Raman analysis

The microRaman analyses discussed were all carried out at room temperature. As was stated in the introduction, the ultimate aim of an investigation of this type is to perform *in situ* analysis in the kiln.

There are practical difficulties with performing analysis of this type at elevated temperatures. The largest physical problem is the overwhelming effect on the Raman spectrum caused by black body emission. At temperatures over 800 °C this is particularly acute (Dr. K. Williams pers. comm.) and leads to the weak Raman bands being hidden beneath a very strong background. With long excitation wavelengths i.e. near-IR, the problem is exacerbated. Selecting an excitation wavelength as far as possible from the IR presents the only solution. Howard Sands (internal Renishaw plc report, 2000) notes that wavelengths below 500 nm should be used, and preferably in the UV range. However, UV-Raman requires the use of special, quartz optics since glass absorbs UV energy. This makes the instrumentation very expensive. In addition, UV lasers are significantly more expensive than those operating in the visible or near-IR and also require more rigorous safety measures.

In a brief comparison exercise between 514 nm and 785 nm excitation, simple experiments were performed at elevated temperatures. A fragment of aggregated α -quartz grains around 2 mm across was loaded into a water-cooled Linkam T1500 sample cell. This device can be mounted on the microscope stage and allows small samples (<7 mm) to be heated in a controlled manner to 1500°C. Analyses were recorded at various temperature intervals to monitor the quartz “soft-mode” that lies at 207 cm^{-1} . The shift of this band to lower frequencies with increasing temperature is well-documented (e.g. Scott, **In:** Anderson, 1973) and disappears upon the phase transformation to β -quartz at 573°C. Analyses were continued to 600°C with the 785 nm laser and 800°C when using the 514 nm laser. As expected, the background due to thermal effects was very much lower in the visible than in the near-IR. At 600°C the spectra in the near-IR were

dominated by a steeply-sloping background that masked all but the strongest Raman bands. With 514 nm excitation at 800°C the background was very shallow and all bands were clearly resolved. It should be pointed out that the effect on the Raman spectrum is an exponential rise (Dr. I.P. Hayward, pers. comm.) in the background level as temperature increases and that we might expect glass not to be formed in bricks until a temperature of around 900°C is attained. Despite the experiment being terminated at quite moderate temperatures, the data confirm that short excitation wavelengths are preferable for studies at elevated temperatures.

There are several manufacturers of high-temperature probes that are adequate for the purpose outlined. They typically have sapphire windows, which can be problematic since sapphire has very strong photoluminescence bands in the visible spectrum. The bands are well-characterised so could be subtracted but they may mask weak Raman bands that occur in the same region. The probes are based on fibre-optic technology. Whilst the efficiency of the fibres is good, the coupling between the laser and fibre can be rather inefficient, introducing losses. This requires the use of much higher-powered lasers. Also, the minimum laser spot size achievable beyond the probe is limited by the diameter of the fibre; typically fifty micrometers. This greatly reduces the spatial resolution that can be achieved.

With a suitable laser (perhaps a high powered 457 nm, 488 nm, 514 nm or even 532 nm) and probe, it may be possible to successfully record bulk Raman spectra from brick samples within a kiln. It may be advantageous to analyse the anti-Stokes region since these bands will be shifted to longer shorter wavelengths and thus be ‘further’ from the heat-induced luminescence. As stated in section 2 the population of molecules in elevated energy states is also higher at elevated temperatures.

2.6 – Conclusion

Despite the inconclusive results presented here, microRaman spectroscopy may well add to the research into brick mineralogy. This may be the first application of dispersive microRaman spectroscopy to the study of fired brick samples. Several of the mineral phases were identified and the technique is able to distinguish between all of the phases listed in Table 12.1. The Renishaw database of mineral spectra is based upon gemmological samples, however, it does

contain a huge variety of rock-forming minerals and minerals whose rarity is a function of their more extreme stability fields, i.e. mullite. A database of minerals and materials relevant to the brick-making industry would be advantageous in further studies of this nature. Of particular relevance to this study would be to obtain the Raman spectra of pseudorutile and crichtonite.

Results from Raman spectroscopy presented may indicate the presence of a solid solution series between hematite and ilmenite at the highest temperature of firing. This submission could not have been made without evidence from this technique. XRD analysis of material falling between the two end-member compositions would have produced ambiguous results. EMPA though analysis would help to determine the exact composition it would not have elucidated the structure of the compound.

The high Fe content of the material used in this study limited the investigation. The selection of a different starting assemblage or alternative excitation wavelength may lead to better results.

2.7 – Further studies

An interesting area of further study may be to re-analyse the micro regions that appeared to be damaged by the absorption of the incident laser energy. If the structure could be determined or recognised this could have implications for other high temperature studies of minerals. The power densities available using microRaman are of the order of hundreds of kW cm² (Dr. A. Zimmerman, pers. comm.). There are few other means of supplying energy of this magnitude to minerals and causing highly-localised heating.

The previous discussion clearly leads to a revised program of study. A new starting assemblage was selected based on the basic common mineralogy of UK brick clays. This constitutes a mix of kaolinite (K) or illite (I), quartz (Q), mica (M) or feldspar (F) and very minor hematite (H). It is thought that these raw materials, if adequately pure and a reasonably coarse grain size could be bought together and fired to provide a more workable material to continue the Raman assessment. To provide adequate aluminosilicate and fluxing components the mix would have to be in the approximate proportions: 60% K or I, 30% Q, 8% H and 2% F or M. The firing conditions will more closely follow McKnight's (1991) study and involve different sample

preparation methods. Essentially this will involve the use of alumina crucibles and firing to greater temperatures and soaking for longer periods of time.

The microRaman analysis of the samples should also be carried out under confocal optical conditions. This would allow much greater spatial resolution by reducing the effects of refraction. This method represents the maximum spatial resolution available for structural and chemical differences across grain boundaries using Raman. However, the transformations may well be on a sub-micrometer range and require a different technique, such as TEM.

Studies based on the use of high temperature probes should only be initiated when the microRaman technique has been shown to provide data on the mineral transformations that occur on firing. The first step might be to perform real time analyses in a high temperature cell mounted on the microscope stage of a microRaman instrument. The Linkam T1500 is capable of heating a small volume of sample to 1500 °C in a controlled manner. Raman spectra recorded at set temperature intervals may record the important transformations and the crystallisation of mullite and the nucleation and growth of glass, for example.

13 - Investigation of limestone organic content

This section concentrates on an application of the ‘Global Raman imaging’ facility of the Renishaw RM 2000 instrument. In this fourth assessment of Raman spectroscopy applied to investigating processes affecting natural materials, imaging is used to examine the spatial distribution of the organic matter present in a limestone.

13.1 – Introduction

Some limestones are well known to contain appreciable organic matter. Petrography and residue analyses have shown that the concentration may be significant. The presence of organic matter reflects the ‘original organic input and subsequent processes of diagenesis and metamorphism’ (Tucker, 1991). For organic matter to persist in a lithified rock then either anoxic conditions must have prevailed since deposition (Tucker, 1991) or the organic material represents an extremely recent event.

The distribution of the organic matter is of interest since it might allow a greater understanding of the mechanisms controlling fluid flow through lithified bodies. This can be important, for example, in locating fossil fuel reserves or deposits of economically important minerals.

Carbon in geological materials is well-studied using Raman spectroscopy. References in Jehlička *et al* (1997) describe the characterisation of coals, anthracites, kerogens and graphitoids from metasediments as well as graphites and diamonds. A clear advantage of using Raman spectroscopy to study carbon is that the technique is able to distinguish not only between carbon bound in the structure of minerals, e.g. the carbonate anion CO_3^{2-} , and organic carbon, but also between the different polymorphs of carbon. Whilst XRD can differentiate between the crystalline forms, amorphous C has no diffraction pattern. Of the few chemical methods available, none are microtechniques. The technique has also been applied to synthetic carbon compounds, pigments and catalysts (references in Jehlička *et al*, 1997). There are also technological applications using Diamond-Like-Carbon (DLC) films where the first order carbon Raman spectrum is used to quantify film quality and thickness.

13.2 – Samples

The samples used were collected by Mr. C.A. Jeffrey from Carboniferous Limestones sequences from Derbyshire, England. Representative samples from each horizon collected were prepared as uncovered thin sections for petrography. These sections were also used for the microRaman analysis in this study. The sequence contains both dark and light coloured calcareous rocks, the former containing significantly greater proportions of organic matter. The organic, bituminous matter probably represents ancient flora and fauna. There are differing postulations of the distribution of the organic matter. It may reflect the transportation to the sedimentary sequence of an allogenic component, probably related to fluid movement associated with the North Sea oil field and driven by vast hydrostatic pressure. Alternatively, the distribution within the sections studied resembles that of organic-filled stylolites. Irregular, suture-like boundaries are observed to exist in some limestones and evaporites in response to chemical compaction (Tucker, 1991). Overburden or tectonic stresses can cause increased solubility along grain boundaries, leading to pressure-dissolution of the grains; insoluble residue including clay particles, organic matter and iron minerals can become concentrated along the stylolites that cut across grains, cement and matrix (Tucker, 1991).

Petrography

The carbonate rocks used in this study would be classified as biosparite or biomicrite to bio-oosparite or bio-oosparite (after Folk, 1962, in Tucker, 1991), or as skeletal grainstones using the nomenclature of Dunham (1962 **In:** Tucker, 1991). The grains are quite brown and turbid in those thin sections with a high presence of organic matter. Matrix grains are relatively large (centimicron-sized) and anhedral to subhedral with straight and irregular grain boundaries. A fine-grained, micritic matrix is also present in these heterogeneous samples. Raman spectroscopy of the matrix reveals the presence of calcite, quartz and organic matter. Commonly, a drusy mosaic replacement occurs with the infilling of voids in bioclastic fragments. The origins of the bioclastic are largely *mollusa*; brachiopods, bivalves, gastropods, echinoderms and foraminifera. There are also coral remnants. The petrography suggests a carbonate shelf slope or reef or other wave-dominated shallow marine depositional environment. The bioclastic nature of the rock is highlighted in Figure 13.1.

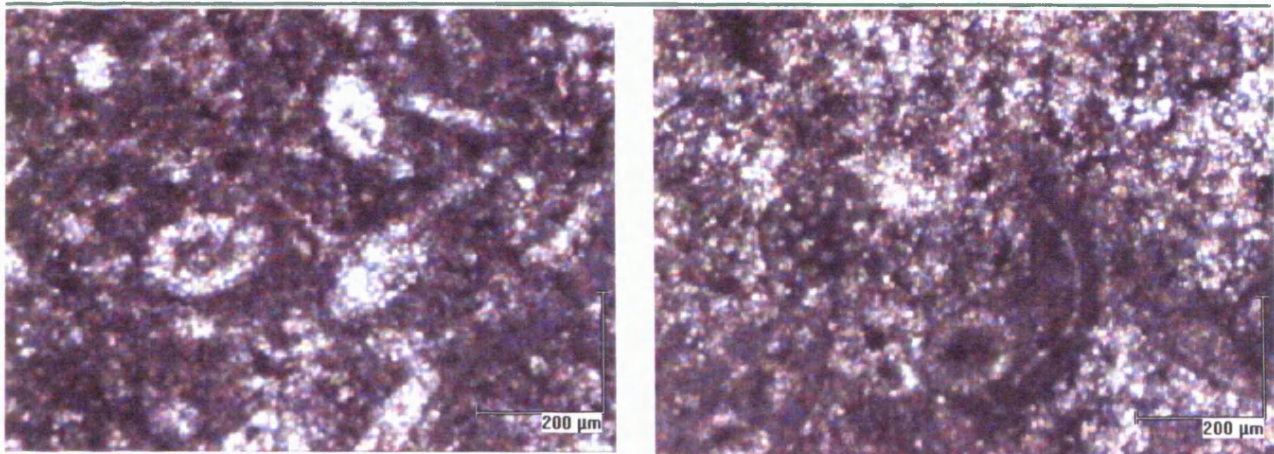


Fig. 13.1. Low magnification PPL images of bioclastic limestone. Note the rich presence of bioclastic fragments.

The organic matter is characterised by persistent, opaque ‘strands’ that resemble stylolites. In places the strands bifurcate and split or collect in much thicker ‘seams’. Generally, the strands pass along grain boundaries but the bitumen also collects in ‘ponds’ and in bioclastic fragments and voids. Without the benefit of the hand specimens or the field relationships, the overall trends in orientation of the bituminous matter cannot be determined. The thickness of the strands varies greatly; thin coatings following grain boundaries can be resolved using the microscope whilst in places visual inspection of the thin section easily reveals the irregular and erratic paths of the jet-black material in places. Captured images of thin grain coatings and thicker ‘seams’ are displayed in Figure 13.2.

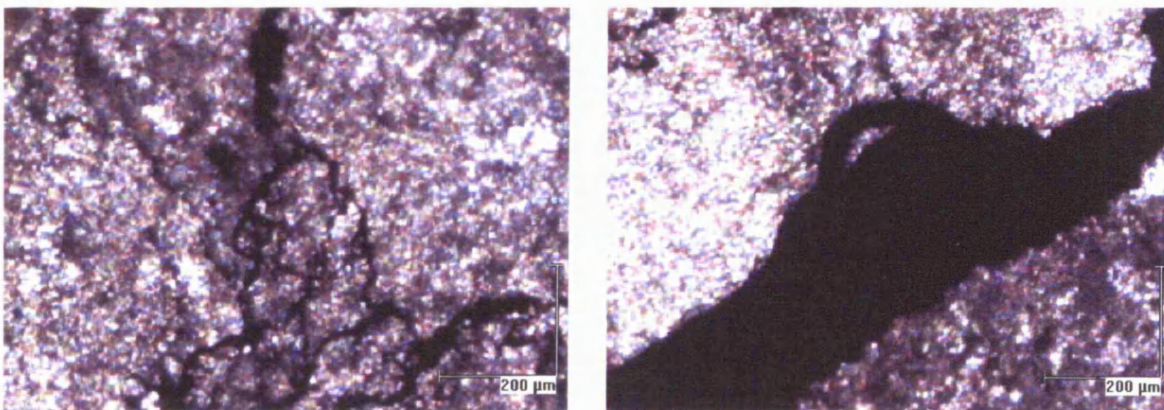


Fig. 13.2. White light images (PPL) of bituminous matter in limestones.

13.3 – Experimental procedure

For experiments using global Raman imaging (for description of the analytical method see 3.3) regions within the thin sections were selected that had distinctive patterns of organic content. Selection of these areas would facilitate the correlation with Raman images created. The size of the regions had to be carefully considered. Raman images can be collected theoretically with any of the objectives available (5x, 10x, 20x, 50x and 100x). Images of larger areas are possible using the low magnification objectives, however, since the NA, i.e. the light-collecting efficiency, increases with magnification and the free working distance decreases (i.e. less potential for stray light contamination) there is a trade-off. Table 13.1 summarises the relevant optical properties of two of the objectives used when recording Raman images.

Objective	NA	Free working distance/ micrometers	Field of view/ micrometers	Defocused spot diameter/ micrometers
x20 NPlan	0.4	1100	~250	~75
x50 NPlan	0.75	380	~100	~30

Table 13.1. Properties of the 20x and 50x objectives for imaging experiments.

A Raman grating spectrum was recorded from a region of the opaque, bituminous matter using 514 nm excitation to determine the position of the band that could be used to image. The spectrum displayed in Figure 13.3 is typical of amorphous carbon with two main broad bands. The higher frequency band is called the ‘G’ (or ‘graphite’) band and is a representation of the E_{2g2} vibration (Jehlička *et al*, 1997). Other, weaker G bands appear in regions of the Raman spectrum not covered in this study. The main lower frequency band is termed the ‘D’ (‘defect’ or ‘diamond’) band. The main D band (‘D₁’) at 1360 cm^{-1} is accompanied by four other defect bands. The intensity of the defect band indicates the disordered nature of the bituminous material. The positions of all five bands are indicated in the curve-fit in Figure 13.4. The Raman spectra of ordered graphites have a much higher intensity ratio of G to D and the bands are much sharper than in amorphous carbon. In diamond only the D band is present. It is extremely intense and may have a FWHM of only several wavenumbers.

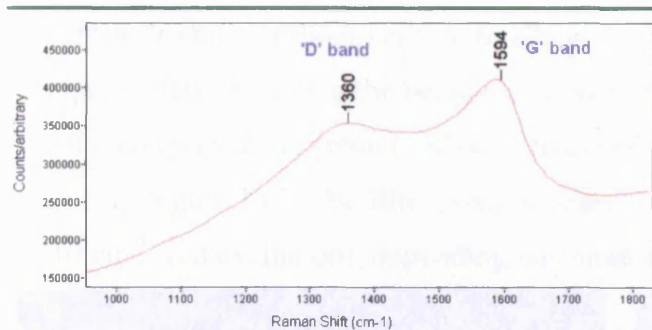


Fig. 13.3. Raman spectrum of amorphous, bituminous matter.

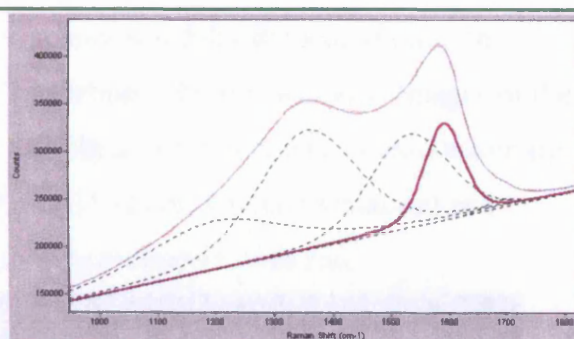


Fig. 13.4. Curve fitting of five first order carbon Raman bands.

The G band was selected to use for imaging. It is significantly sharper (approximately 80 cm^{-1}) than the D_1 band (approximately 200 cm^{-1}) although slightly less intense. A Raman spectrum using the filters instead of the grating was performed with the scan range between 1500 cm^{-1} and 1700 cm^{-1} with a one second exposure at each position. Curve-fitting the resulting spectrum indicates the position at which the filter should be centred. The filter spectrum and curve-fit are shown respectively in Figures 13.5 and 13.6.

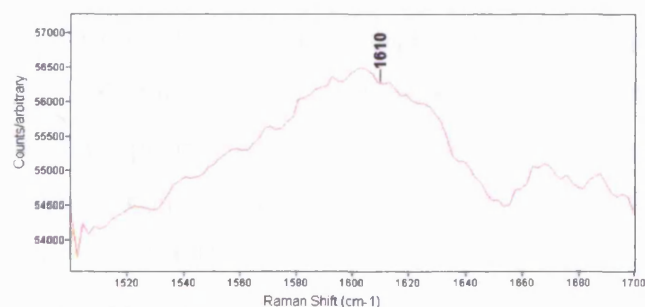


Fig. 13.5. Filter spectrum of G band.

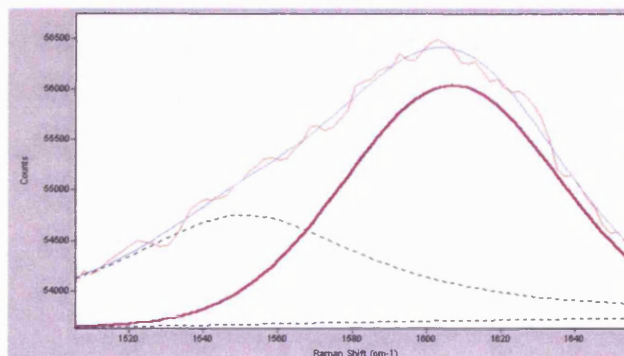


Fig. 13.6. Curvefit of G band (thick line) and a defect band (dashed) to data (red line).

There is a significant discrepancy between the positions of the centres of the G band recorded using the grating and the filters. The difference arises due to the different calibration procedures between the grating spectrometer and the filter path. Since the imaging is not used in this instance for qualitative analysis, i.e. determining the species, the difference in band position can be ignored.

Images were created with both 514 nm (green) and 633 nm (red) lasers during different analytical periods. Either of the visible excitation wavelengths is suited for producing a Raman

spectrum from amorphous carbon. In all cases, the laser spot was fully defocused on to the sample surface by setting the beam expander in the 'Experiment Set-up' window. Images of the defocused spots using green (x50 objective) and red (x5 objective) lasers on a silicon wafer are shown in Figure 13.7. The filter position was centered at 1592 cm^{-1} (green excitation) and 1610 cm^{-1} (red excitation), depending when the imaging experiments were run.

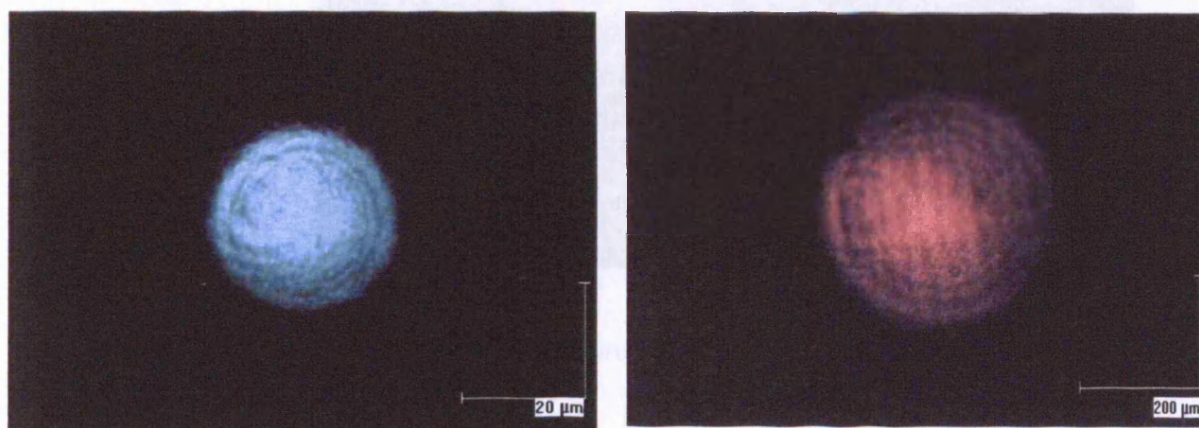


Fig. 13.7. Defocused spots with green and red excitation.

Exposure times used for image collection varied between 60s and 1000s. Similarly, the x5, x20 and x50 objectives were experimented with to determine which gave the best results. As with grating spectra, the signal strength of images depends upon the scattering potential of the species. As with conventional photographic cameras, very long exposure times will result in poor image quality. With Raman images, an over-exposure time causes a loss in the spatial resolution as the image becomes blurred. Conversely, if exposure times are too short, insufficient signal might be collected to form a quality image. Figure 13.8 is a Raman image reproduced from Figure 3.11 that shows the distribution of micrometer-sized grains of pyrite disseminated in quartz.

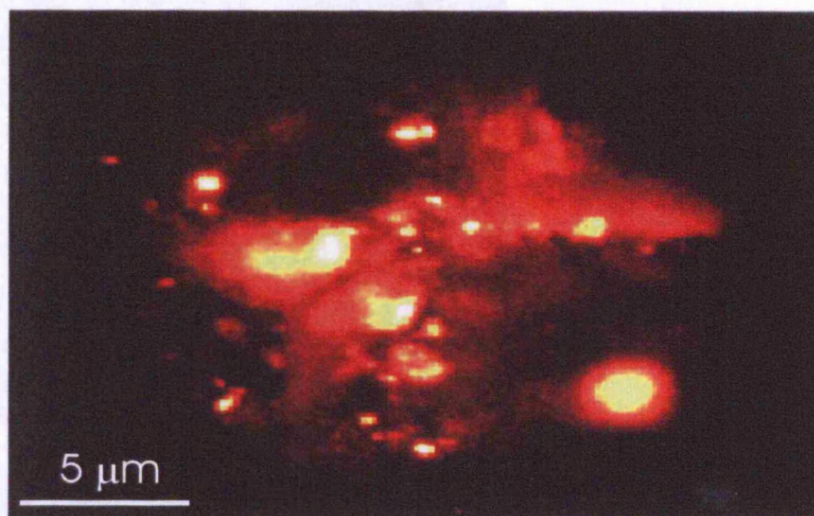


Fig. 13.8. Raman image of pyrite in quartz to highlight spatial resolution.

13.4 – Results

Several imaging experiments were carried out. Some results are presented in Figures 13.9 and 13.10 with the corresponding white light image captured from the microscope camera. An approximate position of the imaged area is given. The Raman images are coloured using the ‘Fire’ and ‘Earth’ colour schemes for clarity. In each case the brighter areas correspond to greatest intensity of the signal that passed through the filter. Some images were also created by selecting the $\nu_1(\text{CO}_3)$ band of the calcite at around 1086 cm^{-1} .

None of the Raman images shown were flat-fielded to correct for the effects of non-uniform illumination of the sample surface. The images could be misleading without this correction; bright areas might simply be caused by increased Raman signal corresponding to increased excitation by the laser, since the intensity of the Raman is proportional to the intensity of the laser. A good example is that shown in image E. From the white light we might conclude that the gastropod whorl is essentially uniformly distributed with organic matter. From the Raman image the distribution appears greater in the centre and to the right.

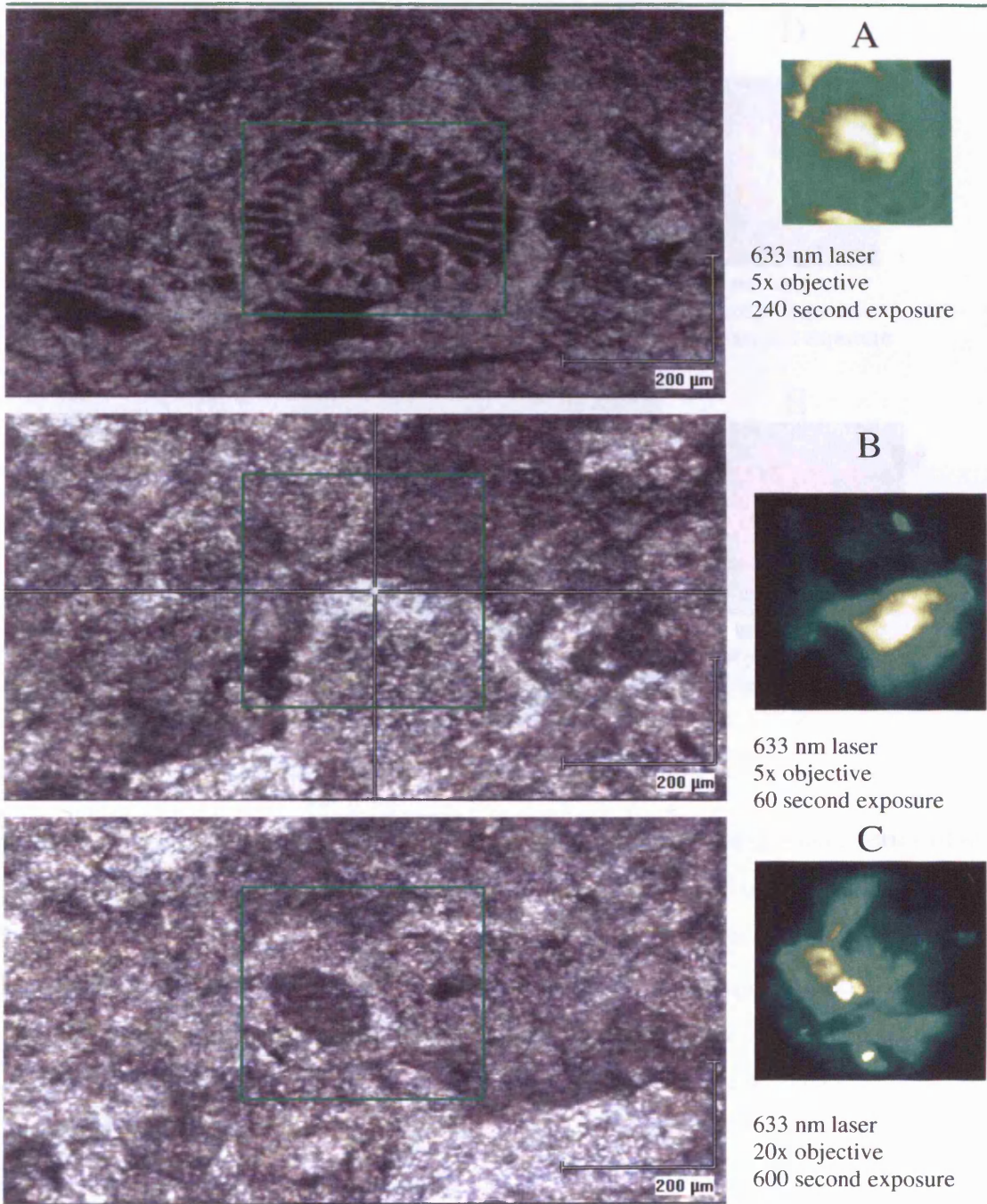


Fig. 13.9. Imaging of bituminous matter in limestones.

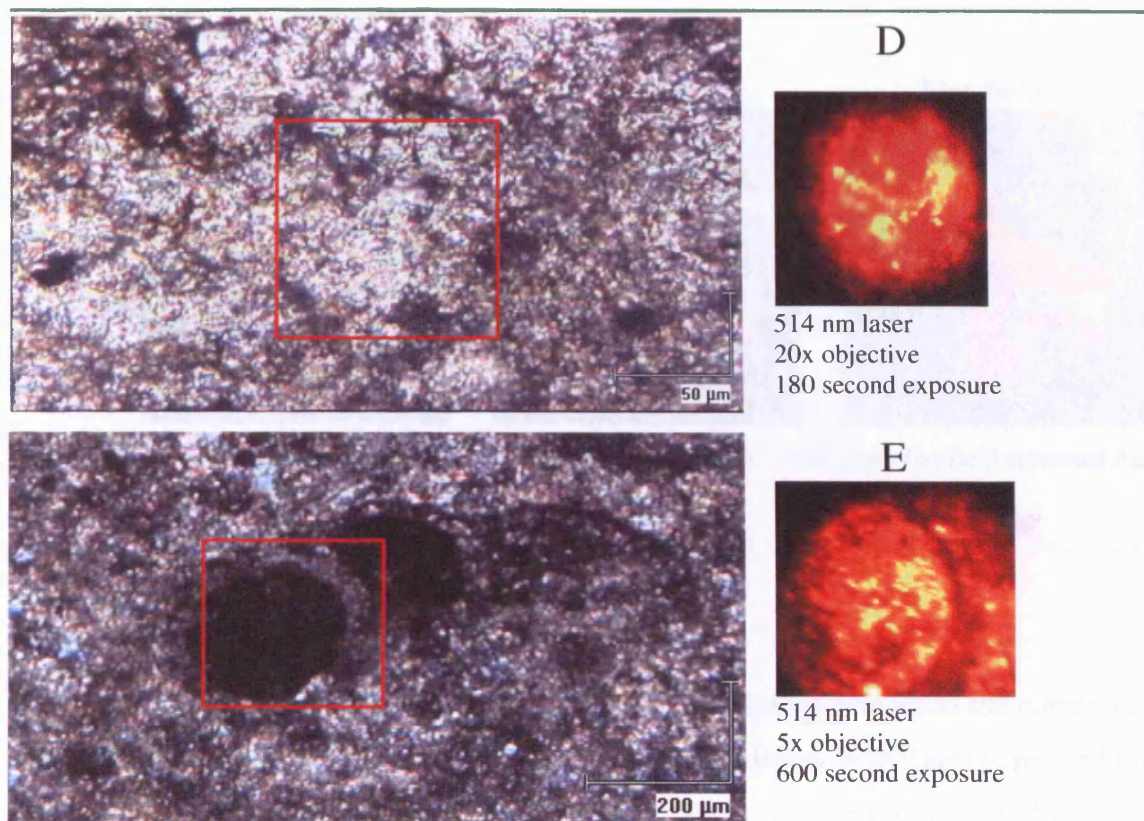


Fig. 13.10. Imaging of bituminous matter in limestones.

Flat-fielding was applied to some Raman images recorded during a later series of experiments on the limestone samples. Figure 13.11 shows a raw, uncorrected image compared with two corrected versions. In each, the colour range, or Look Up Table (LUT) has been altered through the software to improve the contrast of the image. This technique is routinely used in the analysis of both Raman images and maps. During the alteration, the data is not changed, merely the way the map or image appears. The bright areas correspond to the presence of the carbon 'G' band. Flat field correction 1 was performed using an image recorded from a Si wafer prior to the acquisition of images from the sample. The second Si image file was created later with slight change in laser power to demonstrate the importance of rigorous analytical procedure. Errors in the correction can be seen as slightly brighter areas both in and around the illuminated region.

In all three images in Figure 13.11 the main regions of carbon in the illuminated area are clearly identifiable. Applying the correction has the effect of slightly increasing the spatial resolution of the image.

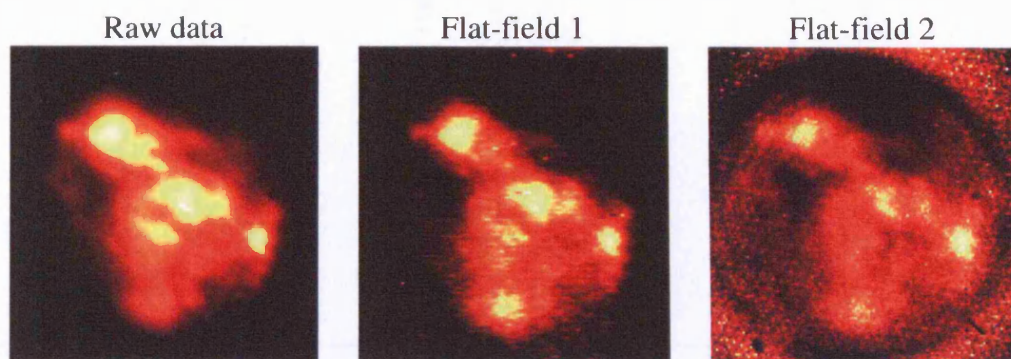


Fig. 13.11. Raman image from uncorrected data and two images from flat-field corrected data

13.5 – Discussion

It proved difficult to match many of the features in the Raman images to the corresponding white light image. It appears that that in the version of the Renishaw WiRE software used that the images were 'flipped' both horizontally and vertically relative to the white light image. In some cases, however, it was possible to correlate features of the images once this had been corrected. For example, the foraminifera chambers in A, the distinctive shape of grains in C and the gastropod chamber wall in E. The Raman image in D shows a significant amount of detail. However, none of the features can be correlated to the white light image.

The Raman images created during these experiments are not of very high spatial resolution. Organic matter (amorphous carbon in this case) is not suitable for Raman imaging due to the large bandwidths of the main first order D and G bands (200 cm^{-1} and 80 cm^{-1} , respectively). The bandpass of the filters used to screen out the unwanted signal is only approximately 20 cm^{-1} . Figure 13.12 indicates the approximate position of the filter within the spectral range covered.

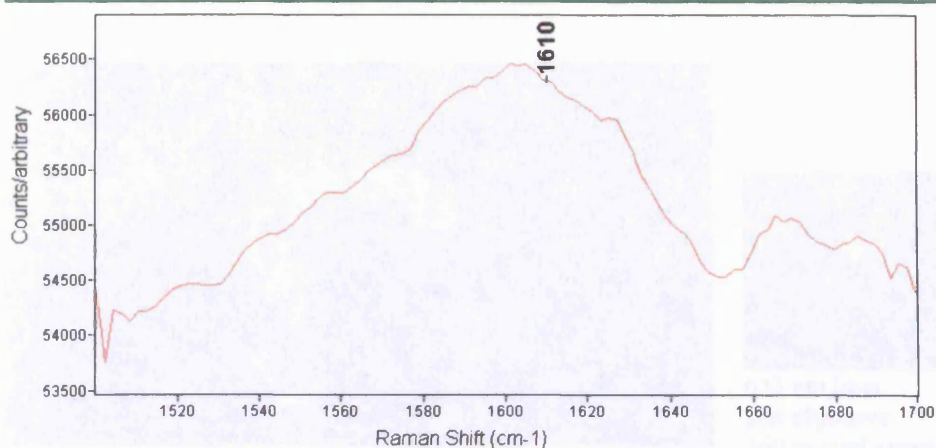


Fig. 13.12. Filter spectrum of G band and approximate position of filter bandpass.

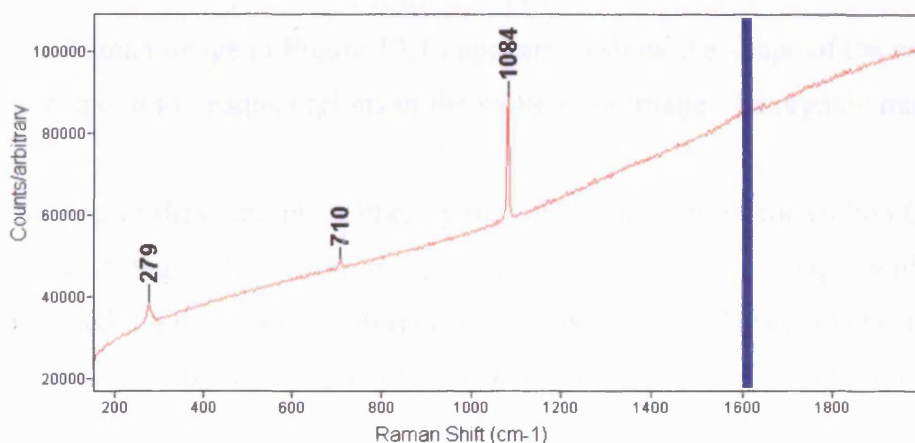


Fig. 13.13. Grating spectrum of calcite from limestone used and the position of the filter. Note the high background.

It is clear that the G band is significantly wider than the bandpass. Considering the very high background signal in the grating Raman spectrum shown in Figure 13.13 it is not surprising that there is low spatial resolution in the images. Images with better resolution might be expected from imaging the $\nu_1(\text{CO}_3)$ band. Figure 13.13 points to the inherent sharpness of this band (a FWHM value of 3.9 cm^{-1} was determined from the data), a function of the highly ordered nature of the anion and the symmetry of the structure and the vibration. Two images were created in the same manner as outlined for the carbon G bands. A filter spectrum was recorded from a calcite grain to determine the optimal filter position for imaging experiments. Of these two images, that displayed in Figure 13.14 gave the better image.

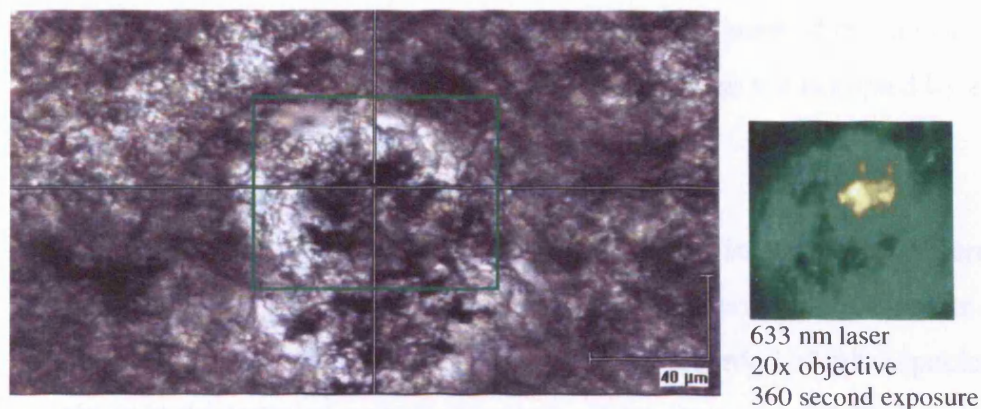


Fig. 13.14. Raman imaging of calcite grains with organic matter.

The Raman image in Figure 13.14 appears to show the shape of the calcite grains. Dark patches correspond to opaque regions in the white light image; the organic matter.

Imaging of these samples either by the carbonate band or the carbon G band is clearly affected by the strong background present in the Raman spectrum. Images with better resolution would be obtained if a background subtraction were performed. This could be an image recorded in the same manner but in a region of the spectrum where there are no Raman bands.

Flat fielding should be applied to images generated. Figure 13.11 indicates that often the raw data is sufficient to determine the spatial distribution of imaged components but that spatial resolution can be improved by the application of a mathematical correction for laser power distribution. However, in this study attempts to improve the images by correction were generally unsuccessful. Spurious signals can arise from the division of very large numbers, i.e. the intensity of the Raman signal or background from the sample, by very small numbers, i.e. the very low background given by the silicon wafer used for flat-fielding corrections. Consequently the intensity scales of the resulting image data can become extremely wide and the images become far less convincing than before flat-fielding correction. It is vital that the acquisition of correction data, i.e. a Raman image of the silicon wafer, be performed rigorously, immediately prior to or just after the sample images and checked for spurious features.

The technique of Raman imaging may be more applicable and suited to other geological or mineralogical samples than the ones studied here. The method requires a relatively strong, sharp band to image that is in a region of the Raman spectrum not occupied by another species, for example, the host mineral.

It may be useful for the technique to perform multiple images using different bands. It can be time-consuming to set up the imaging experiment, potentially eroding the speed advantage the method has over point-by-point mapping. Images recorded of other species would offer far more insight in to the sampled regions. Similarly, there are no post-collection analyses available. For example, mapping experiments permit the collection of a complete Raman spectrum at each point, allowing the data to be analysed and to comment on regions of the area studied rather than just to comment on the intensity of the imaged species.

In this study Raman images were collected with predominantly the 5x and 20x objectives. This was because the areas of interest were relatively large. Each performed adequately although better resolution appeared to be offered by the 20x objective. This is probably related to the smaller depth of field and increase in inherent confocality when using objectives of higher NA. The objective, then, becomes the limiting factor when projecting the incident laser over a large area.

13.6 – Conclusion

The imaging experiments in this study were partly successful. In the examples given in Figures 13.8, 9, 10, 11 and 14 it is possible to distinguish the selected species. The natural broadness of the G band and the high background signal contributed to the low spatial resolution when imaged. The latter also affected the images when the sharp ‘carbonate band’ was selected. Images with increased spatial resolution would be obtained with a sharp ($<20\text{ cm}^{-1}$) band and a low background.

The results suggest that the spatial resolution is insufficient for very thin strands of bitumen and can only be used to determine the distribution of much thicker strands. Obviously, these can be

determined from optical petrography. However for substances that have sharper Raman bands, the spatial resolution of the technique has been shown to be of the order of one micrometer.

Whilst imaging the calcite (e.g. the very sharp and intense $\nu_1(\text{CO}_3)$ mode) was able to define the grain boundaries it gave no indication of the nature of the material along the boundaries. Further 'point' grating Raman spectra would still be required to acquire this information.

Raman imaging is a powerful technique although experiments require careful preparation of the experiment and even some knowledge of the sample before analysis. It would be advantageous to record a background spectrum and remove this from the imaging data.

The values set for the exposure of the signal to the detector is also crucial. In general, image exposures might be ten/hundred times longer than that used to record a grating Raman spectrum. This value clearly depends upon the Raman scattering ability of the species.

13.7 – Further work

Clearly there is scope for the use of Raman imaging in studying Earth Science materials. The technique is only available with Renishaw RM 2000 instruments, which has limited its use. There is little published work using the method and of these very little is applied to minerals.

Penetration of the laser *through* the sample surface has been alluded to as a possible cause of low spatial resolution in the Raman images created in this study. Longer wavelengths penetrate further than shorter wavelengths and it would be of interest to examine further this effect on the resolution of the images. Various excitation wavelengths are available in the visible region. In addition, the effect of refraction of the laser upon encountering the surface will have some effect of the Raman signal generated. Incident light will 'bend' as it enters the sample and excite a far greater volume than is desired. The use of an oil and oil immersion objective may reduce the effects of refraction and reduce the excited volume, increasing the spatial resolution of the image. As has been stated, it is not possible to improve the confocality, i.e. the spatial resolution

beyond that determined by the objective selected but the use of these methods may be improve the results.

This study has attempted to use imaging in the 'conventional' manner, i.e. to discriminate spatially one species from another. However, the technique could potentially image the *change* in intensity and not just the presence of one species (i.e. Raman band) in another. For example, the chemical zonation in feldspars or other minerals that forms a solid solution that exhibit two-mode behaviour could be detected. Figure 13.15 displays an impression of a Raman image that could be generated from a concentrically chemically zoned crystal. The different colours represent different positions along the solid solution.

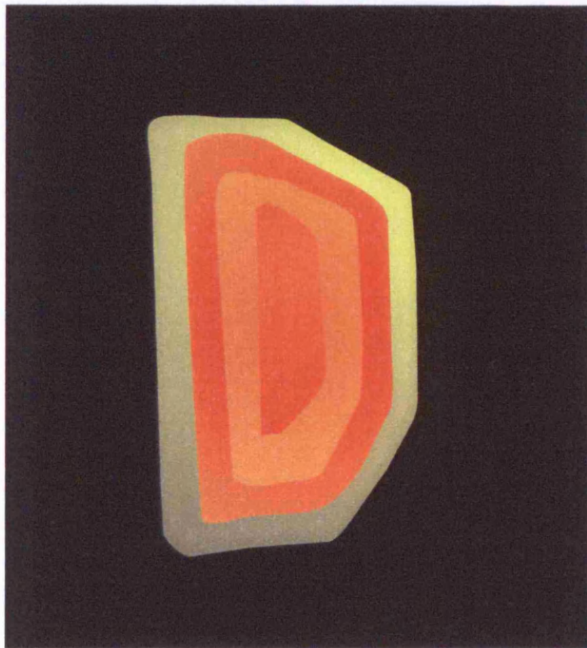


Fig. 13.15. Possible response of chemically zoned crystal to Raman imaging.

One-mode behaviour might also be detectable if the position of the active band sweeps *through* the bandpass of the filter. The images created may reflect a change in intensity if the transmission of the filter is greater towards its central position e.g. a Gaussian transmission profile. Optically this type of zonation may be detected by studying the birefringence, where it is of a high enough order. In some systems the birefringence change may be negligible or be masked by a strong mineral body colour and require EMPA analysis to detect.

Another application in petrology may be to determine the presence of overgrowths. If later crystal growth is chemical or structural e.g. non-epitaxial, there could be a difference in intensity that is detectable by using the filters. This method would be much faster than Raman point mapping and lead to information concerning the growth conditions and availability of elements, for example.

Chapter 5 – Technique development

This chapter comprises sections 14, 15 and 16 of the current work. During the course of this research project there appeared the need, and opportunities for, the technique and instrument to be developed to aid the analysis of minerals.

The design and construction of a macrochamber to attach to a fibre-probe head suitable for containing and manipulating gemstones is discussed. An assessment is given of the usefulness of adding a quarter-wave plate to the analysis of minerals and the design of a sample holder suitable for holding separated mineral grains for radiometric dating is discussed.

14 – Gem analysis macrochamber

The development of a macrochamber to facilitate the portable Raman identification of gemstones is seen as a crucial aspect in the development of the technique. This section describes the design and manufacture of a macrochamber for use with a fibre-coupled probe-head laser Raman spectrometer.

14.1 – Introduction

Raman spectroscopy increasingly forms part of the gemmologist's arsenal of testing devices. Many laboratories around the world use the technique to identify gemstone species. Its success in this arena is based on its non-destructive nature and unambiguity of results. The presence of fillers used to mask defects in the stone can be identified, as can the nature of inclusions. These may occur naturally and aid the determination of the provenance of the stone that in many cases has dramatic influence on the value. Similarly, certain inclusions are characteristic of crystals grown synthetically so can be used to distinguish natural from laboratory-grown specimens.

For many routine gemstone applications of the technique, it is the confirmation of identity that is required.

14.2 – Macrochamber design and use

Well-equipped gem-testing laboratories use bench-top research grade microRaman spectrometers. However, it was felt that there is a need for a much simpler version of the instrument that could perform the identification by Raman scattering but without the expense and that could provide greater mobility. Much of the cost of the laboratory versions of commercial Raman spectrometers is proportioned to the greater analytical flexibility, research-grade microscope and high spectral and spatial resolution available. Renishaw, plc manufacture a Raman system based on a hand-held probe-head linked to the laser source and the rugged spectrometer via fibre optic cable, the Raman Analyser, RA100. The probe-head is equipped with the necessary notch filters to remove the Rayleigh scattering from the excited signal. A small camera can be mounted on top of the housing to record a visual image through the objective lens. A representation of the RA 100 layout is shown in Figure 14.1. The laser

spot at the sample is limited by the diameter of the fibre carrying the laser, which is 60 micrometers.

Typical applications for the RA100 include production line quality control. Fibre-optic cable can efficiently carry signal over a distance of the order of 10's of metres, thus permitting the siting of the probe-head on the production line and the spectrometer and computer in another room, for example.

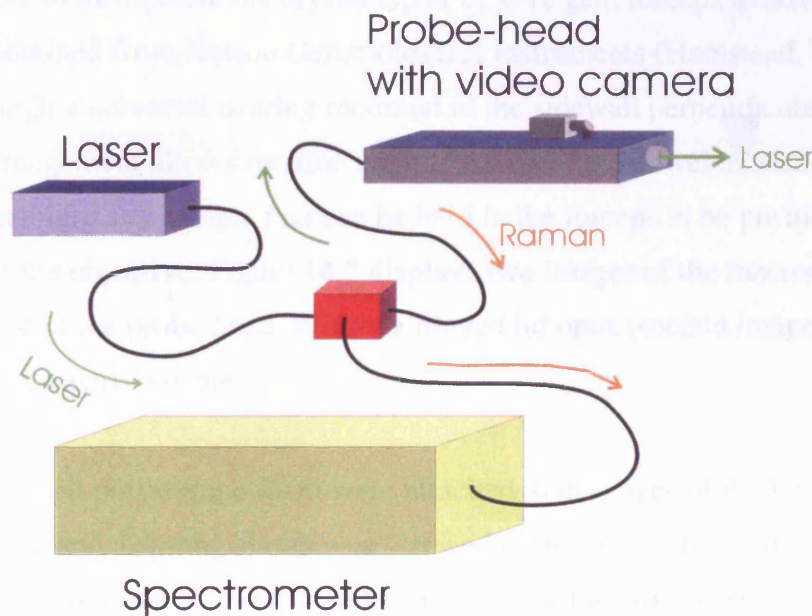


Fig. 14.1. Hardware configuration of RA 100 equipped with fibre probe head and camera.

To coincide with a display at the International Jewellery London trade show, September 5th to 8th 1999, a macrochamber was to be designed that could be attached to the probe-head to facilitate the Raman analysis of gemstones and other large crystals. The aim was to demonstrate the benefits of using Raman spectroscopy to distinguish between samples submitted by the public. The macrochamber device had to incorporate certain features:

- To be simply attached to the existing probe-head and retain the ability to change objective lenses
- To be capable of supporting a crystal up to around 2 cm in diameter and to provide some means by which the stone can be oriented to achieve best optical focus
- Be light-tight such that the device can be used in public without the possibility of stray light being emitted from the box.

A polycarbonate box measuring 130mm x 130mm x 75mm with a hinged lid was selected as the basis of a prototype because its volume was thought to be adequate for housing the largest crystal expected. A hole was drilled in one of the sidewalls so that the chamber could be slid over the objective, which protrudes from the probe-head. A brass adapter was produced that could screw into the probe-head such that objectives with the Olympus® thread could be used in place of the Leica objectives. A rubber o-ring is placed around the collar of the objective either side of the box sidewall to prevent light leakage.

To hold and be able to manipulate the crystal a pair of wire gem forceps attached to a long steel dowel was obtained from Nelson Gemmological Instruments (Hamstead, London). The dowel passes through a universal bearing mounted in the sidewall perpendicular to the objective. This arrangement allows rotation about the axis of the dowel as well as movement in three planes¹ enabling any sample that can be held in the forceps to be positioned within the focal length of the objective. Figure 14.2 displays two images of the macrochamber mounted on the end of the probe-head. With the hinged lid open (second image) the objective and gem forceps are clearly visible.

Thin strips of expanded polystyrene foam were attached to the edges of the lid to further prevent light leakage and a sprung clamp was screwed to the box such that the lid could be closed tightly against the foam. To reduce reflections inside the box a dark-coloured matt adhesive coating was applied.

In any microRaman analysis, the strongest Raman signal comes from the point at which the laser is focused on that sample. For most applications this is the surface and the effects of refraction or other penetration are ignored. When analysing samples in the macrochamber it was found that with the crystal held in the forceps, the lid closed and the laser engaged it proved difficult to achieve the optimum crystal position using just the reflections of the laser from the crystal surface recorded by the video camera and relayed to the computer screen. To improve the sample positioning a small, battery-powered torch was fixed inside the lid so that the crystal was sufficiently illuminated with the lid closed to position the sample in 'white

¹ y and z movements are more limited than in x, the axis of the dowel, and the movements are arcs about the centre of the universal bearing. However for small movements and with adjustment of x, orthogonal movements can be approached.

light' before the laser was engaged. Comparisons between the Raman spectra recorded with the torch on or off showed a negligible difference; the notch filter removing almost all but the Raman scattered radiation.

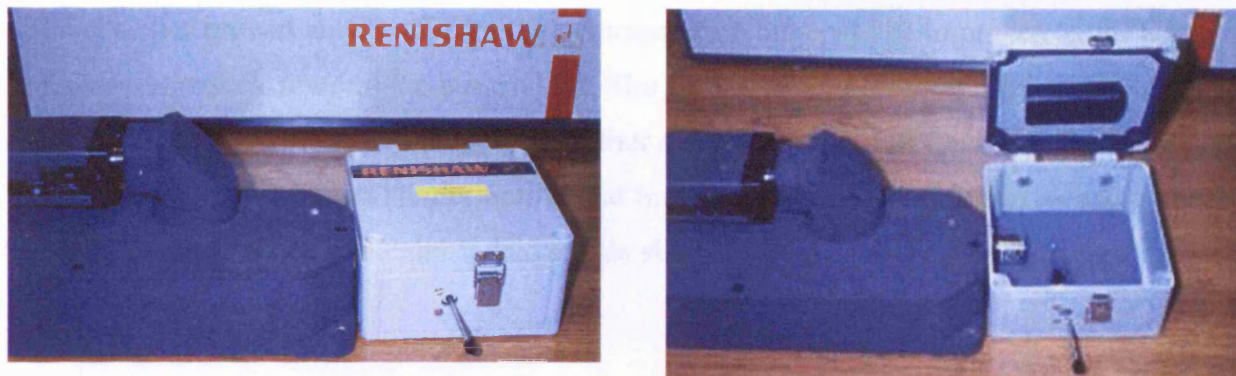


Fig. 14.2 Gem analysis macrochamber. Note the specimen forceps held in the universal bearing.

With the Raman spectrum of the crystal recorded in the usual way² the identification is performed by comparison to those in the reference database based on a choice of mathematical algorithms and the results listed in order of closeness of match.

The macrochamber proved to be successful and Raman spectra were recorded from almost all samplers submitted; the only failure to acquire a Raman spectrum was that of a sample too large to fit inside the chamber.

14.3 - Conclusion

Sample identification is one of the principal applications of Raman spectroscopy. The inherent non-destructive nature and the lack sample preparation make it attractive to the gem testing laboratories. Compared with many other techniques the results are far less ambiguous yet it can be applied to the gamut of mineral species the gemmologist may be faced with. A simple macrochamber attached to a more basic Raman spectrometer than the laboratory version could widen the technique's appeal to the gem trade and may even progress further to a truly portable design.

The chamber was used successfully at the jewelery trade show and in subsequent demonstrations of the technique since its development. The development of a macro-sampling

set for forensic materials is under investigation at the time of writing and the use of gem forceps held in a universal bearing as described is being considered as part of the set.

14.4 – Further work

The chamber proved very useful for the demonstration but could be improved by the addition of a laser interlock fitted to the box and lid. The current design presents a risk of exposure to reflected laser light with the lid open and either a crystal or the gem forceps in the beam path. The fibre probe-head has a shutter button that must be pressed to avoid this risk and a door interlock could be electronically linked to this shutter.

² The RA100, at the time of macrochamber development, had slightly different operating conditions to the RM models. Analysis was achieved in the same manner but with less flexibility. Some of the components of the spectrometer differed, requiring a modified software interface.

15 - Investigation of circularly polarised light

Although polarisation measurements form a principal aspect of the vibrational analysis of many crystal studies, the effects are not always desired. In the second section describing a technique development, the notion of using depolarised excitation energy to record orientation-independent Raman spectra from minerals is examined. The work described follows on from a very limited initial study in conjunction with Dr. J.B. Nelson.

15.1 – Introduction

It is well known that crystal orientation effects affect Raman spectroscopy. With the exception of isotropic, cubic crystals, it can be shown that the orientation of a mineral's crystallographic axes, relative to the orientation of the plane of polarisation of the incident laser, can strongly influence the spectrum obtained. Empirically, it is found that for different crystal orientations relative to the polarisation direction of the laser, the frequencies of the Raman bands are unchanged yet their relative intensities may be considerably different. Some bands may be unobservable in certain orientations. This polarisation dependence can be used to elucidate on a crystal's structure. This difference in intensities is due to the degree of asymmetry of the vibrational mode and the coincidence of the electric vector with the bonds.

In certain applications of the Raman technique, however, this orientation dependence can be undesirable. For the qualitative determination of crystalline mineral species by Raman spectroscopy, several measurements may have to be made at different sample orientations to ensure that the correct assignment is made. Whilst this may be straightforward for large, euhedral crystals it may be less obvious for very small, millimetre-sized samples, those prepared as petrographic thin sections or for samples that display little external crystal form. Although seemingly the antithesis of many Raman investigations, the aim of this investigation is to determine whether orientation-*independent* Raman spectra can be obtained routinely. The most immediate benefit would be to increase the accuracy of database determinations of crystal species using Raman spectroscopy. Liang *et al* (1998) highlighted the need for such a development based on their work to discriminate between what are termed by Liang *et al* as natural and synthetic gem 'handicrafts'. The term is not explained but probably refers to carved

or shaped objects with Eastern cultural or religious significance, formed from semi-precious minerals. They point out that few gem pieces can sacrifice a portion to be ground to permit powder XRD analysis and that frequently cleavages, as an aid to orientation, are not readily apparent.

Theoretically, powdered pure mineral samples are not affected by orientation dependence if their particle size is less than the area of the analysis spot since all crystal orientations are simultaneously presented to the beam.

15.2 – Polarisation of Raman bands

The polarisation of Raman bands was briefly introduced in 2.5. In the preceding sections, the effects of polarisation have largely been ignored; the studies being based on qualitative spectral data.

The ability to ‘label’ certain modes base on their state of polarisation is thought to be one of the “most useful features” of Raman spectroscopy (Griffith, 1974). It can be shown (see, for example, Griffith, 1974), generally speaking, that totally symmetric vibrations are polarised. The Raman bands of a free molecule excited by plane polarised light will be polarised to some degree, by the nature of the vibrations that are represented by those bands. The depolarisation ratio, ρ , is defined as:

$$\rho = I_{\perp}/I_{\parallel}$$

where I_{\perp} is the intensity of scattered radiation with polarisation perpendicular to the incident energy and I_{\parallel} is the intensity of the scattered energy with polarisation parallel to it. So, measurement of the intensities, using polarising material where necessary, gives an indication of the depolarisation ratio. Thus, totally symmetric vibrations have a ρ of close to 0. It can be shown that non-totally symmetric vibrations, and those of anisotropic crystals, have ρ of close to 0.75, that is, much of the energy scattered from that vibration has a polarisation state that differs from the incident energy.

In a crystal, the molecules and bonds that give rise to the Raman bands are essentially fixed. The electric field of the incident energy may lead to an induced dipole as a result of charge separation in that molecule. The size of the induced dipole, and more importantly, the polarisability is partly dependent on the orientation of the molecule relative to the electric field direction. Changing the orientation of a crystal relative to the laser in a microRaman system may lead to a significant change in the intensity of some, none or all of the Raman bands. This principle is exploited in the oriented crystal studies to identify and assign Raman bands to particular vibrations.

Liang *et al* (1998) comment on the factor group analysis of the seven crystal systems. They state that the totally symmetric vibrations of monoclinic crystals are always non-zero, regardless of the orientation of the incident electric field. Furthermore, some vibrations in trigonal, tetragonal and hexagonal crystals are present in “most cases” except when the electric field is parallel to the crystal’s c-axis. It is inferred that the vibrations in the other crystal systems requires the crystal to lie in some special orientation relative to the incident electric field in order to obtain all the vibrational modes.

15.3 – Circularly polarised light

It has long been recognised that delivering monochromatic light of all polarisation directions, i.e. polarisation-scrambled light, to the sample, ought to negate orientation effects. Elliptically polarised light can be achieved by retarding the polarised light by 90° , i.e. a quarter of a wave. Linearly and circularly polarised light are the special cases of elliptically polarised light (Long, 1977). These cases result when the sensitive tint plate is mounted orthogonally or at 45° to the plane of the original polarisation direction of the laser, respectively. By definition, circularly polarised light contains all polarisation directions of the electric field in equal intensity. Figure 15.1 attempts to show the effect of retarding the linearly polarised laser light by a quarter wave, i.e. $\pi/2$ or $\lambda/4$ (only the electric vector is shown for clarity). If this retarded wave is instead rotated through 45° relative to the y-axis, the two waves will interfere to produce a ‘helical’ or ‘corkscrew’ arrangement of circularly polarised light propagating in z towards the sample (however, the effect is difficult to produce in the plane of the paper). Thus, all polarisation directions are presented to the sample.

Liang *et al* (1998) approached this problem by employing a “45° scattering geometry” although it is unclear whether the inelastically scattered energy was collected at 45° relative to the propagation of the incident energy or if polarisation-scrambled energy was used.

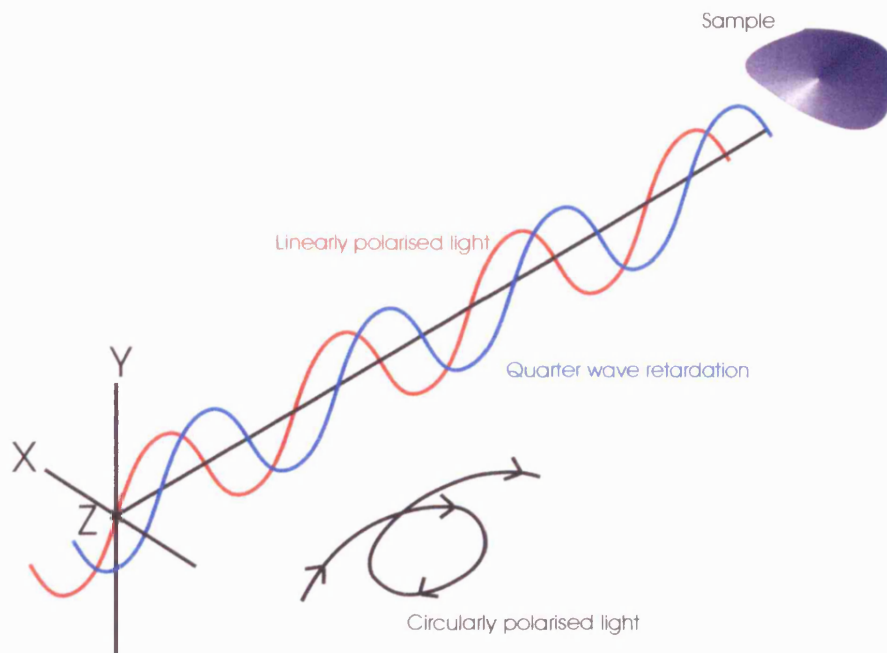


Fig. 15.1. Effect of adding a quarter wave plate at 45° to the linear polarisation direction.

A piece of $\lambda/4$ polarising material was inserted in the microscope’s parallel accessory plate slot to test the theory. Since the laser produces E-W polarised light, placing a piece of N-S polaroid in the beam path very effectively blocks further propagation. Using the polaroid sheet and a power meter it was shown that with the $\lambda/4$ mounted at 45° to the vibration direction of the laser light circularly polarised light could be produced i.e. a constant power reading recorded after the microscope objective resulted from whichever angle the N-S polaroid sheet was held in the path of the laser. Figure 15.2 indicates the arrangement used to test the circularity of the polarised light. The results of the laser power readings for both 633 nm and 514 nm excitation both with and without the quarter wave plate are presented in Figure 15.3. The Lieca DMLM microscope used by Renishaw has a 45° accessory mounting plate slot just before the objective lens. This position is optimal for the purpose of recording scrambled Raman experiments since both the incident and scattered light is scrambled. The requisite part was obtained from Leica so that tests on minerals could be performed.

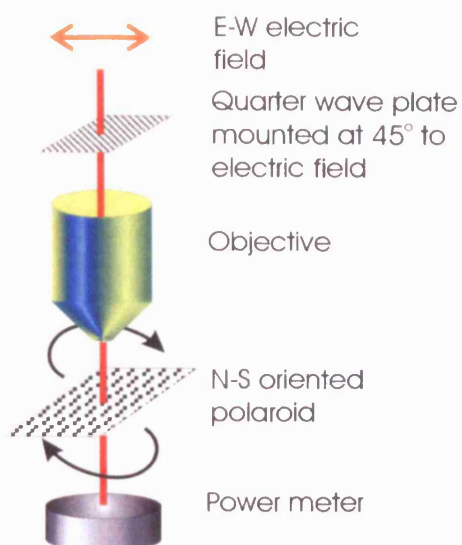


Fig. 15.2. Procedure to test circularity of polarised light using quarter wave plate.

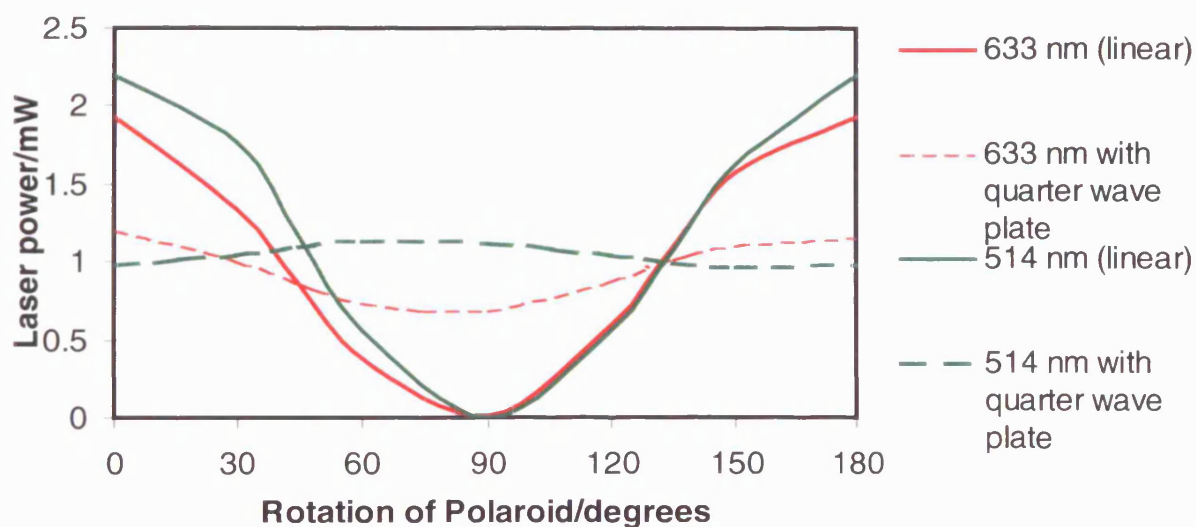


Fig. 15.3. Effect of adding a quarter wave plate to red and green linearly polarised excitation.

Figure 15.3 clearly shows that by adding the $\lambda/4$ plate at 45° the polarisation of the visible excitation tends towards circularity. By recasting the data as vectors, it is apparent that the effect of adding the accessory plate is far more pronounced for the green wavelength, i.e. the polarisation is more circular. Figure 15.4 compares the circularity of the red and green wavelength data. Approximate ellipses have been fitted to highlight the differences between the data.

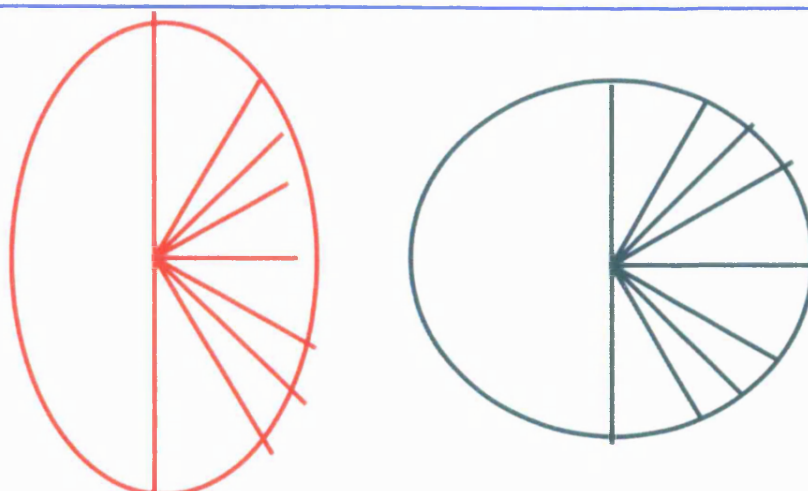


Fig. 15.4. Ellipses fitted approximately to the vectors from Figure 15.2.

The use of the $\lambda/4$ plate does caused a measured decrease of around 5% in the laser power at the sample. Although many minerals are inherently weak Raman scatterers, this factor should not be problematic and no significant difference is expected in the intensities of spectra recorded with the plate inserted. It should be mentioned that the interaction of the circularly polarised light with optical components (e.g. lenses and mirrors) has the effect of restoring linearity to the beam (Dr. I. Haywood, pers. comm.). The design of the Renishaw instrument has very few optical components in the Raman scattered light path so this effect, too, is thought to be small. Also, the efficiency of the holographic grating is known to be both wavelength- and polarisation-dependent.

Some preliminary experiments were carried out on zircon and rutile (Nelson, submitted), which both belong to the tetrahedral crystal system. Later, a single euhedral crystal of elbaite tourmaline was examined (M.J. Bloomfield, 1st Year Report). Tourmaline was chosen because the direction of the optic axes are simple to determine and therefore simple to position perpendicular or parallel to the laser's vibration direction. Figure 15.5 compares the Raman spectra acquired with linear and circularly polarised light with the crystal in orthogonal orientations. The agreement between the spectra acquired from different crystal orientations with scrambled polarisation is excellent. In contrast, with linearly polarised light there are many spectral differences. The spectra acquired between 200 cm^{-1} and 900 cm^{-1} with circularly polarised light have been offset in intensity for clarity.

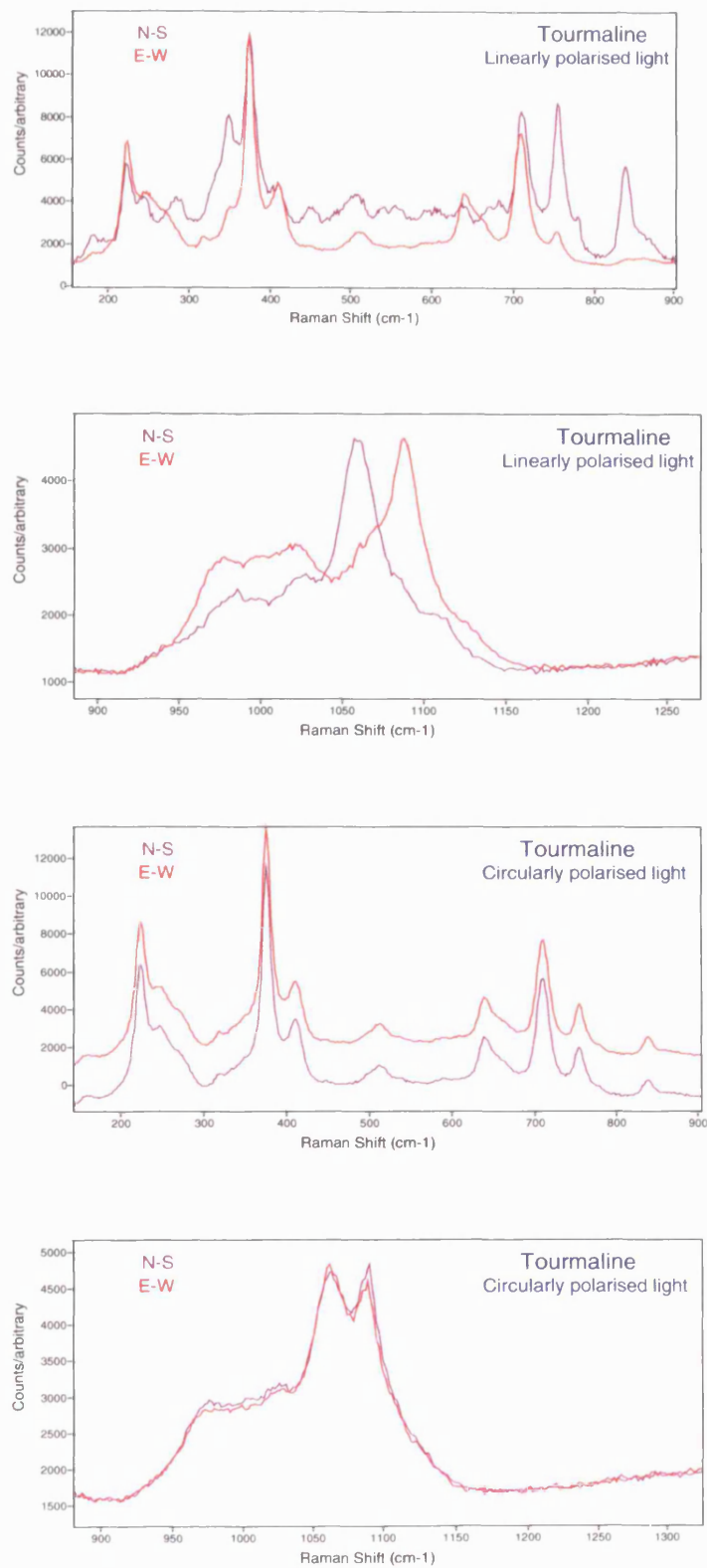


Fig. 15.5. Tourmaline Raman spectra using linear and circular polarised light.

15.4 – Samples

While it was demonstrated that the use of circularly polarised light was effective in scrambling the incident and scattered energy for a trigonal crystal, the method would be required to work for minerals belonging to all crystal systems. Commonly occurring minerals belonging to the different systems were selected for further analyses. The single crystal samples are listed and images shown in Table 15.1.

The samples were selected from a limited collection supplied by Dr. J. B. Nelson.

Representatives of all the crystal systems were identified, rejecting those that may belong to two systems or a pseudo-system. Several assumptions had to be made concerning the nature of the samples used. The crystal system of some minerals may depend upon their composition.

Deviation from stoichiometry may result in a modification to the structure, at least locally.

Similarly, structural homogeneity had to be assumed. Stressed or deformed crystals would not be appropriate to this study as their Raman spectra might be expected to differ from the undeformed state. Without quantitative chemical and structural analyses for the samples the only method of ensuring an accurate determination of the samples was, paradoxically, by using the Raman spectra. Samples were selected that most closely matched the Renishaw Raman database and example spectra in the literature.

15.5 – Results

All analyses were carried out with 514 nm excitation on an RM 2000 instrument. Each sample in turn was placed on the microscope stage, generally in an orientation such that an identifiable feature, for example, a long axis, could be used to reference the subsequent rotation. Analyses were made in both ‘E-W’ and ‘N-S’ orientations with linearly polarised light and then repeated with the quarter wave plate inserted. Spectral acquisition times were dependent upon the sample. The spectra are displayed in figures A15.1 to A15.7 in the Appendix. A summary of the results are tabulated and given in Table 15.2.

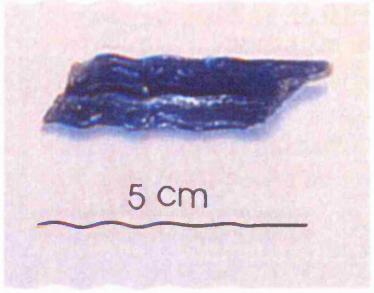
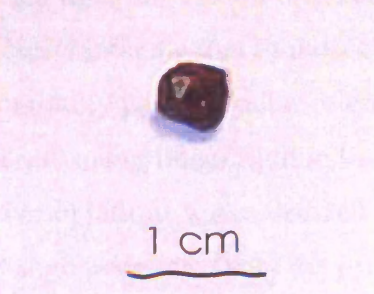
Mineral/ Crystal system		Mineral/ Crystal system	
Kyanite/ Triclinic		Tourmaline/ Trigonal	
Diopside/ Monoclinic		Anglesite/ Orthorhombic	
Vesuvianite/ Tetragonal		Nepheline/ Hexagonal	
Garnet/Cubic		<p>Kyanite, tourmaline, diopside and vesuvianite were oriented by their long axes. The anglesite crystal was oriented relative to a cleavage plane. Two sets of measurements were carried out on the nepheline sample. The first saw the crystal rotated about the c-axis – parallel to the propagation direction of the laser. Secondly, the crystal was positioned such that it rested on a prism face. In this orientation, the laser direction was parallel to the a(b)-axis. The garnet was rather small and not given a specific orientation to the laser (since it is cubic).</p>	

Table 15.1. Sample minerals selected and their system.

Sample/crystal system	Results	
Kyanite/triclinic	Linear	Several differences in the relative intensities of bands between the EW and NS orientations. No bands missing. Notable differences in the band system around 950 cm ⁻¹ .
	Circ.	Spectra are identical throughout the range analysed.
Tourmaline/trigonal	Linear	Strong differences in the EW and NS spectra. Some bands are absent in the EW spectrum below 900 cm ⁻¹ . The band system centred at around 1050 cm ⁻¹ is markedly different.
	Circ.	Spectra are identical throughout out the range.
Diopside/monoclinic	Linear	Spectra were identical in EW and NS orientations.
	Circ.	Spectra were identical in EW and NS orientations.
Anglesite/orthorhombic	Linear	Spectra identical except for one weak band at 640 cm ⁻¹ .
	Circ.	Spectra identical throughout the range, although significantly different to those with linear light.
Vesuvianite/tetragonal	Linear	Significant differences in relative intensities of many bands.
	Circ.	Spectra identical (over 20 bands distinguishable) except for the relative intensity of one band.
Nepheline/hexagonal First orientation	Linear	Spectra virtually identical throughout range (small difference in fluorescence)
	Circ.	Spectra virtually identical throughout range (small difference in fluorescence only)
Nepheline/hexagonal Second orientation	Linear	Significant differences in relative intensities
	Circ.	Spectra almost identical. Minor differences in relative intensity of few weak bands.
Garnet/cubic	Linear	Spectra identical throughout range.
	Circ.	Spectra identical throughout range.

Table 15.2. Summary of circularly polarised light experiments.

15.6 – Discussion

Using the quarter wave plate to retard the linearly polarised laser energy and create circularly polarised, scrambled light and record orientation independent Raman spectra appears to be successful. The results indicate that in most cases identical Raman spectra were obtained from crystals in two nominally perpendicular orientations using this method. Interestingly, the spectra were far less different using linear light in each case than expected. This may be explained by the fact that only two orientations were used and in general, these orientations were strongly related to optic axes, although not necessarily the principal, c-axis. Had the experiments been conducted on several truly random orientations then several corresponding Raman spectra may have been derived.

The kyanite and tourmaline data indicate that the 'scrambled' spectra are 'average' spectra of the 'extremes' obtained with linear light. This is most obvious from the tourmaline data, in Figure 15.5. The linear light spectra show two strong bands in the region 1050 cm^{-1} to 1100 cm^{-1} separated by some 30 cm^{-1} . In one orientation, one band is detected and in the other orientation, the other band is present. The spectra from the circular light measurements have identical 'double' band systems. This effect should be investigated with other, random orientations. It may be related to the fact that these systems have very little symmetry.

As might have been expected (Liang *et al* op. cit.), the diopside Raman spectra are unaffected by orientation. Since the orientations used were strongly related to the optic axes and the crystal has perpendicular axes of symmetry, the spectra may exhibit differences if other, off-axis orientations are used.

The anglesite sample gave virtually identical spectra for the different orientations using linearly polarised light. However, using circularly polarised light striking difference was noted. The linear light spectra show a strong band at around 450 cm^{-1} with a weak shoulder. With circular light the shoulder becomes an equally strong and highly distinct band. This difference could strongly affect the species determination of this sample were it to be presented as an unknown. The sulphate family of minerals can display extensive solid solution that can be reflected in small differences in the Raman spectra, such as increased separation between two close bands. Again, this difference between the spectra could be related to orthorhombic symmetry and that the rotation of the crystal was in one plane through 90 degrees.

The nepheline crystal was initially oriented such that the laser propagation direction was oriented parallel to the c-axis. The spectra were determined to be almost identical in the orientation rotations around the c-axis when linear light was used. When the crystal was re-oriented such that the laser was perpendicular to the c-axis the linear light spectra show several differences. Figure 15.6 indicates the two orientations of the nepheline crystal described.

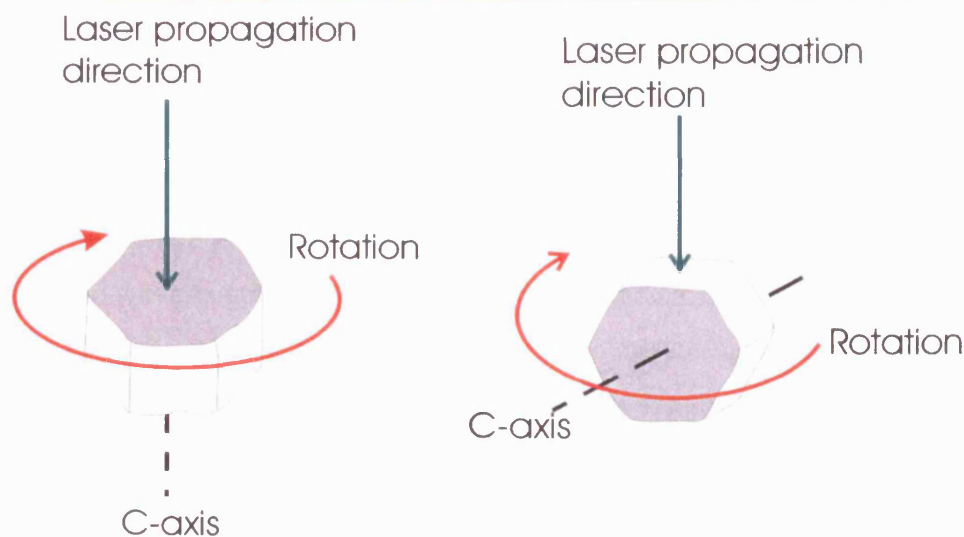


Fig. 15.6. Orientations of the nepheline crystal used for experiments.

The two sets of data highlight the importance of the orientation of the principal optic axis relative to the propagation direction, and therefore, the electric field, of the incident laser. With the laser propagation direction parallel to the a- (b-) axis, the linear light spectra provide an example of how a relatively broad band comprised of two close, unresolved bands is observed when circularly polarised light is used but when linearly polarised light is used, the band is resolved into two bands when different crystal orientations are used. One can imagine that if linear light only was used to analyse this sample, the spectra may be interpreted incorrectly.

The results indicate that the orientation of the c-axis relative to the direction of propagation of the laser, i.e. the electric field orientation, appears to be very important, as the nepheline example shows. In this study relatively large samples were used and it would be of interest to repeat with 'grain-sized' samples where the external morphology and cleavage were less apparent.

The use of a quarter wave plate may also have implications for polarisation studies of minerals. As previously discussed, polarisation studies essentially involve the ratio of the intensity of a band with polarisation parallel and perpendicular to the incident beam. However, polarisation leakage can occur, which can lead to inaccurate measurements of the depolarisation ratio. In addition, the use of high NA objectives can cause depolarisation of the Raman scattered light. It

may be that by scrambling the Raman signal and then passing the signal through the polariser might be a more efficient way of determining the polarisation of bands.

The circular polarisation studies were only carried out with 514 nm laser. Hecht & Zajac (1974) state that commercial wave plates are generally designated by their linear retardation, i.e. one quarter of a specific wavelength (± 20 nm). The ellipticity indicated from figures 15.3 and 15.4 (and which was marked with 633 nm excitation) of the polarisation, as measured with the power meter, could be ascribed to this. The Raman spectral results suggest that the 'circularity' achieved with the green excitation was adequate. Although the Leica quarter wave plate is 'calibrated for the visible region' of the spectrum it is certainly better in the green portion of the spectrum than the red. Purely circularly polarised light may have resulted in even closer matches of the spectra recorded at different crystal orientations.

The effects of the grating efficiency have not been taken into account. The datasheet supplied by the grating manufacturer indicates that the grating appears to be far more efficient in the red than the green. It would be useful to obtain a 'red' quarter wave plate and repeat the experiments.

The potential effect of refraction and birefringence has not been considered. Intense, monochromatic light incident on an isotropic sample surface will be refracted into the sample by a greater or lesser amount. Scattered Raman energy could thus be affected by increased excitation along 'preferred' axes. The position of the quarter wave plate in the collection path may mitigate or even negate this effect. It is possible that the effect may be increased in polarisation studies of oriented crystals. To reduce any potential effects of refraction the spot could be made more confocal or oil immersion method could be used. The use of a shorter excitation wavelength for reduced surface penetration would require a matched quarter wave plate.

15.7 – Conclusion

Raman spectra acquired using polarisation-scrambled light with Dr. Nelson from tetragonal crystals indicated that the technique was successful for minerals crystallising in that system.

Later experiments with tourmaline, a trigonal mineral, were also successful and prompted the further study described.

Some examples of the crystal orientation-dependence of the Raman spectra of crystals have been shown. Minerals representing the seven crystal systems have been used to show that the position of the optic axes relative to the polarisation of the linearly polarised laser can have a marked effect on the relative intensities of some Raman bands. In extreme cases, bands may not appear to be present. This could potentially lead to the incorrect analysis of Raman spectra where the frequency of certain bands has a bearing on the measured stress in that crystal, for example. The use of an accessory quarter wave plate has been demonstrated to introduce a retardation of the energy, that when combined with a specific orientation of the accessory plate, can interfere to produce circularly polarised light. The examples given indicate that the use of scrambled light is effective in recording orientation-independent Raman spectra from crystals. Unless polarised data is required, the quarter wave plate accessory, i.e. circularly polarised light, should always be used when recording mineral Raman spectra. This conclusion is in agreement with Nelson (submitted), which was based upon the analysis of two species from a single crystal system.

The findings of this study appear to be the only systematic study of the Raman response of minerals from all seven crystal systems when subjected to circularly polarised light. There are important implications for Raman databases and the qualitative determination of samples; not only for minerals, but for other crystalline materials. The study highlights the importance of recording spectra from several crystal orientations for reference samples and also for unknown samples.

The effect of a slight decrease in laser power should be borne in mind, as should the wavelength dependence of the accessory plate. Where possible, the accessory plate should be optimised for the excitation wavelength used.

15.8 – Further work

The current work has underlined the importance of the orientation of the principal optic axes when recording Raman spectra. It would be invaluable to further explore the potential of using

circularly polarised light to record orientation-independent Raman spectra by repeating the experiments using several random orientations.

16 – Automated mineral discrimination

The third section that covers technique development describes the design and manufacture of a sample holder specifically for minute grain separates. The intended use of the holder is for the automated discrimination of grains that would be used for geochronology.

16.1 - Introduction

Dating rocks and minerals using radiogenic isotopes has a very important place in the modern study of geology. Using the relative proportions of particular elements and knowledge of their decay schemes it is possible, in many cases, to define the age at which an event (e.g. formation, metamorphic event, volcanic eruption) occurred with some accuracy and precision. The error margin very strongly depends up the decay scheme used, which is largely controlled by the minerals present in the rock.

The availability of highly sensitive analytical instruments is increasing as the cost of technology decreases. At the same time, new methods are devised and old methods adapted. The ability to carry out detailed and accurate chemical analyses is now within the realms of almost all research scientists.

Whilst there is still some way to go before Raman spectroscopy can be used to provide quantitative data it can be used to efficiently discriminate between separated grains of similar physical properties used for chemical analysis.

16.2 - Decay schemes

The common decay schemes used in the study of rocks are summarised in Table 16.1. These minerals are predominantly used to date igneous and metamorphic events although by *relative* dating many are used to date sedimentary rocks and processes. For the study of single crystals the analytical method will be one of two types: a 'selected area' microanalysis for example LA-ICP-MS where only minute regions of the crystal are volatilised, or one in which the entire crystal is destroyed, usually by thermal ionisation or by dissolution in acid. These are the 'whole grain' methods.

16.3 - Physical properties

The collection of mineral separates suitable for analysis using one of the decay schemes outlined in Table 16.1 involves a high degree of preparation. After the sample is crushed it is sieved to retain that entire fraction that falls, typically, between 250 and 500 micrometers or 500 and 1000 micrometers. This size fraction is then purified with respect to the desired mineral species. This process usually exploits physical property differences between minerals. A range of methods is applied although all are somewhat inefficient and fallible. Table 16.2 summarises the common methods and some of their limitations.

Isotope scheme	Common minerals used
U/Th-Pb	uraninite , thorianite, zircon , thorite, allanite, monazite , apatite , xenotime, sphene .
K/Ar	sanidine , anorthoclase , plagioclase , leucite, nepheline, biotite , phlogopite , muscovite , lepidolite, glauconite, hornblende (ss) , pyroxenes, sylvite, langbeinite.
Sm/Nd	bastnaesite, monazite , cerite, apatite , zircon, allanite, feldspars, biotite.
Ar/Ar	as K/Ar
Rb/Sr	micas, k-feldspar, sylvite, carnalite, certain clay minerals, apatite, plagioclase, CaCO ₃ .
Lu/Hf	apatite , monazite , garnet , (biotite, monazite, xenotime, euxenite, samarskite, allanite, gadolinite, plagioclase, amphibole, pyroxene, olivine, zircon)
Re/Os	osmiridium, laurite, sulphides of Mo and Cu, gadolinite, columbite, tantalite.
K/Ca	as Rb/Sr
Fission track	apatite, sphene, zircon, muscovite, epidote, volcanic glass.

Table 16.1. Summary of minerals frequently used for isotopic dating. Minerals that appear in **bold** are those most commonly used in each case. After Faure (1986).

16.4 - Raman spectroscopy

In contrast to the methods very briefly listed in Table 16.2 Raman spectroscopy is widely acknowledged as an effective method of discriminating between minerals species. The characteristic Raman scattering spectrum recorded for a sample is usually referred to a database of mineral spectra or the literature. The analysis method is rapid and defined by many as unambiguous.

Technique	Drawbacks
Density contrast using heavy liquids	<ul style="list-style-type: none"> • Is only effective if Δdensity between the species is significantly large • Is inefficient when minerals belonging to a solid solution are presented or those containing significant amounts of impurities or inclusions
Density contrast using centrifuge	<ul style="list-style-type: none"> • Few, isolated facilities • Expensive • Inefficient
Magnetic susceptibility	<ul style="list-style-type: none"> • Can only be used for those minerals that are Fe-bearing • Is inefficient if the assemblage contains more than one Fe-bearing mineral or if the Fe content is low
Hand picking and sorting	<ul style="list-style-type: none"> • Requires significant experience. Even with considerable knowledge some minerals are very hard to distinguish between on the basis of morphology (which may be lost), and features including colour, cleavage and twinning. It can be a very inefficient method. • Time consuming

Table 16.2. Common methods of separating minerals on the basis of physical properties, and their drawbacks.

Sample holder

Analysis by microRaman spectroscopy usually requires the specimen (single crystal, small hand specimen, thin section or powder) to be placed on the stage of a microscope coupled to the instrument housing the spectrometer and focused upon using the conventional microscope optics. With the laser engaged analysis is achieved typically in seconds although this is highly sample-dependent. Regions as small as 1 micrometer across (e.g. Baldwin *et al* 2001) can be analysed.

MicroRaman spectroscopy appears to offer the ability to remove the inaccuracy and ambiguity inherent in the traditional methods that exploit the physical differences between mineral species. However, loading each single grain by forceps to the microscope stage is a delicate and time-consuming process. The idea that the process could largely be automated arose after considering the point-mapping technique already used in microRaman spectroscopy.

The design of a specialised sample holder needed to fulfil certain specifications:

- fit into the existing aperture in the motorised stage with no lateral movement

- be lightweight, yet durable and easy to make
- hold a large number of grains in precise locations

An aluminium sheet 75mm x 50mm x 5mm was prepared with a regular array of 126 ‘cells’ drilled into the surface at 5 mm intervals. Each cell has a diameter of 1000 micrometers and a cylindrical depth of 1000 micrometers and terminating in a steep cone. A CNC machine was used for precision drilling. Figure 16.1 shows the technical drawing supplied to the CNC-programmer and Figure 16.2 shows the completed test model.

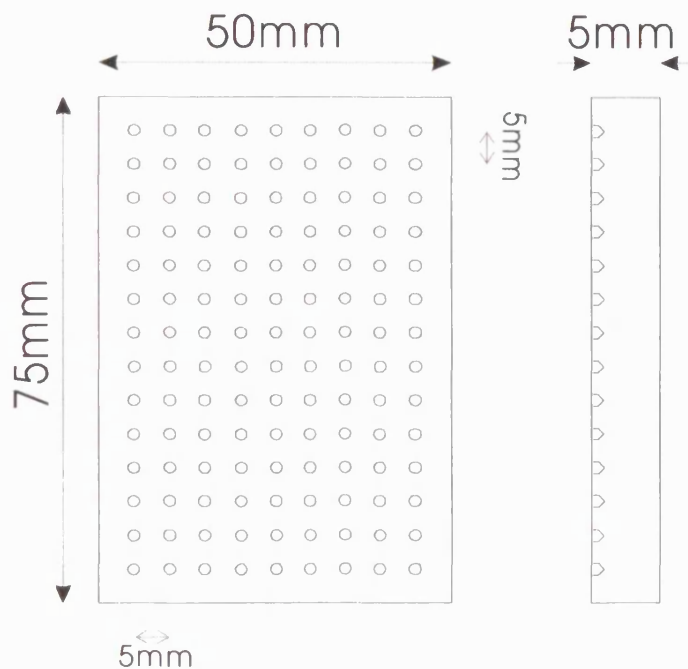


Figure 16.1. Technical drawing of the design submitted for the manufacture of a prototype sample holder.

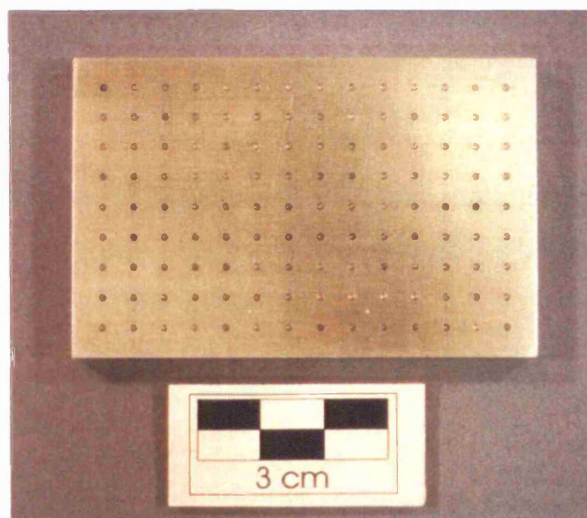


Fig. 16.2. Photograph of the prototype aluminium sample holder.

Analytical procedure

Sample grains would be loaded individually into the drilled cells in the plate using very fine forceps, or by pouring grains onto the plate and using a gentle vibrating table to settle them in the cells. The conical shape was used in an attempt to ensure that the crystal is located centrally within the cell. It is envisaged that a standard 50x dry metallurgical objective be used for the analysis. This is the objective routinely used for analysis of a wide variety of substances in microRaman spectroscopy. Oil immersion objectives have also been shown to provide high quality spectra with the sample under oil. Grains used for geochronology are usually hand-picked under oil so that they are not affected by electrostatic forces and can be positioned wherever the analyst requires. It is possible that the grains could be loaded into the sample plate and analysed in a droplet of oil placed in the pit. The plate is mounted on a Prior motorised stage of a Leica DMLM microscope and controlled using Renishaw encoders. Precise movement between successive pits is achieved with an error of <0.1 micrometers. Excitation using a 514 nm laser is widely regarded as the best 'all purpose' wavelength for the generation of mineral Raman spectra. A slit width of 50 micrometers permits good spectral resolution and good throughput of signal.

16.5 - Software/Graphical User Interface

The following is a discussion of what the software interface might include for an automated mineral discrimination. An impression of the graphic user interface is shown in Figure 16.3. The software interface is used to define the basic acquisition of Raman spectra and let the user decide which method will be used.

With reference to Figure 16.3:

Acquisition

The basic parameters of excitation wavelength selection, grating selection, exposure time and accumulations are controlled from dropdowns. Dwell time has been added for those instances where photo-bleaching improves the collection of data.

Auto options

By selecting a value from the dropdown the user can define the minimum acceptable value of signal to noise ratio for each mineral. Essentially, the software would calculate the rms of the

background noise and compare this to the intensity of the strongest band. Accumulations would be co-added until the specified value was reached.

Since there may be some variation in the height of the grains, an 'Autofocus' option could be added. This function would use the size of the spot of reflected laser light falling on the video camera; in the same way that Renishaw WiRE™ 1.3 software currently achieves autofocusing.

Although not part of the prototype separates holder, small pieces of Si wafer perhaps 2 mm by 2 mm, could be attached at the corners of the sample holder as a means of providing a quick calibration standard. If the 'Si calibration' option were selected, then the entire experiment would begin (and end) with an analysis of the wafer. The position of the strong Si Raman band would automatically be curve-fitted by the software and an auto-offset of the grating applied if required.

The grid below the 'Acquisition' and 'Auto options' dropdowns is a representation of the sample holder. By dragging and dropping the red rectangle with the computer mouse, only that region of the holder would be included in the experiment; potentially saving time by not analysing vacant cells.

Select discrimination method

Options are suggested here where the user can define the type of experiment he wishes to perform.

If 'Decay scheme' is selected, the dropdown becomes active and the range of schemes outlined in Table 16.1 becomes available. The software correlates this selection with a list of minerals that could be used in such analyses. Curves would be fitted to the bands of the sample spectra and compared with those determined for the reference species. More specifically, the 'Select minerals' option activates a dropdown list of minerals from which the user can select one or a number. This selects the region of the spectrum in which the software 'looks' for the characteristic peak of that species. For example, to distinguish between zircon and rutile the region between 900 cm^{-1} and 1200 cm^{-1} might be selected (see Figures. 16.4 and 16.5 for representative spectra of zircon and rutile, respectively). By only analysing a portion of the spectrum analysis time can be reduced, even when multiple scans are required to

improve signal strength. The parameters of the analysis could be optimised for that species i.e. relatively poorer Raman scatterers may require several accumulations and thermally-sensitive minerals may demand less laser power intensity. Selecting the desired mineral could automatically engage and override the experimental parameters. To avoid fluorescence, it could even be possible to change the excitation wavelength automatically when a mineral species known to respond more favourably to certain wavelength is selected from the menu. As an extension from selecting the mineral species to be identified, the option to 'Identify minerals' is added. The software will try to match the spectrum acquired from each cell to those of the database.

Precision

The user would have the option to decide whether band position and/or the FWHM of the characteristic band(s) would be used to determine the quality of the match with the reference. Dropdown lists could be used so that the user can decide how close to the reference is acceptable as a good, fair, or poor match. A 'traffic light' system of green, amber and red would signify the quality of the match.

If there is more than one reference database of reference spectra, then the option to select which is used is provided. For example, if other microRaman studies have been performed on minerals from rocks of the same suite and the spectra saved in a database format, then this could be used and may give better matches than a general database. Variations in composition may exist such that the general database classifies good matches as fair.

Displaying results

With the experiment defined, the program can be initiated. The sample stage would move to the first selected pit and perform the analysis under the criteria set. The use of an encoded stage would make the movement between each pit precise. To test this, the prototype holder was loaded onto the stage and the crosshairs aligned with the centre of a cell. The Video Viewer window of the existing WiRE™ software allows the user to command the stage to move a set number of micrometers. A value of 5000 was inserted in the 'X' window and the stage moved repeatedly with high precision to the next and subsequent cells.

Automated mineral discrimination set-up

Acquisition

Excitation/nm 514 ▼

Grating/g mm⁻¹ 1800 ▼

Exposure/s 10 ▼

Accumulations 10 ▼

Dwell time/s 20 ▼

Auto options

Signal to noise 10 ▼

Autofocus ON ▼

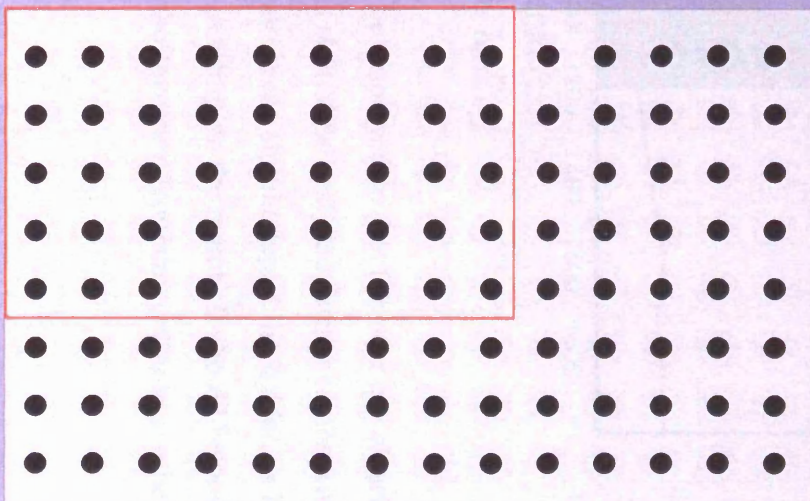
Si calibration ON ▼

Select discrimination method

Decay scheme Sm/Nd ▼

Select minerals Apatite ▼

Identify minerals YES ▼



Precision

Band position/cm⁻¹

Band FWHM/cm⁻¹

Green +/- cm⁻¹ 2 ▼

Amber < cm⁻¹ 5 ▼

Red > cm⁻¹ 5 ▼

Database

Carribbean Plateau ▼

Fig. 16.3. Impression of the graphical user interface for mineral discrimination.

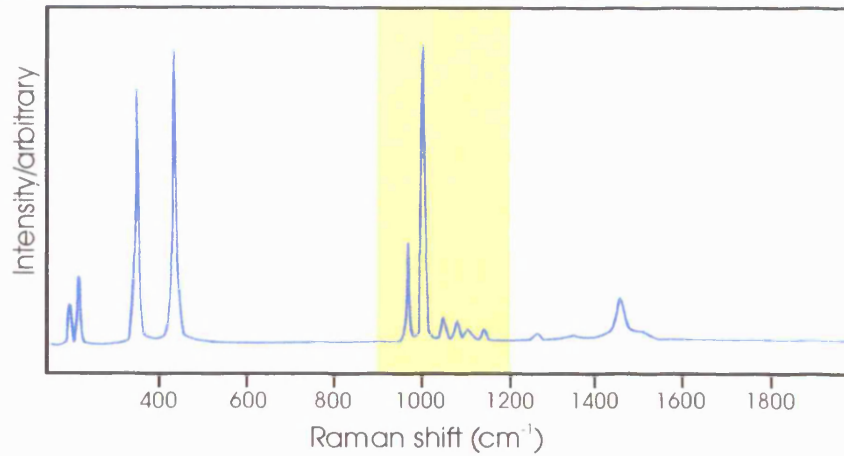


Fig. 16.4. Raman spectrum recorded for zircon.

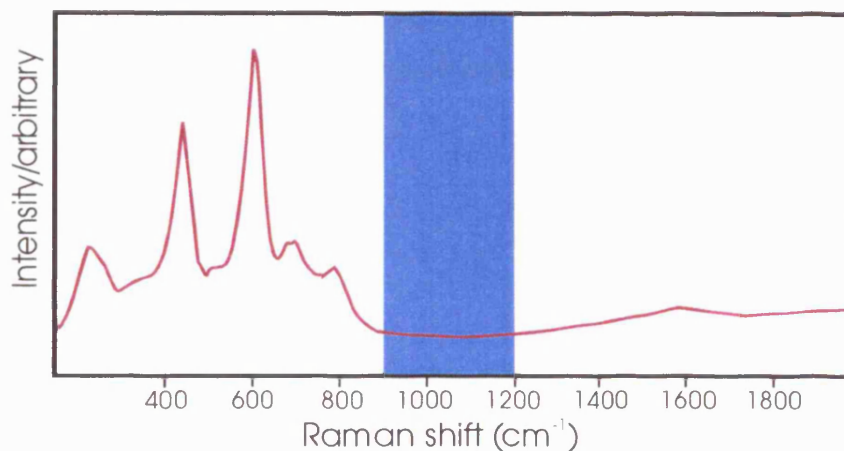


Fig. 16.5. Raman spectrum recorded for rutile.

Upon completing the program, the results should be displayed so that the user can clearly identify which matches are the best (green), which should be analysed further (amber) and which should be discarded (red). The active display screen should depict the holder, as in Figure 16.3, with green, amber and red circles, depending on the match. It should be possible for the user to use the computer mouse to call up the spectrum from any cell into another window to visually assess the data.

Once the plate is removed the desired 'green' grains can be removed using a suitable suction-type pipette or fine tweezers and separated from the deleterious or unwanted 'red' grains. 'Amber' grains could be further investigated individually.

16.6 - Conclusion

MicroRaman spectroscopy offers a rapid, non-destructive means of discriminating between different species of minerals that have otherwise very similar physical properties. Compared to traditional methods of sorting a separated crystal size fraction, an automated technique using Raman spectroscopy would have the advantages of high efficiency, speed and little requirement of the user for knowledge of crystal morphology and other factors that lead to ambiguity in discrimination.

Chapter 6 – Conclusions and further work

Section 17 attempts to draw together and summarise the findings of this research project in to the applicability and usefulness of microRaman spectroscopy applied to aspects of Earth science materials.

Some suggestions are made for further study; however, the preceding sections in chapters 2, 3, 4 and 5 provide greater detail.

17 – Conclusions and further work

17.1 Introduction

Section 4 of this work identified that the aims of this research were to ‘...*apply microRaman spectroscopy to a variety of materials of interest to the mineralogist, petrologist or crystallographer and to assess the applicability and usefulness of the technique in the context of the analytical instrumentation widely used in the Earth sciences*’.

It was noted that the application potential of the technique in this field was vast. To date, the scope of published studies that have used Raman spectroscopy in the Earth sciences is dominated by mineral identification and characterisation, the investigation of crystal structure and of fluid inclusion analysis. In the latter, it has proved to be a potent device. To this end, a series of case studies were defined; some were rejected at an early stage, others evolved during the course of the investigation. The focus was on mineral identification, the structural study of minerals and of applying the techniques of Raman mapping and global Raman imaging to mineralogical samples. Some of the case studies drew on more than one of these key elements. Each study has been discussed and concluded independently. Whilst attempting to avoid excessive repetition, it serves to draw together the conclusions within the framework of the project as set out in section 4.

17.2 - Chapters 2, 3 4 and 5

The ability to identify minerals from their Raman spectra has long been recognised. Central to this is the ability to construct databases of reference spectra. The starting point, then, in this investigation, was to assess the existing Renishaw database of mineral spectra. Section 5 describes the removal of some data and the extensive editing and addition of important information including the general formula, group or family name, the rock associations and related minerals for all entries. Whilst the database has a large number of spectra, the confidence the user has in its use would be enhanced by greater numbers of spectra from the same samples and from samples of the same mineral from different provenance. This should help to match unknown samples where deviations from stoichiometry that can arise regionally or locally affect

the Raman spectra of that mineral. The addition of well-characterised minerals that form solid solution series' would also be beneficial.

Some suggestions were made for further, specific databases. These included the construction of compilations of spectra from minerals from economic deposits, industrial minerals, environmental mineralogy and from igneous, volcanogenic and metamorphic settings. The key to an accurate and useful database is the acquisition of well-characterised samples, preferably with supporting EMPA and XRD data, and a rigorous approach to the collection of spectra. From the section dealing with technique development an important stipulation is that a quarter wave plate be used so that the spectra (unknown sample and reference samples) are orientation-independent.

Section 6 describes the application of the technique to mineral identification. In this case, the technique was directed towards the analysis of a suspected coesite inclusion in eclogite from NW Scotland. In what might have proved to be an almost routine polymorph identification, the analytical results had implications for the petrogenetic history of the rock and also for published accounts where there may be some doubt over the identity of mineral species based upon petrography alone.

Minerals were identified in other samples during this research. In each case, the analysis was significantly more straightforward than had existing methods been used. Section 7 includes the identification of zircon, monazite and apatite micro-inclusions *within* biotite grains. Furthermore, Raman spectroscopy was shown to be more sensitive to the mineral constitution than XRD by detecting unambiguously, the presence of dolomite and minute amounts of pyrite and rutile in discoloured marble in section 11. The analysis was very rapid and performed non-destructively on a hand specimen.

Section 12 describes the use of the technique in a preliminary investigation of bricks. Minerals were identified from thin sections. This study, in particular, highlighted some of the limitations of the technique. Excessive fluorescence masked Raman bands in many analyses; in some cases this fluorescence was the result of the absorption of the laser energy with concomitant sample

damage, albeit, on a very localised scale. In addition, the very fine particle sizes present in the sample made it difficult to acquire good spectra.

There are many examples in the literature that have used Raman spectroscopy, and the complementary technique of infrared spectroscopy, to determine aspects of atomic structure of minerals and other crystals. The case studies presented in this work focused on using changes in the Raman spectra to comment upon structural change. In this context, the aim was to assess the applicability of the technique over XRD, which also permits the analysis of crystal structure. Section 7 describes the how use of microRaman spectroscopy, in isolation, was effective in probing the crystal structure of radiohaloes in biotite. Line mapping, i.e. translating the sample beneath the microscope objective in one direction, such that point spectra can be taken at regular intervals, was very effective in establishing the extent of the structural damage. The conclusion that significant damage had been caused to the local biotite structure as a result of the recoil of nuclei after the emission of α -particles echoed another published study, although the mechanisms differed. Crucially, the other group of researchers identified microRaman spectroscopy as a key element in their approach.

A suite of cubic zirconias, doped with trivalent ions to transform their colour, was analysed and results discussed in section 8. The frequency of the strong F_{2g} band that arises from the symmetric stretching of the O—Zr—O bond may be correlated with a change in the dopant ion; the loose association was based on too few data points to be confirmed. Other conclusions drawn from the data were that regions of monoclinic zirconia might exist as discrete regions within the cubic structure and result from the local decrease in coordination around defects caused by doping. The technique is probably too insensitive for studying colour mechanisms, however, laser-excited photoluminescence can be recorded using the same instrumentation and may provide a more sensitive method.

Further crystal structure investigations using Raman spectroscopy were performed on zircon grains. Comprehensive reviews of radiometric dating, metamictisation and the loss of Pb in zircons were provided as background to underline the need for a simple and reliable technique for distinguishing poorly crystalline grains, and regions within grains, from well-crystalline

material. Zircons adversely affected by self-irradiation are well-studied and microRaman spectroscopy has proved invaluable in this research. The studies described in section 9 exploit the different analytical functions that the Renishaw instrument offers. There are no other known instances where depth profiling, line focus mapping and global Raman imaging have been applied to zircons. All proved to be effective in distinguishing regions of differing crystallinity.

There are many established analytical techniques available to research scientists. Often, a significant amount of their use is for research into materials of an industrial nature. Whilst some of this is purely of academic interest, much is in the direct application of a technique to solve a particular industrial problem. Chapter 4 hoped to make use of the different analytical methods available using Raman spectroscopy in the study of materials of an industrial nature where other techniques might not be applicable. Sections 10, 11, 12 and 13 indicate that there is great scope for using this technique in the industrial sphere; a sector of the analytical market that is probably largely unaware of the technique's existence.

Although proven to be an effective means of analysing stress in many crystalline materials, the application of microRaman spectroscopy, using a line-mapping approach, to undulose quartz proved inconclusive. This was explained in section 10 either by the ease by which quartz re-equilibrates or by the mechanism by which quartz physically deforms.

Section 11 was concerned with the investigation of stained marble dimension stone. Analysis was principally concerned with identifying the discolouring agent's identity. The sample represented an example of where microRaman spectroscopy could assist in solving a real world problem. As detailed above, it proved trivial to identify minerals present in the sample that XRD could not detect. Furthermore, spectral features appeared to provide evidence of hematite, a known oxidation product of pyrite, also identified in the sample. Other significant Raman bands were tentatively ascribed to a sulphate species that could be accounted for by the action of sulphurous acids; either atmospheric in origin or as a cleaning product. Research into this problem was carried out in the laboratory, however, it is clear to see the potential that a truly field-based tool would have in a similar situation.

The analysis of the limestones rich in organic matter was originally perceived as an assessment of the global Raman imaging technique. The stylolite-like distribution of organic matter was selected to serve as a useful example whereby the Raman images could be easily correlated with the optical images. However, the bituminous matter proved not to be a good candidate for imaging due to the very large bandwidths of its Raman bands. Examples were also shown of the effect of flat-field correcting the data and the conclusion is that it should always be applied.

A common aim of studies into brick-making is to achieve bricks of the desired physical properties (strength, durability) but in a more thermally-efficient manner. Key to this is identifying the various phase transformations that occur during the firing process. As explained above, this study highlighted the few limitations of the technique applied. However, there is still great scope for research in this area and with this technique.

During the course of the current work there arose opportunities to develop the analytical method to solve issues in the analysis of minerals. Chapter 5 details these problems and solutions proposed. A macrochamber was designed and built to facilitate the Raman analysis of gemstones when using the fibre-coupled probe-head. The design was successfully demonstrated in public and at other occasions. The use of a polarisation scrambler was examined in section 15. The author wishes to acknowledge Dr. J.B. Nelson for the original suggestion that the effect be investigated further after initial analyses of tetragonal crystals. The section was concluded with the suggestion that scrambled light should always be used in the assessment of unknown minerals. A sample holder for sub 500 micrometer-sized mineral separate grains akin to a well-plate used in chemical research is described in section 16. The purpose is to speed up the process whereby grains of this type, separated for use in dating schemes, can be unambiguously identified using microRaman spectroscopy. Although designed and manufactured and suggestions made for the graphical user interface discussed, the sample holder has not been used.

17.3 – Summary of conclusions

The current work tries to assess the applicability and usefulness of microRaman spectroscopy to materials of a mineralogical nature. Because this area of the Earth sciences is so great, the

samples used have been wide-ranging. It is hoped that the approach taken has demonstrated the key features and methods of analysis available when using the instrumentation described.

The use of databases of reference mineral spectra has been identified as crucial in the use of the technique. MicroRaman spectroscopy has been shown to provide a much more sensitive means of identifying minerals than XRD, currently one of the favoured approaches. Databases need to be extensive, from well-characterised materials and rigorously analysed. A diverse range of materials in different formats was used to demonstrate the effectiveness of the technique as a mineral discrimination tool. Critically, samples can be presented as thin sections, hand specimens, powders, or even in solution, although this was not demonstrated. Analysis is non-destructive, permitting the subsequent re-analysis by the same or other techniques. The limitations are generally of highly fluorescing materials and possible ambiguity arising from almost identical spectra.

Raman mapping has been demonstrated with line-, area-, depth- and line focus-mapping approaches on different samples. Using the mapping function, microRaman spectroscopy has been shown to be an excellent tool permitting the spatial analysis of structure, and in some cases composition by inference, of mineral samples. The acquisition of some map data can be time consuming – a problem exacerbated by the low Raman scattering potential of many minerals. It is very important that the correct wavelength is selected and the effects of refraction often require that confocal analyses be performed. No other technique, except perhaps some IR-based methods (where spectral resolution is at best around 10 micrometers), appears to offer the ability to collect structural information on the micro-scale from minerals *in situ*. This is of fundamental importance since it preserves the spatial relationships present.

The number of published accounts of the use of Raman imaging is low. The function is only available on Renishaw microprobes, which accounts for this. The studies described in this research demonstrate that the potential for using the method in the study of minerals is high. There are many instances where mapping is not applicable. The limitations are that for successful images to be acquired, the species of interest must be a rather strong Raman scatterer and possess relatively sharp bands well removed in the spectrum from those of the matrix. The

size of the species needs to be on a micrometer-scale and the distribution needs to be within an area usually less than 200 micrometers in diameter. Images were shown from organic-rich limestones, pyrite in quartz and, perhaps best, from zircon grains. In each of these cases, however, the imaged species could have been observed with the microscope or identified using the Raman 'spot' analysis. Perhaps the most powerful application of this technique is where the species of interest is optically indistinguishable from the host or surrounding material.

This study finds that microRaman spectroscopy is highly applicable to the study of minerals and materials of interest to the Earth scientist. Its usefulness lies in the diversity of analytical approach ('spot' analyses, different means of mapping and imaging) and in the type of information that can be acquired. There are few limitations and those that exist can often be surmounted. The technique has much to offer the study of minerals and could become a routine tool in Earth science laboratories.

17.4 – Other general conclusions

The conclusions given above relate directly to the areas of research described. There are, however, several other conclusions that can be drawn from this research project, that are pertinent to those studying minerals.

MicroRaman spectroscopy represents a powerful tool for the mineralogist, offering a new direction for analysis. It is a very different type of tool to the familiar X-ray based techniques providing information about the structure instead of the chemistry although some inferences can often be made.

The technique has its limitations: it can be difficult to interpret spectra and can give ambiguous results. However, those used to IR data will find it more useful since the bands are sharper and many minerals appear to have more Raman-active modes than IR-active modes. Some samples are not amenable to this type of analysis, particularly those that fluoresce. Unfortunately, its not always possible to predict those that will respond in this way. Fluorescence, and by the same token, resonance (not considered in the current work) are largely unpredictable and often the

only way of negotiating the effects of fluorescence, the overwhelming of Raman bands, is to attempt analysis with an alternative laser wavelength. A consequence of this is that for a Raman microprobe to be versatile and use to a wide range of samples, generally two lasers are required at least, and this makes the instrumentation expensive.

The technique has a lot to offer as a mineral/crystal structure tool. Analyses can be performed equally on thin sections and probe sections as well as bulk samples. Thin sections allow traditional petrographic analysis and preserve the textural relationships. It is a simple and rapid identification tool, when compared to XRD, which has been used traditionally in the study of minerals. Another advantage is that analyses are performed often without the need for sample preparation; with the single caveat that samples coated with carbon for use in EMPA or SEM chambers, for example, must either be cleaned thoroughly to remove the carbon before Raman analysis, or that the samples be analysed by the Raman technique prior to coating. Raman spectroscopy is a highly sensitive technique and the detection of amorphous carbon particles on a nanometre-scale is possible.

As with many analytical tools, the use of microRaman spectroscopy alone will rarely solve all the problems and answer all the questions raised by sample. It is important to use it in conjunction with other tools. As an example, the study of radiohaloes in biotite from the current work suggested structural collapse but that of another study, using Raman in addition to other techniques, reached a more comprehensive conclusion not involving structural collapse. This hints to the need for a combined instrument. Some areas of this study would have benefited from an SEM-microRaman instrument so that qualitative chemical information could be acquired at the same time, and from the same sampling point, as structural information. At the time of writing Renishaw plc are working on this project with a major SEM manufacturer and it will be fascinating to investigate this development.

Mineralogical samples are generally weak Raman scatterers, particularly the silicates that form the largest group of minerals. Raman bands at very low shifts from the excitation energy appear not to be of sufficient importance in the study of naturally occurring samples to warrant the use of double or triple spectrometers. Consequently, the use of instruments with filter rejection

technology and with high signal throughput is to be encouraged. Also, these are cheaper to manufacture, are better suited to multi-technique laboratories and require less expert knowledge for their optimal operation.

Griffith (1974) and Wilkinson (In: Anderson, 1973) are amongst many that state that the use of Raman in mineralogy for characterising minerals is to be 'encouraged'. How might this come about? The technique is perceived as requiring a thorough knowledge of the physical mechanisms that underpin the Raman phenomenon. This study shows that only an understanding of the basic principals is required; indeed, mineralogists familiar with XRD and the various X-ray based techniques probably only understand the basic principals behind these techniques yet the methods and data are routinely used. MicroRaman spectroscopy has distinct advantages over some of the existing techniques that make it an attractive analytical tool to the mineralogist. Notable among these are the lack of sample preparation and ability to examine thin sections, single crystals and hand specimens. If the unfamiliarity obstacle can be overcome, there is little to stop the technique from becoming routine in this environment.

17.5 - Further work

The preceding sections detailing the case studies undertaken were each discussed and suggestions made for further work.

Suggestions have been made for the development of databases of mineral spectra. As discussed, the samples need to be well-characterised, diverse and encompass as many species as possible. Ideally, samples would belong to reference collections such that the samples could be referred to easily. The advancement and progression of databases is regarded by this study as of crucial importance to the technique becoming more widespread in Earth science laboratories.

Many minerals are not strong Raman scatterers. Where appropriate, the shortest available excitation wavelength (514 nm, green) has been used where possible in this study to exploit the relationship between wavelength and intensity of Raman scattering. But perhaps further investigation of UV to blue excitation of minerals should be carried out to further explore the

potential of the technique. Ultra violet laser sources operating at 325 nm and 244 nm sources are increasingly available but remain very expensive. There are also safety issues with UV excitation. The use of UV lasers introduces instrumental issues; they require quartz optics (very expensive) and the sensitivity of CCD detectors is best in the visible. An additional advantage of UV-excitation is the further avoidance of fluorescence.

In order for the technique to become more accessible and exploited in the Earth sciences, an issue that should be addressed, perhaps, is the cost of the instrumentation. Over time the cost of components falls (manufacturing costs decrease), but the complexity of the instrumentation rises (through user demand and commercial pressures). The Renishaw RM instrument is an example of the very simple optical geometry that is required to produce a microRaman instrument of high signal throughput and good stability. However, it is also an example of how instruments can be designed to be ‘flexible’ and ‘modular’, i.e. they have the potential to perform an increasingly complicated range of experiments with an array of variables. There are a few requirements that a routine instrument, to be used in an academic mineralogy department, needs to fulfil:

- A high-quality optical microscope. The ‘front-end’ of an instrument in this market is of paramount importance
- Laser safety. The instrument must be inherently safe to use by the range of users.
- Stability. The optical geometry should be as uncomplicated as possible to minimise the need for the user to have to make adjustments.
- Sufficient resolution. Spatial resolution of around one micrometer appears to be readily achievable and is not required to be any better than this. Spectral resolution need be no better than, say, 2 cm^{-1} given that the main use might be to make qualitative assessments of the sample. A fixed dispersion grating system, perhaps with a combination of beam splitters and mirrors to achieve a 2000 cm^{-1} spectral range would be sufficient.
- Visible excitation. 514 nm excitation has been shown to permit the successful analysis of many mineralogical samples. 532 nm diode lasers can be obtained at low cost. Visible excitation towards the blue end of the spectrum, i.e. 457 nm from an Ar^+ laser may provide an advantage over the green wavelengths and can be used without specialised optics. Of the Ar^+ laser lines, the 488 nm is the strongest so may offer the optimum mix of a relatively short

visible excitation, delivering sufficiently high power to generate Raman signals from weak scatterers without inducing sample damage.

- Low cost. By removing much of the motorisation and automation of the current microRaman instruments the cost could be reduced significantly. Using one laser removes the technical difficulties involved with switching wavelengths, i.e. laser alignment, grating and optics switching.

In addition to the suggestions made for further work made at the end of each section in chapters 2, 3, 4 and 5, a proposed project of further work would be a multi-disciplinary approach to design and build a simple low-cost microRaman instrument specifically aimed at mineralogical samples. Allied to this would be an assessment of the use of the combined SEM-Raman instrument in this area.

Appendix

Tables A7.1 to A7.6 – EMPA data from traverses across biotite grains

Figures A8.1 to A8.10 – XRF data from cubic zirconia samples

Figures A8.10 to A8.17 – Raman spectra

Figures A15.1 to A15.7 – Comparison of linearly and circularly polarised light spectra.

Press release to accompany re-launch of inorganic database after extensive editing.

Appendix

Analysis no.										
	1	2	3	4	5	6	7	8	9	10
SiO ₂	34.93	34.93	34.93	34.19	34.47	34.74	34.64	34.58	34.85	34.93
TiO ₂	3.60	3.27	3.16	3.50	3.69	3.64	3.67	3.76	3.69	3.59
Al ₂ O ₃	19.77	19.80	19.87	19.46	19.55	19.53	19.70	19.59	19.67	19.67
FeO	22.07	21.79	21.92	21.76	21.77	22.17	21.96	21.55	21.62	21.76
MgO	4.32	4.21	4.32	4.12	4.07	4.01	4.15	4.15	3.96	4.24
CaO	0.00	0.00	0.00	0.00	0.00	0.00	0.00	0.00	0.00	0.00
Na ₂ O	0.29	0.38	0.30	0.40	0.32	0.32	0.34	0.30	0.33	0.29
K ₂ O	9.72	9.64	9.47	9.43	9.50	9.50	9.54	9.45	9.58	9.40
F	1.55	1.64	1.59	1.48	1.56	1.64	1.61	1.59	1.57	1.49
-O=F	0.65	0.69	0.67	0.62	0.66	0.69	0.68	0.67	0.66	0.63
Cl	0.21	0.19	0.22	0.24	0.25	0.25	0.26	0.28	0.28	0.24
-O=Cl	0.05	0.04	0.05	0.05	0.06	0.06	0.06	0.06	0.06	0.05
BaO	0.15	0.00	0.10	0.07	0.24	0.04	0.22	0.06	0.10	0.03
La ₂ O ₃	0.03	0.07	0.00	0.05	0.00	0.04	0.01	0.00	0.00	0.08
Ce ₂ O ₃	0.00	0.04	0.00	0.00	0.00	0.06	0.09	0.02	0.05	0.04
ThO ₂	0.00	0.00	0.05	0.00	0.00	0.00	0.00	0.06	0.00	0.06
Total	95.94	95.23	95.21	94.03	94.70	95.19	95.45	94.66	94.98	95.14
O	22.000	22.000	22.000	22.000	22.000	22.000	22.000	22.000	22.000	22.000
Si	5.526	5.564	5.560	5.518	5.531	5.553	5.523	5.541	5.564	5.553
Ti	0.428	0.392	0.378	0.425	0.445	0.438	0.440	0.453	0.443	0.429
Al	3.687	3.718	3.728	3.702	3.697	3.679	3.703	3.700	3.702	3.686
Fe ₂	2.920	2.903	2.918	2.937	2.921	2.964	2.928	2.888	2.887	2.893
Mg	1.019	1.000	1.025	0.991	0.973	0.955	0.986	0.991	0.943	1.005
Ca	0.000	0.000	0.000	0.000	0.000	0.000	0.000	0.000	0.000	0.000
Na	0.089	0.117	0.093	0.125	0.100	0.099	0.105	0.093	0.102	0.089
K	1.962	1.959	1.923	1.942	1.945	1.937	1.941	1.932	1.951	1.907
Ba	0.009	0.000	0.006	0.004	0.015	0.003	0.014	0.004	0.006	0.002
La	0.002	0.004	0.000	0.003	0.000	0.002	0.001	0.000	0.000	0.005
Ce	0.000	0.002	0.000	0.000	0.000	0.004	0.005	0.001	0.003	0.002
Th	0.000	0.000	0.002	0.000	0.000	0.000	0.000	0.002	0.000	0.002
Total	15.642	15.659	15.634	15.648	15.627	15.634	15.646	15.606	15.601	15.574
F	0.776	0.826	0.800	0.755	0.792	0.829	0.812	0.806	0.793	0.749
Cl	0.056	0.051	0.059	0.066	0.068	0.068	0.070	0.076	0.076	0.065

Table A7.1. EMPA results for the first traverse (perpendicular to cleavage) from unaltered biotite (no. 1) to monazite inclusion (no. 10).

	Analysis no.														
	11	12	13	14	15	16	17	18	19	20	21	22	23	24	25
SiO ₂	34.59	34.98	34.94	34.55	34.68	34.78	34.76	34.69	34.65	34.73	34.60	34.12	33.77	34.35	21.58
TiO ₂	3.69	3.68	3.56	3.70	3.64	3.51	3.53	3.64	3.77	3.53	3.71	3.39	3.52	3.49	1.56
Al ₂ O ₃	19.51	19.80	19.64	19.61	19.51	19.68	19.66	19.66	19.61	19.76	19.71	19.23	19.17	18.61	11.88
FeO	21.76	22.15	21.94	21.82	22.08	21.75	21.94	21.53	21.79	21.82	21.77	21.29	21.34	21.45	10.20
MgO	4.08	4.11	4.04	4.06	4.15	4.13	4.08	4.15	4.11	4.11	4.12	3.86	0.96	4.15	2.92
CaO	0.00	0.00	0.00	0.00	0.03	0.00	0.00	0.00	0.00	0.00	0.00	0.02	1.08	0.75	0.83
Na ₂ O	0.31	0.32	0.30	0.34	0.34	0.38	0.33	0.32	0.36	0.35	0.35	0.42	0.41	0.27	0.00
K ₂ O	9.58	9.51	9.57	9.43	9.51	9.37	9.41	9.48	9.49	9.38	9.34	9.28	9.44	9.41	3.94
F	1.39	1.58	1.68	1.47	1.61	1.54	1.48	1.59	1.76	1.72	1.42	1.56	1.71	2.46	1.10
-O=F	0.59	0.67	0.71	0.62	0.68	0.65	0.62	0.67	0.74	0.72	0.60	0.66	0.72	1.04	0.46
Cl	0.30	0.30	0.27	0.27	0.24	0.22	0.27	0.23	0.26	0.24	0.24	0.24	0.22	0.22	0.15
-O=Cl	0.07	0.07	0.06	0.06	0.05	0.05	0.06	0.05	0.06	0.05	0.05	0.05	0.05	0.05	0.03
BaO	0.00	0.13	0.12	0.10	0.05	0.13	0.00	0.00	0.05	0.00	0.04	0.12	0.00	0.12	0.00
La ₂ O ₃	0.10	0.00	0.00	0.08	0.05	0.02	0.00	0.01	0.01	0.00	0.09	0.00	0.00	0.03	4.39
Ce ₂ O ₃	0.00	0.00	0.02	0.00	0.00	0.00	0.00	0.00	0.00	0.01	0.00	0.12	0.00	0.09	12.27
ThO ₂	0.00	0.00	0.00	0.01	0.00	0.00	0.05	0.00	0.13	0.00	0.00	0.00	0.00	0.00	3.31
Total	94.65	95.82	95.31	94.76	95.16	94.81	94.83	94.58	95.19	94.88	94.74	92.94	90.85	94.31	73.64
O	22.000	22.000	22.000	22.000	22.000	22.000	22.000	22.000	22.000	22.000	22.000	22.000	22.000	22.000	22.000
Si	5.534	5.543	5.574	5.527	5.540	5.554	5.550	5.552	5.545	5.557	5.520	5.573	5.685	5.636	5.183
Ti	0.444	0.439	0.427	0.445	0.437	0.422	0.424	0.438	0.454	0.425	0.445	0.416	0.446	0.431	0.282
Al	3.679	3.698	3.693	3.698	3.674	3.704	3.700	3.709	3.699	3.727	3.707	3.702	3.804	3.599	3.363
Fe ₂	2.911	2.936	2.927	2.919	2.950	2.905	2.930	2.882	2.916	2.920	2.905	2.908	3.004	2.943	2.049
Mg	0.973	0.971	0.961	0.968	0.988	0.983	0.971	0.990	0.980	0.980	0.980	0.940	0.241	1.015	1.045
Ca	0.000	0.000	0.000	0.000	0.005	0.000	0.000	0.000	0.000	0.000	0.000	0.004	0.195	0.132	0.214
Na	0.096	0.098	0.093	0.105	0.105	0.118	0.102	0.099	0.112	0.109	0.108	0.133	0.134	0.086	0.000
K	1.955	1.923	1.948	1.925	1.938	1.909	1.917	1.936	1.938	1.915	1.901	1.934	2.027	1.970	1.207
Ba	0.000	0.008	0.008	0.006	0.003	0.008	0.000	0.000	0.003	0.000	0.003	0.008	0.000	0.008	0.000
La	0.006	0.000	0.000	0.005	0.003	0.001	0.000	0.001	0.001	0.000	0.005	0.000	0.000	0.002	0.389
Ce	0.000	0.000	0.001	0.000	0.000	0.000	0.000	0.000	0.000	0.001	0.000	0.007	0.000	0.005	1.079
Th	0.000	0.000	0.000	0.000	0.000	0.000	0.002	0.000	0.005	0.000	0.000	0.000	0.000	0.000	0.181
Total	15.598	15.616	15.632	15.599	15.645	15.604	15.594	15.606	15.652	15.634	15.574	15.625	15.535	15.827	14.991
F	0.703	0.792	0.848	0.744	0.813	0.778	0.747	0.805	0.891	0.870	0.717	0.806	0.910	1.277	0.836
Cl	0.081	0.081	0.073	0.073	0.065	0.060	0.073	0.062	0.071	0.065	0.065	0.066	0.063	0.061	0.061

Table A7.2. EMPA results for the second traverse (parallel to cleavage) from monazite inclusion (no. 11) to unaltered biotite (no. 25).

Appendix

	Analysis no.													
	26	27	28	29	30	31	32	33	34	35	36	37	38	39
SiO ₂	35.86	35.88	35.91	36.23	35.98	35.18	35.91	36.07	36.36	35.88	35.89	35.50	35.08	33.40
TiO ₂	2.58	2.48	2.27	2.50	2.77	2.66	2.63	2.54	2.51	2.56	2.76	2.61	2.93	2.75
Al ₂ O ₃	20.08	20.11	20.22	20.20	20.50	20.52	20.26	20.44	20.51	20.37	20.22	20.18	20.10	18.98
FeO	19.86	20.02	20.20	20.17	20.77	20.99	20.45	20.03	20.10	20.32	20.88	21.75	21.67	19.56
MgO	4.97	4.97	5.07	4.89	4.79	4.47	4.78	4.80	4.79	4.82	4.63	4.63	4.48	4.20
CaO	0.00	0.01	0.00	0.04	0.01	0.00	0.00	0.00	0.00	0.00	0.03	0.02	0.05	0.33
Na ₂ O	0.32	0.30	0.24	0.32	0.31	0.32	0.31	0.30	0.31	0.30	0.27	0.26	0.38	0.40
K ₂ O	8.99	9.15	9.18	9.43	9.51	9.38	9.46	9.58	9.54	9.65	9.38	9.26	9.13	8.21
F	1.75	1.84	1.46	1.92	1.89	1.91	1.72	1.76	1.93	1.85	1.78	1.59	1.62	1.43
-O=F	0.74	0.77	0.61	0.81	0.80	0.80	0.72	0.74	0.81	0.78	0.75	0.67	0.68	0.60
Cl	0.16	0.17	0.16	0.16	0.17	0.18	0.17	0.13	0.18	0.18	0.18	0.22	0.23	0.21
-O=Cl	0.04	0.04	0.04	0.04	0.04	0.04	0.04	0.03	0.04	0.04	0.04	0.05	0.05	0.05
BaO	0.05	0.01	0.00	0.13	0.02	0.02	0.00	0.00	0.00	0.05	0.14	0.17	0.09	0.12
La ₂ O ₃	0.05	0.00	0.04	0.00	0.00	0.05	0.00	0.07	0.01	0.00	0.04	0.00	0.02	0.44
Ce ₂ O ₃	0.06	0.00	0.01	0.00	0.00	0.08	0.00	0.00	0.00	0.00	0.00	0.06	0.01	1.20
ThO ₂	0.04	0.00	0.00	0.00	0.03	0.00	0.00	0.01	0.00	0.00	0.01	0.00	0.03	0.50
Total	93.99	94.13	94.11	95.14	95.91	94.92	94.93	94.96	95.39	95.16	95.42	95.53	95.09	91.08
O	22.000	22.000	22.000	22.000	22.000	22.000	22.000	22.000	22.000	22.000	22.000	22.000	22.000	22.000
Si	5.702	5.708	5.679	5.720	5.648	5.606	5.672	5.686	5.718	5.671	5.663	5.608	5.574	5.574
Ti	0.309	0.297	0.270	0.297	0.327	0.319	0.312	0.301	0.297	0.304	0.327	0.310	0.350	0.345
Al	3.763	3.771	3.769	3.759	3.793	3.854	3.772	3.798	3.802	3.795	3.760	3.757	3.764	3.733
Fe ₂	2.641	2.664	2.672	2.663	2.727	2.797	2.701	2.641	2.644	2.686	2.755	2.873	2.880	2.730
Mg	1.178	1.179	1.195	1.151	1.121	1.062	1.125	1.128	1.123	1.136	1.089	1.090	1.061	1.045
Ca	0.000	0.002	0.000	0.007	0.002	0.000	0.000	0.000	0.000	0.000	0.005	0.003	0.009	0.059
Na	0.099	0.093	0.074	0.098	0.094	0.099	0.095	0.092	0.095	0.092	0.083	0.080	0.117	0.129
K	1.824	1.857	1.852	1.899	1.905	1.907	1.906	1.927	1.914	1.946	1.888	1.866	1.851	1.748
Ba	0.003	0.001	0.000	0.008	0.001	0.001	0.000	0.000	0.000	0.003	0.009	0.011	0.006	0.008
La	0.003	0.000	0.002	0.000	0.000	0.003	0.000	0.004	0.001	0.000	0.002	0.000	0.001	0.027
Ce	0.003	0.000	0.001	0.000	0.000	0.005	0.000	0.000	0.000	0.000	0.000	0.003	0.001	0.073
Th	0.001	0.000	0.000	0.000	0.001	0.000	0.000	0.000	0.000	0.000	0.000	0.000	0.001	0.019
Total	15.526	15.570	15.514	15.603	15.619	15.653	15.583	15.577	15.592	15.633	15.582	15.602	15.614	15.491
F	0.880	0.926	0.730	0.959	0.938	0.963	0.859	0.877	0.960	0.925	0.888	0.794	0.814	0.755
Cl	0.043	0.046	0.043	0.043	0.045	0.049	0.046	0.035	0.048	0.048	0.048	0.059	0.062	0.059

Table A7.3. EMPA results for the third traverse (perpendicular to cleavage) from unaltered biotite (no. 26) to monazite inclusion (no. 39).

	Analysis no.										
	40	41	42	43	44	45	46	47	48	49	50
SiO ₂	35.06	35.17	34.69	34.90	34.80	34.78	34.95	35.33	33.64	34.94	26.97
TiO ₂	2.95	3.01	2.87	2.75	3.06	2.95	2.87	2.97	2.92	2.86	1.81
Al ₂ O ₃	20.31	20.25	20.10	20.27	20.11	20.21	20.38	20.37	20.42	20.69	16.12
FeO	21.88	21.52	21.39	21.57	21.41	21.41	21.70	21.22	21.04	20.62	13.22
MgO	4.35	4.38	4.34	4.36	4.38	4.33	4.34	4.39	4.39	4.30	3.63
CaO	0.01	0.00	0.00	0.01	0.00	0.00	0.00	0.00	0.00	0.00	0.54
Na ₂ O	0.30	0.25	0.31	0.33	0.31	0.26	0.31	0.25	0.30	0.29	0.12
K ₂ O	9.60	9.51	9.49	9.51	9.58	9.43	9.50	9.62	9.59	9.39	5.85
F	1.47	1.37	1.65	1.71	1.67	1.54	1.47	1.60	1.56	1.66	1.26
-O=F	0.62	0.58	0.69	0.72	0.70	0.65	0.62	0.67	0.66	0.70	0.53
Cl	0.23	0.19	0.19	0.21	0.22	0.21	0.24	0.21	0.22	0.18	0.13
-O=Cl	0.05	0.04	0.04	0.05	0.05	0.05	0.05	0.05	0.05	0.04	0.03
BaO	0.00	0.10	0.01	0.04	0.00	0.03	0.00	0.00	0.08	0.00	0.06
La ₂ O ₃	0.05	0.00	0.00	0.05	0.00	0.03	0.02	0.05	0.03	0.05	3.32
Ce ₂ O ₃	0.09	0.00	0.00	0.00	0.06	0.02	0.02	0.08	0.01	0.15	8.19
ThO ₂	0.00	0.03	0.00	0.06	0.00	0.03	0.00	0.00	0.05	0.00	1.96
Total	95.63	95.16	94.31	95.00	94.85	94.53	95.13	95.37	93.54	94.39	82.62
O	22.000	22.000	22.000	22.000	22.000	22.000	22.000	22.000	22.000	22.000	22.000
Si	5.540	5.557	5.563	5.568	5.555	5.553	5.543	5.585	5.452	5.569	5.336
Ti	0.351	0.358	0.346	0.330	0.367	0.354	0.342	0.353	0.356	0.343	0.269
Al	3.783	3.771	3.800	3.812	3.784	3.803	3.810	3.795	3.901	3.887	3.759
Fe ₂	2.891	2.844	2.869	2.878	2.858	2.859	2.878	2.805	2.852	2.749	2.187
Mg	1.025	1.032	1.038	1.037	1.042	1.031	1.026	1.034	1.061	1.022	1.071
Ca	0.002	0.000	0.000	0.002	0.000	0.000	0.000	0.000	0.000	0.000	0.114
Na	0.092	0.077	0.096	0.102	0.096	0.080	0.095	0.077	0.094	0.090	0.046
K	1.935	1.917	1.942	1.936	1.951	1.921	1.922	1.940	1.983	1.910	1.477
Ba	0.000	0.006	0.001	0.003	0.000	0.002	0.000	0.000	0.005	0.000	0.005
La	0.003	0.000	0.000	0.003	0.000	0.002	0.001	0.003	0.002	0.003	0.242
Ce	0.005	0.000	0.000	0.000	0.004	0.001	0.001	0.005	0.001	0.009	0.593
Th	0.000	0.001	0.000	0.002	0.000	0.001	0.000	0.000	0.002	0.000	0.088
Total	15.626	15.563	15.654	15.671	15.658	15.607	15.619	15.597	15.707	15.581	15.187
F	0.735	0.685	0.837	0.863	0.843	0.778	0.737	0.800	0.800	0.837	0.788
Cl	0.062	0.051	0.052	0.057	0.060	0.057	0.065	0.056	0.060	0.049	0.044

Table A7.4. EMPA results for the fourth traverse (parallel to cleavage) from monazite inclusion (no. 40) to unaltered biotite (no. 50).

Appendix

	Analysis no.																		
	51	52	53	54	55	56	57	58	59	60	61	62	63	64	65	66	67	68	69
SiO2	35.09	35.38	35.05	35.16	35.27	35.21	35.10	35.15	35.06	35.16	35.16	35.07	35.32	34.91	35.35	35.08	35.08	34.99	35.07
TiO2	2.53	2.90	2.77	3.02	2.81	2.88	3.00	2.80	2.82	2.71	2.98	3.11	2.78	3.03	3.26	3.20	3.15	3.33	3.27
Al2O3	20.42	20.23	20.29	20.24	20.42	20.45	20.37	20.42	20.40	20.33	20.29	20.35	20.17	20.12	20.31	20.33	20.17	20.05	20.00
FeO	21.52	21.61	21.53	21.60	21.58	21.66	21.56	21.88	21.66	21.57	21.88	21.51	21.44	22.03	22.07	21.63	21.77	21.92	21.47
MgO	4.43	4.56	4.53	4.47	4.59	4.51	4.51	4.46	4.48	4.43	4.47	4.48	4.56	4.44	4.38	4.36	4.30	4.28	4.40
CaO	0.00	0.00	0.01	0.00	0.00	0.00	0.00	0.00	0.00	0.01	0.00	0.00	0.00	0.01	0.00	0.00	0.00	0.00	0.02
Na2O	0.22	0.27	0.30	0.30	0.30	0.28	0.27	0.27	0.29	0.30	0.24	0.25	0.25	0.25	0.26	0.26	0.31	0.29	0.33
K2O	9.64	9.74	9.70	9.65	9.68	9.76	9.62	9.71	9.70	9.67	9.72	9.62	9.74	9.67	9.77	9.71	9.68	9.72	9.57
F	1.82	2.05	1.70	1.80	1.52	1.84	1.62	1.59	1.75	1.56	1.48	1.79	1.73	1.70	1.51	1.71	1.51	1.58	1.52
-O=F	0.77	0.86	0.72	0.76	0.64	0.77	0.68	0.67	0.74	0.66	0.62	0.75	0.73	0.72	0.64	0.72	0.64	0.67	0.64
Cl	0.18	0.21	0.23	0.20	0.20	0.21	0.19	0.19	0.22	0.23	0.21	0.23	0.20	0.22	0.20	0.23	0.20	0.22	0.21
-O=Cl	0.04	0.05	0.05	0.05	0.05	0.05	0.04	0.04	0.05	0.05	0.05	0.05	0.05	0.05	0.05	0.05	0.05	0.05	0.05
BaO	0.20	0.00	0.20	0.16	0.13	0.08	0.16	0.08	0.07	0.22	0.08	0.01	0.14	0.07	0.06	0.01	0.18	0.02	0.14
La2O3	0.00	0.12	0.00	0.00	0.12	0.14	0.08	0.00	0.00	0.00	0.01	0.00	0.00	0.00	0.00	0.00	0.00	0.00	0.13
Ce2O3	0.02	0.10	0.03	0.07	0.09	0.08	0.02	0.06	0.00	0.00	0.00	0.00	0.11	0.02	0.02	0.00	0.00	0.02	0.13
ThO2	0.00	0.00	0.00	0.12	0.06	0.04	0.05	0.10	0.00	0.00	0.00	0.14	0.00	0.00	0.00	0.00	0.00	0.00	0.00
Total	95.26	96.26	95.57	95.98	96.08	96.32	95.83	96.00	95.66	95.48	95.85	95.76	95.66	95.70	96.50	95.75	95.66	95.70	95.57
O	22.00				22.00	22.00					22.00		22.00	22.00	22.00	22.00		22.00	22.00
	0	22.000	22.000	22.000	0	0	22.000	22.000	22.000	22.000	0	22.000	0	0	0	0	22.000	0	0
Si	5.590	5.602	5.563	5.566	5.548	5.560	5.544	5.545	5.558	5.570	5.541	5.555	5.595	5.542	5.537	5.550	5.546	5.539	5.551
Ti	0.303	0.345	0.331	0.360	0.332	0.342	0.356	0.332	0.336	0.323	0.353	0.370	0.331	0.362	0.384	0.381	0.375	0.396	0.389
Al	3.834	3.776	3.796	3.777	3.786	3.806	3.792	3.797	3.812	3.796	3.769	3.800	3.766	3.765	3.750	3.791	3.758	3.741	3.731
Fe2	2.867	2.862	2.858	2.860	2.839	2.860	2.848	2.887	2.872	2.858	2.884	2.850	2.840	2.925	2.891	2.862	2.878	2.902	2.842
Mg	1.052	1.076	1.072	1.055	1.076	1.062	1.062	1.049	1.059	1.046	1.050	1.058	1.077	1.051	1.023	1.028	1.013	1.010	1.038
Ca	0.000	0.000	0.002	0.000	0.000	0.000	0.000	0.000	0.000	0.002	0.000	0.000	0.000	0.002	0.000	0.000	0.000	0.000	0.003
Na	0.068	0.083	0.092	0.092	0.092	0.086	0.083	0.083	0.089	0.092	0.073	0.077	0.077	0.077	0.079	0.080	0.095	0.089	0.101
K	1.959	1.968	1.964	1.949	1.943	1.966	1.938	1.954	1.962	1.954	1.954	1.944	1.968	1.959	1.952	1.960	1.952	1.963	1.932
Ba	0.012	0.000	0.012	0.010	0.008	0.005	0.010	0.005	0.004	0.014	0.005	0.001	0.009	0.004	0.004	0.001	0.011	0.001	0.009
La	0.000	0.007	0.000	0.000	0.007	0.008	0.005	0.000	0.000	0.000	0.001	0.000	0.000	0.000	0.000	0.000	0.000	0.000	0.008
Ce	0.001	0.006	0.002	0.004	0.005	0.005	0.001	0.003	0.000	0.000	0.000	0.000	0.006	0.001	0.001	0.000	0.000	0.001	0.008
Th	0.000	0.000	0.000	0.004	0.002	0.001	0.002	0.004	0.000	0.000	0.000	0.005	0.000	0.000	0.000	0.000	0.000	0.000	0.000
Total	15.68				15.64	15.70					15.63		15.67	15.68	15.62	15.65		15.64	15.61
	6	15.725	15.693	15.677	0	1	15.640	15.659	15.693	15.654	1	15.659	0	7	0	2	15.629	4	2
F	0.917	1.027	0.853	0.901	0.756	0.919	0.809	0.793	0.877	0.782	0.738	0.897	0.867	0.854	0.748	0.856	0.755	0.791	0.761
Cl	0.049	0.056	0.062	0.054	0.053	0.056	0.051	0.051	0.059	0.062	0.056	0.062	0.054	0.059	0.053	0.062	0.054	0.059	0.056

Table A7.5. EMPA results for the fifth traverse (perpendicular to cleavage) from unaltered biotite (no. 51) to inclusion (no.69).

	Analysis no.													
	70	71	72	73	74	75	76	77	78	79	80	81	82	83
SiO ₂	35.18	35.22	34.99	34.94	34.84	35.08	34.95	35.10	34.93	34.84	35.07	34.74	34.75	34.43
TiO ₂	3.17	3.02	3.04	3.10	2.89	3.28	3.20	3.46	3.35	3.07	3.29	3.34	3.27	3.33
Al ₂ O ₃	20.10	20.25	20.13	20.14	20.16	20.12	20.07	20.06	20.01	20.01	20.12	20.02	20.04	19.45
FeO	21.71	22.05	21.59	21.68	21.92	21.85	21.58	21.63	21.73	21.68	21.85	21.65	21.88	21.62
MgO	4.42	4.42	4.38	4.24	4.32	4.37	4.27	4.34	4.29	4.27	4.23	4.26	4.27	3.69
CaO	0.00	0.00	0.00	0.00	0.01	0.00	0.00	0.00	0.02	0.02	0.01	0.00	0.00	0.01
Na ₂ O	0.28	0.24	0.23	0.22	0.25	0.28	0.22	0.29	0.27	0.29	0.31	0.31	0.35	0.31
K ₂ O	9.56	9.58	9.65	9.57	9.70	9.64	9.68	9.73	9.66	9.71	9.59	9.53	9.60	9.51
F	1.56	1.53	1.53	1.46	1.64	1.62	1.69	1.54	1.67	1.49	1.48	1.43	1.28	1.61
-O=F	0.66	0.64	0.64	0.61	0.69	0.68	0.71	0.65	0.70	0.63	0.62	0.60	0.54	0.68
Cl	0.18	0.21	0.18	0.20	0.23	0.20	0.21	0.22	0.21	0.19	0.20	0.19	0.22	0.21
-O=Cl	0.04	0.05	0.04	0.05	0.05	0.05	0.05	0.05	0.05	0.04	0.05	0.04	0.05	0.05
BaO	0.09	0.14	0.15	0.16	0.07	0.26	0.11	0.09	0.09	0.19	0.00	0.18	0.18	0.05
La ₂ O ₃	0.08	0.00	0.02	0.03	0.00	0.00	0.00	0.00	0.00	0.02	0.00	0.00	0.00	0.10
Ce ₂ O ₃	0.07	0.00	0.06	0.02	0.00	0.03	0.00	0.00	0.00	0.07	0.00	0.14	0.13	0.17
ThO ₂	0.05	0.00	0.00	0.00	0.03	0.00	0.00	0.00	0.00	0.00	0.04	0.00	0.00	0.00
Total	95.75	95.97	95.27	95.10	95.32	96.00	95.22	95.76	95.48	95.18	95.52	95.15	95.38	93.76
O	22.000	22.000	22.000	22.000	22.000	22.000	22.000	22.000	22.000	22.000	22.000	22.000	22.000	22.000
Si	5.556	5.550	5.552	5.549	5.549	5.542	5.564	5.542	5.548	5.543	5.544	5.520	5.504	5.583
Ti	0.377	0.358	0.363	0.370	0.346	0.390	0.383	0.411	0.400	0.367	0.391	0.399	0.389	0.406
Al	3.742	3.761	3.765	3.770	3.784	3.746	3.766	3.733	3.746	3.753	3.749	3.749	3.741	3.718
Fe ₂	2.867	2.906	2.865	2.879	2.920	2.887	2.873	2.856	2.887	2.885	2.889	2.877	2.898	2.932
Mg	1.041	1.038	1.036	1.004	1.026	1.029	1.013	1.022	1.016	1.013	0.997	1.009	1.008	0.892
Ca	0.000	0.000	0.000	0.000	0.002	0.000	0.000	0.000	0.003	0.003	0.002	0.000	0.000	0.002
Na	0.086	0.073	0.071	0.068	0.077	0.086	0.068	0.089	0.083	0.089	0.095	0.096	0.107	0.097
K	1.926	1.926	1.954	1.939	1.971	1.943	1.966	1.960	1.958	1.971	1.934	1.932	1.940	1.968
Ba	0.006	0.009	0.009	0.010	0.004	0.016	0.007	0.006	0.006	0.012	0.000	0.011	0.011	0.003
La	0.005	0.000	0.001	0.002	0.000	0.000	0.000	0.000	0.000	0.001	0.000	0.000	0.000	0.006
Ce	0.004	0.000	0.003	0.001	0.000	0.002	0.000	0.000	0.000	0.004	0.000	0.008	0.008	0.010
Th	0.002	0.000	0.000	0.000	0.001	0.000	0.000	0.000	0.000	0.000	0.001	0.000	0.000	0.000
Total	15.610	15.621	15.620	15.592	15.680	15.640	15.641	15.619	15.647	15.641	15.601	15.601	15.606	15.618
F	0.779	0.762	0.768	0.733	0.826	0.809	0.851	0.769	0.839	0.750	0.740	0.719	0.641	0.826
Cl	0.048	0.056	0.048	0.054	0.062	0.054	0.057	0.059	0.057	0.051	0.054	0.051	0.059	0.058

Table A7.6. EMPA results for the sixth traverse (parallel to cleavage) from unaltered biotite (no. 70) to inclusion (no. 83).

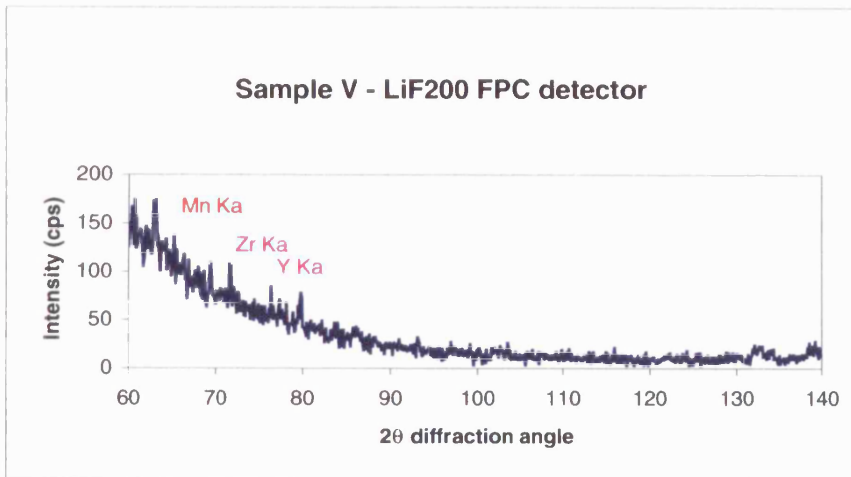


Fig. A8.1. Sample V XRF 2θ scan.

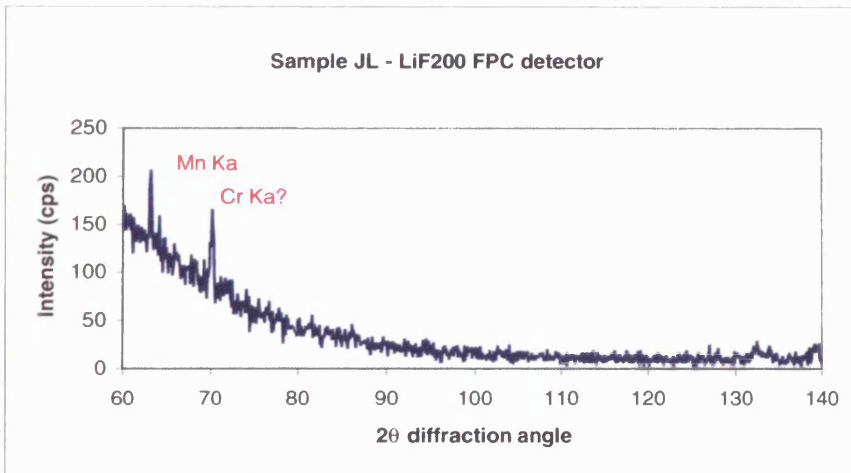


Fig. A8.2. Sample JL XRF 2θ scan.

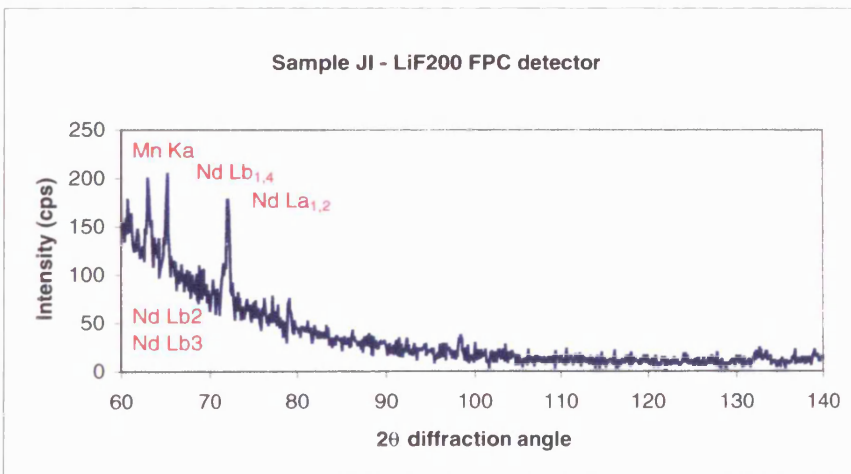


Fig. A8.3. Sample JI XRF 2θ scan.

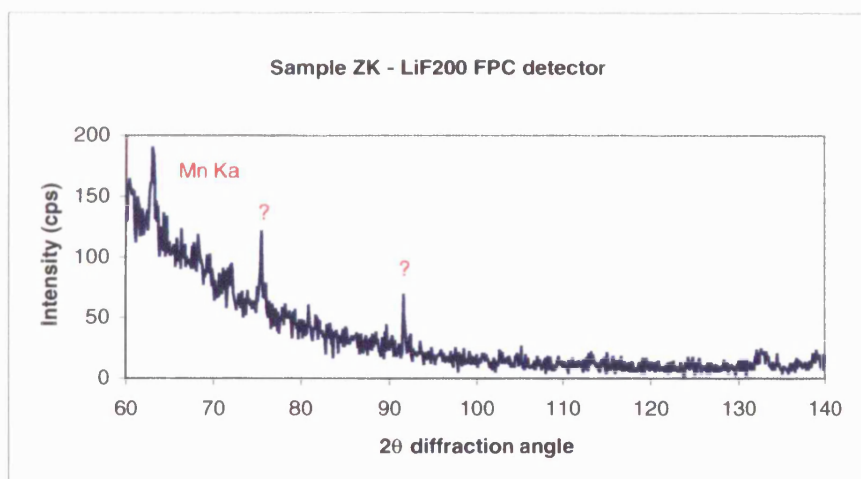


Fig. A8.4. Sample ZK XRF 2θ scan.

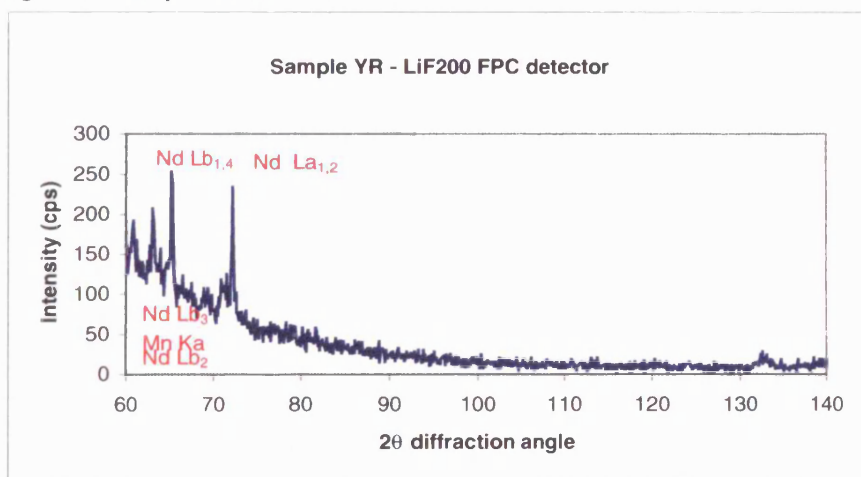


Fig. A8.5. Sample YR XRF 2θ scan.

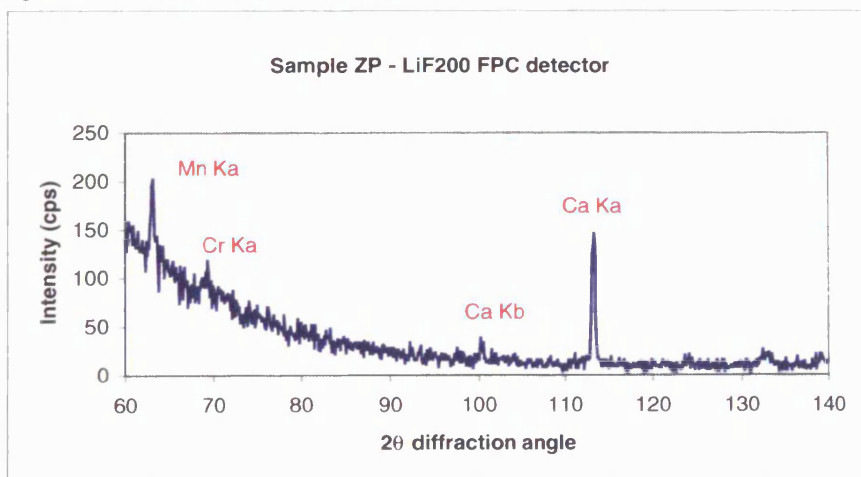


Fig. A8.6. Sample ZP XRF 2θ scan.

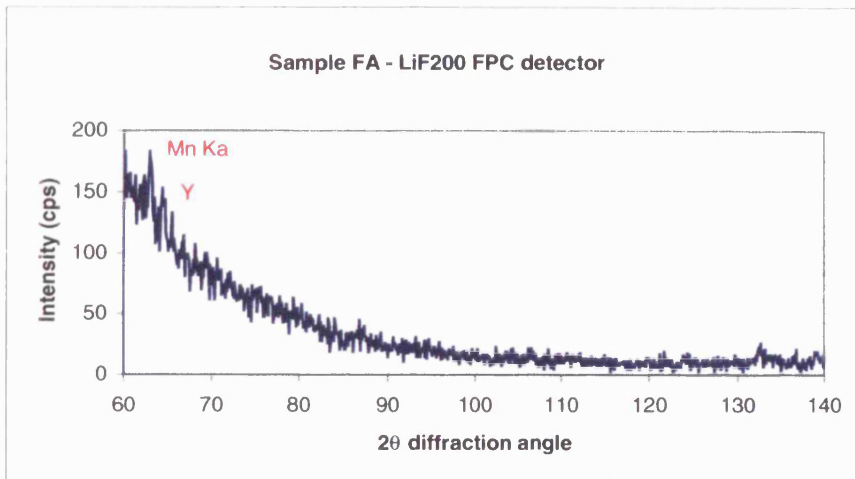


Fig. A8.7. Sample FA XRF 2θ scan.

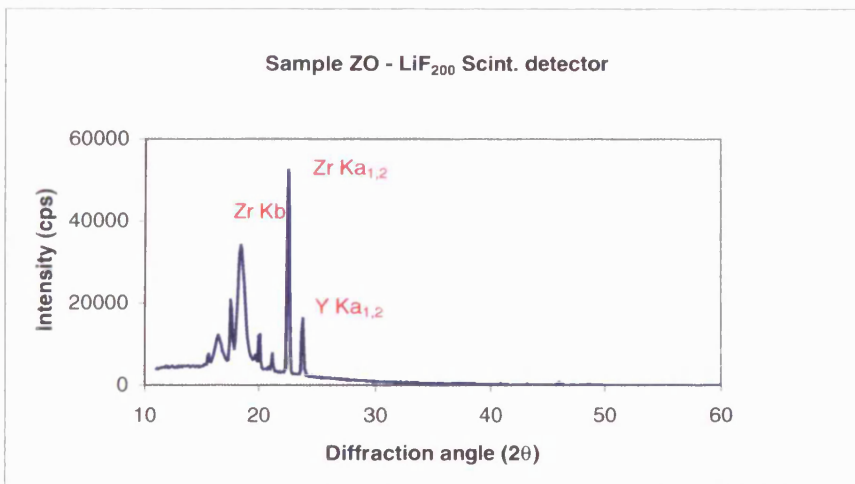


Fig. A8.8. Sample ZO XRF 2θ scan.

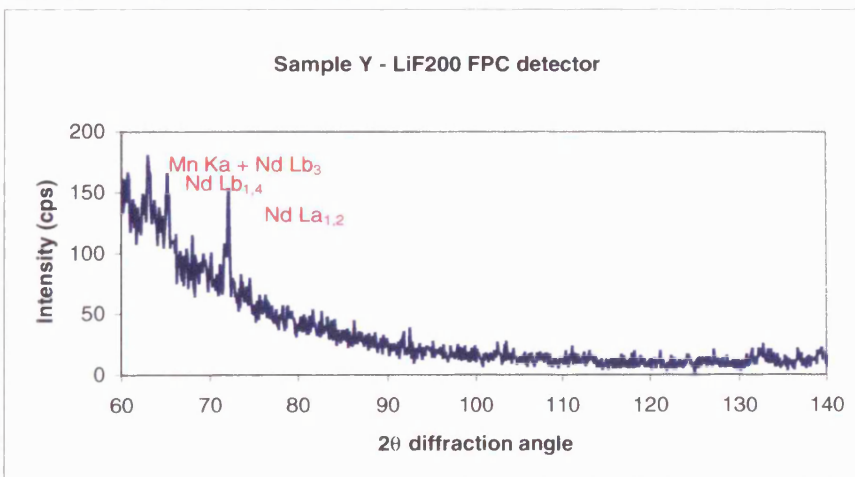


Fig. A8.9. Sample ZN XRF 2θ scan.

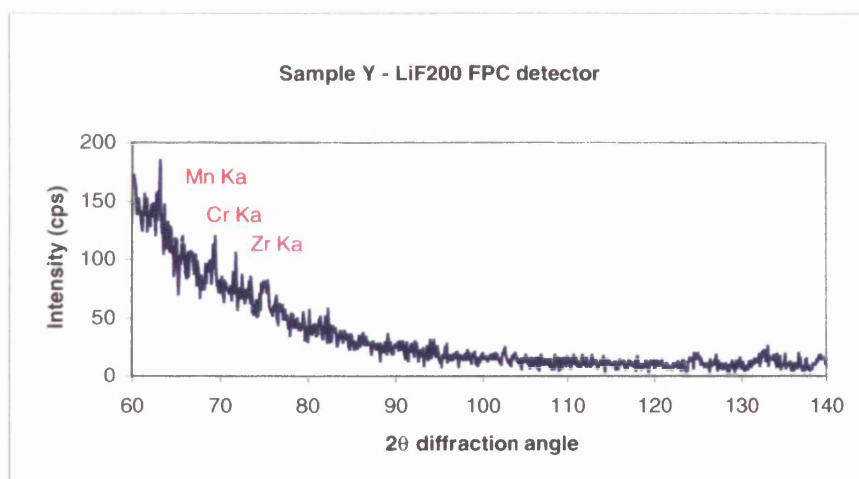


Fig. A8.10. Sample ZR XRF 2θ scan.

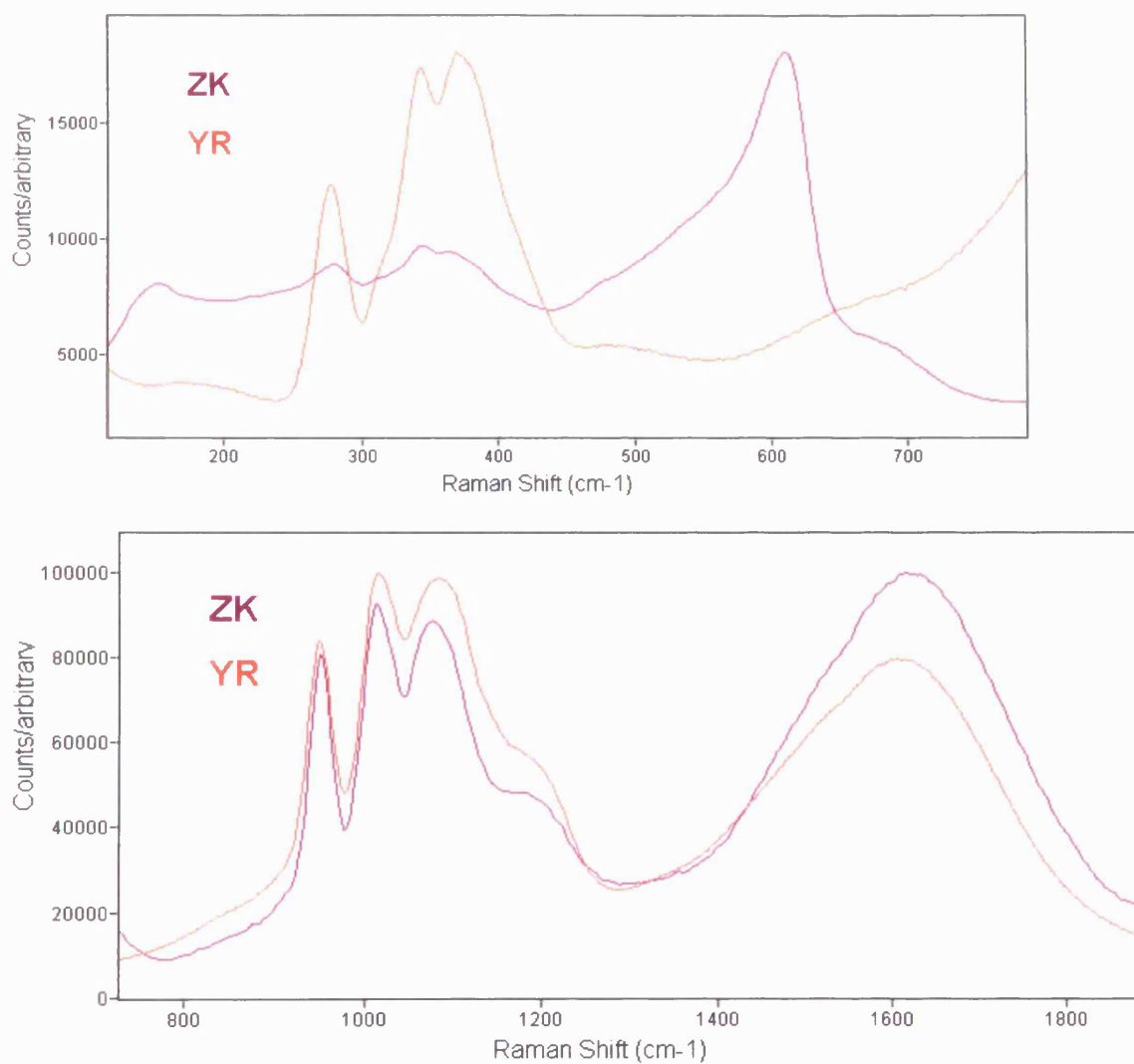


Fig. A8.11. Raman spectra of samples ZK (offset -6 cm^{-1}) and YR determined by spectroscopy as containing Er^{3+} .

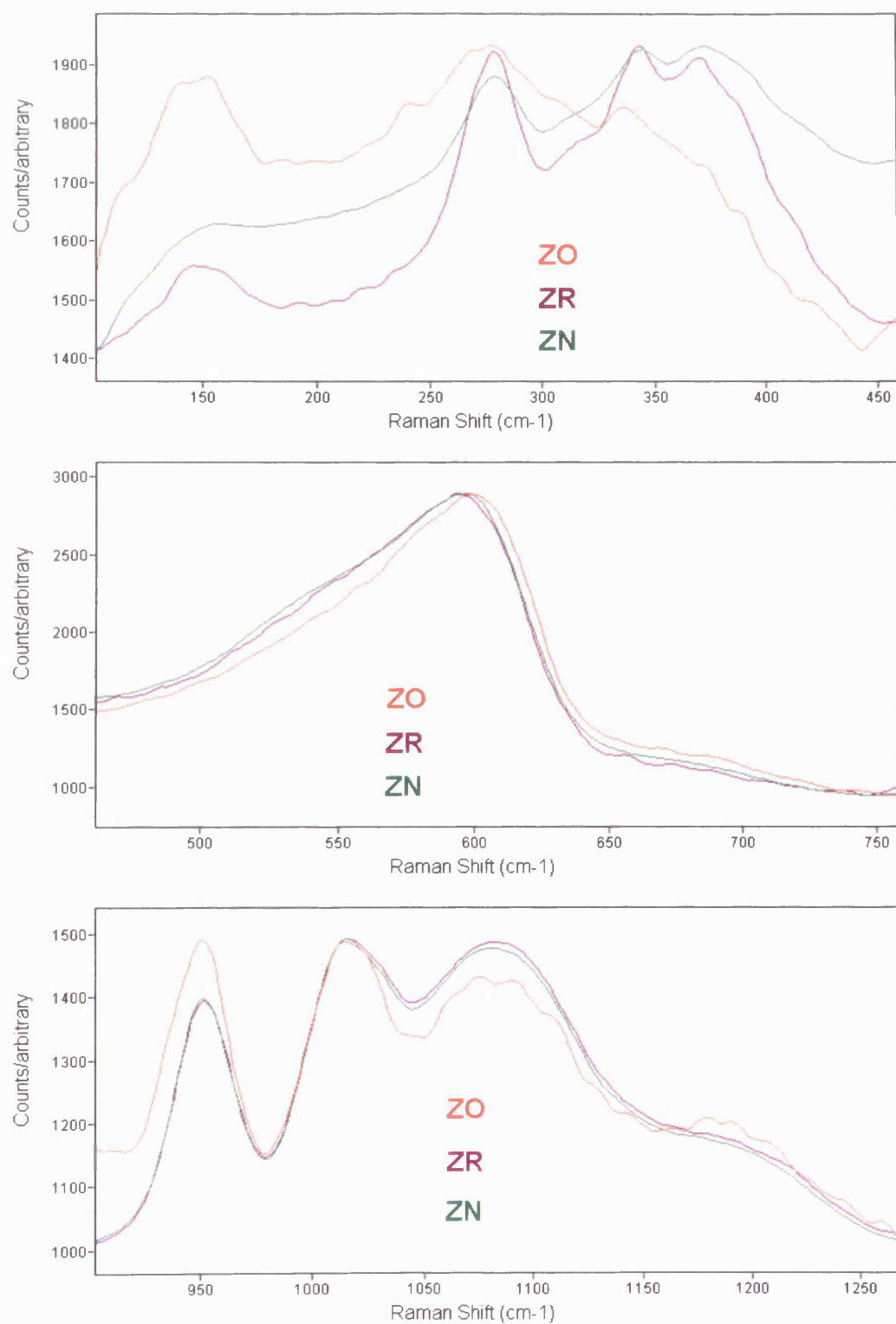


Fig. A8.12. Raman spectra of samples ZN, ZO and ZR determined by spectroscopy as containing Nd³⁺.

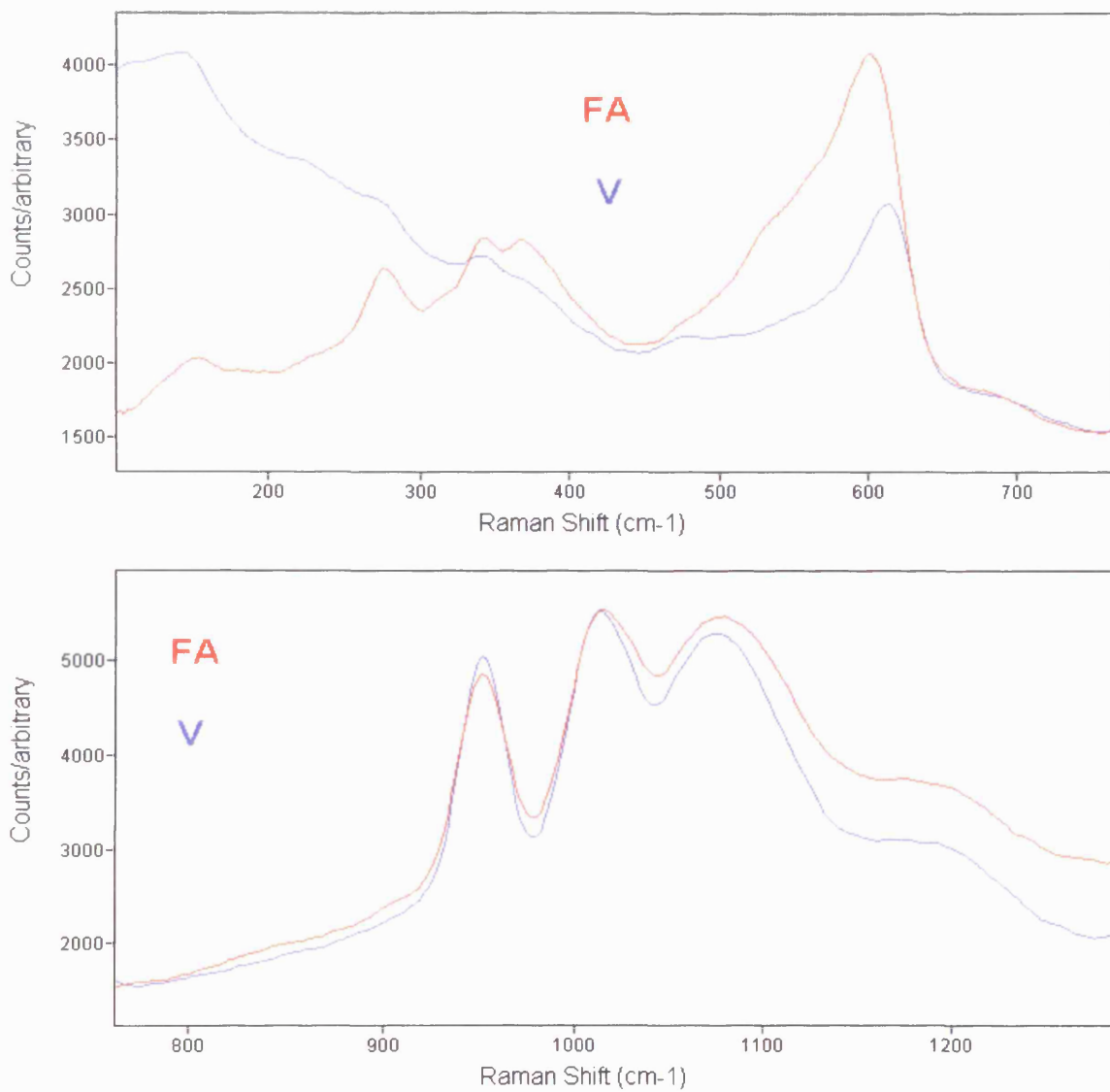


Fig. A8.13. Raman spectra of samples V and FA determined by XRF as containing Y^{3+} .

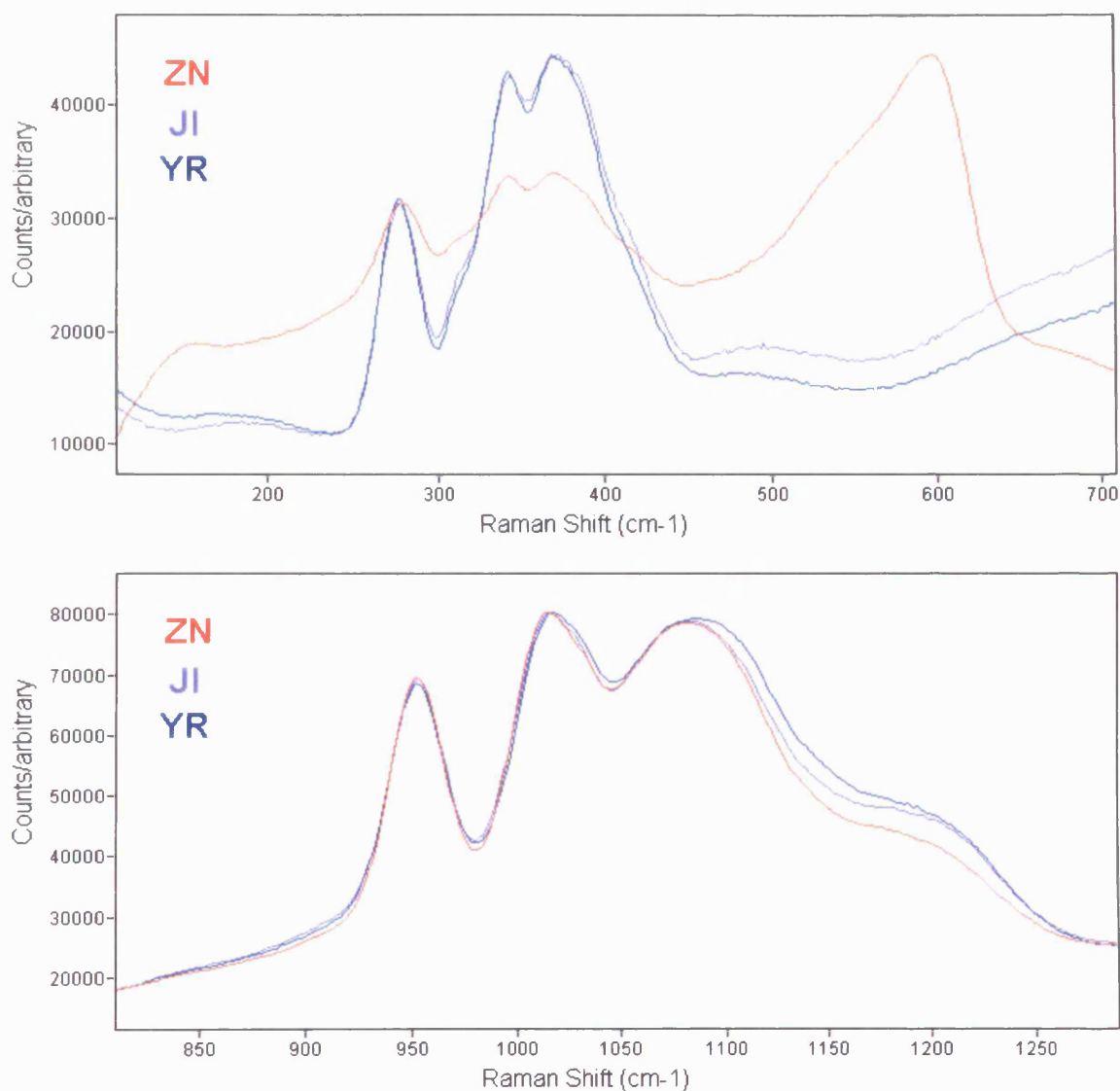


Fig. A8.14. Raman spectra of samples JI, YR and ZN determined by XRF as containing Nd³⁺.

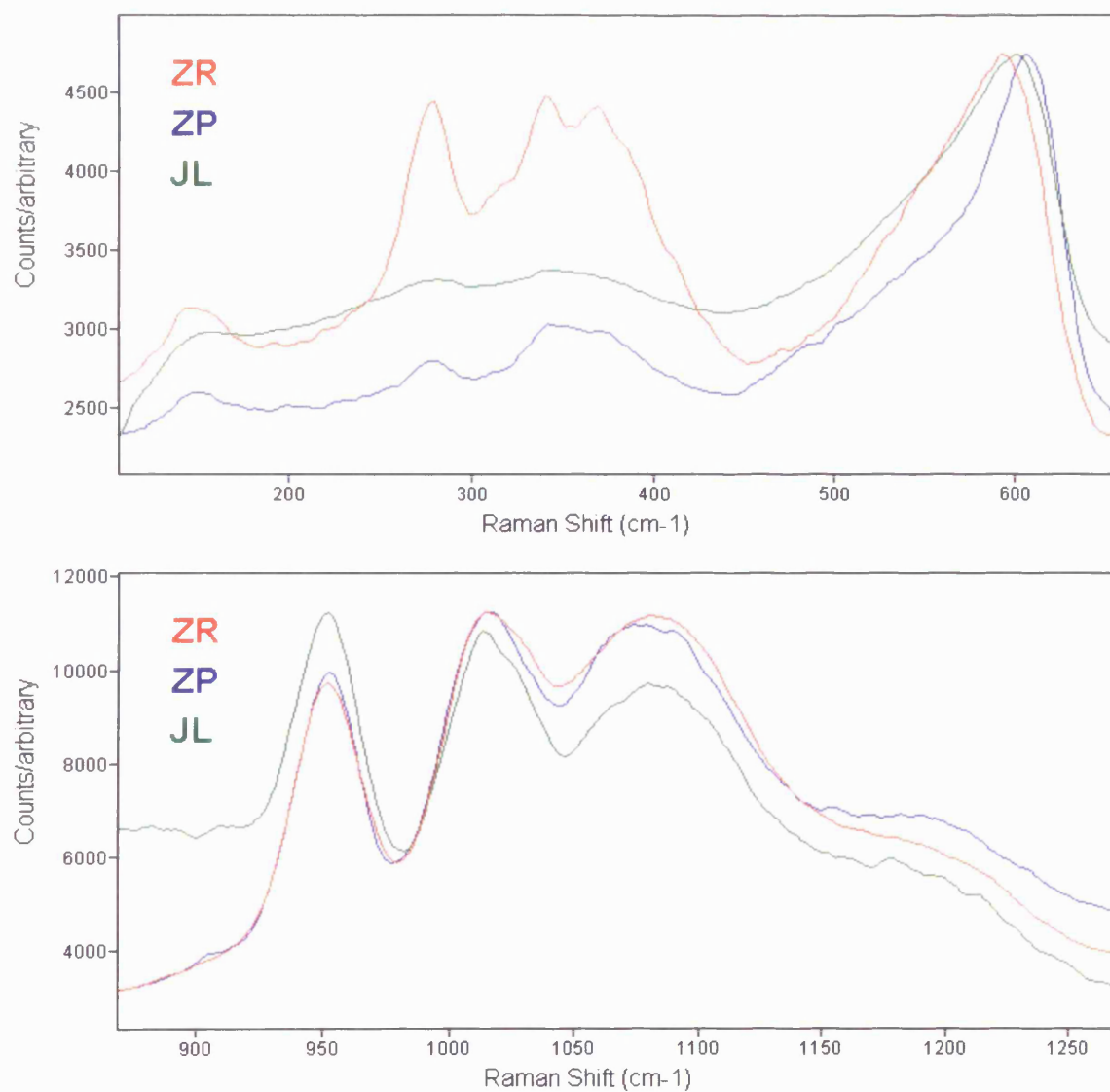


Fig. A8.15. Raman spectra of samples JL, ZP and ZR determined by XRF as containing Cr³⁺.

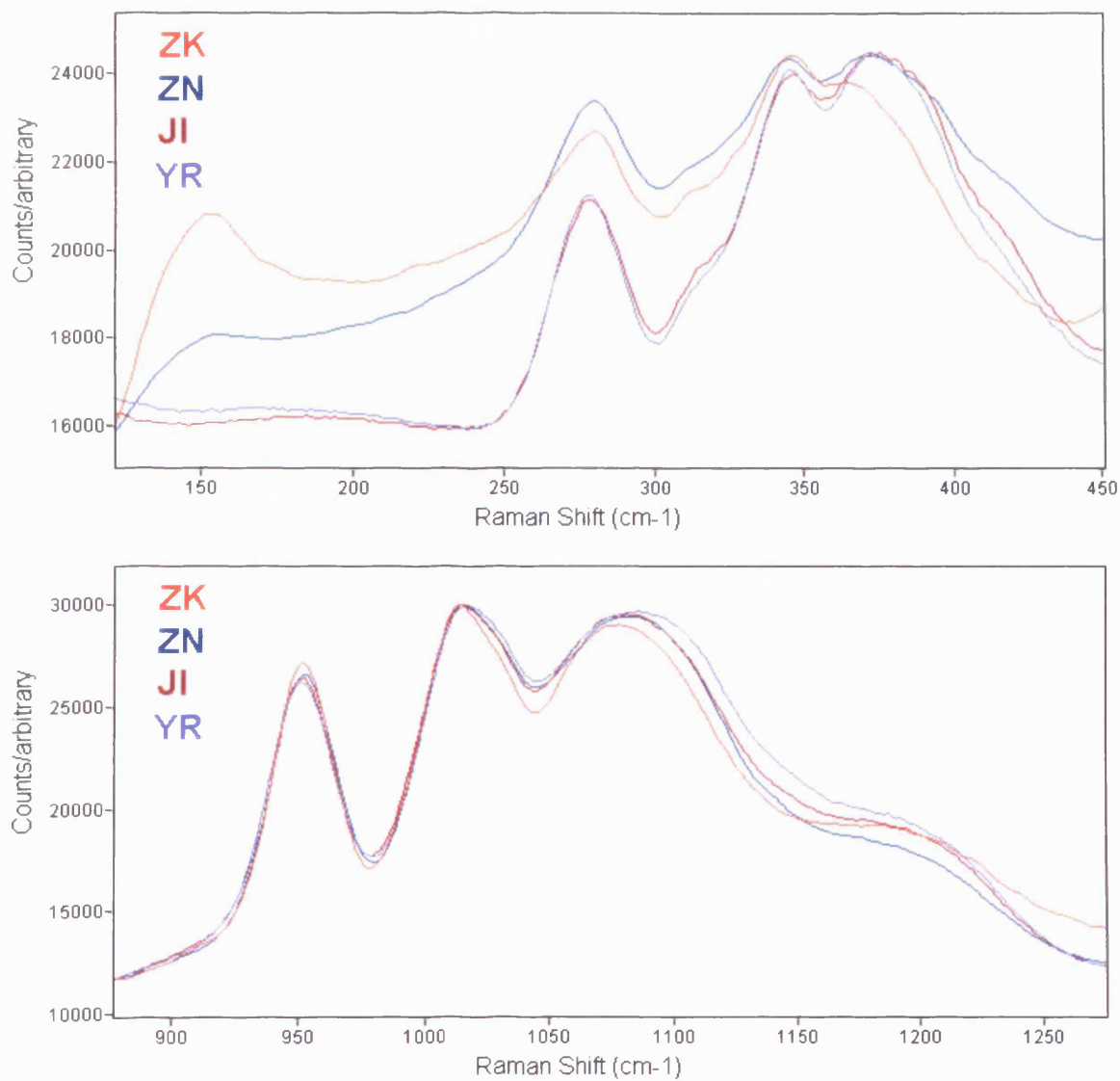


Fig. A8.16. Raman spectra of samples JI, ZK, ZN and YR. All are pale pinks and lavenders in colour.

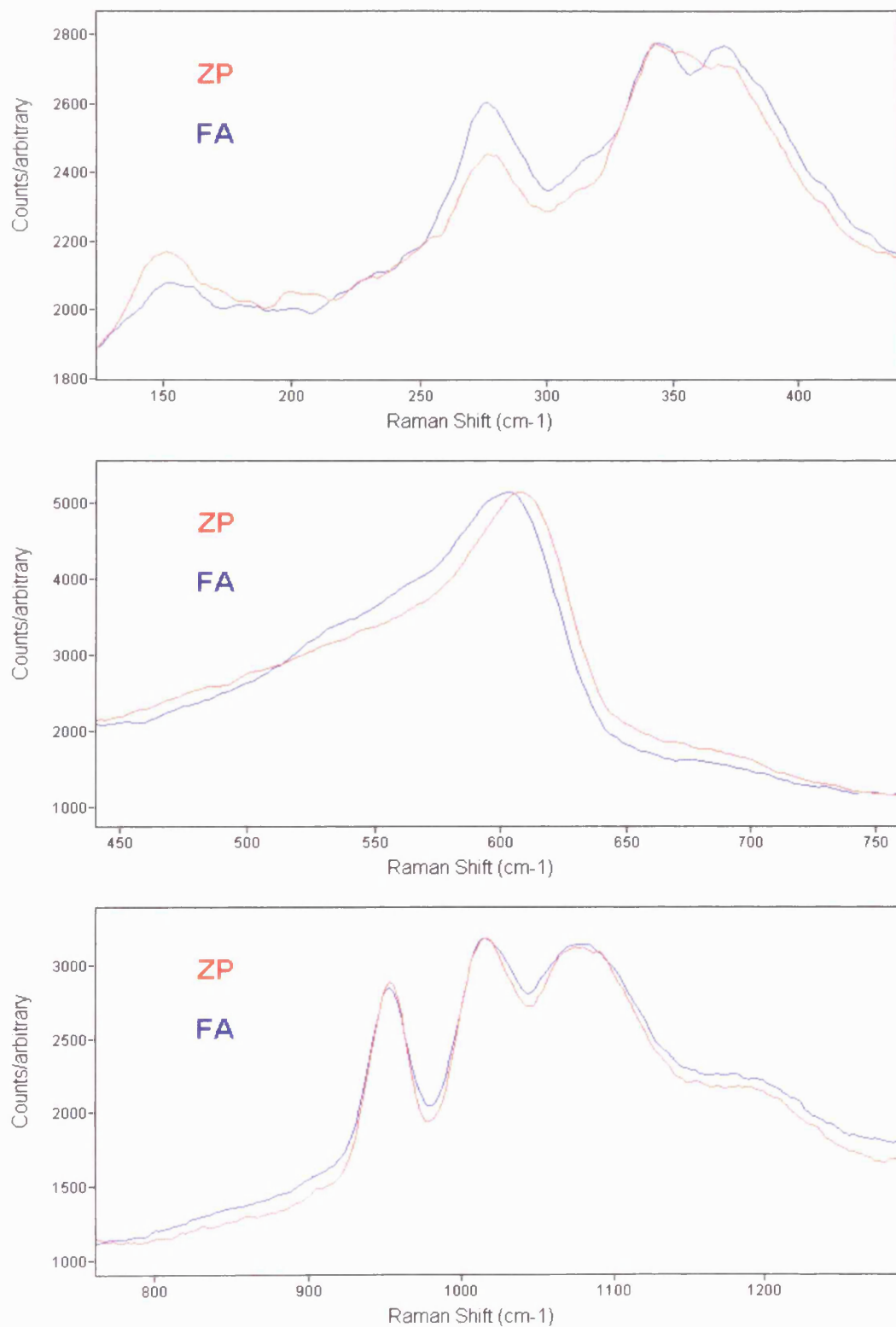
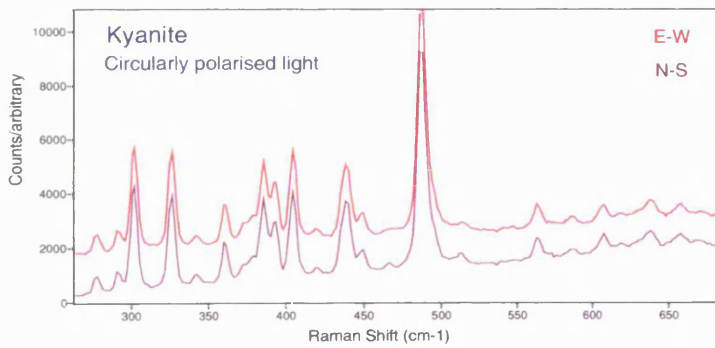
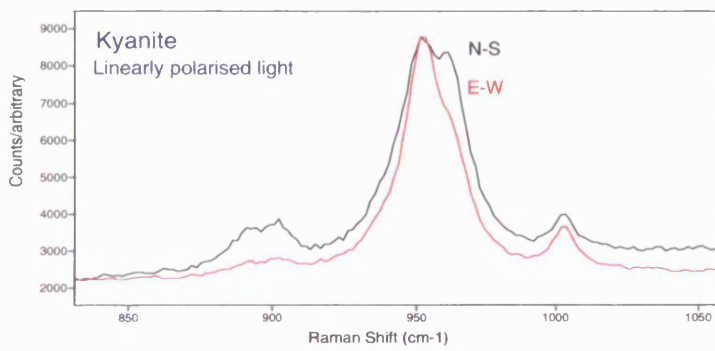
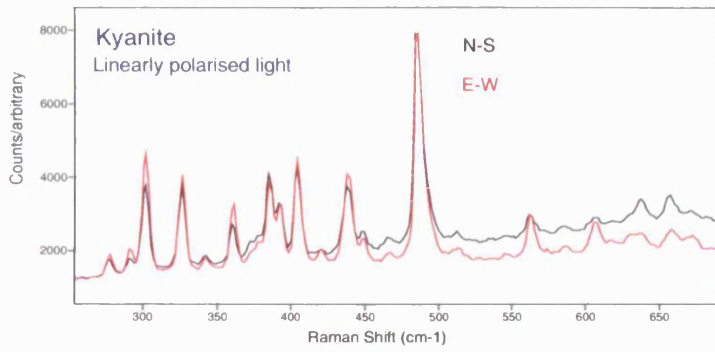


Fig. A8.17. Raman spectra of samples ZP and FA. Both are deep golden yellow in colour.



*

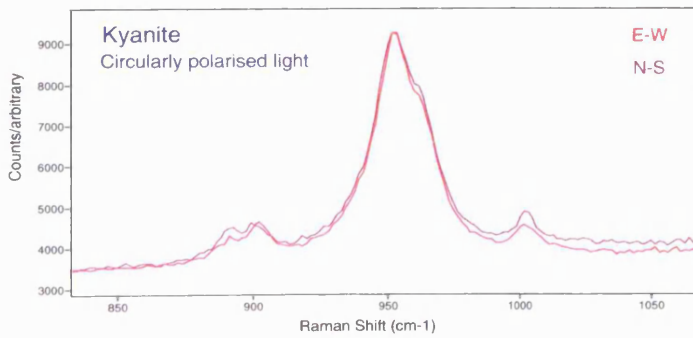


Fig. A15.1. Kyanite Raman spectra using linear and circular polarised light (* - offset in intensity for clarity).

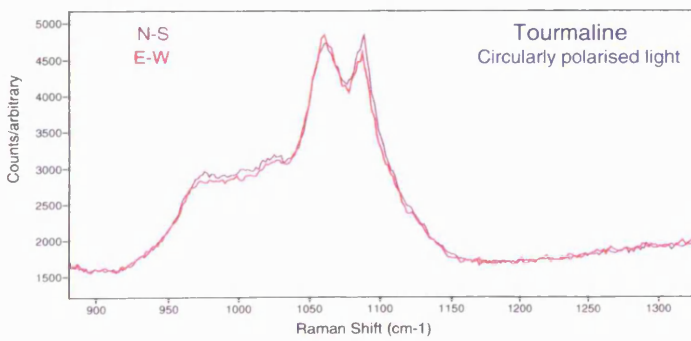
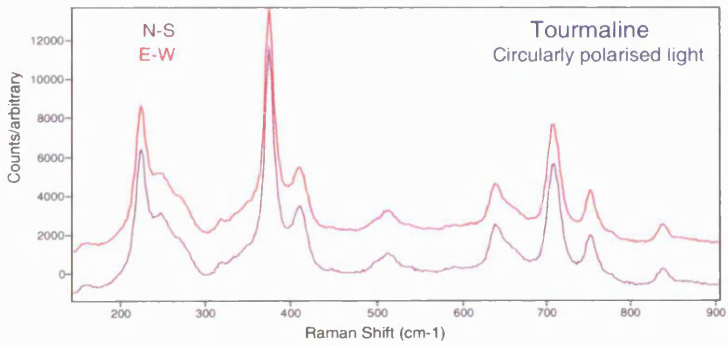
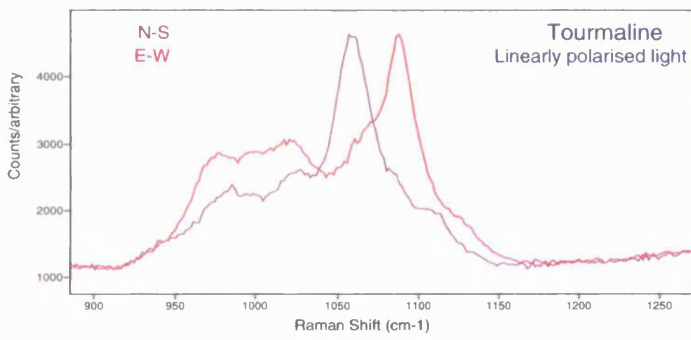
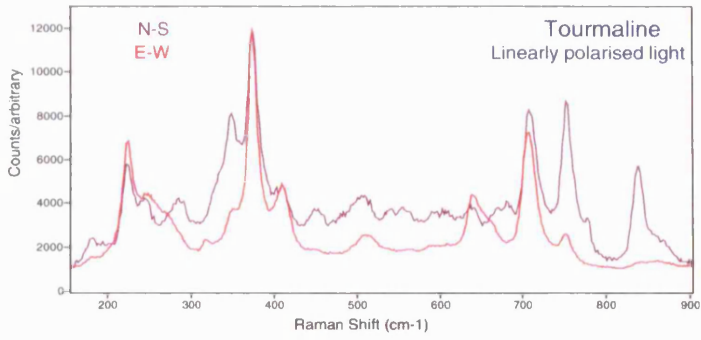


Fig. A15.2. Tourmaline Raman spectra using linear and circular polarised light (* - offset in intensity for clarity).

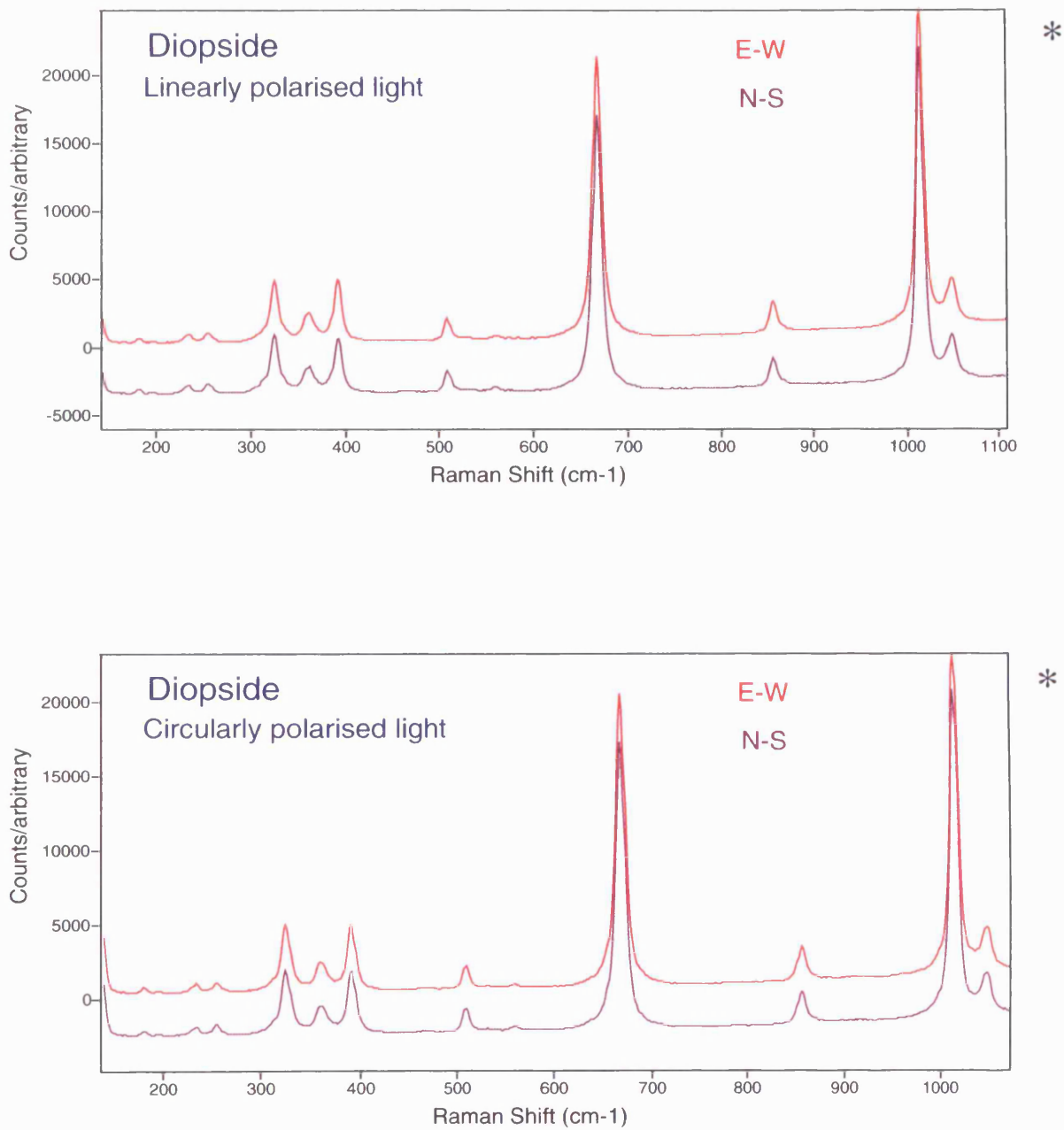


Fig. A15.3. Diopside Raman spectra using linear and circular polarised light (* - offset in intensity for clarity).

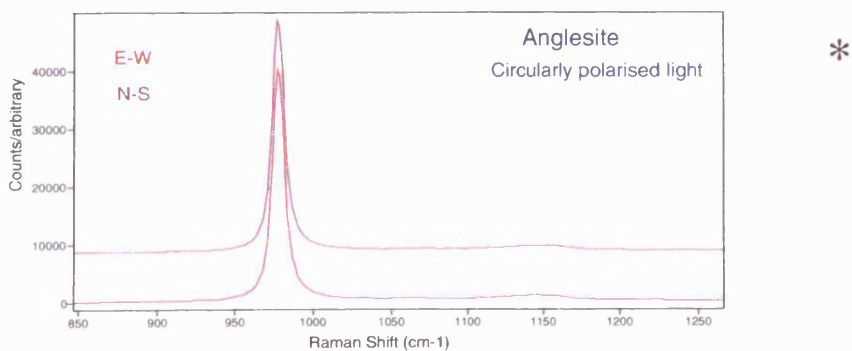
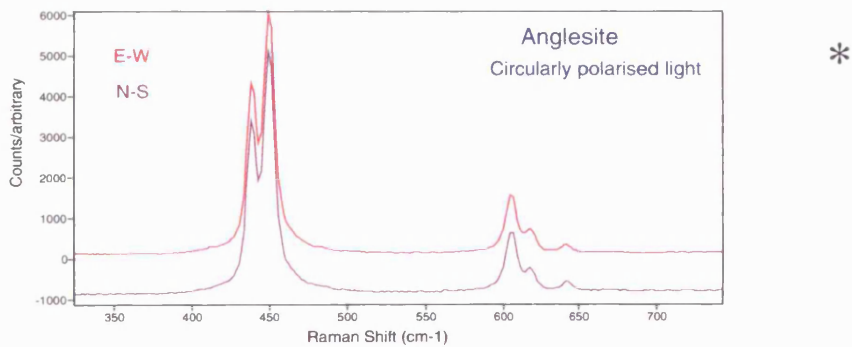
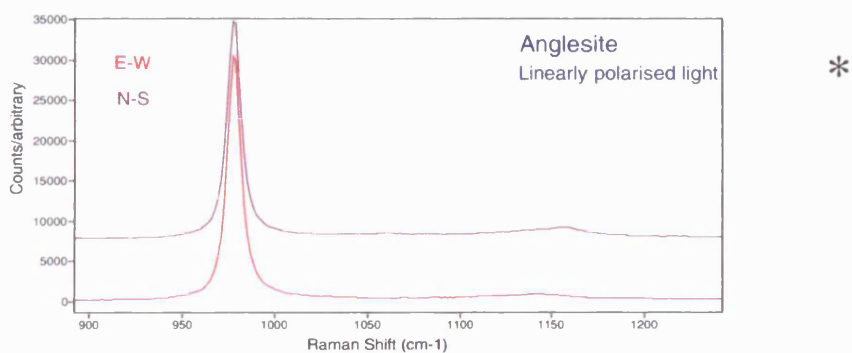
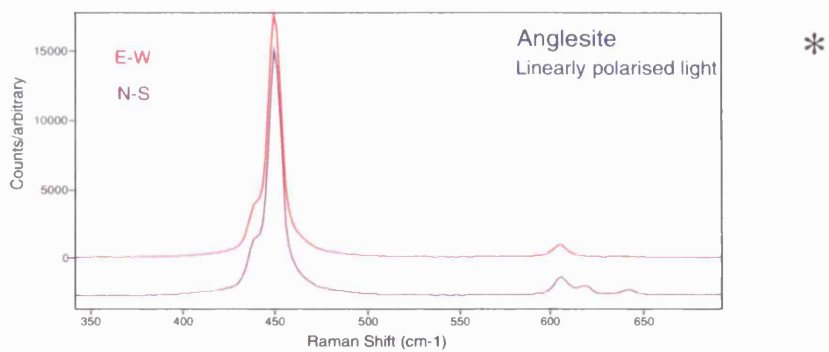


Fig. A15.4. Anglesite Raman spectra using linear and circular polarised light (* - offset in intensity for clarity).

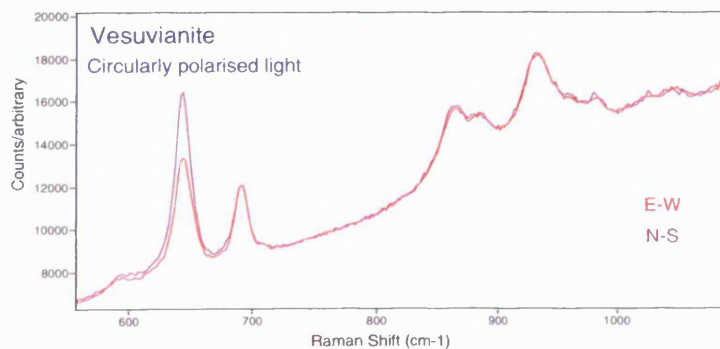
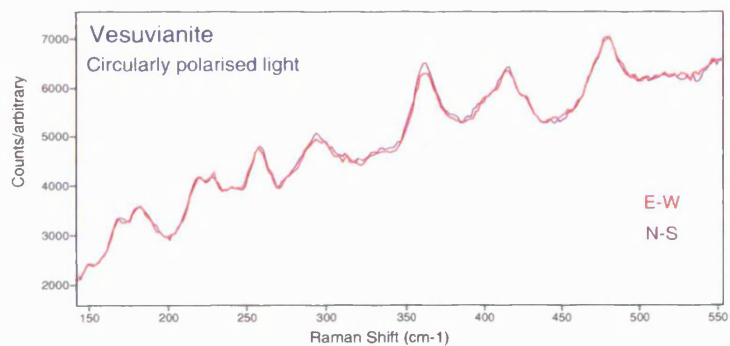
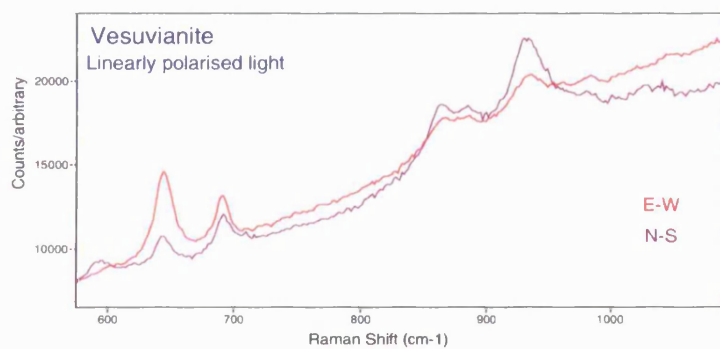
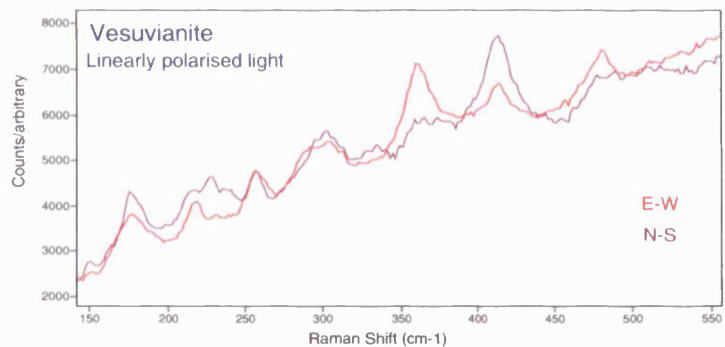


Fig. A15.5. Vesuvianite Raman spectra using linear and circular polarised light.

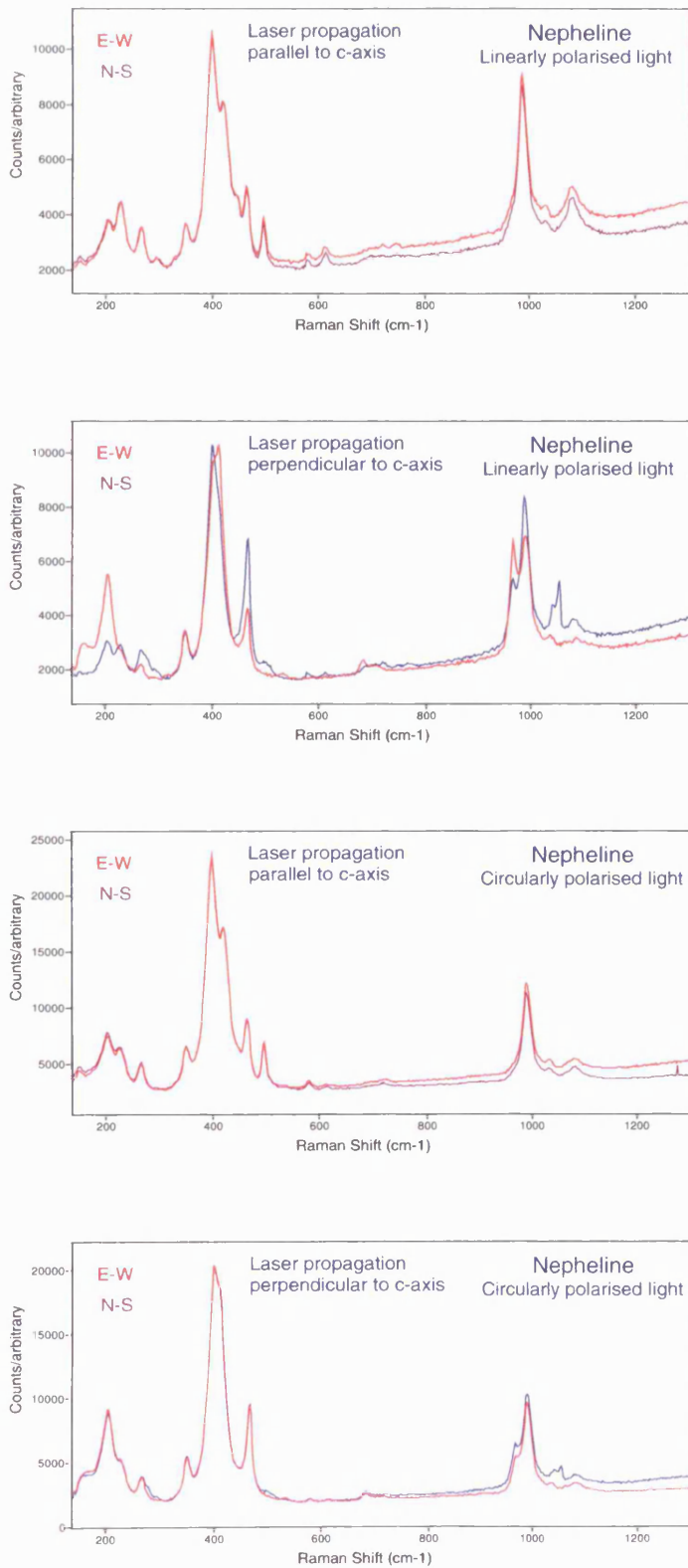


Fig. A15.6. Nepheline Raman spectra using linear and circular polarised light.

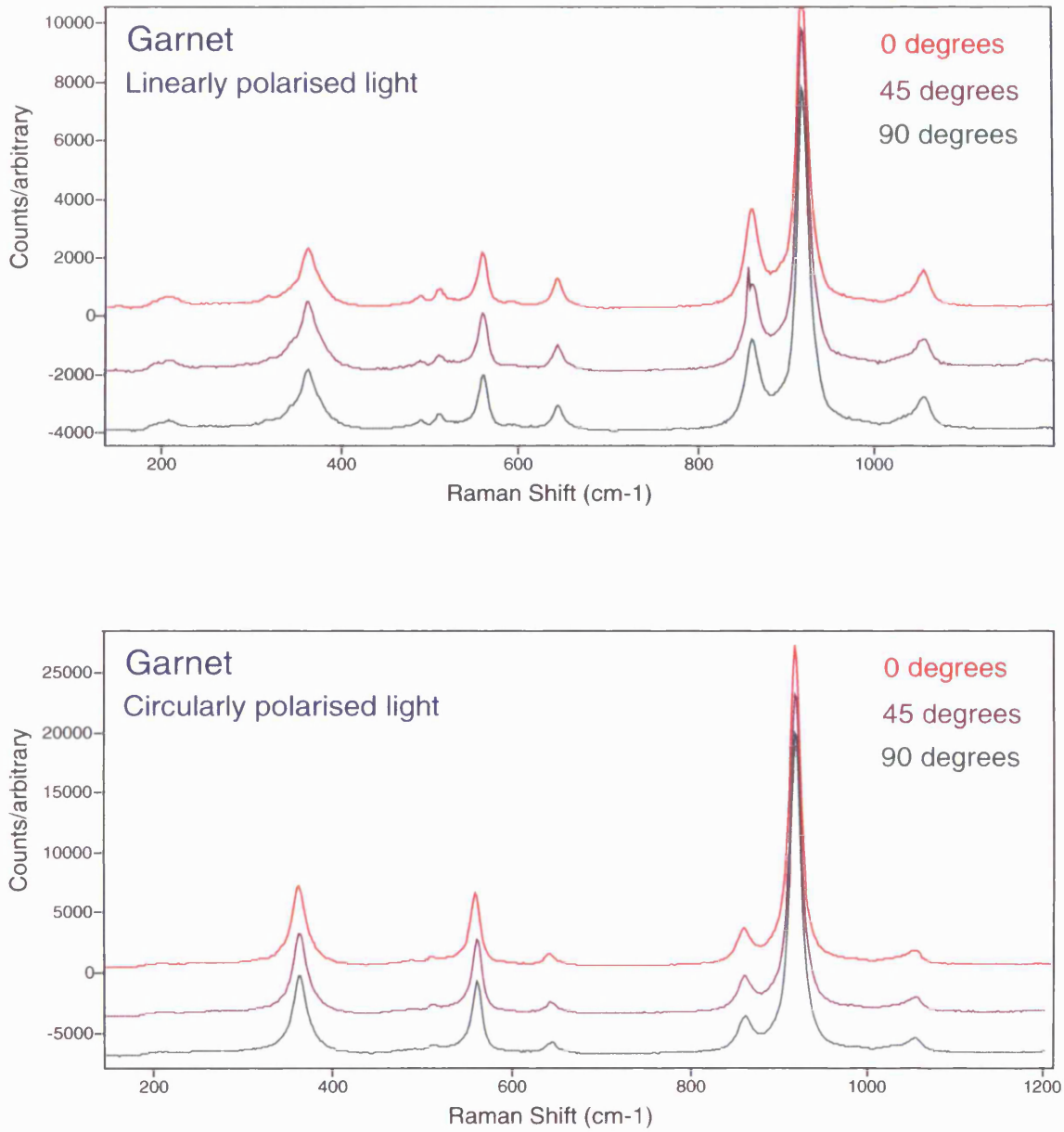


Fig. A15.7. Garnet Raman spectra using linear and circular polarised light. Spectra offset in intensity for clarity.

[Spectroscopy](#) | [Information](#) | [News](#)

Renishaw spectroscopy news releases

Renishaw plc releases its new inorganic Raman database

July 1999 - The Renishaw inorganic Raman database was introduced to fill a clear need for an enhanced identification tool for the gemologist. Since its introduction in 1997 its use and diversity of applications have increased greatly.

The database has now been extensively edited, and is significantly more powerful and easier to use than before. The spectrum descriptors have been expanded, now providing the sample name and its group/family, and a chemical/crystal structure description of the group or family, or a brief chemical identification. The main peak positions are listed, together with the geographical origin of the sample (where available).

One of the many new features is the inclusion of pointers to areas for further study. We have provided keywords that include the names of minerals commonly associated with the specimen, and other terms used to describe the specimen or the kinds of rocks or geological settings in which this type of mineral occurs. These enhancements make the text search facility of the database very powerful. For example, a text search for 'Feldspar' gives 50 hits for spectra from 8 different species from the Feldspar group. This keyword search facility is especially useful in cases where solid solution mechanisms shift the positions of the characteristic Raman peaks making direct spectral searching difficult. A text search can be performed using a rock type, to generate a list of minerals that are commonly found in that type of lithology.

The database has also been expanded significantly; it now contains over 1100 spectra. The source samples have been selected from an enormous and thoroughly catalogued collection belonging to one of the leading gemologists in the field, ensuring the data are of high quality.

Please contact the Spectroscopy Products Division of Renishaw plc at the details given below if you would like a copy.

For further information contact:
Dr Ken Williams,
Renishaw plc
Old Town, Wotton-under-Edge,
Gloucestershire, GL12 7DW, UK.
Telephone: +44 (0) 1453 844302, Fax: +44 (0) 1453 844236,
email: spectroscopy.products@renishaw.com

[\[Spectroscopy\]](#) | [\[Information\]](#) | [\[News releases\]](#)[\[Renishaw home page\]](#)

It is a condition of us allowing you free access to the material on this web site that you accept that Renishaw will not be liable for any action you take in reliance on the information provided.

Last modified 26 July 1999

References

- Aftalion M. and Max M. (1987) U-Pb zircon geochronology from the PreCambrian Annagh Division gneisses and the Terman Granite, NW County Mayo, Ireland. *Journal of the Geological Society* **144**, 401-406.
- Alia J. M., Edwards H. G. M., Garcia-Navarro F. J., Parras-Armenteros J., and Sanchez-Jimenez C. J. (1999) Applications of FT-Raman spectroscopy to quality control in brick clays firing process. *Talanta* **50**(2), 291-298.
- Ansdell K. and Kyser T. (1993) Textural and chemical changes undergone by zircon during the Pb-evaporation technique. *American Mineralogist* **78**, 36-41.
- Araki T. and Zoltai T. (1969) Refinement of a coesite structure. *Zeitschrift fur Kristallographie* **129**, 381-387.
- Baldwin K. J., Batchelder D. N., and Webster S. (2001) Raman Microscopy: Confocal and Scanning Near-Field. In *Handbook of Raman Spectroscopy: From the Research Laboratory to the Process Line* (ed. I. R. Lewis and H. G. M. Edwards), pp. 145-190. Marcel Dekker, Inc.
- Banwell C. N. and McCash E. M. (1994) *Fundamentals of Molecular Spectroscopy*. McGraw-Hill.
- Beny-Bassez C. and Rouzaud J. N. (1985) Characterization of Carbonaceous Materials By Correlated Electron and Optical Microscopy and Raman Microspectroscopy. *Scanning Electron Microscopy*, 119-132.
- Black L. (1997) A study into the factors influencing the development of a patina on the surface of architectural lead. Unpublished PhD thesis, University of Bristol.
- Bock J. and Su G.-J. (1970) Interpretation of the Infrared Spectra of Fused Silica. *Journal of the American Ceramic Society* **53**(2), 69-73.
- Bowden M., Dickson G. D., Gardiner D. J., and Wood D. J. (1993) Patterns of stress-induced phase transformations in MgO-stabilized zirconia ceramic revealed using micro-Raman imaging. *Journal of Materials Science* **28**, 1031-1036.
- Bowie B. T., Chase D. B., and Griffiths P. R. (2000) Factors affecting the performance of bench-top Raman spectrometers. Part I: Instrumental effects. *Applied Spectroscopy* **54**(5), 164A-173A.
- Bowie B. T., Chase D. B., and Griffiths P. R. (2000) Factors affecting the performance of bench-top Raman spectrometers. Part II: Effect of sample. *Applied Spectroscopy* **54**(6), 200A-207A.
-

-
- Boyer H. (1984) Examples On the Use of Raman Microanalysis. *Spectrochimica Acta Part B-Atomic Spectroscopy* **39**(12), 1527-1532.
- Boyer H. (1984) Introduction to Raman Microanalysis. *Spectrochimica Acta Part B-Atomic Spectroscopy* **39**(12), 1523-1525.
- Boyer H. and Oswald J. (2000) Dispersive Raman microscopy. *Analysis* **28**(1), 3-10.
- Boyer H., Smith D. C., Chopin C., and Lasnier B. (1985) Raman Microprobe (RMP) Determinations of Natural and Synthetic Coesite. *Physics and Chemistry of Minerals* **12**(1), 45-48.
- Bremard C., Dhamelincourt P., Laureyns J., and Turrell G. (1985) The Effect of High-Numerical-Aperture Objectives On Polarization Measurements in Micro-Raman Spectrometry. *Applied Spectroscopy* **39**(6), 1036-1039.
- Buhn B., Rankin A. H., Radtke M., Haller M., and Knochel A. (1999) Burbankite, a (Sr,REE,Na,Ca)-carbonate in fluid inclusions from carbonatite-derived fluids: Identification and characterization using Laser Raman spectroscopy, SEM-EDX, and synchrotron micro- XRF analysis. *American Mineralogist* **84**(7-8), 1117-1125.
- Caby R. (1994) Precambrian Coesite From Northern Mali - 1st Record and Implications For Plate-Tectonics in the Trans-Saharan Segment of the Pan-African Belt. *European Journal of Mineralogy* **6**(2), 235-244.
- Cai J., Raptis Y. S., and Anastassakis E. (1993) Stabilized cubic zirconia: A Raman study under uniaxial stress. *Applied Physics Letters* **62**(22), 2781-2783.
- Calas G. and Petiau J. (1983) Structure of Oxide Glasses - Spectroscopic Studies of Local Order and Crystallochemistry - Geochemical Implications. *Bulletin De Mineralogie* **106**(1-2), 33-55.
- Capitani G. C., Leroux H., Doukhan J. C., Rios S., Zhang M., and Salje E. K. H. (2000) A TEM investigation of natural metamict zircons: structure and recovery of amorphous domains. *Physics and Chemistry of Minerals* **27**(8), 545-556.
- Cesare B. and Maineri C. (1999) Fluid-present anatexis of metapelites at El Joyazo (SE Spain): constraints from Raman spectroscopy of graphite. *Contributions to Mineralogy and Petrology* **135**(1), 41-52.
- Chakoumakos B. C., Murakami T., Lumpkin G. R., and Ewing R. C. (1987) Alpha-Decay Induced Fracturing in Zircon - the Transition From the Crystalline to the Metamict State. *Science* **236**(4808), 1556-1559.
-

-
- Cherniak D. J. and Watson E. B. (2001) Pb diffusion in zircon. *Chemical Geology* **172**(1-2), 5-24.
- Chopelas A. (1991) Single-Crystal Raman-Spectra of Forsterite, Fayalite, and Monticellite. *American Mineralogist* **76**(7-8), 1101-1109.
- Chopin C. (1984) Coesite and Pure Pyrope in High-Grade Blueschists of the Western Alps - a 1st Record and Some Consequences. *Contributions to Mineralogy and Petrology* **86**(2), 107-118.
- Clark R. J. H. (2002) Pigment identification by spectroscopic means: an arts/science interface. *C. R. Chimie* **5**, 7-20.
- Collins A. T., Kanda H., and Kitawaki H. (2000) Colour changes produced in natural brown diamonds by high-pressure, high-temperature treatment. *Diamond and Related Materials* **9**, 113-122.
- Colombo M., Chrosch J., and Salje E. K. H. (1999) Annealing metamict zircon: A powder X-ray diffraction study of a highly defective phase. *Journal of the American Ceramic Society* **82**(10), 2711-2716.
- Colthup N. B., Daly L. W., and Wiberley S. E. (1964) *Introduction to Infrared and Raman spectroscopy*. Academic Press.
- Connelly J. N. (2001) Degree of preservation of igneous zonation in zircon as a signpost for concordancy in U/Pb geochronology. *Chemical Geology* **172**(1-2), 25-39.
- Cooney T. F., Scott E. R. D., Krot A. N., Sharma S. K., and Yamaguchi A. (1999) Vibrational spectroscopic study of minerals in the Martian meteorite ALH84001. *American Mineralogist* **84**(10), 1569-1576.
- Dahl P. S. (1996) The crystal-chemical basis for Ar retention in micas: Inferences from interlayer partitioning and implications for geochronology. *Contributions to Mineralogy and Petrology* **123**(1), 22-39.
- Davis D. W. and Krogh T. E. (2001) Preferential dissolution of ^{234}U and radiogenic Pb from alpha-recoil-damaged lattice sites in zircon: implications for thermal histories and Pb isotopic fractionation in the near surface environment. *Chemical Geology* **172**(1-2), 41-58.
- Deer W. A., Howie R. A., and Zussman J. (1963) *Rock forming minerals*. Longmans.
- Dele M. L., Dhamelincourt P., Poirot J. P., Dereppe J. M., and Moreaux C. (1997) Use of spectroscopic techniques for the study of natural and synthetic gems: Application to rubies. *Journal of Raman Spectroscopy* **28**(9), 673-676.
-

-
- Denney R. C. (1982) *A Dictionary of Spectroscopy*. Macmillan Reference Books.
- Dickin A. (1995) Lead isotopes. In *Radiogenic Isotope Geology*, pp. 104-132. Cambridge University Press.
- Dowty E. (1987) Vibrational Interactions of Tetrahedra in Silicate-Glasses and Crystals .2. Calculations On Melilites, Pyroxenes, Silica Polymorphs and Feldspars. *Physics and Chemistry of Minerals* **14**(2), 122-138.
- Dunham A. C. (1992) Developments in industrial mineralogy: I. The mineralogy of brick-making. *Proceedings of the Yorkshire Geological Society* **49**(2), 95-104.
- Dunham A. C. and Mwakarukwa G. M. (1984) The mineralogy of brick-making at Broomfleet, North Humberside. *Proceedings of the Yorkshire Geological Society* **44**(4), 501-517.
- Dyer C. and Smith B. J. E. (1995) Application of Continuous Extended Scanning Techniques to the Simultaneous Detection of Raman-Scattering and Photoluminescence From Calcium Disilicates Using Visible and Near-Infrared Excitation. *Journal of Raman Spectroscopy* **26**(8-9), 777-785.
- Edwards H. G. M., Farwell D. W., de Faria D. L. A., Monteiro A. M. F., Afonso M. C., De Blasis P., and Eggers S. (2001) Raman spectroscopic study of 3000-year-old human skeletal remains from a sambaqui, Santa Catarina, Brazil. *Journal of Raman Spectroscopy* **32**(1), 17-22.
- Enami M. and Zang Q. J. (1990) Quartz Pseudomorphs After Coesite in Eclogites From Shandong Province, East China. *American Mineralogist* **75**(3-4), 381-386.
- Ervin G. J. (1952) Structural interpretation of the Diaspore-Corundum and Boehemite-gamma Al₂O₃ transitions. *Acta Crystallographie* **5**, 103-108.
- Etchepare J., Merian M., and Kaplan P. (1978) Vibrational normal modes of SiO₂. II. Cristobalite and tridymite. *The Journal of Chemical Physics* **68**(4), 1531-1537.
- Etchepare J., Merian M., and Smetankine L. (1974) Vibrational normal modes of SiO₂. I. alpha and beta quartz. *The Journal of Chemical Physics* **60**(5), 1873-1876.
- Farmer V. C. (1974) The Infrared Spectra of Minerals. In *Mineralogical Society Monograph 4*, pp. 514. The Mineralogical Society.
- Farmer V. C. (1974) Vibrational Spectroscopy in Mineral Chemistry. In *The Infrared Spectra of Minerals* (ed. V. C. Farmer), pp. 1-10. The Mineralogical Society.
- Farmer V. C. and Lazarev A. N. (1974) Symmetry and Crystal Vibrations. In *The Infrared Spectra of Minerals* (ed. V. C. Farmer), pp. 51-67. The Mineralogical Society.
-

-
- Fately W. G., McDevitt N. T., and Bentley F. F. (1971) Infrared and Raman Selection Rules for Lattice Vibrations: The Correlation Method. *Applied Spectroscopy* **25**(No. 2), 155-174.
- Faure G. (1986) *Principles of Isotope Geology*. John Wiley & Sons.
- Forbes P. and Dubessy J. (1988) Characterization of Fresh and Altered Montroseite [V, Fe]OOH - a Discussion of Alteration Processes. *Physics and Chemistry of Minerals* **15**(5), 438-445.
- Frogner P., Broman C., and Lindblom S. (1998) Weathering detected by Raman spectroscopy using Al-ordering in albite. *Chemical Geology* **151**(1-4), 161-168.
- Frost R. (1996) The application of Raman microscopy to the study of minerals. *Chemistry in Australia*(October), 446-448.
- Frost R. L. and Shurvell H. F. (1997) Raman microprobe spectroscopy of halloysite. *Clays and Clay Minerals* **45**(1), 68-72.
- Galeener F. L. (1982a) Planar Rings In vitreous Silica. *Journal of Non-Crystalline Solids* **49**(1-3), 53-62.
- Galeener F. L. (1982b) Planar Rings in Glasses. *Solid State Communications* **44**(7), 1037-1040.
- Gardiner D. G. (1989) Non-standard Physical and Chemical Environments. In *Practical Raman Spectroscopy* (ed. D. J. Gardiner and P. R. Graves), pp. 103-118. Springer-Verlag.
- Gerrard D. L. and Bowley H. J. (1989) Instrumentation for Raman Spectroscopy. In *Practical Raman Spectroscopy* (ed. D. J. Gardiner and P. R. Graves), pp. 55-76. Springer-Verlag.
- Gibbs G. V., Prewitt C. T., and Baldwin K. J. (1977) A study of the structural chemistry of coesite. *Zeitschrift fur Kristallographie* **145**, 108-123.
- Gillet P., Ingrin J., and Chopin C. (1984) Coesite in subducted continental crust: P-T history deduced from an elastic model. *Earth and Planetary Science Letters* **70**, 426-436.
- Gogen K. and Wagner G. A. (2000) Alpha-recoil track dating of Quaternary volcanics. *Chemical Geology* **166**(1-2), 127-137.
- Gramaccioli C. M. (1991) Application of Mineralogical Techniques to Gemmology. *European Journal of Mineralogy* **3**(4), 703-706.
- Graves P. R. (1989) Calibration and Data Processing. In *Practical Raman Spectroscopy* (ed. D. J. Gardiner and P. R. Graves), pp. 77-102. Springer-Verlag.
- Griffith W. P. (1974) Raman spectroscopy of minerals. In *The infrared spectra of minerals* (ed. V. C. Farmer), pp. 119-136. The Mineralogical Society.
-

-
- Griffith W. P. (1975) Raman spectroscopy of terrestrial minerals. In *Infrared and Raman spectroscopy of lunar and terrestrial minerals* (ed. C. Karr), pp. 299-323. Academic Press.
- Haley L. V., Wylie I. W., and Koningstein J. A. (1982) An Investigation of the Lattice and Interlayer Water Vibrational Spectral Regions of Muscovite and Vermiculite Using Raman Microscopy - a Raman Microscopic Study of Layer Silicates. *Journal of Raman Spectroscopy* **13**(2), 203-205.
- Hass M. (1970) Raman Spectra of Vitreous Silica, Germania and Sodium Silicate Glasses. *Journal of Physics and Chemistry of Solids*. **31**, 415-422.
- Hawthorne F. C. and Waychunas G. A. (1988) Spectrum-fitting methods. In *Spectroscopic methods in Mineralogy and Geology*, Vol. 18 (ed. F. C. Hawthorne), pp. 63-98. Mineralogical Society of America.
- Hecht E. and Zajac A. (1974) *Optics*. Addison-Wesley Publishing Co.
- Herman R. G., Bogdan C. E., Sommer A. J., and Simpson D. R. (1987) Discrimination Among Carbonate Minerals By Raman-Spectroscopy Using the Laser Microprobe. *Applied Spectroscopy* **41**(3), 437-440.
- Hogdahl K., Gromet L. P., and Broman C. (2001) Low P-T Caledonian resetting of U-rich Paleoproterozoic zircons, central Sweden. *American Mineralogist* **86**, 534-546.
- Houng P. H. (1992) Diamond and diamond simulants as studied by micro-Raman spectroscopy. *Materials Science and Engineering* **B11**, 235-242.
- Huang E., Chen C. H., Huang T., Lin E. H., and Xu J. A. (2000) Raman spectroscopic characteristics of Mg-Fe-Ca pyroxenes. *American Mineralogist* **85**(3-4), 473-479.
- Hunt B. and Miglio B. (1992) Deterioration of stone floors. *Stone Industries*(Jul/Aug), 21-28.
- Ingrin J. and Gillet P. (1986) TEM Investigation of the Crystal Microstructures in a Quartz-Coesite Assemblage of the Western Alps. *Physics and Chemistry of Minerals* **13**(5), 325-330.
- Ishigame M. and Yoshida E. (1987) Study of the defect-induced Raman spectra in cubic zirconia. *Solid State Ionics* **23**, 211-218.
- Ivanda M. and Furic K. (1992) Line Focusing in Micro-Raman Spectroscopy. *Applied Optics* **31**(30), 6371-6375.
- Janz G. J. and Wait S. C., Jr. (1967) Ionic Melts. In *Raman Spectroscopy* (ed. H. A. Szymanski), pp. 139-167. Plenum Press.
-

-
- Jehlicka J., Beny C., and Rouzaud J. N. (1997) Raman microspectrometry of accumulated non-graphitized solid bitumens. *Journal of Raman Spectroscopy* **28**(9), 717-724.
- Kagi H., Tsuchida I., Wakatsuki M., Takahashi K., Kamimura N., Iuchi K., and Wada H. (1994) Proper Understanding of Down-Shifted Raman-Spectra of Natural Graphite - Direct Estimation of Laser-Induced Rise in Sample Temperature. *Geochimica Et Cosmochimica Acta* **58**(16), 3527-3530.
- Karali T., Can N., Townsend P. D., Rowlands A. P., and Hanchar J. M. (2000) Radioluminescence and thermoluminescence of rare earth element and phosphorus-doped zircon. *American Mineralogist* **85**(5-6), 668-681.
- Kingma K. J. and Hemley R. J. (1994) Raman-Spectroscopic Study of Microcrystalline Silica. *American Mineralogist* **79**(3-4), 269-273.
- Kloprogge J. T., Frost R. L., and Rintoul L. (1999) Single crystal Raman microscopic study of the asbestos mineral chrysotile. *Pccp Physical Chemistry Chemical Physics* **1**(10), 2559-2564.
- Kober B. (1986) Whole grain evaporation for $^{207}\text{Pb}/^{206}\text{Pb}$ age investigations on single zircons using a double-filament thermal ion source. *Contributions to Mineralogy and Petrology* **93**, 482-490.
- Kolesov B. A. and Geiger C. A. (1997) Raman scattering in silicate garnets: an investigation of their resonance intensities. *Journal of Raman Spectroscopy* **28**(9), 659-662.
- Kolesov B. A. and Tanskaya J. V. (1996) Raman spectra and cation distribution in the lattice of olivines. *Materials Research Bulletin* **31**(8), 1035-1044.
- Konnert J. H. and Karle J. (1972) Tridymite-like Structure in Silica Glass. *Nature Physical Science* **236**, 92-94.
- Kribek B., Zak K., Spangenberg J., Jehlicka J., Prokes S., and Kominek J. (1999) Bitumens in the late Variscan hydrothermal vein-type uranium deposit of Příbram, Czech Republic: Sources, radiation-induced alteration, and relation to mineralization. *Economic Geology and the Bulletin of the Society of Economic Geologists* **94**(7), 1093-1114.
- Lazarev A. N. (1974) The dynamics of crystal lattices. In *The Infrared Spectra of Minerals* (ed. V. C. Farmer), pp. 69-85. The Mineralogical Society.
- Lewis I. R. and Griffiths P. R. (1996) Raman spectrometry with fiber-optic sampling. *Applied Spectroscopy* **50**(10), A12-A30.
-

-
- Liang E. J., Liu S. W., Guo M. T., and Gao G. Z. (1998) Applications of Raman spectroscopy to the identification of natural gem handicraft articles. *XVI International Conference on Raman Spectroscopy*, 734-735.
- Liou J. G. and Zhang R. Y. (1996) Occurrences of intergranular coesite in ultrahigh-P rocks from the Sulu region, eastern China: Implications for lack of fluid during exhumation. *American Mineralogist* **81**(9-10), 1217-1221.
- Liu L., Mernagh T. P., and Hibberson W. O. (1997) Raman spectra of high-pressure polymorphs of SiO₂ at various temperatures. *Physics and Chemistry of Minerals* **24**(6), 396-402.
- Liu L. G., Mernagh T. P., and Jaques A. L. (1990) A Mineralogical Raman-Spectroscopy Study On Eclogitic Garnet Inclusions in Diamonds From Argyle. *Contributions to Mineralogy and Petrology* **105**(2), 156-161.
- Long D. A. (1977) *Raman spectroscopy*. McGraw International Book Company.
- Long J. V. P. (1995) Microanalysis from 1950 to the 1990's. In *Microprobe Techniques in the Earth Sciences*, Vol. No. 6 (ed. P. J. Potts, J. F. W. Bowles, S. J. B. Reed, and M. R. Cave), pp. 1-48. Chapman & Hall.
- Loucks R. R. (1991) The Bound Interlayer H₂O Content of Potassic White Micas - Muscovite-Hydromuscovite-Hydrophyrophyllite Solutions. *American Mineralogist* **76**(9-10), 1563-1579.
- Louden J. D. (1989) Raman Microscopy. In *Practical Raman Spectroscopy* (ed. D. J. Gardiner and P. R. Graves), pp. 119-151. Springer-Verlag.
- Malezieux J.-M. (1990) Contribution of Raman microspectrometry to mineral studies. In *Absorption Spectroscopy in Mineralogy* (ed. A. Mottana and F. Burrigato), pp. 40-59. Elsevier.
- Mao H., Hemley R. J., and Chao E. C. T. (1987) The Application of Micro-Raman Spectroscopy to Analysis and Identification of Minerals in Thin-Section. *Scanning Microscopy* **1**(2), 495-501.
- McCreery R. L. (2000) Raman Spectroscopy for Chemical Analysis. In *Chemical Analysis: a series of monographs on Analytical Chemistry and its Applications.*, Vol. 157 (ed. J. D. Winefordner), pp. 420. John Wiley and Sons, Inc.
- McKeown D. A., Bell M. I., and Etz E. S. (1999a) Raman spectra and vibrational analysis of the trioctahedral mica phlogopite. *American Mineralogist* **84**(5-6), 970-976.
- McKeown D. A., Bell M. I., and Etz E. S. (1999b) Vibrational analysis of the dioctahedral mica: 2M(1) muscovite. *American Mineralogist* **84**(7-8), 1041-1048.
-

-
- McMillan P. (1984) Structural Studies of Silicate-Glasses and Melts - Applications and Limitations of Raman-Spectroscopy. *American Mineralogist* **69**(7-8), 622-644.
- McMillan P. (1985) Vibrational Spectroscopy in the Mineral Sciences. *Reviews in Mineralogy* **14**, 9-63.
- McMillan P. F. (1989) Raman-Spectroscopy in Mineralogy and Geochemistry. *Annual Review of Earth and Planetary Sciences* **17**, 255-283.
- McMillan P. and Piriou B. (1982) The Structures and Vibrational-Spectra of Crystals and Glasses in the Silica-Alumina System. *Journal of Non-Crystalline Solids* **53**(3), 279-298.
- McMillan P. and Piriou B. (1983) Raman-Spectroscopic Studies of Silicate and Related Glass Structure - a Review. *Bulletin De Mineralogie* **106**(1-2), 57-75.
- McMillan P. F. and Hoffmeister A. M. (1988) Infrared and Raman Spectroscopy. In *Spectroscopic methods in Mineralogy and Geology*, Vol. 18 (ed. F. C. Hawthorne), pp. 99-159. Mineralogical Society of America.
- Meldrum A., Boatner L. A., Weber W. J., and Ewing R. C. (1998) Radiation damage in zircon and monazite. *Geochimica et Cosmochimica Acta* **63**(17), 2693-2693.
- Meldrum A., Boatner L. A., Zinkle S. J., Wang S. X., Wang L. M., and Ewing R. C. (1999a) Effects of dose rate and temperature on the crystalline-to- metamict transformation in the ABO(4) orthosilicates. *Canadian Mineralogist* **37**, 207-221.
- Mernagh T. P. (1991) Use of the Laser Raman Microprobe For Discrimination Amongst Feldspar Minerals. *Journal of Raman Spectroscopy* **22**(8), 453-457.
- Mernagh T. P. and Hoatson D. M. (1997) Raman spectroscopic study of pyroxene structures from the Munni Munni layered intrusion, Western Australia. *Journal of Raman Spectroscopy* **28**(9), 647-658.
- Mernagh T. P. and Liu L. G. (1991) Raman-Spectra From the Al₂SiO₅ Polymorphs At High-Pressures and Room-Temperature. *Physics and Chemistry of Minerals* **18**(2), 126-130.
- Mernagh T. P. and Liu L. G. (1998) Raman and infrared spectra of phase E, a plausible hydrous phase in the mantle. *Canadian Mineralogist* **36**, 1217-1223.
- Mernagh T. P. and Trudu A. G. (1993) A Laser Raman Microprobe Study of Some Geologically Important Sulfide Minerals. *Chemical Geology* **103**(1-4), 113-127.
- Mernagh T. P. and Wilde A. R. (1989) The Use of the Laser Raman Microprobe For the Determination of Salinity in Fluid Inclusions. *Geochimica Et Cosmochimica Acta* **53**(4), 765-771.
-

-
- Moenke H. H. W. (1974) Vibrational spectra and the crystal-chemical classification of minerals. In *The Infrared Spectra of Minerals* (ed. V. C. Farmer), pp. 111-118. The Mineralogical Society.
- Mohanani K., Sharma S. K., and Bishop F. C. (1993) A Raman Spectral Study of Forsterite-Monticellite Solid-Solutions. *American Mineralogist* **78**(1-2), 42-48.
- Mosenfelder J. L. and Bohlen S. R. (1997) Kinetics of the coesite to quartz transformation. *Earth and Planetary Science Letters* **153**(1-2), 133-147.
- Mozzi R. L. and Warren B. E. (1969) The structure of vitreous silica. *Journal of Applied Crystallography* **2**, 164-172.
- Mukaida H., Okumura H., Lee J. H., Daimon H., Sakuma E., Misawa S., Endo K., and Yoshida S. (1987) Raman-Scattering of SiC - Estimation of the Internal-Stress in 3c-SiC On Si. *Journal of Applied Physics* **62**(1), 254-257.
- Murad E. (1997) Identification of minor amounts of anatase in kaolins by Raman spectroscopy. *American Mineralogist* **82**(1-2), 203-206.
- Murakami T., Chakoumakos B. C., Ewing R. C., Lumpkin G. R., and Weber W. J. (1991) Alpha-Decay Event Damage in Zircon. *American Mineralogist* **76**(9-10), 1510-1532.
- Murphy P. J. and LaGrange M. S. (1998) Raman spectroscopy of gold chloro-hydroxy speciation in fluids at ambient temperature and pressure: A re-evaluation of the effects of pH and chloride concentration. *Geochimica et Cosmochimica Acta* **62**(21-22), 3515-3526.
- Nasdala L., Irmer G., and Wolf D. (1995) The Degree of Metamictization in Zircon - a Raman-Spectroscopic Study. *European Journal of Mineralogy* **7**(3), 471-478.
- Nasdala L., Pidgeon R. T., and Wolf D. (1996) Heterogeneous metamictization of zircon on a microscale. *Geochimica Et Cosmochimica Acta* **60**(6), 1091-1097.
- Nasdala L., Pidgeon R. T., Wolf D., and Irmer G. (1998) Metamictization and U-Pb isotopic discordance in single zircons: a combined Raman microprobe and SHRIMP ion probe study. *Mineralogy and Petrology* **62**(1-2), 1-27.
- Nasdala L., Wenzel M., Andrut M., Wirth R., and Blaum P. (2001a) The nature of radiohaloes in biotite: Experimental studies and modeling. *American Mineralogist* **86**(4), 498-512.
- Nasdala L., Wenzel M., Vavra G., Irmer G., Wenzel T., and Kober B. (2001b) Metamictisation of natural zircon: accumulation versus thermal annealing of radioactivity-induced damage. *Contributions to Mineralogy and Petrology* **141**, 125-144.
-

-
- Nasdala L., Wenzel T., Pidgeon R. T., and Kronz A. (1999) Internal structures and dating of complex zircons from Meissen Massif monzonites, Saxony. *Chemical Geology* **156**(1-4), 331-341.
- Nelson J. B. Inclusion identification with the Raman light microprobe. *submitted*, 1-56.
- Noons R. E., Devonshire R., Clapp T. V., Ojha S. M., and McCarthy O. (accepted March 2002) Analysis of Waveguide Silica Glasses using Confocal Raman Microscopy. *Journal of Non-Crystalline Solids*.
- Ostanin S., Craven A. J., McComb D. W., Vlachos D., Alavi A., Finnis M. W., and Paxton A. T. (2000) Effect of relaxation on the oxygen K-edge electron energy-loss near-edge structure in yttria-stabilised zirconia. *Physical Review B* **62**(22), 14728-14735.
- Parke S. (1974) Glasses. In *The Infrared Spectra of Minerals*, Vol. 4 (ed. V. C. Farmer), pp. 483-514. Mineralogical Society.
- Parkinson C. D. and Katayama I. (1999) Present-day ultrahigh-pressure conditions of coesite inclusions in zircon and garnet: Evidence from laser Raman microspectroscopy. *Geology* **27**(11), 979-982.
- Pasteris J. D. (1989) *In situ* Analysis in Geological Thin-Sections By Laser Raman Microprobe Spectroscopy - a Cautionary Note. *Applied Spectroscopy* **43**(3), 567-570.
- Pasteris J. D. (1998) The Laser Raman Microprobe as a Tool for the Economic Geologist. In *Applications of Microanalytical Techniques to Understanding Mineralizing Processes.*, Vol. 7 (ed. M. A. McKibben, W. C. I. Shanks, and W. I. Ridley), pp. 233-250. Society of Economic Geology.
- Pasteris J. D., Kuehn C. A., and Bodnar R. J. (1986) Applications of the Laser Raman Microprobe Ramanor U-1000 to Hydrothermal Ore-Deposits - Carlin As an Example. *Economic Geology* **81**(4), 915-930.
- Pasteris J. D. and Wopenka B. (1991) Raman-Spectra of Graphite As Indicators of Degree of Metamorphism. *Canadian Mineralogist* **29**, 1-9.
- Pasteris J. D., Wopenka B., and Freeman J. J. (1984) Some Geologic Applications of the Laser Raman Microprobe. *Abstracts of Papers of the American Chemical Society* **187**(APR), 26-GEOC.
- Pasteris J. D., Wopenka B., and Seitz J. C. (1988) Practical Aspects of Quantitative Laser Raman Microprobe Spectroscopy For the Study of Fluid Inclusions. *Geochimica et Cosmochimica Acta* **52**(5), 979-988.
- Patel A. R. and Raju K. S. (1970) Radiation Damage in Gypsum. *Journal of Physics and Chemistry of Solids* **31**, 331-335.
-

-
- Prasad P. S. R. (1999) Raman intensities near gypsum-bassanite transition in natural gypsum. *Journal of Raman Spectroscopy* **30**(8), 693-696.
- Richardson D. (1993) The staining of natural stone. *Construction Repair*(Mar/Apr).
- Rios S. and Salje E. K. H. (1999) Diffuse X-ray scattering from weakly metamict zircon. *Journal of Physics-Condensed Matter* **11**(45), 8947-8956.
- Rios S., Salje E. K. H., Zhang M., and Ewing R. C. (2000) Amorphization in zircon: evidence for direct impact damage. *Journal of Physics-Condensed Matter* **12**(11), 2401-2412.
- Roberts S. and Beattie I. (1995) Micro-Raman spectroscopy in the Earth Sciences. In *Microprobe Techniques in the Earth Sciences*, Vol. No. 6 (ed. P. J. Potts, J. F. W. Bowles, S. J. B. Reed, and M. R. Cave), pp. 387-408. Chapman & Hall.
- Rodgers K. A. (1993) Routine Identification of Aluminum Hydroxide Polymorphs With the Laser Raman Microprobe. *Clay Minerals* **28**(1), 85-99.
- Rodgers K. A., Gregory M. R., and Cooney R. P. (1989) Bayerite, Al(OH)₃, From Raoul Island, Kermadec Group, South- Pacific. *Clay Minerals* **24**(3), 531-538.
- Rosasco G. J. (1982) Raman Microprobe Spectroscopy. In *Raman and Resonance Raman studies of Biological Systems* (ed. R. J. H. Clark and R. E. Hester), pp. 223-282. Jon Wiley & Sons.
- Rousseau D. L., Bauman R. P., and Porto S. P. S. (1981) Normal Mode Determination in Crystals. *Journal of Raman Spectroscopy* **10**(JAN), 253-290.
- Salje E. K. H., Chrosch J., and Ewing R. C. (1999) Is "metamictization" of zircon a phase transition? *American Mineralogist* **84**(7-8), 1107-1116.
- Sasaki K. (1997) Raman study of the microbially mediated dissolution of pyrite by *Thiobacillus ferroxidans*. *The Canadian Mineralogist* **35**, 999-1008.
- Sasaki K., Tanaike O., and Konno H. (1998) Distinction of jarosite-group compounds by Raman spectroscopy. *Canadian Mineralogist* **36**, 1225-1235.
- Schaffer R. J. (1932) The weathering of natural building stones. Department of Scientific and Industrial Research: Building Research.
- Schopf J. W., Kudryavtsev A. B., Agresti D. G., Wdowiak T. J., and Czaja A. D. (2002) Laser-Raman imagery of Earth's earliest fossils. *Nature* **416**(March), 73-76.
- Schulman J. H. and Compton W. D. (1962) *Colour Centres in Solids*. Pergamon Press.
-

-
- Sharma S. K. (1990) Applications of Raman spectroscopy in Earth and planetary sciences. In *From mantle to meteorites* (ed. K. Gopalan, V. K. Gaur, B. L. K. Somayajulu, and J. D. MacDougall), pp. 263-308. Indian Acad. Sci.
- Sharma S. K., Mammone J. F., and Nicol M. F. (1981) Raman Investigation of Ring Configurations in Vitreous Silica. *Nature* **292**(5819), 140-141.
- Shelby J. E., Vitko J., and Benner R. E. (1982) Quantitative-Determination of the Hydroxyl Content of Vitreous Silica. *Journal of the American Ceramic Society* **65**(4), C59-C60.
- Skinner B. J. and Fahey J. J. (1963) Observations on the Inversion of Stishovite to Silica Glass. *Journal of Geophysical Research* **68**(no. 19), 5595-5604.
- Smith A. S. (1997) Quartz-bearing aggregates and their role in the alkali-silica reaction in concrete prism tests. Unpublished Ph.D. thesis., University of Leicester.
- Smith C. P., Bosshart G., Ponahlo J., Hammer V. M. F., Klapper H., and Schmetzer K. (2000) GE POL diamonds: Before and After. *Gems & Gemmology* (Fall), 192-215.
- Smith D. C. (1984) Coesite in Clinopyroxene in the Caledonides and Its Implications For Geodynamics. *Nature* **310**(5979), 641-644.
- Sykes D. and Kubicki J. D. (1996) Four-membered rings in silica and aluminosilicate glasses. *American Mineralogist* **81**(3-4), 265-272.
- Taylor M. and Brown G. E. J. (1979) Structure of mineral glasses--II. The SiO₂-NaAlSiO₄ join. *Geochimica et Cosmochimica Acta* **43**, 1467-1743.
- Thomas R. (2000) Determination of water contents of granite melt inclusions by confocal laser Raman microprobe spectroscopy. *American Mineralogist* **85**(5-6), 868-872.
- Tlili A., Smith D. C., Beny J. M., and Boyer H. (1989) A Raman Microprobe Study of Natural Micas. *Mineralogical Magazine* **53**(370), 165-179.
- Tobin M. C. (1971) Laser Raman Spectroscopy. In *Chemical Analysis: A Series of Monographs on Analytical Chemistry and its Applications* (ed. P. J. Elving and I. M. Kolthoff), pp. 171. Wiley-Interscience.
- Trajkovska M., Soptrajanov B., Jovanovski G., and Stafilov T. (1992) Vibrational-Spectra of Some Sulfide Minerals From Alsar. *Journal of Molecular Structure* **267**, 191-196.
- Tucker M. E. (1991) *Sedimentary Petrology: An introduction to the origin of sedimentary rocks*. Blackwell Science Ltd.
-

-
- Uchino T., Tokuda Y., and Yoko T. (1998) Vibrational dynamics of defect modes in vitreous silica. *Physical Review B-Condensed Matter* **58**(9), 5322-5328.
- Urmos J., Sharma S. K., and Mackenzie F. T. (1991) Characterization of Some Biogenic Carbonates With Raman- Spectroscopy. *American Mineralogist* **76**(3-4), 641-646.
- Wang A., Dhamelincourt P., and Turrell G. (1988) Raman Microspectroscopic Study of the Cation Distribution in Amphiboles. *Applied Spectroscopy* **42**(8), 1441-1450.
- Wang S. L. and Johnston C. T. (2000) Assignment of the structural OH stretching bands of gibbsite. *American Mineralogist* **85**(5-6), 739-744.
- Wang X. M., Liou J. G., and Mao H. K. (1989) Coesite-Bearing Eclogite From the Dabie Mountains in Central China. *Geology* **17**(12), 1085-1088.
- Weber W. J., Ewing R. C., and Wang L.-M. (1994) The radiation-induced transition crystalline-to-amorphous transition in zircon. *Journal of Materials Research* **9**(3), 688-698.
- Weller M., Damson B., and Lakki A. (2000) Mechanical loss of cubic zirconia. *Journal of Alloys and Compounds* **310**, 47-53.
- Whiffen D. H. (1972) *Spectroscopy*. Longman.
- Wilkinson G. (1973) Raman Spectra of Ionic, Covalent and Metallic Crystals. In *The Raman Effect*, Vol. 2: Applications (ed. A. Anderson), pp. 405-938. Marcel Dekker, Inc.
- Williams K. P. J., Pitt G. D., Batchelder D. N., and Kip B. J. (1994b) Confocal Raman Microspectroscopy Using a Stigmatic Spectrograph and CCD Detector. *Applied Spectroscopy* **48**(2), 232-235.
- Williams K. P. J., Pitt G. D., Smith B. J. E., Whitley A., Batchelder D. N., and Hayward I. P. (1994a) Use of a Rapid-Scanning Stigmatic Raman Imaging Spectrograph in the Industrial-Environment. *Journal of Raman Spectroscopy* **25**(1), 131-138.
- Williams K. P. J., Wilcock I. C., Hayward I. P., and Whitley A. (1996) Applications of state-of-the-art Raman microscopy and direct Raman imaging - Progress in corrosion, mineralogy, and materials research. *Spectroscopy* **11**(3), 45-50.
- Williams Q. (1995) Infrared, Raman and Optical Spectroscopy of Earth Materials. In *Mineral Physics and Crystallography. A Handbook of Physical Constants.*, Vol. 2 (ed. T. J. Ahrens), pp. 291-302. American Geophysical Union.
- Wirth R. (1985) Dehydration of Mica (Phengite) By Electron-Bombardment in a Transmission Electron-Microscope (Tem). *Journal of Materials Science Letters* **4**(3), 327-330.
-

-
- Wolverson D. (1995) Raman Spectroscopy. In *An Introduction to Laser Spectroscopy* (ed. D. L. Andrews and A. A. Demidov), pp. 91-114. Plenum.
- Woodhead J. A., Rossman G. R., and Silver L. T. (1991a) The Metamictization of Zircon - Radiation Dose-Dependent Structural Characteristics. *American Mineralogist* **76**(1-2), 74-82.
- Woodhead J. A., Rossman G. R., and Thomas A. P. (1991b) Hydrous Species in Zircon. *American Mineralogist* **76**(9-10), 1533-1546.
- Wopenka B., Freeman J. J., and Grew E. (1999) Raman spectroscopic identification of B-free and B-rich kornerupine (prismatine). *American Mineralogist* **84**(4), 550-554.
- Wopenka B., Jolliff B. L., Zinner E., and Kremser D. T. (1996) Trace element zoning and incipient metamictization in a lunar zircon: Application of three microprobe techniques. *American Mineralogist* **81**(7-8), 902-912.
- Wopenka B. and Pasteris J. D. (1986) Limitations to Quantitative-Analysis of Fluid Inclusions in Geological Samples By Laser Raman Microprobe Spectroscopy. *Applied Spectroscopy* **40**(2), 144-151.
- Zhang M., Salje E. K. H., Capitani G. C., Leroux H., Clark A. M., Schluter J., and Ewing R. C. (2000b) Annealing of alpha-decay damage in zircon: a Raman spectroscopic study. *Journal of Physics-Condensed Matter* **12**(13), 3131-3148.
- Zhang M., Salje E. K. H., Ewing R. C., Farnan I., Rios S., Schluter J., and Leggo P. (2000c) Alpha-decay damage and recrystallization in zircon: evidence for an intermediate state from infrared spectroscopy. *Journal of Physics-Condensed Matter* **12**(24), 5189-5199.
- Zhang M., Salje E. K. H., Farnan I., Graeme-Barber A., Daniel P., Ewing R. C., Clark A. M., and Leroux H. (2000a) Metamictization of zircon: Raman spectroscopic study. *Journal of Physics-Condensed Matter* **12**(8), 1915-1925.
- Zhang R. Y. and Liou J. G. (1996) Coesite inclusions in dolomite from eclogite in the southern Dabie Mountains, China: The significance of carbonate minerals in UHPM rocks. *American Mineralogist* **81**(1-2), 181-186.
- Zoltai T. and Buerger M. J. (1959) The crystal structure of coesite, the dense, high-pressure form of silica. *Zeitschrift fur Kristallographie* **111**, 129-141.
-